Effects of Glaciation on Volcanism in Iceland

A Numerical Study

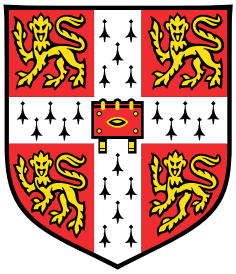

Isarapong Eksinchol

Department of Earth Sciences
University of Cambridge

This dissertation is submitted for the degree of
Doctor of Philosophy

Trinity College June 2019

To my loving parents.

Declaration

I hereby declare that this dissertation is the result of my own work and includes nothing which is the outcome of work done in collaboration except as declared in the Preface and specified in the text. It is not substantially the same as any that I have submitted, or, is being concurrently submitted for a degree or diploma or other qualification at the University of Cambridge or any other University or similar institution except as declared in the Preface and specified in the text. I further state that no substantial part of my dissertation has already been submitted, or, is being concurrently submitted for any such degree, diploma or other qualification at the University of Cambridge or any other University or similar institution except as declared in the Preface and specified in the text. This dissertation does not exceed 275 numbered pages of which not more than 225 pages are text, appendices, illustrations and bibliography.

Isarapong Eksinchol
June 2019

Acknowledgements

My thanks to Dr. John Rudge for all his patient guidance, encouragement and support throughout my time as his student. I have been extremely lucky to have a supervisor who responded to my questions and queries so promptly.

I would also like to thank my co-supervisor, Dr. John Maclennan, for numerous research ideas he has provided and all his invaluable advice with patience and kindness.

Lastly, this research would not have been possible without the financial support from the Cambridge Trust, the Leverhulme Trust, the Royal Thai Government and Trinity College.

Abstract

Volcanic eruption rates in Iceland during the last deglaciation increased 5–30 fold from the steady-state rates. This has been understood by the unloading of ice, which increases the decompression rates in the mantle, causing enhanced mantle melting rates. However, existing theoretical work cannot account for large variations of Rare Earth Element (REE) concentrations in the Icelandic lavas. Lavas erupted during the last deglaciation are depleted in REEs by up to 70%; whereas, existing models can only produce at most 20% depletion. This dissertation attempts to find the causes of this mismatch and provides the first models that take account of the diachronous response of volcanism to deglaciation.

Numerical models of mantle flow and mantle melting response to the glaciation and deglaciation are developed. A time-lag sampler is incorporated to represent the time lag between the melt production at depths and the eruption on the Earth's surface due to finite rate of melt transport. The model results for the last deglaciation in Iceland show that the variations of REE concentrations are strongly dependent on the melt ascent velocity. This explains the REE concentration mismatch between the previous theoretical work and the observations. Comparison between the model results (timing of the bursts in volcanic eruptions, REE concentration variations, and volume proportions of the subglacial, finiglacial and postglacial eruptions) and the observational data suggests that the melt ascent velocity during the last deglaciation beneath Iceland is of the order of $\sim$100 m/year.

The effects of glacial loading during the last glacial period on mantle melting are also investigated. It is found that glacial loading suppresses mantle melting and modulates the average REE concentrations in the melts due to the depth-dependent profile of mantle melting suppression. In addition, this dissertation explores how different deglaciation histories can result in different REE concentrations in the early-postglacial lavas. This may explain why lava shields formed during the Termination II have different geochemical compositions from that formed during the Termination I. Lastly, predictions for the future of the Icelandic volcanic eruption rates are made based on given estimated deglaciation rates of the current Icelandic glaciers.

Preface

Chapters 1 and 5 have been published in Eksinchol et al. (2019), which is a collaboration between my main supervisor (Dr. John F. Rudge), my co-supervisor (Dr. John Maclennan) and I. In Eksinchol et al. (2019), I am the developer of the numerical models under the supervision of Dr. John F. Rudge. Observational data used in this work are mainly gathered by Dr. John Maclennan from previous published works. I analyse and make comparison of the model results to the observational data under the guidance of Dr. John Maclennan.

Chapters 2 and 4 provide details of the theoretical works behind the numerical models of Eksinchol et al. (2019). Chapter 3 develops the Eksinchol et al. (2019) models further to include the effect of glacial loading on mantle melting. The model predictions of the glacial loading effect during the last glacial period are discussed in Chapter 6. Chapter 8 uses the Eksinchol et al. (2019) models to predict the future of the Icelandic volcanic eruption rates.

Table of contents

List of figures

List of tables

Chapter 1

Introduction

1.1 Deglaciation and volcanism in Iceland

Iceland is located where a mantle plume meets the Mid-Atlantic Ridge (White et al., 1992). The mantle plume and the spreading center are responsible for the upwelling of the mantle underneath Iceland, which induces decompression melting in the upper mantle (McKenzie and Bickle, 1988). This decompression melting produces magma that supplies the production of the Icelandic crust and volcanic eruptions. Geological observations indicate that eruption rates in the volcanic zones of Iceland were significantly elevated during a burst of activity that took place after the end of the last major deglaciation (Eason et al., 2015; Maclennan, 2008; Maclennan et al., 2002; Sigvaldason et al., 1992; Sinton et al., 2005; Slater et al., 1998). This period of high productivity, perhaps 30 times or more, may have started about 15 kyrBP and ended before 9 kyrBP.

The cause of the surge in eruption rates has been examined theoretically by Jull and McKenzie (1996). In their model, post-glacial rebound induced by the last deglaciation increases the rate of pressure drop in the upper mantle by up to 50-fold from the steady-state value. This increase in the decompression rate significantly increases the melting rate in the upper mantle, which leads to greater melt supply.

Jull and McKenzie (1996) also showed that the decompression rate due to post-glacial rebound has its maximum value at the surface and decays exponentially with depth. This means that the additional melt production in the mantle during the deglaciation occurs mostly at shallow depths. The melts generated at these depths are depleted in Rare Earth Elements (REEs). These additional melts produced during the deglaciation will therefore dilute the concentrations of REEs in the aggregated melts. By assuming that the melt transport is instantaneous, Jull and McKenzie (1996)

calculated that the REE concentrations in the melts decrease by around 20% during the last deglaciation compared to melts generated at other times when the ice-load is thought to have been close to steady-state. However, geological observations indicate that lavas erupted during the surge in volcanic eruption rates are depleted in REEs by up to $\approx 70\%$ (Eason et al., 2015; Maclennan, 2008; Maclennan et al., 2002; Sinton et al., 2005; Slater et al., 1998), which is significantly higher than that calculated by Jull and McKenzie (1996).

Slater et al. (1998) attempted to account for this mismatch by developing an inverse model similar to that of McKenzie and O'Nions (1991), which used the observed variations of REE concentrations to constrain the melt productivity function. Slater et al. (1998) showed that there exists a melt productivity function that matches the Jull and McKenzie (1996) theoretical variations of the REE concentrations with the geological data. However, in order for such a melt productivity function to exist, model parameters had to be modified including reducing the initial ice sheet radius to 90 km, which is significantly smaller than the likely radius of the ice sheet as inferred from observational studies (Hubbard et al., 2006; Licciardi et al., 2007; Patton et al., 2017; Pétursson et al., 2015; Sigmundsson, 1991).

Maclennan et al. (2002) previously used the relative timing of the last deglaciation and the surge in volcanic eruption rates in the Northern Volcanic Zone (NVZ) of Iceland to estimate that the melt ascent velocity is at least 50 m/yr. The Icelandic melt ascent velocity during the mid-Holocene has also been estimated from a time lag of ≈ 600 yr (Swindles et al., 2017) obtained from the cross-correlation between the Icelandic volcanic eruption rates and the change in the atmospheric circulation pattern indicated by sodium concentrations in Greenland Ice Sheet Project 2 (GISP2). This ≈ 600 yr time lag gives an estimated Icelandic melt ascent velocity of ≈ 50–100 m/yr during the mid-Holocene.

This dissertation investigates how the melt ascent velocity in the mantle and the crust influences the variations of REE concentrations. By incorporating a finite rate melt transport model into the model of Jull and McKenzie (1996), we show that variations of REE concentrations depend significantly on the melt ascent velocity. With an appropriate melt ascent velocity, our model demonstrates that the model variations of REE concentrations can be matched with those observed geologically. While Jull and McKenzie (1996) used a very simple ice-load model with a constant ice radius, our model combines an ice-load history with melt generation and transport and therefore enables prediction of the volumes and compositions of melt that are erupted either subglacially or in ice-free settings. This feature of the model allows for direct

comparison with geological observations, which use edifice geomorphology and volcanic facies analysis to determine whether an eruption is subglacial or not. Therefore, not only does this work help us understand how melt transport affects REE concentrations and eruption types in different places on Iceland, but also it can be useful as a tool to constrain the melt transport rate.

1.2 Outline of this work

In Chapters 2, 3 and 4, we develop numerical models of mantle flow and mantle melting response to the glaciation and deglaciation. A time-lag sampler is incorporated to represent the time-lag between the melt production at depths and the eruption on the Earth's surface due to finite rate of melt transport.

Chapter 5 explores how the finite rate of melt transport can affect the Lanthanum (La) concentrations and compares the model results (timing of the bursts in volcanic eruptions, La concentration variations and volume proportions of the subglacial, finiglacial and postglacial eruptions) for the last deglaciation in Iceland with the geological observations across three different volcanic zones: the Northern Volcanic Zone (NVZ), the Western Volcanic Zone (WVZ) and the Reykjanes Peninsula (REP or REYK). This Chapter explains the REE concentration mismatch between the previous theoretical work and the observations.

Chapter 6 studies the effects of glacial loading during the last glacial period on mantle melting. We find that glacial loading suppresses mantle melting and modulates the average La concentrations in the melts due to the depth-dependent profile of mantle melting suppression.

Chapter 7 investigates how different deglaciation histories can result in different La concentrations in the early-postglacial lavas. This may explain why lava shields formed during the Termination II have different geochemical compositions from that formed during the Termination I.

Finally, in Chapter 8, we make predictions for the future of the Icelandic volcanism based on given estimated deglaciation rates of the current Icelandic glaciers.

Chapter 2

Mantle Flow

2.1 Spreading-Ridge-Induced Mantle Flow

Mantle flow beneath a Mid-Ocean Ridge (MOR) is induced by the spreading ridge. In this work, we call it the *steady-state* mantle flow because it is unchanged with time provided that the spreading rate is constant. This steady-state flow proceeds even when there is no effect induced by the ice-load. We model the steady-state flow to follow the corner flow solution (Spiegelman and McKenzie, 1987). In this section, we present the derivation of the corner flow solution adopted from Batchelor (2000).

The mantle is assumed to be an incompressible Stokes fluid. That is, the governing equations of the flow are

1. the conservation of mass equation

$$0 = \boldsymbol{\nabla} \cdot \boldsymbol{v} \tag{2.1}$$

and

2. the Stokes equation

$$0 = -\boldsymbol{\nabla} p + \eta \nabla^2 \boldsymbol{v} + \rho_{\mathrm{s}} \boldsymbol{g}. \tag{2.2}$$

where $\boldsymbol{v}$ is the velocity field, p is the pressure, η is the viscosity of mantle, ρ_{s} is the density of mantle and $\boldsymbol{g}$ is the acceleration due to gravity.

Equation (2.1) implies that the velocity field can be written in terms of a vector potential as

$$\begin{aligned} \boldsymbol{v} &= \boldsymbol{\nabla} \times \boldsymbol{A} \\ &= \hat{\boldsymbol{x}} \left(\partial_y A_z - \partial_z A_y \right) + \hat{\boldsymbol{y}} \left(\partial_z A_x - \partial_x A_z \right) + \hat{\boldsymbol{z}} \left(\partial_x A_y - \partial_y A_x \right). \end{aligned} \tag{2.3}$$

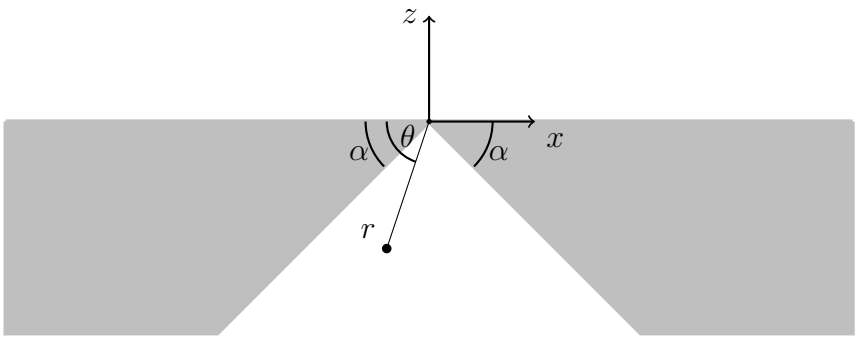

Fig. 2.1 Diagram illustrating the definition of the coordinates we use for deriving the corner flow solution. The origin is on the Earth's surface at the ridge. In Cartesian coordinates, x-axis is parallel to the Earth's surface and perpendicular to the ridge axis, y-axis is parallel to the ridge axis with positive direction pointing into the page, z-axis is perpendicular to the Earth's surface and is positive in the upward direction. In cylindrical polar coordinates, r is the radial distance from the ridge axis and θ is the angle measured counter-clockwise relative to the $-x$-axis in the vertical plane. Based on the right-hand grip rule, the polar axis is parallel to the ridge axis with positive direction of the unit vector $\hat{\boldsymbol{z}}_{\mathbf{p}}$ pointing out of the page ($\hat{\boldsymbol{z}}_{\mathbf{p}} = -\hat{\boldsymbol{y}}$).

Taking the curl of Equation (2.2), we get

$$\begin{aligned} 0 &= \eta\nabla^2\left(\boldsymbol{\nabla}\times\boldsymbol{v}\right) \\ &= \eta\nabla^2\left(\boldsymbol{\nabla}\times\left(\boldsymbol{\nabla}\times\boldsymbol{A}\right)\right) \\ &= \eta\nabla^2\left(\boldsymbol{\nabla}\left(\boldsymbol{\nabla}\cdot\boldsymbol{A}\right)-\nabla^2\boldsymbol{A}\right). \end{aligned} \tag{2.4}$$

Figure 2.1 illustrates the definition of the Cartesian and cylindrical polar coordinates we use in this section. By symmetry of the rift geometry, the y-component of the velocity field (v_y) is zero and the vector potential $\boldsymbol{A}$ is independent of y. The latter implies that $\partial_y A_i = 0\ \forall i$ and equation (2.3) can be reduced to

$$\boldsymbol{v} = -\partial_z A_y\hat{\boldsymbol{x}} + \partial_x A_y\hat{\boldsymbol{z}}. \tag{2.5}$$

The vector potential also reduces to $\boldsymbol{A} = A_y\hat{\boldsymbol{y}} = \psi\hat{\boldsymbol{z}}_{\mathbf{p}}$ (see Figure 2.1 for the definition of $\hat{\boldsymbol{z}}_{\mathbf{p}}$) and $\boldsymbol{\nabla}\cdot\boldsymbol{A} = \partial_y A_y = 0$. By substituting these into Equation (2.4) and dropping η and $\hat{\boldsymbol{z}}_{\mathbf{p}}$, we obtain the biharmonic equation

$$0 = \nabla^2\left(\nabla^2\psi\right). \tag{2.6}$$

The general solution to Equation (2.6) in cylindrical polar coordinates is known as the Michell solution (Michell, 1899)

$$\begin{aligned}\psi(r,\theta) = {} & A_0 r^2 + B_0 r^2 (\log r - 1) + C_0 \log r + D_0 \theta \\ & + \Big(A_1 r + B_1 r^{-1} + B_1' \theta r + C_1 r^3 + D_1 r \log r\Big) \cos\theta \\ & + \Big(E_1 r + F_1 r^{-1} + F_1' \theta r + G_1 r^3 + H_1 r \log r\Big) \sin\theta \\ & + \sum_{n=2}^{\infty} \Big(A_n r^n + B_n r^{-n} + C_n r^{n+2} + D_n r^{-n+2}\Big) \cos n\theta \\ & + \sum_{n=2}^{\infty} \Big(E_n r^n + F_n r^{-n} + G_n r^{n+2} + H_n r^{-n+2}\Big) \sin n\theta.\end{aligned}$$

For the corner flow, the continuity of velocity field at the lithosphere-asthenosphere boundary implies that the boundary conditions are

$$\frac{1}{r}\partial_\theta \psi = v_r = \begin{cases} +U_0 \cos\alpha, & \theta = \alpha, \\ +U_0 \cos\alpha, & \theta = \pi - \alpha, \end{cases}$$

and

$$-\partial_r \psi = v_\theta = \begin{cases} -U_0 \sin\alpha, & \theta = \alpha, \\ +U_0 \sin\alpha, & \theta = \pi - \alpha, \end{cases}$$

where we related ψ to $\boldsymbol{v}$ using the relation $\boldsymbol{v} = \boldsymbol{\nabla} \times (\psi \hat{\boldsymbol{z}}_{\mathbf{p}})$ with $\hat{\boldsymbol{z}}_{\mathbf{p}}$ being the unit vector along the positive z-axis of the cylindrical polar coordinates. $\hat{\boldsymbol{z}}_{\mathbf{p}} = -\hat{\boldsymbol{y}}$ according to the right-hand grip rule (see Figure (2.1)). U_0 is the half-spreading velocity of the ridge and α is the ridge angle from the horizontal.
By imposing the boundary conditions on the Michell solution, we obtain the stream function for the corner flow as

$$\psi(r,\theta) = B\, r \left[\left(\frac{\pi}{2} - \theta\right) \sin\theta - \sin^2\alpha \cos\theta\right] \tag{2.7}$$

where

$$B = \frac{2U_0}{\pi - 2\alpha - \sin(2\alpha)}.$$

In Cartesian coordinates,

$$\psi(x,z) = B\left[-z \arctan\frac{x}{z} + x \sin^2\alpha\right] \tag{2.8}$$

where x and z are related to r and θ by $x = -r\cos\theta$ and $z = -r\sin\theta$ (see Figure 2.1).

Let v_x be the horizontal velocity component perpendicular to the ridge, v_y be the horizontal velocity component parallel to the ridge and v_z be the velocity component in the upward direction. From Equation (2.5), we have $v_x = \partial_z \psi$, $v_y = 0$ and $v_z = -\partial_x \psi$. Hence, the corner flow solution in Cartesian coordinates is

$$\begin{aligned} v_x(x,y,z) &= \frac{B\,x\,z}{x^2+z^2} - B\arctan\left(\frac{x}{z}\right), \\ v_y(x,y,z) &= 0, \\ v_z(x,y,z) &= \frac{B\,z^2}{x^2+z^2} - B\sin^2(\alpha). \end{aligned} \tag{2.9}$$

Since $\boldsymbol{\nabla}\psi = \partial_x\psi\,\hat{\boldsymbol{x}} + \partial_z\psi\,\hat{\boldsymbol{z}} = -v_z\,\hat{\boldsymbol{x}} + v_x\,\hat{\boldsymbol{z}}$ is perpendicular to $\boldsymbol{v}$, the corner flow streamlines correspond to lines of constant stream function. From equations (2.7)–(2.8), We can eliminate r to obtain the corner flow streamlines in Cartesian coordinates in parameterized form as

$$\begin{aligned} x(\theta) &= \frac{-2\,(\psi/B)\cos\theta}{(\pi-2\theta)\sin\theta - 2\sin^2\alpha\,\cos\theta}, \\ \text{and}\;\; z(\theta) &= \frac{-2\,(\psi/B)\sin\theta}{(\pi-2\theta)\sin\theta - 2\sin^2\alpha\,\cos\theta}. \end{aligned}$$

$2(\psi/B)$ can be written in terms of the depth of the streamline at the lithosphere-asthenosphere boundary $z(\theta=\alpha) \equiv z_\alpha$ and $z(\theta=\pi-\alpha) \equiv z_{\pi-\alpha}$ as

$$2\,(\psi/B) = \begin{cases} -\left(\pi - 2\alpha - \sin 2\alpha\right) z_\alpha, & \theta \in \left[\alpha, \frac{\pi}{2}\right), \\ +\left(\pi - 2\alpha - \sin 2\alpha\right) z_{\pi-\alpha}, & \theta \in \left(\frac{\pi}{2}, \pi-\alpha\right]. \end{cases}$$

The streamlines equations then become

$$\begin{aligned} x(\theta) &= \begin{cases} \frac{(\pi-2\alpha-\sin 2\alpha)\,z_\alpha \cos\theta}{(\pi-2\theta)\sin\theta - 2\sin^2\alpha\,\cos\theta} & \text{for } \theta \in \left[\alpha, \frac{\pi}{2}\right), \\ \frac{-(\pi-2\alpha-\sin 2\alpha)\,z_{\pi-\alpha} \cos\theta}{(\pi-2\theta)\sin\theta - 2\sin^2\alpha\,\cos\theta} & \text{for } \theta \in \left(\frac{\pi}{2}, \pi-\alpha\right], \end{cases} \\ \text{and}\;\; z(\theta) &= \begin{cases} \frac{(\pi-2\alpha-\sin 2\alpha)\,z_\alpha \sin\theta}{(\pi-2\theta)\sin\theta - 2\sin^2\alpha\,\cos\theta} & \text{for } \theta \in \left[\alpha, \frac{\pi}{2}\right), \\ \frac{-(\pi-2\alpha-\sin 2\alpha)\,z_{\pi-\alpha} \sin\theta}{(\pi-2\theta)\sin\theta - 2\sin^2\alpha\,\cos\theta} & \text{for } \theta \in \left(\frac{\pi}{2}, \pi-\alpha\right]. \end{cases} \end{aligned} \tag{2.10}$$

We plot the corner flow streamlines on Figure (2.2).

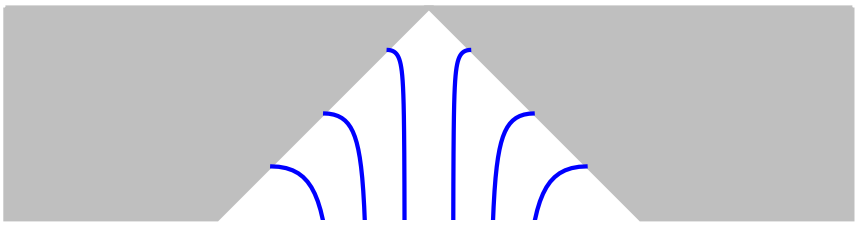

Fig. 2.2 Streamlines of the corner flow plotted using Equation (2.10). The coordinate axes layout is the same as in Figure 2.1.

2.2 Glacially-Induced Mantle Flow

In addition to the steady-state flow induced by the spreading ridge, the mantle can flow due to the change of the glacial load. This effect is known as Glacially-induced Isostatic Adjustment (GIA). In this section, we model the GIA response of the mantle to a prescribed glacial load.

We assume that the ice sheet has an axisymmetric shape. We model the mantle as a half-space filled with an incompressible viscous fluid. Therefore, this GIA model is based on the same governing equations to the corner flow solution (Equations (2.1) and (2.2))

$$0 = \boldsymbol{\nabla} \cdot \boldsymbol{v} \tag{2.11}$$

$$\text{and} \qquad 0 = -\boldsymbol{\nabla} p + \eta \nabla^2 \boldsymbol{v} + \rho_s \boldsymbol{g}. \tag{2.12}$$

Figure 2.3 illustrates the layout of the cylindrical polar coordinates (r, θ, z) we use in the GIA model. The z-axis coincides with the symmetry axis of the ice sheet. The positive direction of the z-axis is upwards perpendicular to the Earth's surface. When there is no load due to the ice sheet and the mantle is in isostatic equilibrium, the upper surface of the mantle is at $z = 0$ and the mantle extends from $z = 0$ to $z = -\infty$ (hence $z > 0$ above the Earth's surface).

Similar to the corner flow solution (Equation (2.3)), we write the velocity field in terms of the vector potential in cylindrical polar coordinates as

$$\begin{aligned} \boldsymbol{v} &= \boldsymbol{\nabla} \times \boldsymbol{A} \\ &= \hat{\boldsymbol{r}} \left(\frac{1}{r} \partial_\theta A_z - \partial_z A_\theta \right) + \hat{\boldsymbol{\theta}} \left(\partial_z A_r - \partial_r A_z \right) + \hat{\boldsymbol{z}} \left(\frac{1}{r} \partial_r \left(r A_\theta \right) - \frac{1}{r} \partial_\theta A_r \right). \end{aligned} \tag{2.13}$$

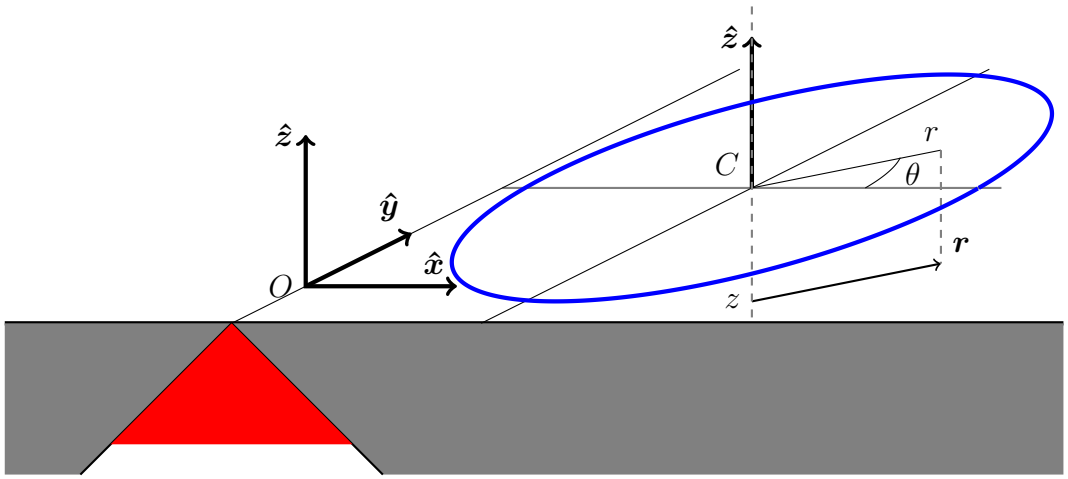

Fig. 2.3 Diagram illustrating the coordinate systems we use for the GIA (cylindrical polar coordinates) and the corner flow (Cartesian coordinates) modelling. The vertical cross-section shows the triangular-shaped melting region in red and the lithosphere in grey. The origin of the Cartesian coordinates for the corner flow modelling is at point O, which is on the unperturbed Earth's surface on the ridge axis. $\hat{\boldsymbol{x}}$ is horizontal and perpendicular to the ridge axis, $\hat{\boldsymbol{y}}$ is parallel to the ridge axis and $\hat{\boldsymbol{z}}$ is in the upward direction perpendicular to the Earth's surface. The blue circle drawn on the Earth's surface outlines a snapshot of the glacier terminus. The center of ice sheet is not necessarily on the ridge axis. The origin of the cylindrical polar coordinates for the GIA modelling is at point C, which is on the symmetry axis of the ice sheet at the unperturbed Earth's surface level. The cylindrical polar axis overlaps with the symmetry axis of the ice sheet. r is the radial distance from the cylindrical polar axis. θ is the cylindrical polar angle measured relative to the x-axis. $z < 0$ below the Earth's surface.

where $\hat{\boldsymbol{r}}$ is the radial unit vector, $\hat{\boldsymbol{\theta}}$ is the unit vector in the azimuthal direction and $\hat{\boldsymbol{z}}$ the unit vector in the $+z$ direction.

Due to cylindrical symmetry of the system, the velocity field has zero component in the azimuthal direction ($v_\theta = 0$) and the vector potential is independent of θ ($\partial_\theta A_i = 0$ $\forall i$). Equation (2.13) therefore reduces to

$$\begin{aligned} \boldsymbol{v} &= v_r \hat{\boldsymbol{r}} + v_z \hat{\boldsymbol{z}} \\ &= -\hat{\boldsymbol{r}} \partial_z A_\theta + \hat{\boldsymbol{z}} \frac{1}{r} \partial_r \left(r A_\theta \right). \end{aligned} \tag{2.14}$$

and the vector potential reduces to $\boldsymbol{A} = A_\theta \hat{\boldsymbol{\theta}}$.

By taking the curl of Equation (2.12) and noting that $\boldsymbol{\nabla} \cdot \boldsymbol{A} = \partial_\theta A_\theta / r = 0$, we get

$$\begin{aligned} 0 &= \eta \nabla^2 (\boldsymbol{\nabla} \times \boldsymbol{v}) \\ &= \eta \nabla^2 (\boldsymbol{\nabla} \times (\boldsymbol{\nabla} \times \boldsymbol{A})) \\ &= \eta \nabla^2 \left(\boldsymbol{\nabla} (\boldsymbol{\nabla} \cdot \boldsymbol{A}) - \nabla^2 \boldsymbol{A} \right) \\ &= -\eta \nabla^2 \nabla^2 \boldsymbol{A} \\ &= -\eta \nabla^2 \nabla^2 \left(A_\theta \hat{\boldsymbol{\theta}} \right). \end{aligned} \tag{2.15}$$

By re-writing $A_\theta = \psi / r$ in Equation (2.15) and dropping $-\eta$, we obtain

$$\begin{aligned} 0 &= \nabla^2 \nabla^2 \left(\frac{\psi}{r} \hat{\boldsymbol{\theta}} \right) \\ &= \hat{\boldsymbol{\theta}} \left(\nabla^2 - \frac{1}{r^2} \right) \left(\nabla^2 - \frac{1}{r^2} \right) \frac{\psi}{r} \\ &= \hat{\boldsymbol{\theta}} \left(\frac{E^2 E^2 \psi}{r} \right) \end{aligned}$$

where

$$E^2 = r \frac{\partial}{\partial r} \left(\frac{1}{r} \frac{\partial}{\partial r} \right) + \frac{\partial^2}{\partial z^2}.$$

Therefore,

$$0 = E^2 E^2 \psi \tag{2.16}$$

with (from equation (2.14))

$$v_r = -\frac{1}{r} \frac{\partial \psi}{\partial z} \qquad \text{and} \qquad v_z = \frac{1}{r} \frac{\partial \psi}{\partial r}. \tag{2.17}$$

Equation (2.16) is a 4^{th}-order Partial Differential Equation (PDE). In order to solve this PDE, we let $E^2 \psi \equiv \chi$. Equation (2.16) then becomes

$$0 = E^2 \chi = \left(E_r^2 + \partial_z^2 \right) \chi \tag{2.18}$$

where $E_r^2 = r \frac{\partial}{\partial r} \left(\frac{1}{r} \frac{\partial}{\partial r} \right)$.
This equation can be solved by the method of separation of variables. We substitute $\chi(r, z) = R(r) Z(z)$ into it and divide both sides by $R(r) Z(z)$ to obtain

$$0 = \frac{E_r^2 R(r)}{R(r)} + \frac{\partial_z^2 Z(z)}{Z(z)}. \tag{2.19}$$

On the right-hand side of this equation, the first term is a function of r only and the second term is a function of z only. Both terms can only add to zero for all r and z if each of the terms is equal to a constant $\frac{\partial_z^2 Z(z)}{Z(z)} = m$ and $\frac{E_r^2 R(r)}{R(r)} = -m$. By the separation of variable, the PDE is transformed into two coupling Ordinary Differential Equations (ODEs). $\frac{\partial_z^2 Z(z)}{Z(z)} = m$ implies

$$Z(z) = \begin{cases} a_- \sin(kz) + b_- \cos(kz), & m \equiv -k^2 < 0, \\ a_0 z + b_0, & m = 0, \\ a_+ e^{kz} + b_+ e^{-kz}, & m \equiv k^2 > 0. \end{cases}$$

From equation (2.17), we can write χ in terms of v_r and v_z as

$$\begin{aligned} \chi \equiv \left(E_r^2 + \partial_z^2\right)\psi &= r\partial_r v_z - r\partial_z v_r \\ &= -r\hat{\boldsymbol{\theta}} \cdot (\boldsymbol{\nabla} \times \boldsymbol{v}) \\ &= -r\hat{\boldsymbol{\theta}} \cdot \boldsymbol{\omega} \end{aligned} \tag{2.20}$$

where $\boldsymbol{\omega} = \boldsymbol{\nabla} \times \boldsymbol{v}$ is the vorticity. The requirement that the vorticity decays to zero as z goes to $-\infty$ means that $\chi \to 0$ as $z \to -\infty$. This implies that $Z(z) \sim e^{kz}$. So,

$$\begin{aligned} &\frac{E_r^2 R(r)}{R(r)} = -k^2 \\ &\Rightarrow R(r) = ar\mathrm{J}_1(kr) + br\mathrm{Y}_1(kr) \end{aligned}$$

where J_1 and Y_1 are the 1^{st}-order Bessel function of the first and second kind respectively. Since $\mathrm{Y}_1(kr) \to -\infty$ as $r \to 0$, the requirement that the vorticity (equation (2.20)) is finite at $r = 0$ implies that the $r\mathrm{Y}_1(kr)$ term in $R(r)$ vanishes ($b = 0$). So, $R(r) \sim r\mathrm{J}_1(kr)$ and

$$\chi(r, z) = \int_0^\infty \tilde{\chi}(k)\, e^{kz} r\mathrm{J}_1(kr)\mathrm{d}k$$

where the integration integrates all the possible terms together, each of the terms is weighted by the amplitude $\tilde{\chi}(k)$, which is determined by the boundary conditions.

From the definition $E^2\psi = \chi$, we therefore have

$$E^2\psi = \int_0^\infty \tilde{\chi}(k)\, e^{kz} r\mathrm{J}_1(kr)\mathrm{d}k. \tag{2.21}$$

This is an inhomogeneous 2$^{\text{nd}}$-order PDE. The complementary solution $\psi_{\text{c}}(r,z)$ satisfies $E^2\psi_{\text{c}} = 0$, which is in the same form as equation (2.18). $\psi_{\text{c}}(r,z)$ can therefore be found by the method of separation of variables similar to that used for finding $\chi(r,z)$. The requirements that $v_r = -\frac{1}{r}\partial_z\psi$ and $v_z = \frac{1}{r}\partial_r\psi$ are finite at $r = 0$ and that they both decay to zero as z approaches $-\infty$ imply that

$$\psi_{\text{c}}(r,z) = \int_0^\infty \tilde{\psi}_{\text{c}}(k)\, e^{kz} r \mathrm{J}_1(kr) \mathrm{d}k \tag{2.22}$$

where $\tilde{\psi}_{\text{c}}(k)$ is determined by the boundary conditions.
For the particular integral, it can be verified by direct substitution of $\psi = \psi_{\text{p}}(r,z)$ into equation (2.21) that

$$\psi_{\text{p}}(r,z) = \int_0^\infty \frac{\tilde{\chi}(k)}{2k}\, z e^{kz} r \mathrm{J}_1(kr) \mathrm{d}k \tag{2.23}$$

makes the left-hand side of equation (2.21) equal to the right-hand side. Hence, the general solution to equation (2.21) is

$$\begin{aligned}
\psi(r,z) &= \psi_{\text{c}}(r,z) + \psi_{\text{p}}(r,z) \\
&= \int_0^\infty \left(\tilde{\psi}_{\text{c}}(k) + \frac{\tilde{\chi}(k)}{2k}\, z \right) e^{kz} r \mathrm{J}_1(kr) \mathrm{d}k \\
&= \int_0^\infty \left(A(k) + B(k)\, z \right) e^{kz} r \mathrm{J}_1(kr)\, k \, \mathrm{d}k
\end{aligned} \tag{2.24}$$

where we have replaced $\tilde{\psi}_{\text{c}}(k)$ by $k\,A(k)$ and $\tilde{\chi}(k)$ by $2k^2\,B(k)$ for simplicity in the following analysis. Both $A(k)$ and $B(k)$ can be determined by the boundary conditions.

By substituting ψ from equation (2.24) into equation (2.17), we get

$$\begin{aligned}
& v_r = -\int_0^\infty (B + kA + kBz)\, e^{kz} J_1(kr)\, k \, \mathrm{d}k \\
\text{and} \qquad & v_z = \int_0^\infty k(A + Bz)\, e^{kz} J_0(kr)\, k \, \mathrm{d}k.
\end{aligned} \tag{2.25}$$

In order to obtain an expression for the pressure field, we substitute v_r and v_z from equation (2.25) into equation (2.12) and then solve for p. This gives

$$p = -\rho_{\text{s}} g z + 2\eta \int_0^\infty kB\, e^{kz} J_0(kr)\, k \, \mathrm{d}k. \tag{2.26}$$

With an ice load, the surface of the fluid will be displaced from $z = 0$. Let the perturbed surface be at $z = \epsilon(r,t)$, which is dependent on time t and the radial distance r from the center of the ice. Assuming that the surface deformation is small compared to the extend of the ice sheet ($k\epsilon \ll 1$), we will keep only the leading order terms in $k\epsilon$ in the remaining analysis.

Two unknowns, A and B, are constrained by the following boundary conditions:

1. shear stress on the perturbed surface is zero: $\sigma_{rz} = 0$ at $z = \epsilon$,
2. normal stress on the perturbed surface is equal to the ice load: $\sigma_{zz} = -\rho_{\mathrm{i}} g h(r,t)$ at $z = \epsilon$,

where ρ_{i} is the density of ice and $h(r,t)$ is the ice-thickness profile.

From $\sigma_{ij} = -P\delta_{ij} + \eta\left(\frac{\partial v_i}{\partial x_j} + \frac{\partial v_j}{\partial x_i}\right)$, we have

$$\begin{aligned}\sigma_{rz} &= \eta\left(\frac{\partial v_r}{\partial z} + \frac{\partial v_z}{\partial r}\right) \\ &= -2\eta\int_0^\infty k(B + kA + kBz)\, e^{kz} J_1(kr)\, k\,\mathrm{d}k \end{aligned} \tag{2.27}$$

and

$$\begin{aligned}\sigma_{zz} &= -P + 2\eta\frac{\partial v_z}{\partial z} \\ &= \rho_{\mathrm{s}} g z + 2\eta\int_0^\infty k^2(A + Bz)\, e^{kz} J_0(kr)\, k\,\mathrm{d}k. \end{aligned} \tag{2.28}$$

Therefore, applying the zero shear stress boundary condition $\sigma_{rz} = 0$ at the perturbed surface $z = \epsilon$ on equation (2.27) implies that

$$B + kA = 0. \tag{2.29}$$

The normal stress boundary condition $\sigma_{zz} = -\rho_{\mathrm{i}} g h(r,t)$ at the perturbed surface $z = \epsilon$ imposed on equation (2.28) combined with equation (2.29) implies

$$-\rho_{\mathrm{i}} g h(r,t) = \rho_{\mathrm{s}} g\, \epsilon(r,t) - 2\eta\int_0^\infty kB J_0(kr)\, k\,\mathrm{d}k. \tag{2.30}$$

By using the relation $\int_0^\infty kr\, J_\nu(kr) J_\nu(k'r)\,\mathrm{d}r = \delta(k - k')$, we can invert equation (2.30) to obtain

$$B = \frac{1}{\tau}\left(\frac{\rho_{\mathrm{i}}\widetilde{h}}{\rho_{\mathrm{s}}} + \widetilde{\epsilon}\right) \tag{2.31}$$

where $\tau = \frac{2\eta k}{\rho_s g}$ is the rebound time constant,

$$\widetilde{h} = \widetilde{h}(k,t) = \int_0^\infty h(r,t)\, J_0(kr)\, r\, \mathrm{d}r$$

and

$$\widetilde{\epsilon} = \widetilde{\epsilon}(k,t) = \int_0^\infty \epsilon(r,t)\, J_0(kr)\, r\, \mathrm{d}r$$

are the zeroth-order Hankel transform of the ice-thickness profile $h(r,t)$ and the surface deformation function $\epsilon(r,t)$ respectively.
Combining equation (2.31) with equation (2.29) gives

$$A = -\frac{1}{k\tau}\left(\frac{\rho_i \widetilde{h}}{\rho_s} + \widetilde{\epsilon}\right). \tag{2.32}$$

Substituting A and B from equation (2.32) and equation (2.31) respectively into equation (2.25) and equation (2.26) gives

$$v_r(r,z,t) = -\int_0^\infty \frac{1}{\tau}\left(\frac{\rho_i \widetilde{h}}{\rho_s} + \widetilde{\epsilon}\right) kz\, e^{kz} J_1(kr)\, k\, \mathrm{d}k, \tag{2.33}$$

$$v_z(r,z,t) = -\int_0^\infty \frac{1}{\tau}\left(\frac{\rho_i \widetilde{h}}{\rho_s} + \widetilde{\epsilon}\right) (1-kz)\, e^{kz} J_0(kr)\, k\, \mathrm{d}k \tag{2.34}$$

and

$$p(r,z,t) = -\rho_s g z + \underbrace{\rho_s g \int_0^\infty \left(\frac{\rho_i \widetilde{h}}{\rho_s} + \widetilde{\epsilon}\right) e^{kz} J_0(kr)\, k\, \mathrm{d}k}_{p_1}. \tag{2.35}$$

On the right-hand side of equation (2.35), the first term is the lithostatic pressure $-\rho_s g z \equiv p_0$. The second term $\equiv p_1$ is the pressure induced by the ice load.

The surface uplift velocity $= \frac{\partial \epsilon}{\partial t}(r,t)$ is equal to the vertical component of the mantle flow velocity v_z at the perturbed surface. That is,

$$\begin{aligned}
\frac{\partial \epsilon}{\partial t} &= v_z\,|_{z=\epsilon} \\
&= -\int_0^\infty \frac{1}{\tau}\left(\frac{\rho_i \widetilde{h}}{\rho_s} + \widetilde{\epsilon}\right) (1-k\epsilon)\, e^{k\epsilon} J_0(kr)\, k\, \mathrm{d}k \\
&\approx -\int_0^\infty \frac{1}{\tau}\left(\frac{\rho_i \widetilde{h}}{\rho_s} + \widetilde{\epsilon}\right) J_0(kr)\, k\, \mathrm{d}k
\end{aligned} \tag{2.36}$$

where we use equation (2.34) to obtain the second line from the first line and we neglect the higher-order terms in $k\epsilon$ from the the second line to the third line.

This equation can be inverted by using the relation $\int_0^\infty kr\, J_\nu(kr) J_\nu(k'r)\,\mathrm{d}r = \delta(k-k')$ to obtain

$$\frac{\partial \widetilde{\epsilon}}{\partial t} = -\frac{1}{\tau}\left(\frac{\rho_\mathrm{i}\widetilde{h}}{\rho_\mathrm{s}} + \widetilde{\epsilon}\right) \tag{2.37}$$

where

$$\frac{\partial \widetilde{\epsilon}}{\partial t} = \frac{\partial \widetilde{\epsilon}}{\partial t}(k,t) = \int_0^\infty \frac{\partial \epsilon}{\partial t}(r,t)\, J_0(kr)\, r\,\mathrm{d}r$$

is the zeroth-order Hankel transform of $\frac{\partial \epsilon}{\partial t}(r,t)$.

Then, by performing the Laplace transform on both sides of equation (2.37) from the time domain t to the complex frequency domain s, we obtain

$$s\,\widehat{\widetilde{\epsilon}} - \widetilde{\epsilon}|_{t=0} = -\frac{1}{\tau}\left(\frac{\rho_\mathrm{i}\widehat{\widetilde{h}}}{\rho_\mathrm{s}} + \widehat{\widetilde{\epsilon}}\right)$$

where

$$\widehat{\widetilde{h}} = \widehat{\widetilde{h}}(k,s) = \int_0^\infty \widetilde{h}(k,t)\, e^{-st}\,\mathrm{d}t$$

and

$$\widehat{\widetilde{\epsilon}} = \widehat{\widetilde{\epsilon}}(k,s) = \int_0^\infty \widetilde{\epsilon}(k,t)\, e^{-st}\,\mathrm{d}t$$

are the Laplace transform of $\widetilde{h}(k,t)$ and $\widetilde{\epsilon}(k,t)$ respectively.
Therefore,

$$\widehat{\widetilde{\epsilon}}(k,s) = \left(\frac{1}{s\tau+1}\right)\left(-\frac{\rho_\mathrm{i}\widehat{\widetilde{h}}}{\rho_\mathrm{s}} + \tau\,\widetilde{\epsilon}|_{t=0}\right) \tag{2.38}$$

and

$$\frac{1}{\tau}\left(\frac{\rho_\mathrm{i}\widehat{\widetilde{h}}}{\rho_\mathrm{s}} + \widehat{\widetilde{\epsilon}}\right) = \left(\frac{1}{s\tau+1}\right)\left(\frac{s\,\rho_\mathrm{i}\widehat{\widetilde{h}}}{\rho_\mathrm{s}} + \widetilde{\epsilon}|_{t=0}\right). \tag{2.39}$$

If we set the initial time $t=0$ to be at when the system is in isostatic equilibrium then $\rho_\mathrm{i} g\widetilde{h}\,|_{t=0} = -\rho_\mathrm{s} g\widetilde{\epsilon}|_{t=0}$ and equation (2.39) will simplify to

$$\begin{aligned}\frac{1}{\tau}\left(\frac{\rho_\mathrm{i}\widehat{\widetilde{h}}}{\rho_\mathrm{s}} + \widehat{\widetilde{\epsilon}}\right) &= \frac{\rho_\mathrm{i}}{\rho_\mathrm{s}}\left(\frac{1}{s\tau+1}\right)\left(s\,\widehat{\widetilde{h}} - \widetilde{h}\,|_{t=0}\right) \\ &= \frac{\rho_\mathrm{i}}{\rho_\mathrm{s}}\left(\frac{1}{s\tau+1}\right)\widehat{\left(\frac{\partial \widetilde{h}}{\partial t}\right)}\end{aligned} \tag{2.40}$$

where

$$\widehat{\left(\frac{\partial \widetilde{h}}{\partial t}\right)} = \widehat{\left(\frac{\partial \widetilde{h}}{\partial t}\right)}(k,s) = \int_0^\infty \left(\frac{\partial \widetilde{h}}{\partial t}(k,t)\right) e^{-st}\,\mathrm{d}t$$

is the Laplace transform of $\frac{\partial \widetilde{h}}{\partial t}(k,t)$.

By applying the inverse Laplace transform on equation (2.40), we obtain

$$\frac{1}{\tau}\left(\frac{\rho_\mathrm{i}\widetilde{h}}{\rho_\mathrm{s}} + \widetilde{\epsilon}\right) = \frac{\rho_\mathrm{i}}{\rho_\mathrm{s}} \int_0^t \left(\frac{\partial \widetilde{h}}{\partial t}(k,t')\right) e^{-(t-t')/\tau}\,\mathrm{d}t'/\tau.$$

Substituting this expression into equation (2.33), (2.34) and (2.35) yields

$$v_r(r,z,t) = -\frac{\rho_\mathrm{i}}{\rho_\mathrm{s}} \int_0^\infty \tilde{w}(k,t)\, kz\, e^{kz} J_1(kr)\, k\,\mathrm{d}k, \tag{2.41}$$

$$v_z(r,z,t) = -\frac{\rho_\mathrm{i}}{\rho_\mathrm{s}} \int_0^\infty \tilde{w}(k,t)\,(1-kz)\, e^{kz} J_0(kr)\, k\,\mathrm{d}k \tag{2.42}$$

and

$$p(r,z,t) = -\rho_\mathrm{s} g z + \underbrace{\rho_\mathrm{i} g \int_0^\infty \tau\, \tilde{w}(k,t)\, e^{kz} J_0(kr)\, k\,\mathrm{d}k}_{p_1} \tag{2.43}$$

where

$$\tilde{w}(k,t) = \int_0^t \left(\frac{\partial \widetilde{h}}{\partial t}(k,t')\right) e^{-(t-t')/\tau}\,\mathrm{d}t'/\tau. \tag{2.44}$$

These formulae are based on the assumption that at time $t = 0$ the system is in isostatic equilibrium. In many cases, however, it is more convenient to set the time origin $t = 0$ at when the system is *not* in isostatic equilibrium. In this case, the only modification needed for all the formulae we derived above is the lower limit of integration on the right-hand side of equation (2.44), which has now changed from 0 to t_iso = time when the system is in isostatic equilibrium.

In summary, the semi-analytical solutions to the axi-symmetric GIA response in the viscous half-space mantle are

$$
\begin{aligned}
v_r(r,z,t) &= -\frac{\rho_\mathrm{i}}{\rho_\mathrm{s}}\,\mathcal{H}_1^{-1}\left[kz\,e^{kz}\,\widetilde{w}(k,t)\right],\\
v_\theta(r,z,t) &= 0\,,\\
v_z(r,z,t) &= -\frac{\rho_\mathrm{i}}{\rho_\mathrm{s}}\,\mathcal{H}_0^{-1}\left[(1-kz)\,e^{kz}\,\widetilde{w}(k,t)\right],\\
p\,(r,z,t) &= -\rho_\mathrm{s} g z + \rho_\mathrm{i} g\,\mathcal{H}_0^{-1}\left[\tau\,e^{kz}\,\widetilde{w}(k,t)\right],\\
\frac{Dp}{Dt}\,(r,z,t) &= \rho_\mathrm{i} g\,\mathcal{H}_0^{-1}\left[e^{kz}\,\left(\mathcal{H}_0[\dot{h}](k,t) - kz\,\widetilde{w}(k,t)\right)\right],
\end{aligned}
\tag{2.45}
$$

where

$$
\begin{aligned}
\tau \equiv \tau(k) &= \frac{2\,\eta\,k}{\rho_\mathrm{s}\,g}\,,\\
\widetilde{w}\,(k,t) &= \int_{t_\mathrm{iso}}^{t}\left(\mathcal{H}_0[\dot{h}](k,t')\right)\,\exp\left(-\frac{t-t'}{\tau}\right)\mathrm{d}t'/\tau\,,\\
\mathcal{H}_n[f](k) &= \int_0^\infty f(r)\,\mathrm{J}_n(kr)\,r\,\mathrm{d}r\,,\\
\mathcal{H}_n^{-1}[F](r) &= \int_0^\infty F(k)\,\mathrm{J}_n(kr)\,k\,\mathrm{d}k\,.
\end{aligned}
$$

v_r is the radial component of the velocity, v_θ is the azimuthal component of the velocity, v_z is the vertical component of the velocity, p is the pressure in the mantle, $\frac{Dp}{Dt}$ is the convective derivative of the pressure p, ρ_i is the density of ice, ρ_s is the density of the mantle, $\dot{h}$ is the time-derivative of the thickness of ice sheet, $\mathcal{H}_n[f]$ is the n^{th}-order Hankel transform of function f, $\mathcal{H}_n^{-1}[F]$ is the n^{th}-order inverse Hankel transform of function F and J_n is the n^{th}-order Bessel function of the first kind. t_iso in the $\widetilde{w}\,(k,t)$ expression is the time at which the mantle is in isostatic equilibrium.

We assume that the GIA response and the corner flow superimpose linearly. Hence, the net rate of change of pressure is the sum of the corner flow ($(Dp/Dt)_\mathrm{CF} = -\rho_\mathrm{s} g\,v_{z_{CF}}$)

and the GIA ($(Dp/Dt)_{\mathrm{GIA}}$):

$$\begin{aligned}\left(\frac{Dp}{Dt}\right)_{\mathrm{net}} &= \left(\frac{Dp}{Dt}\right)_{\mathrm{CF}} + \left(\frac{Dp}{Dt}\right)_{\mathrm{GIA}} \\ &= -\rho_{\mathrm{s}} g \left(\frac{B\,z^2}{x^2+z^2} - B\sin^2(\alpha)\right) \\ &\quad + \rho_{\mathrm{i}} g \int_0^\infty \left[\frac{\partial \widetilde{h}}{\partial t}(k,t) \underbrace{-kz \int_0^t \left(\frac{\partial \widetilde{h}}{\partial t}(k,t')\right) e^{-(t-t')/\tau}\,\mathrm{d}t'/\tau}_{\text{rebound response}}\right] e^{kz} J_0(kr)\, k\,\mathrm{d}k.\end{aligned} \tag{2.46}$$

On the right-hand side of Equation (2.46), the first term is the steady-state decompression rate due to the corner flow upwelling induced by the spreading ridge. The second term is the compression rate induced by the change of the glacial load. The glacially-induced compression rate consists of two terms inside the square bracket. The first term is the instantaneous response to the change of the ice load. The second term is the rebound response, which is delayed from the time the ice load changes with time constant $\tau = 2\eta k/\rho_{\mathrm{s}} g$ due to finite rebound time of the mantle. The exponential factor e^{kz} in the integrand indicates that the influence of the ice load decays exponentially with depth.

Equation (2.46) can be written in Cartesian coordinate system by substituting $r = \sqrt{(x-x_C)^2 + (y-y_C)^2}$ where $(x_C,\ y_C)$ is the location of point C relative to the origin O. Vector quantities such as the velocity field can be converted from the cylindrical polar coordinates to the Cartesian coordinates by decomposing the vector into components along the Cartesian axes based on the following standard relations:

$$\begin{aligned} \hat{\boldsymbol{r}} &= +\cos\theta\,\hat{\boldsymbol{x}} + \sin\theta\,\hat{\boldsymbol{y}}, \\ \hat{\boldsymbol{\theta}} &= -\sin\theta\,\hat{\boldsymbol{x}} + \cos\theta\,\hat{\boldsymbol{y}} \\ \text{and} \qquad \hat{\boldsymbol{z}} &= \hat{\boldsymbol{z}} \end{aligned}$$

where $\cos\theta = \frac{x-x_C}{r}$ and $\sin\theta = \frac{y-y_C}{r}$.

Chapter 3

Mantle Melting

3.1 Introduction

Mantle upwelling in Mid-Ocean Ridge (MOR) system is relatively fast compared to the rate of heat diffusion. This can be quantified by the Peclet number

$$Pe = \frac{v\,l}{\kappa}$$

where v is the mantle flow velocity, l is a length scale and κ is the thermal diffusivity. The Peclet number is the ratio of the heat advection to the heat diffusion. In a MOR system, $v \approx 10$ mm/yr, $l \approx 100$ km and $\kappa \approx 10^{-6}$ m^2/s. This implies that $Pe \approx 30$ and the heat advection dominates the heat diffusion. Decompression melting in the mantle is therefore very close to an adiabatic process. Heat gain or loss due to heat diffusion can be neglected. Hence, the mantle melting rate DF/Dt can be calculated by (Jull and McKenzie, 1996)

$$\frac{DF}{Dt} = \left(\frac{\partial F}{\partial p}\right)_s \frac{Dp}{Dt} \tag{3.1}$$

where F is the degree of melting by mass fraction relative to the initial mass of the solid mantle, $(\partial F/\partial p)_s$ is the isentropic (=adiabatic+reversible) melt productivity of the mantle and $\frac{D}{Dt}$ is the convective derivative following the solid mantle trajectories. That is, equation (3.1) assumes that the melting is adiabatic and reversible.

Decompression melting in the mantle is near fractional. When the mantle undergoes decompression melting, the melt produced is extracted and the solidus pressure and temperature decrease. The temperature drop of the solid phase is due to the latent heat loss to the melt.

Equation (3.1) assumes that the solid phase is on the solidus and that the rate of change of pressure Dp/Dt is negative (i.e. decompression melting). The assumption that Dp/Dt is negative holds true in deglaciation periods or in the periods when the glacial loading is at a rate that is not high enough to cause the glacially-induced compression rate ($(Dp/Dt)_{GIA}$) to exceed the magnitude of the background steady-state decompression rate ($(Dp/Dt)_{MOR}$) induced by the spreading ridge.

If the glacial loading rate is sufficiently high, the net rate of change of pressure

$$\frac{Dp}{Dt} = \left(\frac{Dp}{Dt}\right)_{GIA} + \left(\frac{Dp}{Dt}\right)_{MOR}$$

will be positive and Equation (3.1) can no longer be applied. A net positive Dp/Dt will increase the pressure of the solid phase adiabatically and will shift the solid phase off the solidus. Because the solid phase is no longer on the solidus, the melting will not readily recommence when the net Dp/Dt has reversed back to a negative value (decompression). The solid mantle will need to be brought back to the solidus by decompression before the melting can proceed again. This means that, a numerical model of the glacial loading/unloading effects on mantle melting that contains a sufficiently rapid glacial advance period must take this non-linear sub-solidus effect into account. In the following section, we present the numerical methods we use for calculating the mantle melting rate.

3.2 Numerical Methods

In the thermodynamic system we are considering, both the compression ($Dp/Dt > 0$) and decompression ($Dp/Dt < 0$) in the mantle are adiabatic. Heat loss due to heat diffusion is relatively small due to a high Peclet number. This means that, in the system we are modelling, the potential temperature and hence the solidus pressure of the mantle will not change when the mantle is not melting. We divide our thermodynamic model into the following 3 scenarios:

1. Adiabatic decompression ($Dp/Dt < 0$) on the solidus: The mantle will undergo decompression melting. The melting rate will follow equation (3.1). The degree of melting F, entropy S and solidus pressure p_s will increase, decrease and decrease respectively (path BC on Figure 3.1a).

2. Adiabatic decompression ($Dp/Dt < 0$) at sub-solidus: The mantle will *not* be melting. So, F, S and p_s at the same S will remain unchanged (Stolper and Asimow, 2007) (path AB on Figure 3.1a).

3. Adiabatic compression ($Dp/Dt > 0$): The mantle will *not* be melting. So, F, S and p_s at the same S will remain unchanged (Stolper and Asimow, 2007) (path BA and CD on Figure 3.1b).

We can see that, in this system, which consists of only these 3 possible scenarios, there is a one-to-one relationship between the degree of melting F and the entropy S. Therefore, the solidus pressure p_s, which is a function of the entropy ($p_s = p_s(S)$) can be considered as a function of the degree of melting ($p_s = p_s(F)$). As the mantle melts, p_s and the solidus depth of the residual solid mantle decrease. p_s at $F = 0$ is called the **primitive solidus pressure** and the solidus depth of the mantle with $F = 0$ is called the **primitive solidus depth**.

When the mantle is not melting, its composition at its solidus will not change. Even though the mantle may undergo phase transition as it is compressed away from the solidus, once the mantle has returned back to the solidus, the phase will return back to that at the last time it was on the solidus. This is because the pressure and temperature at the solidus remain unchanged when the mantle is not melting. Hence, in this mantle melting modelling, the composition and phase of the mantle at the solidus are also functions of the degree of melting F. The conclusion is that the solidus pressure and the composition and phase at the solidus can be determined from the degree of melting F.

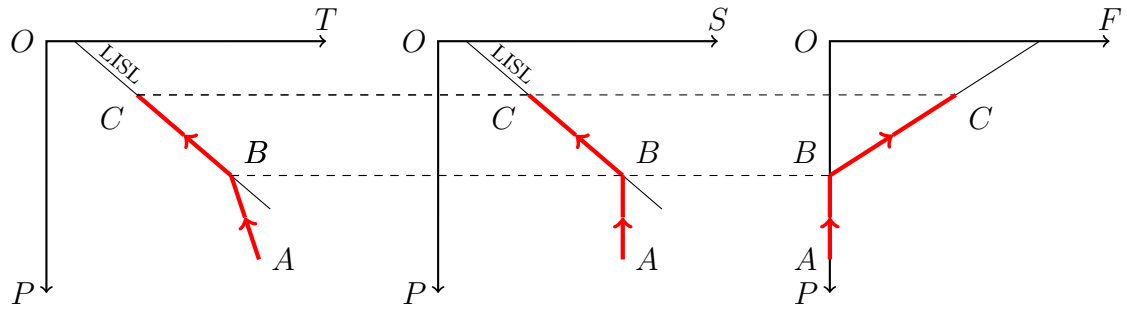

(a) Decompression

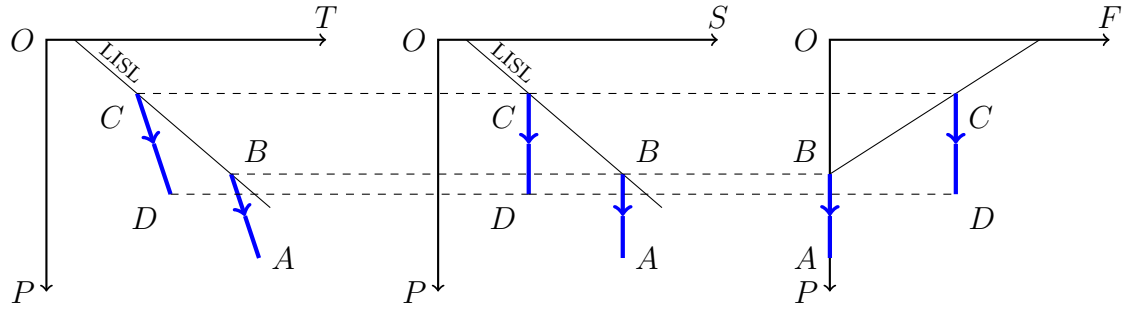

(b) Compression

Fig. 3.1 P-T, P-S and P-F diagrams showing paths of solid mantle during (a) adiabatic decompression and (b) adiabatic compression. LISL is the locus of instantaneous solidus locations. (a) During decompression, a particle at sub-solidus moves along an adiabatic path at constant entropy S and degree of melting F (e.g. path AB at $F = 0 =$ constant); whereas, a particle on the LISL melts with increasing F and decreasing S (due to latent heat loss). (b) When solid mantle is compressed, its pressure increases adiabatically and the mantle follows an adiabat at constant S and F. Path BA corresponds to compression of solid mantle with $F = 0$ and path CD corresponds to compression of solid mantle with $F > 0$.

At sub-solidus, the solid mantle has pressure p higher than the solidus pressure p_s at the same entropy S (and degree of melting F). We define the *excess pressure* as

$$\Delta p = p - p_s(F) \tag{3.2}$$

This excess pressure Δp is equal to the magnitude of the pressure drop required for the mantle to return back to the solidus. We can determine if the solid particle is on the solidus or not by calculating the excess pressure $\Delta p = \Delta p(p, F)$, which requires that we know the pressure p and the degree of melting F.

The pressure p at any location and time can be calculated semi-analytically from Equation (2.43). However, the degree of melting F is dependent on the mantle's history. This means that our numerical model must be able to keep track of F of the particles.

Here, we use the Semi-Lagrangian Scheme (SLS) to advect the degree of melting F forward in time. An advantage of the SLS over the Lagrangian advection scheme is that the grid vertices are stationary. This allows faster numerical computations of mantle flow quantities such as $\boldsymbol{v}$, p and Dp/Dt because some numerical parameters will be unchanged and can be re-used as the time stepping proceeds if the grid vertices' locations are unchanged. Also, the SLS has a higher computational stability than the Eulerian advection scheme when an equal time-step size is used (McDonald, 1984; Staniforth and Côté, 1991).

We discretize the spatial domain using a 3–D rectangular grid with uniform horizontal and vertical resolutions of 5-by-5 km^2 and 0.5 km respectively. The spatial domain covers depths from $z = -150$ km to 0 km, the horizontal distances perpendicular to the ridge axis from $x = -150$ km to 150 km and the horizontal distances along the ridge axis from $y = 0$ km to 300 km.

3.2.1 Semi-Lagrangian Scheme

In this section, we present how the SLS is implemented in our model. The implementation is also summarized as a flowchart in Figure 3.2. Here, we use the upper-case variables to represent quantities at the grid vertices; whereas, the lower-case variables are used for quantities at other locations. We breakdown the SLS into the following 5 steps.

1. We set the grid vertices locations $\boldsymbol{R}$ and initialize the degree of melting F of particles at the grid vertices. Let the inverse of the P-F relationship at solidus ($p_s = p_s(F)$) be $F_s = F_s(p)$, we set the initial $F(t = 0) = F_s(P(t = 0))$ where $P(t = 0)$ is the initial pressure at grid vertices which follows the lithostatic

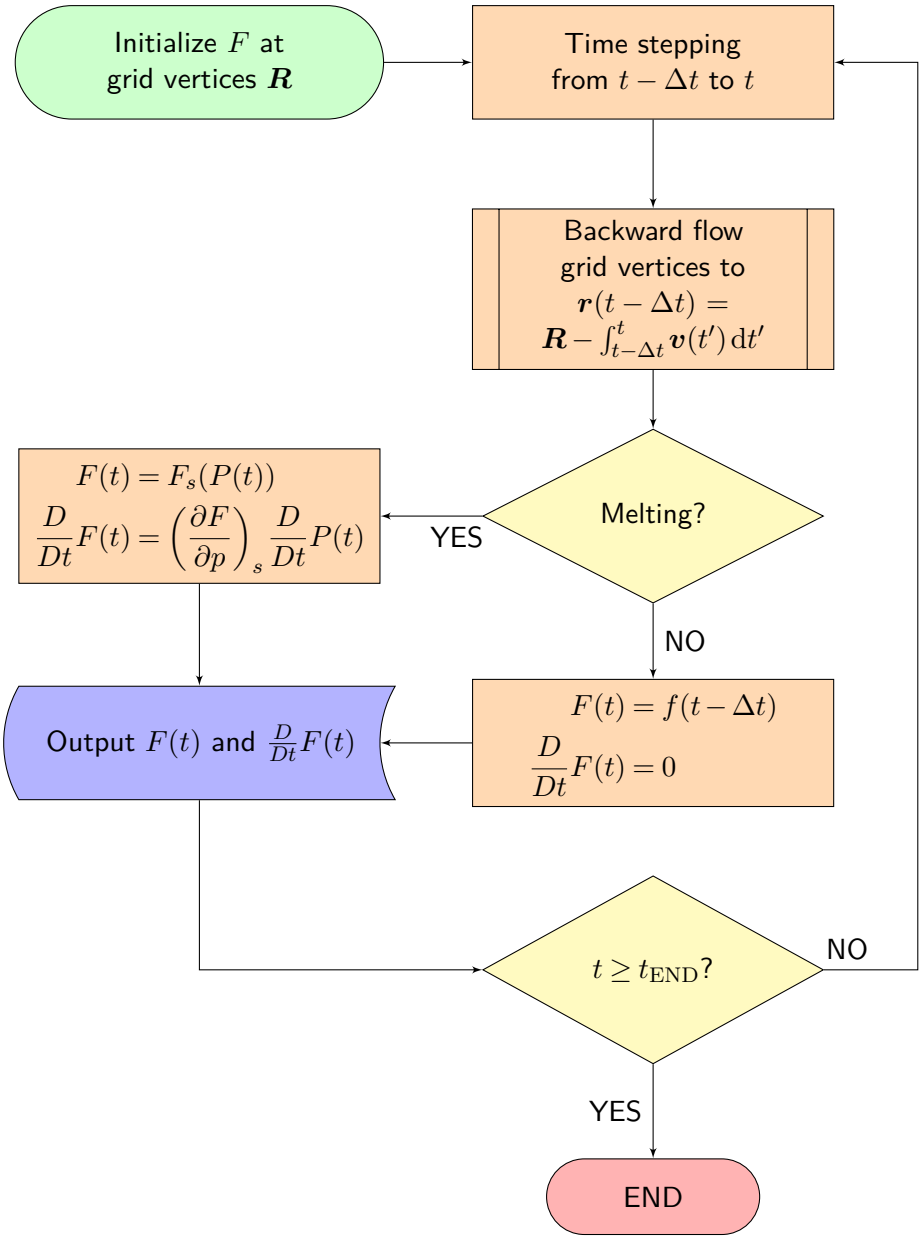

Fig. 3.2 Flowchart of the semi-Lagrangian scheme as implemented in the model. Upper-case variables ($\boldsymbol{R}$, F and P) correspond to quantities at the grid vertices. Lower-case variables ($\boldsymbol{r}$, $\boldsymbol{v}$ and f) correspond to quantities at time as specified in the argument of the particles that are at the grid vertices at time t.

pressure $p = -\rho_s g z$. In other words, all the particles in the melting region are initially on the solidus.

2. Let the time-step size be Δt, we forward the time step from time $t - \Delta t$ to time t. The grid vertices remain at $\boldsymbol{R}$. Particles at the grid vertices at time t were at locations $\boldsymbol{r}(t - \Delta t) = \boldsymbol{R} - \int_{t-\Delta t}^{t} \boldsymbol{v}(t')\,\mathrm{d}t'$ at time $t - \Delta t$ where $\boldsymbol{v}(t')$ is the velocity field of the particles at time t'. We calculate $\boldsymbol{r}(t - \Delta t)$ using the Predictor-Corrector Method (PCM). See Section 3.2.4 for more details about how the PCM is implemented.

3. We perform tri-quadratic interpolation of the degree of melting $F(t - \Delta t)$ at the grid vertices in the previous time step to obtain the degree of melting $f(t - \Delta t)$ of the particles at $\boldsymbol{r}(t - \Delta t)$. See Section 3.2.3 for more details about how the tri-quadratic interpolation is implemented.

4. We determine if a particle is melting or not based on the following criteria. Melting means that the pressure is decompressing ($DP/Dt < 0$) and also that the particle is "crossing" the solidus ($P(t) \leq p_s(f(t - \Delta t))$). In other words, solidus "crossing" means that, at the end of the time step, the pressure p of the particle does not exceed the solidus pressure p_s at the beginning of the time step. When a particle is *not* "crossing" the solidus, the pressure at the end of the time step exceeds the solidus pressure and the particle is at sub-solidus. Figure 3.3 illustrates how the model determine the solidus crossing in each time step.

   (a) If the particle is melting, we update

   $$F(t) = F_s(P(t))$$
   $$\text{and } \frac{D}{Dt}F(t) = \left(\frac{\partial F}{\partial p}\right)_s \frac{D}{Dt}P(t). \tag{3.3}$$

   The former sets F of the particle such that it is exactly on the solidus at its current pressure $P(t)$. The latter is simply the linear decompression melting relation as in Equation 3.1.

   (b) If the particle is not melting, F remains unchanged. So,

   $$F(t) = f(t - \Delta t)$$
   $$\text{and } \frac{D}{Dt}F(t) = 0. \tag{3.4}$$

5. We output F and DF/Dt to harddrive and re-iterate steps 2–5 until the desire temporal coverage is reached.

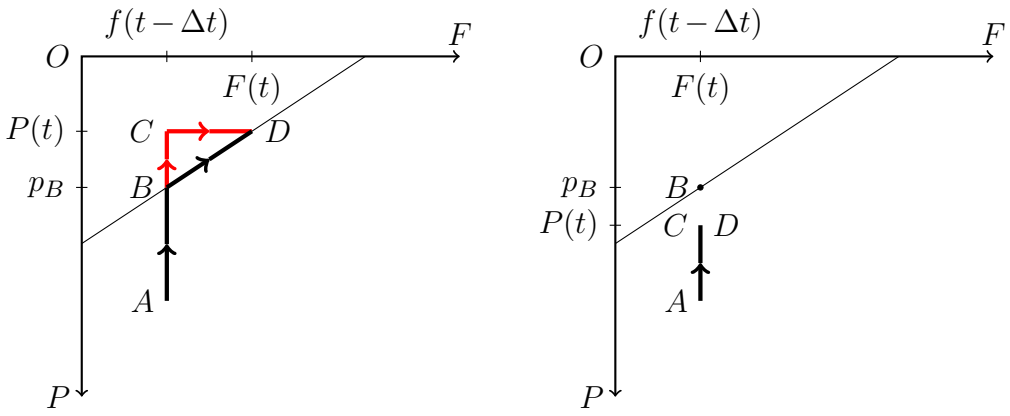

(a) Melting **(b)** Not melting

Fig. 3.3 P-F diagrams illustrating how p and F of a particle change during a time step with decompression from time $t-\Delta t$ to t. At time $t-\Delta t$, the particle is at point A and the degree of melting is $f(t-\Delta t)=F_A$. At time t, the pressure has dropped to $P(t)=p_C$ at point C. (a) Point C is above the solidus ($p_C<p_B$) and the actual path during this time step is ABD (black path). The model updates F to $F(t)=F_D$ at point D on the solidus with $p_D=p_C$. (b) Point C is below the solidus ($p_C\geq p_B$) and the actual path during this time step is AC. The model keeps F unchanged at $F(t)=f(t-\Delta t)$.

Note that there is a discontinuity of the gradient of $F_s(p)$ at the first melting depth (FMD), which is the solidus depth of the primitive mantle. $F_s'(p)$ suddenly changes from zero at just below the FMD to a negative value at the FMD. The discontinuity can cause a significant error in the interpolation of F from the grid vertices to inside a cell. We eliminate this discontinuity by replacing $F_s(p)$ below the FMD by a linear function with gradient equal to the gradient of $F_s(p)$ at the FMD ($=F_s'(p=p_s)$). In other words, we linearly extrapolate $F_s(p)$ downwards from the FMD to region below the FMD and use this modified $F_s(p)$ curve for the whole calculation of mantle melting (see Figure 3.4). The actual $F_s(p)$ at any time step can straightforwardly be obtained from the modified $F_s(p)$ by setting $F_s=0$ wherever $F_s<0$.

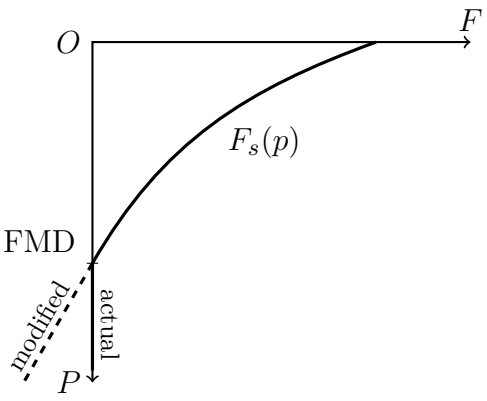

Fig. 3.4 P-F diagram illustrating how we eliminate the discontinuity of the gradient of $F_s(p)$ at the first melting depth (FMD). The section $F = 0$ below the FMD is replaced by a linear function with gradient equal to the gradient at the FMD. This modified section is shown on the figure as dashed line. The actual $F_s(p)$ can straightforwardly be obtained from the modified $F_s(p)$ by setting $F_s = 0$ wherever $F_s < 0$.

3.2.2 Tri-linear Interpolation

In this section, we explain how we implement the tri-linear interpolation method to estimate a quantity inside a cell, given that the numerical values of the quantity at grid vertices are known.

Suppose that a particle at a grid vertex $\boldsymbol{R}$ at time t was at $\boldsymbol{r}_p(t-\Delta t)$ at time $t-\Delta t$. We run the model at time-step size $\Delta t \leq 50$ years. The maximum speed of the mantle flow $|\boldsymbol{v}|_{max}$ does not exceed 1 m/yr. The grid has minimum grid spacing $\Delta r_{min} = 500$ m. This implies that the Courant number

$$\begin{aligned} C &= \frac{|\boldsymbol{v}|\Delta t}{\Delta r} \\ &\leq \frac{|\boldsymbol{v}|_{max}\Delta t_{max}}{\Delta r_{min}} \\ &= 0.1. \end{aligned}$$

Therefore, since the Courant number is well below 1, the time-step size is sufficiently small that $\boldsymbol{r}_p(t-\Delta t)$ falls inside a cell with one of the vertices being $\boldsymbol{R}$. $\boldsymbol{r}_p(t-\Delta t)$ can be inside any of the 8 cells that surround $\boldsymbol{R}$ (see Figure 3.5). We determine which of the 8 cells (octant) $\boldsymbol{r}_p(t-\Delta t)$ falls in by determining the signs of the x, y and z components of $\tilde{\boldsymbol{r}}_p(t-\Delta t) \equiv \boldsymbol{r}_p(t-\Delta t) - \boldsymbol{R}$, which is the displacement vector of $\boldsymbol{r}_p(t-\Delta t)$ from the grid vertex $\boldsymbol{R}$.

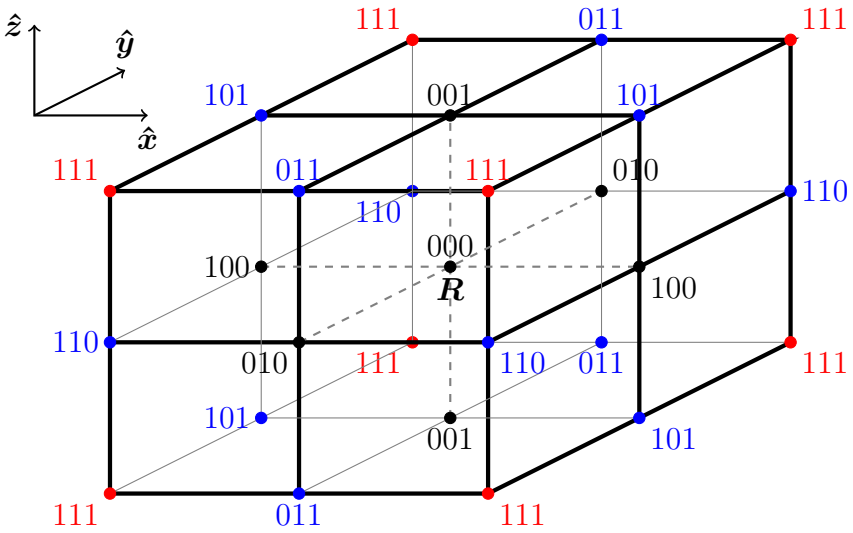

Fig. 3.5 A diagram of the 8 grid cells that surround the grid vertex $\boldsymbol{R}$ together with the convention we use to index the cells' corners in the tri-linear interpolation implementation.

Once we have found which cell $\boldsymbol{r}_p(t-\Delta t)$ is in, we index the 8 corners of the cell as follows. The vertex $\boldsymbol{R}$ is at 000. Vertices adjacent to $\boldsymbol{R}$ along the x-, y- and z-axis are at 100, 010 and 001 respectively. Vertices on the opposite side of the face diagonals to $\boldsymbol{R}$ on the yz-, zx and xy-planes are at 011, 101 and 110 respectively. The vertex on the opposite side of the space diagonal to $\boldsymbol{R}$ is at 111. Figure 3.5 shows the indexing of the cell's corners we define.

Let $\boldsymbol{R} \equiv (x_0, y_0, z_0)$ and $\boldsymbol{r}_p(t-\Delta t) \equiv (x_p, y_p, z_p)$, the tri-linear interpolation of a quantity Q from the grid vertices to the location $\boldsymbol{r}_p(t-\Delta t)$ inside a cell is

$$\begin{aligned} Q_p = & Q_{000}(1-\lambda_x)(1-\lambda_y)(1-\lambda_z) \\ & + Q_{100}\lambda_x(1-\lambda_y)(1-\lambda_z) \\ & + Q_{010}(1-\lambda_x)\lambda_y(1-\lambda_z) \\ & + Q_{001}(1-\lambda_x)(1-\lambda_y)\lambda_z \\ & + Q_{011}(1-\lambda_x)\lambda_y\lambda_z \\ & + Q_{101}\lambda_x(1-\lambda_y)\lambda_z \\ & + Q_{110}\lambda_x\lambda_y(1-\lambda_z) \\ & + Q_{111}\lambda_x\lambda_y\lambda_z \end{aligned} \tag{3.5}$$

where Q_{ijk} is the numerical value of Q at the ijk corner of the cell, $\lambda_x = \frac{x_p - x_0}{x_1 - x_0}$, $\lambda_y = \frac{y_p - y_0}{y_1 - y_0}$ and $\lambda_z = \frac{z_p - z_0}{z_1 - z_0}$.

3.2.3 Tri-quadratic Interpolation

From section 3.2.1 at step 3 of the SLS, the interpolation of F from grid vertices to inside the cell needs to have the order of accuracy at least one higher than that used for the calculation of the displacement at step 2 of the SLS (McDonald, 1987; Staniforth and Côté, 1991) (see also in Section 3.2.6 where we show why the tri-linear interpolation is not appropriate for the interpolation of F at step 3).

In our model, we use the tri-quadratic interpolation at step 3 of the SLS. The order of accuracy of which is one higher than the tri-linear interpolation used at step 2 of the SLS. In this section, we explain how we implement the tri-quadratic interpolation method to estimate a quantity (such as F) inside a cell, given that the numerical values of the quantity at grid vertices are known.

Similar to the tri-linear interpolation (Section 3.2.2), if a particle at a grid vertex $\boldsymbol{R}$ at time t was at $\boldsymbol{r}_c(t-\Delta t)$ at time $t-\Delta t$, $\boldsymbol{r}_c(t-\Delta t)$ will be inside one of the 8 cells that surround $\boldsymbol{R}$ because the Courant number (as calculated in Section 3.2.2) is well below 1. We index the 27 vertices at the corners of the 8 cells as shown in Figure 3.6 using the ijk indexing where i, j and k ($=-1, 0$ or 1) represent the location of the vertex relative to vertex $\boldsymbol{R}$ along the x, y and z direction respectively. $\bar{1}$ means -1. The vertex $\boldsymbol{R}$ is at 000.

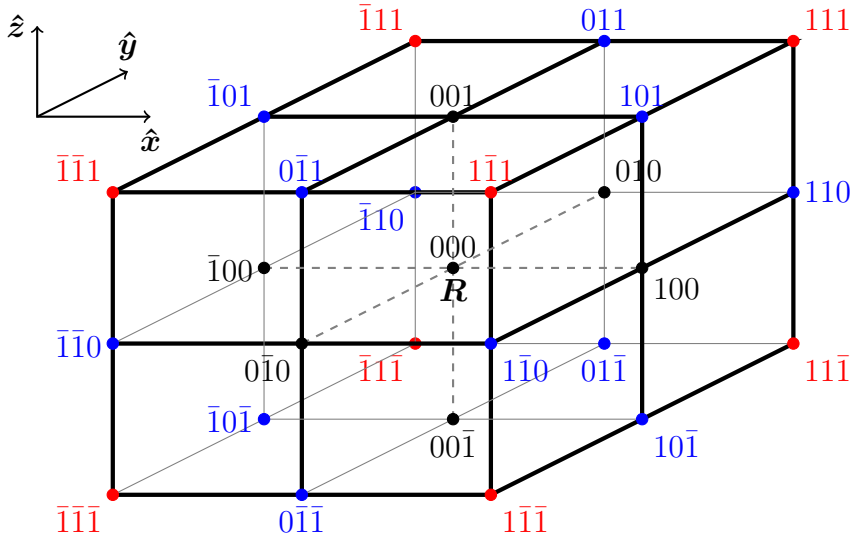

Fig. 3.6 A diagram of the 8 grid cells that surround the grid vertex $\boldsymbol{R}$ together with the convention we use to index the cells' corners in the tri-quadratic interpolation implementation.

Let $\boldsymbol{R} \equiv (x_0, y_0, z_0)$ and $\boldsymbol{r}_c(t-\Delta t) \equiv (x_c, y_c, z_c)$, the tri-quadratic interpolation of a quantity Q from the grid vertices to the location $\boldsymbol{r}_c(t-\Delta t)$ inside a cell is

$$Q_c = \sum_{ijk} c_i^{(x)} c_j^{(y)} c_k^{(z)} Q_{ijk} \tag{3.6}$$

where Q_{ijk} is the numerical value of Q at the ijk vertex and $c_i^{(x)}$, $c_j^{(y)}$ and $c_k^{(z)}$ are the quadratic interpolation coefficients as listed in Table 3.1.

Table 3.1 Coefficients of the 27 terms in the tri-quadratic interpolation formula (Equation 3.6) assuming regular grid spacing Δx, Δy and Δz. $\lambda_x = (x_c - x_0)/\Delta x$, $\lambda_y = (y_c - y_0)/\Delta y$ and $\lambda_z = (z_c - z_0)/\Delta z$.

ν	$c_\nu^{(x)}$	$c_\nu^{(y)}$	$c_\nu^{(z)}$
-1	$\lambda_x(\lambda_x - 1)/2$	$\lambda_y(\lambda_y - 1)/2$	$\lambda_z(\lambda_z - 1)/2$
0	$1 - \lambda_x^2$	$1 - \lambda_y^2$	$1 - \lambda_z^2$
1	$\lambda_x(\lambda_x + 1)/2$	$\lambda_y(\lambda_y + 1)/2$	$\lambda_z(\lambda_z + 1)/2$

3.2.4 Predictor-Corrector Method

In the semi-Lagrangian scheme we implement in the model (Section 3.2.1), we need to find the location of a particle at time $t - \Delta t$, given that the particle is at one of the grid vertices $\boldsymbol{R}$ at time t. The exact location of the particle at time $t - \Delta t$ is

$$\boldsymbol{r}_e(t-\Delta t) = \boldsymbol{R} - \int_{t-\Delta t}^{t} \boldsymbol{v}(t')\mathrm{d}t' \tag{3.7}$$

where $\boldsymbol{v}(t')$ is the velocity of the particle at time t'.

In practice, the velocity field is known only at the grid vertices at discrete time steps. Therefore, the time integration in Equation 3.7 has to be approximated by an appropriate numerical scheme. Here, we use the Predictor-Corrector Method (PCM) as summarized in Figure 3.7 to estimate $\boldsymbol{r}_e(t-\Delta t)$ as follows.

1. In the Prediction step, we estimate $\boldsymbol{r}_e(t-\Delta t)$ by assuming that the velocity is constant $\boldsymbol{v}(t') \approx \boldsymbol{v}(t)$. Since the particle is at a grid vertex at time t, $\boldsymbol{v}(t)$ is the velocity at the grid vertex, which is known and we define it as $\boldsymbol{V}(t)$. This gives

the predicted location

$$\boldsymbol{r}_p(t-\Delta t) = \boldsymbol{R} - \boldsymbol{V}(t)\Delta t. \tag{3.8}$$

It can be shown (see Section 3.2.5) that $\boldsymbol{r}_p(t-\Delta t)$ as an approximation to $\boldsymbol{r}_e(t-\Delta t)$ is 1^{st}-order accurate.

2. In the Correction step, the time integration in Equation 3.7 is approximated by the trapezoidal rule.

$$\boldsymbol{r}_e(t-\Delta t) \approx \boldsymbol{R} - \frac{\Delta t}{2}\left[\boldsymbol{v}(t) + \boldsymbol{v}(t-\Delta t)\right]$$

We define $\boldsymbol{v}_p(t-\Delta t)$ to be the velocity field at time $t-\Delta t$ at the predicted location $\boldsymbol{r}_p(t-\Delta t)$. $\boldsymbol{v}_p(t-\Delta t)$ is used as an approximation to the actual velocity $\boldsymbol{v}(t-\Delta t)$ of the particle at time $t-\Delta t$. The estimated location in the Correction step becomes

$$\boldsymbol{r}_c(t-\Delta t) = \boldsymbol{R} - \frac{\Delta t}{2}\left[\boldsymbol{V}(t) + \boldsymbol{v}_p(t-\Delta t)\right] \tag{3.9}$$

where, as before, we use the fact that $\boldsymbol{v}(t) = \boldsymbol{V}(t)$ since the particle is at the grid vertex at time t.

Figure 3.8 illustrates the locations of $\boldsymbol{r}_p(t-\Delta t)$ and $\boldsymbol{r}_c(t-\Delta t)$ relative to the grid vertices.

In general, $\boldsymbol{r}_p(t-\Delta t)$ is not at one of the grid vertices. So, $\boldsymbol{v}_p(t-\Delta t)$ is not the velocity at a grid vertex. We estimate $\boldsymbol{v}_p(t-\Delta t)$ using the tri-linear interpolation method as explained in Section 3.2.2 to interpolate the velocity $\boldsymbol{V}(t-\Delta t)$ at grid vertices at time $t-\Delta t$ to the location $\boldsymbol{r}_p(t-\Delta t)$. That is, if we let $\boldsymbol{r}_p(t-\Delta t) \equiv (x_p, y_p, z_p)$,

$$\begin{aligned}
\boldsymbol{v}_p(t-\Delta t) = &\left[\boldsymbol{V}_{000}(t-\Delta t)\right](1-\lambda_x)(1-\lambda_y)(1-\lambda_z) \\
&+ \left[\boldsymbol{V}_{100}(t-\Delta t)\right]\lambda_x(1-\lambda_y)(1-\lambda_z) \\
&+ \left[\boldsymbol{V}_{010}(t-\Delta t)\right](1-\lambda_x)\lambda_y(1-\lambda_z) \\
&+ \left[\boldsymbol{V}_{001}(t-\Delta t)\right](1-\lambda_x)(1-\lambda_y)\lambda_z \\
&+ \left[\boldsymbol{V}_{011}(t-\Delta t)\right](1-\lambda_x)\lambda_y\lambda_z \\
&+ \left[\boldsymbol{V}_{101}(t-\Delta t)\right]\lambda_x(1-\lambda_y)\lambda_z \\
&+ \left[\boldsymbol{V}_{110}(t-\Delta t)\right]\lambda_x\lambda_y(1-\lambda_z) \\
&+ \left[\boldsymbol{V}_{111}(t-\Delta t)\right]\lambda_x\lambda_y\lambda_z
\end{aligned} \tag{3.10}$$

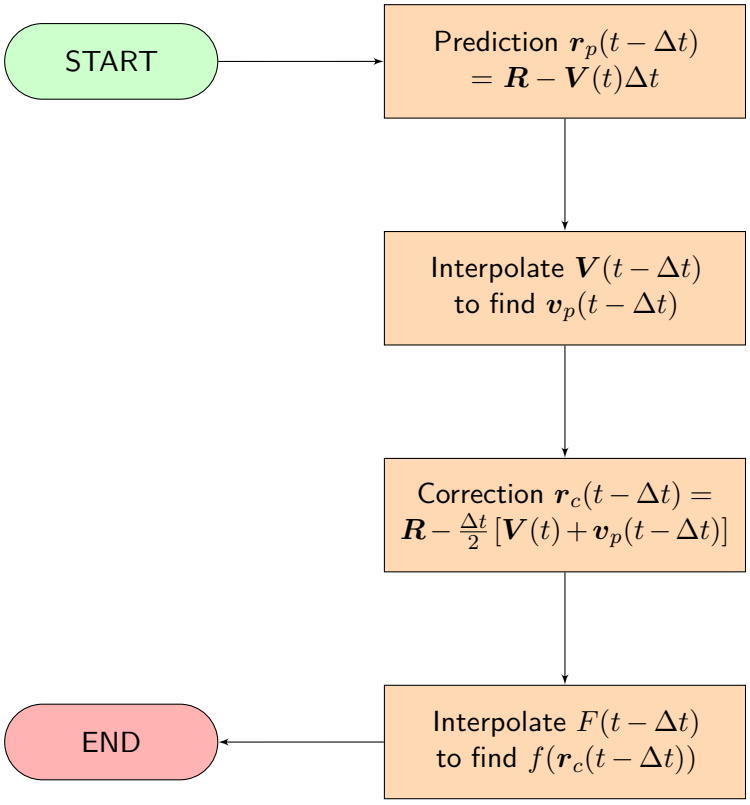

Fig. 3.7 Flowchart summarizing the implementation of the Predictor-Corrector Method for estimating the location and degree of melting of a particle at time $t-\Delta t$, given that the particle is at a grid vertex $\boldsymbol{R}$ at time t. The Prediction step uses the velocity $\boldsymbol{V}(t)$ at the grid vertex at time t to obtain the Predicted location $\boldsymbol{r}_p(t-\Delta t)$. The Correction step then uses the average velocity $= [\boldsymbol{V}(t) + \boldsymbol{v}_p(t-\Delta t)]/2$, where $\boldsymbol{v}_p(t-\Delta t)$ is the velocity at the Predicted location $\boldsymbol{r}_p(t-\Delta t)$, to make correction for the estimated location. The model then performs the tri-quadratic interpolation of the degree of melting from $F(t-\Delta t)$ at the grid vertices at time $t-\Delta t$ to inside the cell at the Correction-step location $\boldsymbol{r}_c(t-\Delta t)$ to obtain an estimate of the degree of melting $f(t-\Delta t)$ of the particle at time $t-\Delta t$.

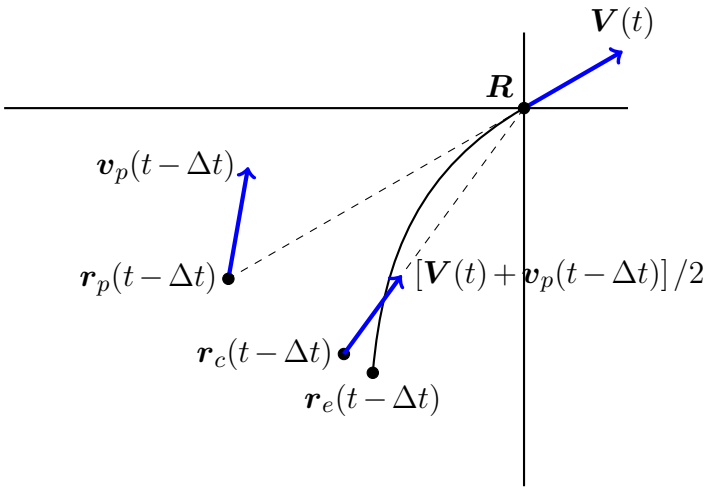

Fig. 3.8 A simplified diagram showing the Predictor-Corrector Method for estimating the location of a particle at time $t-\Delta t$, given that the particle is at a grid vertex $\boldsymbol{R}$ at time t. The Prediction step uses the velocity $\boldsymbol{V}(t)$ at the grid vertex at time t to obtain the Predicted location $\boldsymbol{r}_p(t-\Delta t)$. The Correction step then uses the average velocity $=[\boldsymbol{V}(t)+\boldsymbol{v}_p(t-\Delta t)]/2$, where $\boldsymbol{v}_p(t-\Delta t)$ is the velocity at the Predicted location $\boldsymbol{r}_p(t-\Delta t)$, to make correction for the estimated location. Provided that the velocity field at time $(t-\Delta t)$ does not change abruptly within the cell, the Correction step corrects the estimated location from $\boldsymbol{r}_p(t-\Delta t)$ to $\boldsymbol{r}_c(t-\Delta t)$, which is closer to the exact location $\boldsymbol{r}_e(t-\Delta t)$.

where $\lambda_x=\frac{x_p-x_0}{x_1-x_0}$, $\lambda_y=\frac{y_p-y_0}{y_1-y_0}$, $\lambda_z=\frac{z_p-z_0}{z_1-z_0}$ and $\boldsymbol{V}_{ijk}(t-\Delta t)$ is the velocity at the ijk corner of the cell at time $t-\Delta t$.

We show in Section 3.2.5 that $\boldsymbol{r}_c(t-\Delta t)$ as an approximation to $\boldsymbol{r}_e(t-\Delta t)$ is 2^{nd}-order accurate.

3.2.5 Accuracy of PCM

In this section, we show that the Prediction step of PCM is 1^{st}-order accurate and that the Correction step of PCM is 2^{nd}-order accurate (Press et al., 2007).

We expand $\boldsymbol{v}(t')$ around $t'=t$ using the Taylor series expansion

$$\boldsymbol{v}(t')=\boldsymbol{v}(t)+(t'-t)\frac{D}{Dt}\boldsymbol{v}(t)+\frac{1}{2!}(t'-t)^2\frac{D^2}{Dt^2}\boldsymbol{v}(t)+\ldots$$

where

$$\frac{D}{Dt}=\frac{\partial}{\partial t}+\boldsymbol{v}\cdot\boldsymbol{\nabla}$$

is the convective derivative. Hence, Equation 3.7 becomes

$$\boldsymbol{r}_e(t-\Delta t) = \boldsymbol{R} - \boldsymbol{v}(t)\Delta t + \frac{(\Delta t)^2}{2!}\frac{D}{Dt}\boldsymbol{v}(t) - \frac{(\Delta t)^3}{3!}\frac{D^2}{Dt^2}\boldsymbol{v}(t) + \mathcal{O}((\Delta t)^4) \tag{3.11}$$

By subtracting Equation 3.11 from Equation 3.8 and using the fact that $\boldsymbol{v}(t) = \boldsymbol{V}(t)$ because the particle is at the grid vertex at time t, we obtain the deviation of the Prediction-step location from the exact location.

$$\begin{aligned}\text{Error}_p &\equiv \boldsymbol{r}_p(t-\Delta t) - \boldsymbol{r}_e(t-\Delta t)\\ &= -\frac{(\Delta t)^2}{2!}\frac{D}{Dt}\boldsymbol{v}(t) + \mathcal{O}((\Delta t)^3)\end{aligned}$$

That is, the Prediction step is 1^{st}-order accurate.

In the Correction step, we estimate $\boldsymbol{v}_p(t-\Delta t)$ using the tri-linear interpolation as explained in Section 3.2.4. In order to determine the accuracy of the Correction step, we first Taylor expand all the $\boldsymbol{V}_{ijk}$s in Equation 3.10 around $\boldsymbol{V}_{000} \equiv \boldsymbol{V}$ to obtain

$$\begin{aligned}
\boldsymbol{V}_{100} &= \boldsymbol{V} + \Delta x\,\partial_x\boldsymbol{V} + \frac{1}{2!}(\Delta x)^2\,\partial_x^2\boldsymbol{V} + \mathcal{O}((\Delta x)^3),\\
\boldsymbol{V}_{010} &= \boldsymbol{V} + \Delta y\,\partial_y\boldsymbol{V} + \frac{1}{2!}(\Delta y)^2\,\partial_y^2\boldsymbol{V} + \mathcal{O}((\Delta y)^3),\\
\boldsymbol{V}_{001} &= \boldsymbol{V} + \Delta z\,\partial_z\boldsymbol{V} + \frac{1}{2!}(\Delta z)^2\,\partial_z^2\boldsymbol{V} + \mathcal{O}((\Delta z)^3),\\
\boldsymbol{V}_{011} &= \boldsymbol{V} + \Delta y\,\partial_y\boldsymbol{V} + \Delta z\,\partial_z\boldsymbol{V}\\
&\quad + \frac{1}{2!}(\Delta y)^2\,\partial_y^2\boldsymbol{V} + \frac{2}{2!}\Delta y\Delta z\,\partial_y\partial_z\boldsymbol{V} + \frac{1}{2!}(\Delta z)^2\,\partial_z^2\boldsymbol{V} + \mathcal{O}(\Delta^3),\\
\boldsymbol{V}_{101} &= \boldsymbol{V} + \Delta z\,\partial_z\boldsymbol{V} + \Delta x\,\partial_x\boldsymbol{V}\\
&\quad + \frac{1}{2!}(\Delta z)^2\,\partial_z^2\boldsymbol{V} + \frac{2}{2!}\Delta z\Delta x\,\partial_z\partial_x\boldsymbol{V} + \frac{1}{2!}(\Delta x)^2\,\partial_x^2\boldsymbol{V} + \mathcal{O}(\Delta^3),\\
\boldsymbol{V}_{110} &= \boldsymbol{V} + \Delta x\,\partial_x\boldsymbol{V} + \Delta y\,\partial_y\boldsymbol{V}\\
&\quad + \frac{1}{2!}(\Delta x)^2\,\partial_x^2\boldsymbol{V} + \frac{2}{2!}\Delta x\Delta y\,\partial_x\partial_y\boldsymbol{V} + \frac{1}{2!}(\Delta y)^2\,\partial_y^2\boldsymbol{V} + \mathcal{O}(\Delta^3)\\
\boldsymbol{V}_{111} &= \boldsymbol{V} + \Delta x\,\partial_x\boldsymbol{V} + \Delta y\,\partial_y\boldsymbol{V} + \Delta z\,\partial_z\boldsymbol{V}\\
&\quad + \frac{1}{2!}(\Delta x)^2\,\partial_x^2\boldsymbol{V} + \frac{2}{2!}\Delta x\Delta y\,\partial_x\partial_y\boldsymbol{V}\\
&\quad + \frac{1}{2!}(\Delta y)^2\,\partial_y^2\boldsymbol{V} + \frac{2}{2!}\Delta y\Delta z\,\partial_y\partial_z\boldsymbol{V}\\
&\quad + \frac{1}{2!}(\Delta z)^2\,\partial_z^2\boldsymbol{V} + \frac{2}{2!}\Delta z\Delta x\,\partial_z\partial_x\boldsymbol{V} + \mathcal{O}((\Delta r)^3).
\end{aligned} \tag{3.12}$$

By substituting these expressions into Equation 3.10, we obtain

$$\begin{aligned}\boldsymbol{v}_p(t-\Delta t) = \boldsymbol{V} &+ \lambda_x \Delta x\, \partial_x \boldsymbol{V} + \lambda_y \Delta y\, \partial_y \boldsymbol{V} + \lambda_z \Delta z\, \partial_z \boldsymbol{V} \\ &+ \frac{\lambda_x}{2!}(\Delta x)^2\, \partial_x^2 \boldsymbol{V} + \lambda_x \lambda_y \Delta x \Delta y \partial_x \partial_y \boldsymbol{V} \\ &+ \frac{\lambda_y}{2!}(\Delta y)^2\, \partial_y^2 \boldsymbol{V} + \lambda_y \lambda_z \Delta y \Delta z \partial_y \partial_z \boldsymbol{V} \\ &+ \frac{\lambda_z}{2!}(\Delta z)^2\, \partial_z^2 \boldsymbol{V} + \lambda_z \lambda_x \Delta z \Delta x \partial_z \partial_x \boldsymbol{V} + \mathcal{O}((\Delta r)^3) \end{aligned} \tag{3.13}$$

where all the $\boldsymbol{V}$s are evaluated at time $t - \Delta t$. We Taylor expand this expression further around time t to obtain

$$\begin{aligned}\boldsymbol{v}_p(t-\Delta t) = \boldsymbol{V} &+ \lambda_x \Delta x\, \partial_x \boldsymbol{V} + \lambda_y \Delta y\, \partial_y \boldsymbol{V} + \lambda_z \Delta z\, \partial_z \boldsymbol{V} \\ &+ \frac{\lambda_x}{2!}(\Delta x)^2\, \partial_x^2 \boldsymbol{V} + \lambda_x \lambda_y \Delta x \Delta y\, \partial_x \partial_y \boldsymbol{V} \\ &+ \frac{\lambda_y}{2!}(\Delta y)^2\, \partial_y^2 \boldsymbol{V} + \lambda_y \lambda_z \Delta y \Delta z\, \partial_y \partial_z \boldsymbol{V} \\ &+ \frac{\lambda_z}{2!}(\Delta z)^2\, \partial_z^2 \boldsymbol{V} + \lambda_z \lambda_x \Delta z \Delta x\, \partial_z \partial_x \boldsymbol{V} + \mathcal{O}((\Delta r)^3) \\ &- [\Delta t\, \partial_t \boldsymbol{V} + \lambda_x \Delta x \Delta t\, \partial_x \partial_t \boldsymbol{V} + \lambda_y \Delta y \Delta t\, \partial_y \partial_t \boldsymbol{V} + \lambda_z \Delta z \Delta t\, \partial_z \partial_t \boldsymbol{V}] \\ &+ \mathcal{O}((\Delta r)^2 \Delta t) \\ &+ \frac{1}{2!}(\Delta t)^2\, \partial_t^2 \boldsymbol{V} + \mathcal{O}(\Delta r (\Delta t)^2) + \mathcal{O}((\Delta t)^3) \end{aligned} \tag{3.14}$$

where now all the $\boldsymbol{V}$s are evaluated at time t.

By substituting this expression into Equation 3.9 and then subtracting Equation 3.11 from it, we obtain the deviation of the Correction-step location from the actual location.

$$\begin{aligned}
\text{Error}_c \equiv & \boldsymbol{r}_c(t-\Delta t) - \boldsymbol{r}_e(t-\Delta t) \\
= & -\frac{\Delta t}{2}\left[\lambda_x \Delta x\, \partial_x \boldsymbol{V} + \lambda_y \Delta y\, \partial_y \boldsymbol{V} + \lambda_z \Delta z\, \partial_z \boldsymbol{V}\right] \\
& -\frac{\Delta t}{2}\left[\frac{\lambda_x}{2!}(\Delta x)^2\, \partial_x^2 \boldsymbol{V} + \lambda_x \lambda_y \Delta x \Delta y\, \partial_x \partial_y \boldsymbol{V}\right] \\
& -\frac{\Delta t}{2}\left[\frac{\lambda_y}{2!}(\Delta y)^2\, \partial_y^2 \boldsymbol{V} + \lambda_y \lambda_z \Delta y \Delta z\, \partial_y \partial_z \boldsymbol{V}\right] \\
& -\frac{\Delta t}{2}\left[\frac{\lambda_z}{2!}(\Delta z)^2\, \partial_z^2 \boldsymbol{V} + \lambda_z \lambda_x \Delta z \Delta x\, \partial_z \partial_x \boldsymbol{V}\right] \\
& +\frac{(\Delta t)^2}{2}\left[\lambda_x \Delta x\, \partial_x \partial_t \boldsymbol{V} + \lambda_y \Delta y\, \partial_y \partial_t \boldsymbol{V} + \lambda_z \Delta z\, \partial_z \partial_t \boldsymbol{V}\right] \\
& +\frac{(\Delta t)^2}{2}\partial_t \boldsymbol{V} - \frac{(\Delta t)^3}{2 \cdot 2!}\partial_t^2 \boldsymbol{V} \\
& -\frac{(\Delta t)^2}{2!}\frac{D}{Dt}\boldsymbol{v}(t) + \frac{(\Delta t)^3}{3!}\frac{D^2}{Dt^2}\boldsymbol{v}(t) + \mathcal{O}(\Delta^4)
\end{aligned} \tag{3.15}$$

where all the $\boldsymbol{V}$s are evaluated at time t and $\boldsymbol{v}(t) = \boldsymbol{V}(t)$ because the particle is at the grid vertex at time t.

On the right-hand side of Equation 3.15, we note that inside the square bracket on the first line is equal to $-\Delta t\,(\boldsymbol{V} \cdot \boldsymbol{\nabla})\boldsymbol{V}$ because, by the definition of λ_is in Equation 3.10 and the predicted location $\boldsymbol{r}_p = (x_p, y_p, z_p)$ in Equation 3.8,

$$\begin{aligned}
& \lambda_x \Delta x = x_p - x_0 = -v_x(t)\,\Delta t, \\
& \lambda_y \Delta y = y_p - y_0 = -v_y(t)\,\Delta t \\
\text{and} \qquad & \lambda_z \Delta z = z_p - z_0 = -v_z(t)\,\Delta t.
\end{aligned} \tag{3.16}$$

Hence, by combining this with the fact that $\frac{D}{Dt} = \partial_t + \boldsymbol{v} \cdot \boldsymbol{\nabla}$, the whole first line ($= \frac{(\Delta t)^2}{2}(\boldsymbol{V} \cdot \boldsymbol{\nabla})\boldsymbol{V}$) combined with the first term on the sixth line ($\frac{(\Delta t)^2}{2}\partial_t \boldsymbol{V}$) cancel with the first term on the bottom line ($-\frac{(\Delta t)^2}{2!}\frac{D}{Dt}\boldsymbol{v}(t)$).

We simplify Equation 3.15 further by applying Equation 3.16 to the second, third, fourth and fifth lines to obtain

$$\begin{aligned}\text{Error}_c = &\frac{(\Delta t)^3}{6}\frac{D^2}{Dt^2}\boldsymbol{V} - \frac{(\Delta t)^3}{4}\left[\partial_t^2\boldsymbol{V} + 2\left(\boldsymbol{V}\cdot\boldsymbol{\nabla}\right)\partial_t\boldsymbol{V}\right] \\ &+\frac{(\Delta t)^3}{4}\left[v_x\frac{\Delta x}{\Delta t}\partial_x^2\boldsymbol{V} + v_y\frac{\Delta y}{\Delta t}\partial_y^2\boldsymbol{V} + v_z\frac{\Delta z}{\Delta t}\partial_z^2\boldsymbol{V}\right] \\ &-\frac{(\Delta t)^3}{2}\left[v_x v_y\partial_x\partial_y\boldsymbol{V} + v_y v_z\partial_y\partial_z\boldsymbol{V} + v_z v_x\partial_z\partial_x\boldsymbol{V}\right] \\ &+\mathcal{O}(\Delta^4) \end{aligned} \tag{3.17}$$

Hence, the estimated location in the Correction step is second order accurate.

In the mantle flow system we are modelling, the force is finite and so too is the acceleration $\dot{\boldsymbol{V}}$. However, the force is not necessarily continuous in time. This means that $\ddot{\boldsymbol{V}}$ is not necessarily finite. Since the error of the PCM (Equation 3.17) contains terms proportional to the second-order time derivative of velocity, the error can be significantly large if the time steps are not set appropriately. This error can be minimized by setting the time-step boundaries to match the discontinuity. Figure 3.9 illustrates how this helps minimize the error.

The spatial variation of the velocity field is relatively smooth that its first-order spatial derivatives in all the directions ($\partial_x\boldsymbol{V}$, $\partial_y\boldsymbol{V}$ and $\partial_z\boldsymbol{V}$) are continuous. Hence, all the terms in Equation (3.17) containing the second-order spatial derivatives of $\boldsymbol{V}$ are finite and can be minimized by using a sufficiently high spatial resolution.

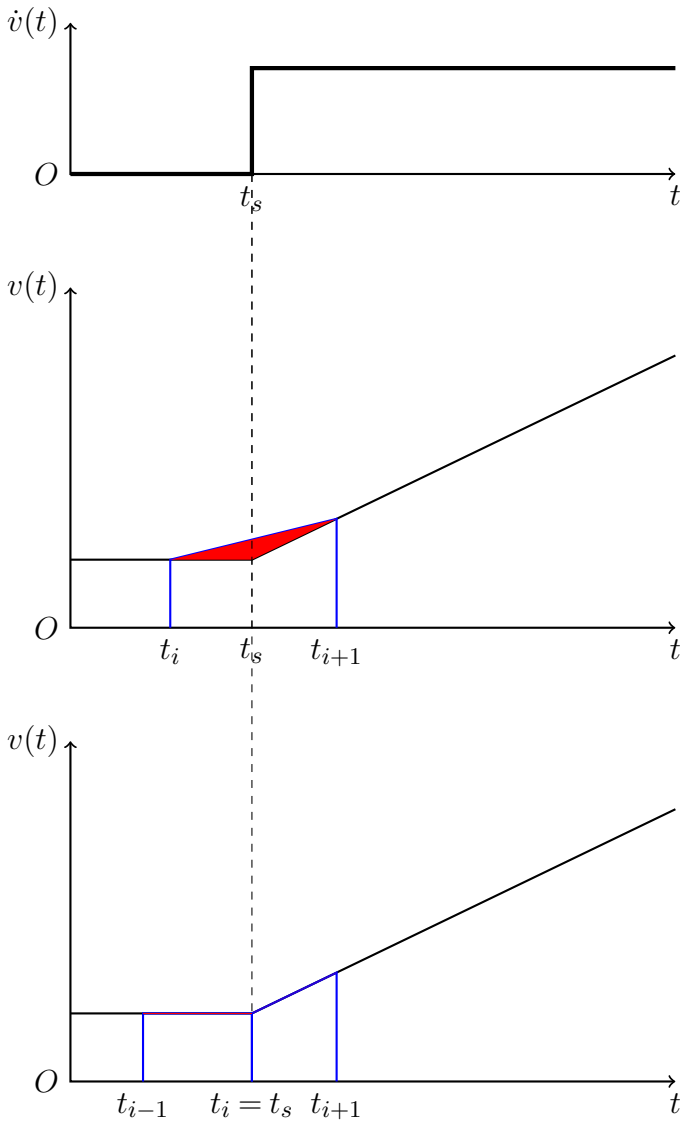

Fig. 3.9 At time t_s, when the acceleration is discontinuous in time, the velocity versus time curve ($v(t)$) will have a kink at time t_s. The distance moved during a time step between time t_i and t_{i+1} is equal to the area under the curve of $v(t)$. When $t_i < t_s < t_{i+1}$, the trapezoidal integration of the distance moved will have an error equal to the shaded area in red. This error can be minimized by setting the time steps such that the kink point matches to one of the trapezoidal boundaries ($t_i = t_s$ for some i).

3.2.6 Accuracy of SLS

We estimate the degree of melting $f(t-\Delta t)$ of the particle at time $t-\Delta t$ by the tri-quadratic interpolation of F_{ijk} at the grid vertices to the PCM-estimated location $\boldsymbol{r}_c(t-\Delta t)$, defined here after as $\tilde{F}(\boldsymbol{r}_c(t-\Delta t))$. The deviation of the estimate from the actual value is

$$\text{Error}_F \equiv \tilde{F}(\boldsymbol{r}_c(t-\Delta t)) - F(\boldsymbol{r}_e(t-\Delta t)) \tag{3.18}$$

From Equation 3.6 in Section 3.2.3, we have

$$\tilde{F}(\boldsymbol{r}_c(t-\Delta t)) = \sum_{ijk} c_i^{(x)} c_j^{(y)} c_k^{(z)} F_{ijk} \tag{3.19}$$

where F_{ijk} is the degree of melting at the ijk vertex evaluated at time $t-\Delta t$ and $c_i^{(x)}$, $c_j^{(y)}$ and $c_k^{(z)}$ are the quadratic interpolation coefficients as listed in Table 3.1.

The Taylor expansion of F_{ijk} around $F_{000} \equiv F$ is

$$\begin{aligned} F_{ijk} = F &+ (i\Delta x)\,\partial_x F + (j\Delta y)\,\partial_y F + (k\Delta z)\,\partial_z F \\ &+ \frac{1}{2!}(i\Delta x)^2\,\partial_x^2 F + (i\Delta x)(j\Delta y)\partial_x\partial_y F \\ &+ \frac{1}{2!}(j\Delta y)^2\,\partial_y^2 F + (j\Delta y)(k\Delta z)\partial_y\partial_z F \\ &+ \frac{1}{2!}(k\Delta z)^2\,\partial_z^2 F + (k\Delta z)(i\Delta x)\partial_z\partial_x F + \mathcal{O}((\Delta r)^3) \end{aligned} \tag{3.20}$$

By substituting this expression into equation 3.19 and summing over all the 27 terms together, we obtain

$$\begin{aligned} \tilde{F}(\boldsymbol{r}_c(t-\Delta t)) = F &+ (\lambda_x\Delta x)\,\partial_x F + (\lambda_y\Delta y)\,\partial_y F + (\lambda_z\Delta z)\,\partial_z F \\ &+ \frac{1}{2!}(\lambda_x\Delta x)^2\,\partial_x^2 F + (\lambda_x\Delta x)(\lambda_y\Delta y)\partial_x\partial_y F \\ &+ \frac{1}{2!}(\lambda_y\Delta y)^2\,\partial_y^2 F + (\lambda_y\Delta y)(\lambda_z\Delta z)\partial_y\partial_z F \\ &+ \frac{1}{2!}(\lambda_z\Delta z)^2\,\partial_z^2 F + (\lambda_z\Delta z)(\lambda_x\Delta x)\partial_z\partial_x F + \mathcal{O}((\Delta r)^3) \end{aligned} \tag{3.21}$$

Likewise, for $F(\boldsymbol{r}_e(t-\Delta t))$, the Taylor expansion around $F_{000} \equiv F$ is

$$\begin{aligned} F(\boldsymbol{r}_e(t-\Delta t)) = F &+ (x_e - x_0)\,\partial_x F + (y_e - y_0)\,\partial_y F + (z_e - z_0)\,\partial_z F \\ &+ \frac{1}{2!}(x_e - x_0)^2\,\partial_x^2 F + (x_e - x_0)(y_e - y_0)\partial_x\partial_y F \\ &+ \frac{1}{2!}(y_e - y_0)^2\,\partial_y^2 F + (y_e - y_0)(z_e - z_0)\partial_y\partial_z F \\ &+ \frac{1}{2!}(z_e - z_0)^2\,\partial_z^2 F + (z_e - z_0)(x_e - x_0)\partial_z\partial_x F + \mathcal{O}((\Delta r)^3) \end{aligned} \tag{3.22}$$

By subtracting Equation 3.22 from 3.21, we obtain the error (as defined in Equation 3.18)

$$\begin{aligned} \text{Error}_F = &\left[\lambda_x \Delta x - (x_e - x_0)\right] \partial_x F \\ &+ \left[\lambda_y \Delta y - (y_e - y_0)\right] \partial_y F \\ &+ \left[\lambda_z \Delta z - (z_e - z_0)\right] \partial_z F \\ &+ \frac{1}{2!}\left[(\lambda_x \Delta x)^2 - (x_e - x_0)^2\right] \partial_x^2 F \\ &+ \frac{1}{2!}\left[(\lambda_y \Delta y)^2 - (y_e - y_0)^2\right] \partial_y^2 F \\ &+ \frac{1}{2!}\left[(\lambda_z \Delta z)^2 - (z_e - z_0)^2\right] \partial_z^2 F \\ &+ \left[(\lambda_x \Delta x)(\lambda_y \Delta y) - (x_e - x_0)(y_e - y_0)\right] \partial_x\partial_y F \\ &+ \left[(\lambda_y \Delta y)(\lambda_z \Delta z) - (y_e - y_0)(z_e - z_0)\right] \partial_y\partial_z F \\ &+ \left[(\lambda_z \Delta z)(\lambda_x \Delta x) - (z_e - z_0)(x_e - x_0)\right] \partial_z\partial_x F \\ &+ \mathcal{O}((\Delta r)^3) \end{aligned}$$

We substitute $\lambda_x = \frac{x_c - x_0}{x_1 - x_0}$, $\lambda_y = \frac{y_c - y_0}{y_1 - y_0}$ and $\lambda_z = \frac{z_c - z_0}{z_1 - z_0}$ into this expression and simplify to obtain

$$\begin{aligned}
\text{Error}_F = {} & (\boldsymbol{r}_c - \boldsymbol{r}_e) \cdot \boldsymbol{\nabla} F \\
& + \frac{1}{2!}(x_c - x_e)(x_c + x_e - 2x_0)\, \partial_x^2 F \\
& + \frac{1}{2!}(y_c - y_e)(y_c + y_e - 2y_0)\, \partial_y^2 F \\
& + \frac{1}{2!}(z_c - z_e)(z_c + z_e - 2z_0)\, \partial_z^2 F \\
& + [(x_c - x_0)(y_c - y_0) - (x_e - x_0)(y_e - y_0)]\, \partial_x \partial_y F \\
& + [(y_c - y_0)(z_c - z_0) - (y_e - y_0)(z_e - z_0)]\, \partial_y \partial_z F \\
& + [(z_c - z_0)(x_c - x_0) - (z_e - z_0)(x_e - x_0)]\, \partial_z \partial_x F \\
& + \mathcal{O}((\Delta r)^3)
\end{aligned} \tag{3.23}$$

On the right-hand side of Equation 3.23, let's define the whole of the first line as Error_1, the second, third and fourth lines together as Error_2 and the fifth, sixth and seventh lines together as Error_3. By substituting $\boldsymbol{r}_c - \boldsymbol{r}_e$ from Equation 3.17 into Error_1, Error_2 and Error_3 and simplify, it is straightforward to show that

$$\begin{aligned}
& \text{Error}_1 = \mathcal{O}((\Delta t)^3, (\Delta t)^2 \Delta r), \\
& \text{Error}_2 = \mathcal{O}((\Delta t)^4, (\Delta t)^3 \Delta r) \\
\text{and} \quad & \text{Error}_3 = \mathcal{O}((\Delta t)^4, (\Delta t)^3 \Delta r).
\end{aligned} \tag{3.24}$$

Hence, the estimation of the degree of melting $F(\boldsymbol{r}_e(t - \Delta t))$ using $\tilde{F}(\boldsymbol{r}_c(t - \Delta t))$ obtained from the tri-quadratic interpolation is second-order accurate.

Note that, if we had used the tri-linear interpolation instead of the tri-quadratic interpolation to find $\tilde{F}(\boldsymbol{r}_c(t - \Delta t))$, the Taylor expansion of $\tilde{F}(\boldsymbol{r}_c(t - \Delta t))$ around $F_{000} \equiv F$ (instead of Equation 3.21) would have been

$$\begin{aligned}
\tilde{F}(\boldsymbol{r}_c(t - \Delta t)) = {} & F + (\lambda_x \Delta x)\, \partial_x F + (\lambda_y \Delta y)\, \partial_y F + (\lambda_z \Delta z)\, \partial_z F \\
& + \frac{\lambda_x}{2!}(\Delta x)^2\, \partial_x^2 F + (\lambda_x \Delta x)(\lambda_y \Delta y) \partial_x \partial_y F \\
& + \frac{\lambda_y}{2!}(\Delta y)^2\, \partial_y^2 F + (\lambda_y \Delta y)(\lambda_z \Delta z) \partial_y \partial_z F \\
& + \frac{\lambda_z}{2!}(\Delta z)^2\, \partial_z^2 F + (\lambda_z \Delta z)(\lambda_x \Delta x) \partial_z \partial_x F + \mathcal{O}((\Delta r)^3)
\end{aligned} \tag{3.25}$$

By subtracting Equation 3.22 from 3.25 and substituting $\lambda_x = \frac{x_c - x_0}{x_1 - x_0}$, $\lambda_y = \frac{y_c - y_0}{y_1 - y_0}$ and $\lambda_z = \frac{z_c - z_0}{z_1 - z_0}$, the error (instead of Equation 3.23) would have been

$$\begin{aligned}
\text{Error}_F = &(\boldsymbol{r}_c - \boldsymbol{r}_e) \cdot \boldsymbol{\nabla} F \\
&+ \frac{1}{2!}\left[(x_c - x_0)(x_1 - x_0) - (x_e - x_0)^2\right] \partial_x^2 F \\
&+ \frac{1}{2!}\left[(y_c - y_0)(y_1 - y_0) - (y_e - y_0)^2\right] \partial_y^2 F \\
&+ \frac{1}{2!}\left[(z_c - z_0)(z_1 - z_0) - (z_e - z_0)^2\right] \partial_z^2 F \\
&+ \left[(x_c - x_0)(y_c - y_0) - (x_e - x_0)(y_e - y_0)\right] \partial_x \partial_y F \\
&+ \left[(y_c - y_0)(z_c - z_0) - (y_e - y_0)(z_e - z_0)\right] \partial_y \partial_z F \\
&+ \left[(z_c - z_0)(x_c - x_0) - (z_e - z_0)(x_e - x_0)\right] \partial_z \partial_x F \\
&+ \mathcal{O}((\Delta r)^3)
\end{aligned} \tag{3.26}$$

By comparing on the right-hand side Equation 3.26 to that of Equation 3.23, the whole of the first line (as Error_1) and the fifth, sixth and seventh lines together (as Error_3) would have remained unchanged. However, the second, third and fourth lines together (as Error_2) would have now become $\mathcal{O}((\Delta t)^2, \Delta t\, \Delta r)$. That is, the estimation of the degree of melting $F(\boldsymbol{r}_e(t - \Delta t))$ using $\tilde{F}(\boldsymbol{r}_c(t - \Delta t))$ obtained from the *tri-linear* interpolation would have been only *first*-order accurate despite the fact that the PCM estimation of the displacement is second-order accurate.

Chapter 4

Icelandic Ice Sheet

4.1 Introduction

The GIA mantle flow model we discuss in Chapter 2 requires a prescribed axisymmetric ice-load profile as an input. Hubbard et al. (2006) and Patton et al. (2017) have created a numerical ice flow model that reconstructs the Icelandic Ice Sheet (IIS) during the last deglaciation (Late Weichselian IIS). However, limited geological records of the Weichselian IIS means that it is not straight-forward for the reconstruction to accurately represent the actual time evolution of the ice sheet profile in every detail.

In the mantle melting model of Jull and McKenzie (1996), the prescribed ice sheet profile of the IIS during the last deglaciation was assumed to be axisymmetric parabolic. The deglaciation was assumed to have taken place in 1 kyr with the ice sheet thickness decreasing linearly with time from 2 km at 10 kyrBP to 0 km at 9 kyrBP; while, the ice radius was kept constant at 180 km.

Here, we modify the ice sheet to be an axisymmetric viscous gravity current (Paterson, 1994) with glacier terminus retreating during the deglaciation. This is a more reasonable representation of the actual ice sheet, allowing the spatial variations of the volcanic response to be examined more accurately. The axisymmetric assumption helps simplify the GIA mantle flow calculation, which significantly reduces the computational cost. In the next section, we present the derivation of the ice thickness profile $h(r,t)$ as a function of the radial distance r and time t as adopted from Huppert (1982) and Paterson (1994).

4.2 Model

4.2.1 Ice Sheet Profile

We assume that the ice can be approximated as an incompressible viscous fluid with axisymmetric shape sitting on top of a flat horizontal surface. Its behaviour follows an incompressible Stokes flow:

$$-\boldsymbol{\nabla} p + \mu \nabla^2 \boldsymbol{v} + \rho_{\mathrm{i}} \boldsymbol{g} = 0 \tag{4.1}$$

and

$$\boldsymbol{\nabla} \cdot \boldsymbol{v} = 0 \tag{4.2}$$

where p is the pressure field, μ is the viscosity of ice, $\boldsymbol{v}$ is the velocity field, ρ_{i} is the density of ice and $\boldsymbol{g}$ is the acceleration due to gravity.

By assuming that the ice is very thin compared to its horizontal extent, the vertical component of the velocity field may be neglected ($v_z \approx 0$). In this case, equation (4.2) becomes

$$\frac{1}{r}\frac{\partial}{\partial r}(r v_r) = 0 \tag{4.3}$$

and the vertical component of equation (4.1) becomes

$$-\frac{\partial p}{\partial z} + \rho_{\mathrm{i}} g = 0.$$

That is,

$$p = \rho_{\mathrm{i}} g (h - z) \tag{4.4}$$

where $h = h(r,t)$ is the ice thickness profile. We substitute equation (4.3) and (4.4) into the radial component of equation (4.1) to obtain

$$-\rho_{\mathrm{i}} g \frac{\partial h}{\partial r} + \mu \frac{\partial^2 v_r}{\partial z^2} = 0. \tag{4.5}$$

We assume the boundary conditions of the ice sheet as follows:

1. Shear stress on the upper surface (at $z = h$) is zero

$$\mu \frac{\partial v_r}{\partial z} \Big|_{z=h} = 0. \tag{4.6}$$

2. Basal shear stress is a constant equal to the yield stress of ice ($= \tau_{\mathrm{B}}$) (Paterson, 1994)
$$\mu \frac{\partial v_r}{\partial z} |_{z=0} = \tau_{\mathrm{B}}. \tag{4.7}$$

Note that the first term on the left-hand side of equation (4.5) is independent of z because $h = h(r,t)$ is independent of z and ρ_{i} and g are constant. Since the second term on the left-hand side of equation (4.5) always cancels with the first term, it means that the second term is also independent of z. We integrate equation (4.5) with respect to z from $z = 0$ to $z = h$ and apply the boundary conditions (equation (4.6) and (4.7)) to obtain
$$-\rho_{\mathrm{i}} g h \frac{\partial h}{\partial r} - \tau_{\mathrm{B}} = 0.$$

Hence,
$$\begin{aligned} h(r,t) &= \sqrt{\frac{2\tau_{\mathrm{B}}}{\rho_{\mathrm{i}} g}[r_{\mathrm{m}}(t) - r]} \\ &= h_{\mathrm{m}}(t)\sqrt{1 - \frac{r}{r_{\mathrm{m}}(t)}} \end{aligned} \tag{4.8}$$

where $r_{\mathrm{m}}(t)$ is the radial extent of ice and $h_{\mathrm{m}}(t)$ is the maximum thickness of ice.

The total volume of ice can be calculated by integrating
$$\begin{aligned} V(t) &= \int_0^{r_{\mathrm{m}}} 2\pi r h \; dr \\ &= 2\pi h_{\mathrm{m}} \int_0^{r_{\mathrm{m}}} r\sqrt{1 - \frac{r}{r_{\mathrm{m}}}} \; dr \\ &= \frac{8}{15}\pi r_{\mathrm{m}}^2 h_{\mathrm{m}}. \end{aligned}$$

Therefore, the maximum thickness and radial extent of ice can be expressed in terms of the ice volume as
$$\begin{aligned} h_{\mathrm{m}}(t) &= \left(\frac{15}{8\pi} V(t)\right)^{\frac{1}{5}} \left(\frac{2\tau_{\mathrm{B}}}{\rho_{\mathrm{i}} g}\right)^{\frac{2}{5}} \\ \text{and} \qquad r_{\mathrm{m}}(t) &= \left(\frac{15}{8\pi} V(t)\right)^{\frac{2}{5}} \left(\frac{\rho_{\mathrm{i}} g}{2\tau_{\mathrm{B}}}\right)^{\frac{1}{5}}. \end{aligned} \tag{4.9}$$

$h_{\mathrm{m}} \sim V^{\frac{1}{5}}$ implies that $\dot{h}_{\mathrm{m}}/h_{\mathrm{m}} = \dot{V}/5V$ and $r_{\mathrm{m}} \sim V^{\frac{2}{5}}$ implies that $\dot{r}_{\mathrm{m}}/r_{\mathrm{m}} = 2\dot{V}/5V$. These expressions will be helpful for simplifying the calculation of the rate of change of the ice thickness $\frac{\partial}{\partial t} h(r,t)$ as follows. We take the time derivative of equation (4.8)

to obtain

$$\begin{aligned}\frac{\partial}{\partial t}h(r,t) &= \dot{h}_{\mathrm{m}}\sqrt{1-\frac{r}{r_{\mathrm{m}}}}+\frac{h_{\mathrm{m}}\,r\,\dot{r}_{\mathrm{m}}}{2r_{\mathrm{m}}^2\sqrt{1-\frac{r}{r_{\mathrm{m}}}}}\\ &= \frac{2\,\dot{h}_{\mathrm{m}}r_{\mathrm{m}}^2\left(1-\frac{r}{r_{\mathrm{m}}}\right)+h_{\mathrm{m}}r\,\dot{r}_{\mathrm{m}}}{2r_{\mathrm{m}}^2\sqrt{1-\frac{r}{r_{\mathrm{m}}}}}\\ &= \frac{2\left(\frac{\dot{V}h_{\mathrm{m}}}{5V}\right)r_{\mathrm{m}}^2\left(1-\frac{r}{r_{\mathrm{m}}}\right)+h_{\mathrm{m}}\,r\left(\frac{2\dot{V}r_{\mathrm{m}}}{5V}\right)}{2r_{\mathrm{m}}^2\sqrt{1-\frac{r}{r_{\mathrm{m}}}}}\\ &= \frac{\dot{V}}{5V}\frac{h_{\mathrm{m}}}{\sqrt{1-\frac{r}{r_{\mathrm{m}}}}}.\end{aligned} \tag{4.10}$$

4.2.2 Hankel Transform

Calculations of the GIA mantle flow quantities in Chapter 2 involves the zeroth-order Hankel transform of the rate of change of ice sheet profile, which is defined as

$$\mathcal{H}_0[\dot{h}](k,t) \equiv \frac{\partial}{\partial t}\widetilde{h}(k,t) = \int_0^\infty \frac{\partial}{\partial t}h(r,t)\,J_0(kr)\,r\,\mathrm{d}r. \tag{4.11}$$

By substituting equation (4.10) into (4.11), we get

$$\begin{aligned}\mathcal{H}_0[\dot{h}](k,t) &= h_{\mathrm{m}}\frac{\dot{V}}{5V}\int_0^{r_{\mathrm{m}}} J_0(kr)\,\frac{r\,\mathrm{d}r}{\sqrt{1-\frac{r}{r_{\mathrm{m}}}}}\\ &= h_{\mathrm{m}}r_{\mathrm{m}}^2\frac{\dot{V}}{5V}\int_0^1 J_0(kr_{\mathrm{m}}s)\,\frac{s\,\mathrm{d}s}{\sqrt{1-s}}\\ &= \frac{3\dot{V}}{8\pi}\int_0^1 J_0(kr_{\mathrm{m}}s)\,\frac{s\,\mathrm{d}s}{\sqrt{1-s}}\end{aligned} \tag{4.12}$$

where we obtain the second line by substituting $r = s\,r_{\mathrm{m}}$ into the right-hand side of the first line. The integral has analytical form:

$$\int_0^1 J_0(\chi s)\,\frac{s\,\mathrm{d}s}{\sqrt{1-s}} = \frac{\pi}{2\sqrt{2}}\left[J_{-\frac{1}{4}}\left(\frac{\chi}{2}\right)J_{\frac{1}{4}}\left(\frac{\chi}{2}\right)+J_{-\frac{3}{4}}\left(\frac{\chi}{2}\right)J_{\frac{3}{4}}\left(\frac{\chi}{2}\right)\right]$$

where $\chi = kr_{\mathrm{m}}$. Hence,

$$\begin{aligned}&\mathcal{H}_0[\dot{h}](k,t) =\\ &\quad\frac{3\sqrt{2}}{32}\dot{V}(t)\left[\mathrm{J}_{-\frac{1}{4}}\left(\frac{k\,r_{\mathrm{m}}(t)}{2}\right)\mathrm{J}_{\frac{1}{4}}\left(\frac{k\,r_{\mathrm{m}}(t)}{2}\right)+\mathrm{J}_{-\frac{3}{4}}\left(\frac{k\,r_{\mathrm{m}}(t)}{2}\right)\mathrm{J}_{\frac{3}{4}}\left(\frac{k\,r_{\mathrm{m}}(t)}{2}\right)\right].\end{aligned} \tag{4.13}$$

4.3 Geological Constraints

The ice volume, radius and thickness as functions of time are required to define the ice-load functions (equation (4.8), (4.10) and (4.12)). We specify these quantities based on geological evidence acquired from previous studies. The timeline of the prescribed ice radius is summarized in Table 4.1.

Table 4.1 Timeline of the model ice radius from 123 to 6 kyrBP.

Geological Period	**Time (kyrBP)**	**Ice Radius (km)**	**Average Ice Thickness (km)**
Last Interglacial	before 123.0	0.0 constant	0.0 constant
MIS 5e/5d transition	$123.0 \rightarrow 109.0$	$0.0 \rightarrow 160.0$	$0.0 \rightarrow 1.02$
MIS 5d–5a	$109.0 \rightarrow 76.0$	160.0 constant	1.02 constant
MIS 5/4 transition	$76.0 \rightarrow 66.0$	$160.0 \rightarrow 180.0$	$1.02 \rightarrow 1.08$
MIS 4–3	$66.0 \rightarrow 35.0$	180.0 constant	1.08 constant
MIS 3/2 transition	$35.0 \rightarrow 23.0$	$180.0 \rightarrow 300.0$	$1.08 \rightarrow 1.39$
Last Glacial Maximum	23.0	300.0	1.39
Offshore deglaciation	$23.0 \rightarrow 17.0$	$300.0 \rightarrow 180.0$	$1.39 \rightarrow 1.08$
Pre Bølling-Allerød	$17.0 \rightarrow 15.0$	180.0 constant	1.08 constant
Bølling-Allerød	$15.0 \rightarrow 13.8$	$180.0 \rightarrow 160.0$	$1.08 \rightarrow 1.02$
Younger Dryas	$13.8 \rightarrow 11.7$	160.0 constant	1.02 constant
Early Holocene	$11.7 \rightarrow 10.5$	$160.0 \rightarrow 45.0$	$1.02 \rightarrow 0.54$
Holocene	$10.5 \rightarrow 6.0$	45.0 constant	0.54 constant

This section explains how we use glacial-geological proxies to reconstruct the Icelandic Ice Sheet (IIS) over the last interglacial-glacial cycle.

4.3.1 Last Glacial Maximum

From the Last Glacial Maximum (LGM) (≈ 23 kyrBP) to early Holocene (10 kyrBP), we adopt the geological observations as reviewed in Patton et al. (2017) together with their numerical-modelling results to constrain the chronology and spatial profile of the IIS.

Glacial striae and landforms indicate the presence of IIS in the past, and so, they give a minimum extent of the IIS. While, sediments containing organic materials and end moraines can be interpreted as spatial limits of the IIS extent because these sediments could only be formed on subaerial and submarine/subaqueous environment. Some samples collected from moraines and sediments were radiocarbon dated. This helps control the chronology of the IIS advances and retreats.

The existence of glacial landforms on the continental shelf around Iceland such as meltwater channels as observed from the Olex database of Icelandic continental shelf bathymetry (Spagnolo and Clark, 2009) indicates that the maximum extent of the Weichselian IIS is beyond the present-day coastline. The presence of submarine moraines at continental shelf edge in different locations around Iceland (Boulton et al., 1988; Egloff and Johnson, 1979; Syvitski et al., 1999) indicates that the glaciation during the LGM of Iceland is likely to have reached the continental shelf break (Patton et al., 2017).

Radiocarbon dates of glacio-marine sediments distributed around the Icelandic continental shelf constrain the LGM timing of Iceland to be between 25 and 21 kyrBP (Andrews et al., 2002b; Andrews and Helgadóttir, 2003; Geirsdóttir et al., 2002; Patton et al., 2017; Principato et al., 2005). This timing coincides with the global ice-sheet maximum (Past Interglacials Working Group of PAGES, 2016). Based on these pieces of evidence, we set the model timing of the LGM at 23 kyrBP with the ice radius $= 300$ km extending to the continental shelf break.

4.3.2 Pre Last Glacial Maximum

The spatial and chronological constraints on the Icelandic glacier prior to the LGM are unfortunately lacking due to erosion and weathering. The two main proxies that we use for the IIS reconstruction prior to the LGM are the globally-averaged benthic δ^{18}O of Lisiecki and Raymo (2005) (called LR04 δ^{18}O) and the Red Sea relative sea sevel (RSL)

of Rohling et al. (2009), which are believed to reflect the global temperature and global ice-sheet volume. We plot these two proxies together with our model ice-load volume in Figure 4.1. We also summarize the approximate RSL from the last interglacial to present day in Table 4.2 . More details about numerical parameters of the model ice load will be discussed later in Section 4.3.4.

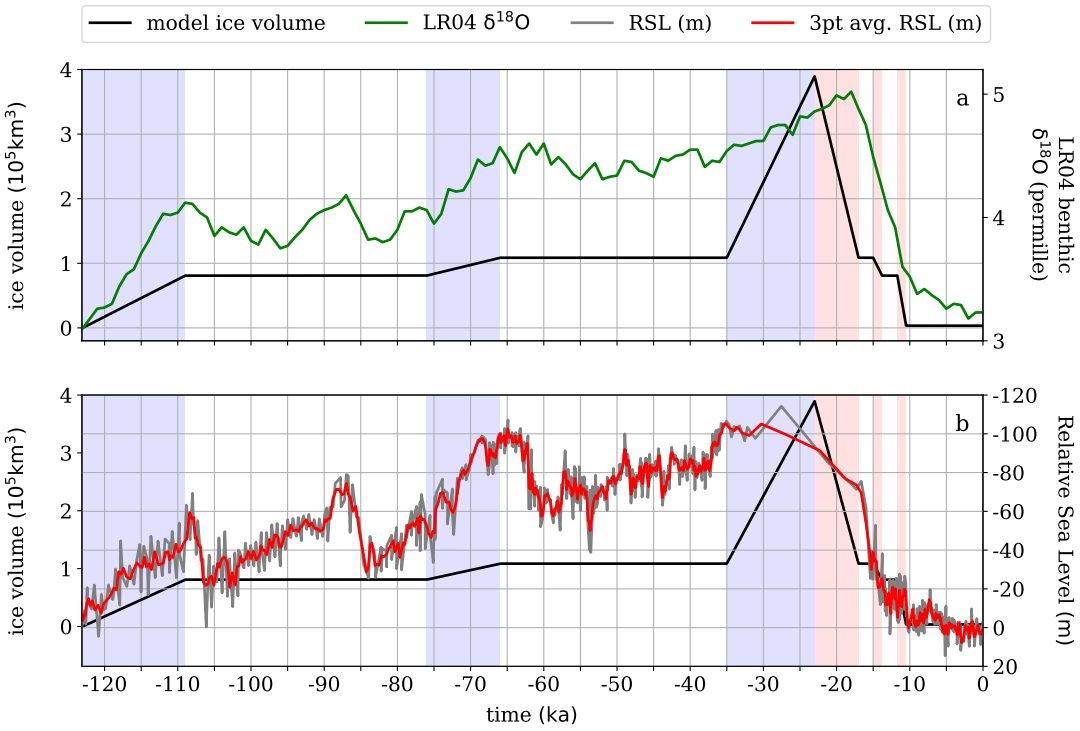

Fig. 4.1 The globally-averaged benthic δ^{18}O of Lisiecki and Raymo (2005) (green curve) and the Red Sea relative sea sevel (RSL) of Rohling et al. (2009) (grey curve with red curve as the 3-point moving average) plotted with the modelling-input ice volume from 123 kyrBP to present. Blue-shaded and red-shaded areas are the periods during which the model ice advances and retreats respectively.

During the last interglacial, the RSL was at about the same level as present day with approximately the same globally-averaged temperature as indicated by the LR04 δ^{18}O. The last interglacial terminated at $\approx$ 123 kyrBP (Elderfield et al., 2012; Lisiecki and Raymo, 2005; Past Interglacials Working Group of PAGES, 2016; Rohling et al., 2009), which marked the beginning of the decline of RSL and rise of LR04 δ^{18}O. In our model before 123 kyrBP, we assume that Iceland was ice-free until at the last interglacial termination (123 kyrBP) when our prescribed ice-load volume begins to increase linearly with time.

Table 4.2 Estimated ages and Relative Sea Level (RSL) at different Marine Isotope Stages (MIS) over the last glacial period.

MIS	**Age** (kyrBP)	**RSL** (m above present)
5e	123	0
5e/5d	116	decreasing to ≈ -50
5d	109	between -20 and -80
5c	96	
5b	87	
5a	82	
5/4	71	decreasing to ≈ -80
4/3	57	between -40 and -100
3/2	29	decreasing to ≈ -110
2/1	14	increasing to 0
1	0	0

Following the end of the last interglacial at 123 kyrBP, the RSL decreased to between -20 and -80 m during the Marine Isotope Stage 5d–5a (MIS 5d–5a) at ≈ 109–76 kyrBP (the left-most unshaded region of Figure 4.1). The LR04 δ^{18}O indicates that this period is relatively colder than the last interglacial. We assume in our model that the advance of IIS, which begins at 123 kyrBP, ends at 109 kyrBP with its extent remaining within the present-day coast line with ice radius = 160 km. The pause of the IIS expansion in our prescribed ice load takes place from 109 to 76 kyrBP (the left-most unshaded region of Figure 4.1), corresponding to MIS 5d–5a.

From ≈ 76 to 66 kyrBP, the RSL dropped further until it reached ≈ -100 m, marking a cold period called MIS 4. LR04 δ^{18}O indicates that this period is colder than the MIS 5d–5a (Lisiecki and Raymo, 2005). In our model, we assume that the IIS advance recommences at 76 kyrBP and that the IIS volume expands linearly with time during the MIS 5/4 transition (76–66 kyrBP) until the coverage reaches the present-day coastline with the ice radius = 180 km at 66 kyrBP.

During 66–35 kyrBP before the MIS 2, we assume in our model that the ice load stays constant with radius = 180 km. In this period, the RSL fluctuated between 40 and 100 m below the present day level until at ≈ 35 kyrBP when the RSL began to decline further until it reached its lowest value of ≈ -110 m during the MIS 2 at ≈ 23 kyrBP, which coincided with the global LGM.

We discussed previously in Section 4.3.1 that the IIS extent at the LGM was likely to attain the continental-shelf break. Geological evidence to constrain the IIS extent just before the LGM is very limited to the Reykjanes Pennisula. The presence of marine shells in a few locations on the coastal area of Reykjanes Pennisula with weighted mean ages of 25.8 kyrBP at Njarðvíkurheiði (Norðdahl and Pétursson, 2005), 28.1 kyrBP at Sandgerði (Norðdahl and Pétursson, 2005) and 31.6 kyrBP at Sudernes (Eiríksson et al., 1997) indicates that the extent of the ice sheet in Reykjanes Pennisula at ≈ 28 kyrBP just before the LGM was still within the present-day coastline. Based on the evidence of marine shells, Patton et al. (2017) believed and showed in their IIS model that most area of the continental-shelf break around Iceland was still ice-free at 28 kyrBP. Given that the IIS extent attained the continental-shelf break at 23 kyrBP, the IIS advance during 28–23 kyrBP must have been very rapid (Patton et al., 2017). In our model, the prescribed IIS advance recommences at 35 kyrBP after the pause between 66 and 35 kyrBP at 180-km radius. The prescribed ice volume increases linearly with time to its peak value at the LGM at 23 kyrBP with the ice radius $= 300$ km.

4.3.3 Last Deglaciation

Following the LGM, the globally-averaged temperature began to rise, the RSL began to drop (Figure 4.1) and the retreat of IIS soon followed as evidenced by the radiocarbon dates of glacio-marine sediment cores in many locations on the continental shelf (Figure 1b of Patton et al. (2017)). We also plot the locations and ages of the sediments in Figure 4.2 using the sediment data as provided in Table 1 of Patton et al. (2017).

These sediment data indicate that the glacier retreat on the continental shelf began before 22.8 kyrBP and that the retreat had reached the mid shelf before 18.6 kyrBP. The presence of sediments aged 14.8 and 14.9 kyrBP on shore near the present-day coastline in the west and east respectively suggests that most area off shore on the continental shelf was ice-free by 14.8 kyrBP.

The retreat is also evidenced by high-raised marine shoreline limits (ML) of 105–150 ma.s.l. with radiocarbon dates between 15.1 and 14.7 kyrBP (Pétursson et al., 2015). The high-raised ML indicates that these coastal areas were already ice-free at the time but still submerged below the sea level due to the surface depression caused by the ice load.

The ice flow model of Patton et al. (2017) showed that the deglaciation on the continental shelf (we call hereafter as the Offshore Deglaciation) was likely to have happened between ≈ 23 and 17 kyrBP. This period is followed by a pause at the present-day coastline from ≈ 17 to 15 kyrBP. In our model, we assume that the

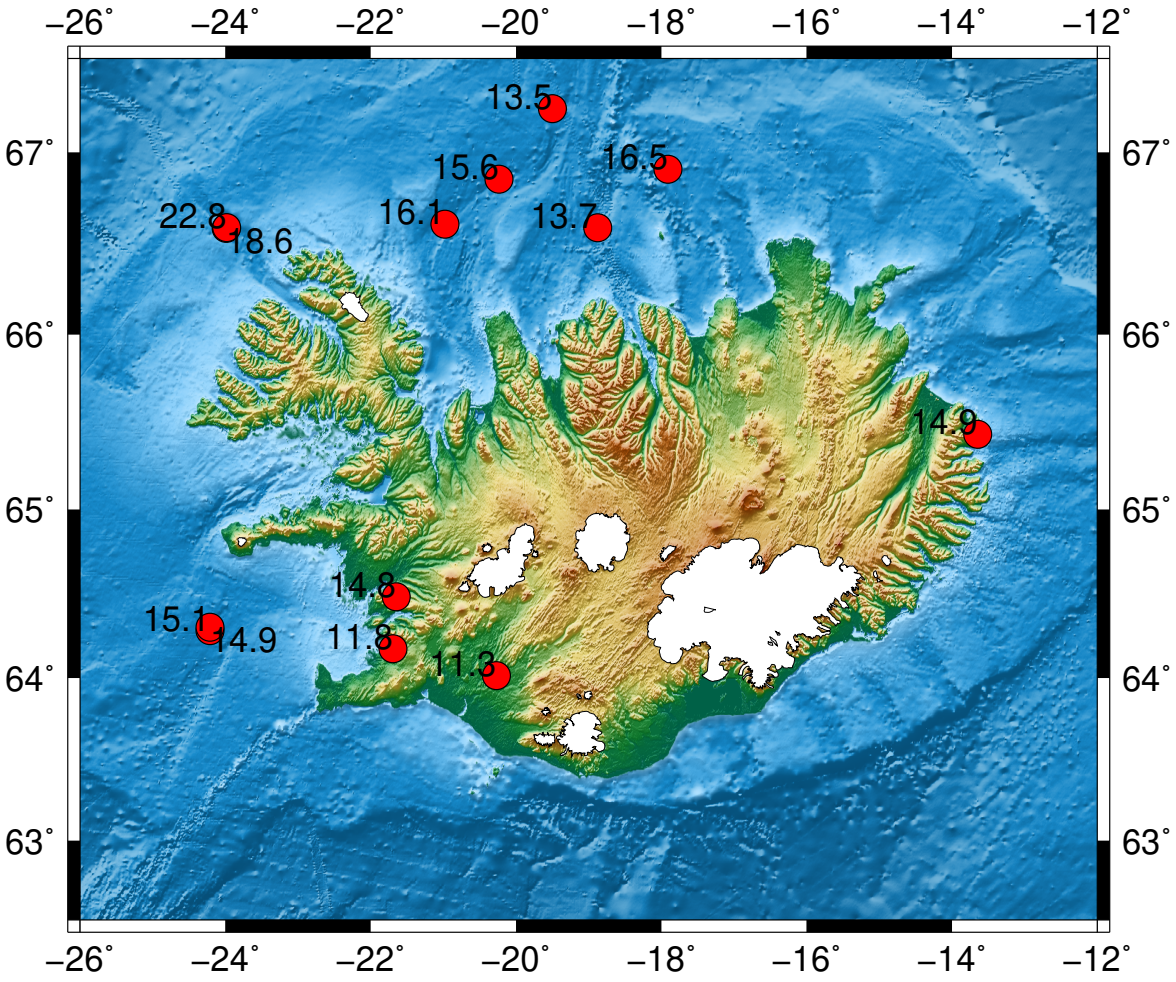

Fig. 4.2 Locations of sediments (red-filled circles) with radiocarbon dates (labelling numbers in kyrBP) to constrain the deglaciation of the Late Weichselian IIS following the LGM. The present-day glaciers are filled with white color.

Offshore Deglaciation begins at 23 kyrBP with the ice volume decreasing linearly with time until at 17 kyrBP when the deglaciation pauses at the ice radius of 180 km.

The deglaciation in the ice flow model of Patton et al. (2017) then recommenced after the pause at 15 kyrBP until at ≈ 13.5 kyrBP when a relatively cold period called the Younger Dryas began and the IIS re-advanced slightly. The presence of end moraines with Younger Dryas age (12.1–11.9 kyrBP) constrains the glacier advance to be within the present-day coastline (Geirsdóttir, 2011; Geirsdóttir et al., 1997; Norðdahl and Pétursson, 2005). In our model, we assume that after the pause at 15 kyrBP the ice volume decreases linearly with time until the ice radius has dropped to 160 km at 13.8 kyrBP. Following this period, our presumed deglaciation pauses at the ice radius of 160 km from 13.8 to 11.7 kyrBP corresponding approximately to the Younger Dryas.

Following the Younger Dryas, the glacier retreat in the ice flow model of Patton et al. (2017) recommences at ≈ 11.7 kyrBP until most of the ice is gone at ≈ 10 kyrBP. The presence of the the Saksunarvatn tephra aged 10.2 kyrBP (Andrews et al., 2002a; Grönvold et al., 1995) in many locations of Iceland suggests that the majority of the IIS had disappeared by 10.2 kyrBP. In our model, we assume that between 11.7 and 10.5 kyrBP the ice volume decreases linearly with time from the ice radius of 160 km to 45 km. Figure 4.3 shows the model ice-load history during the last deglaciation.

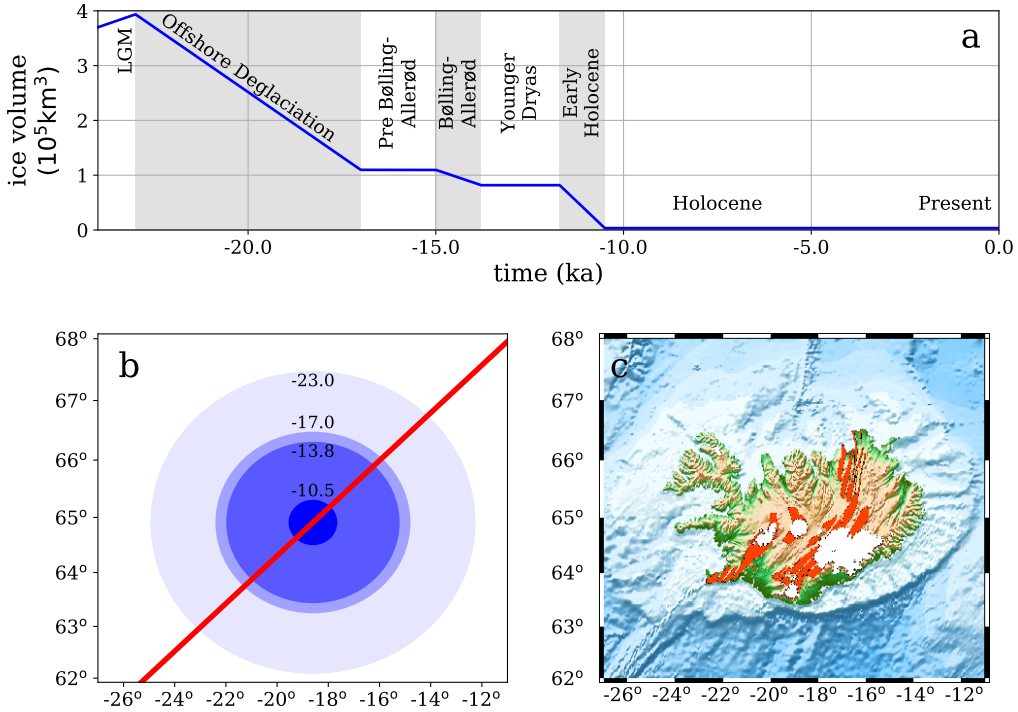

Fig. 4.3 (a) The modelling-input ice volume history with grey bars labelling deglaciation periods. (b) Top-view of the model rift (red line) with snapshots of the modelling-input ice coverage (blue circles) at time $t = -23.0$, -17.0, -13.8 and -10.5 kyr as labelled at the edges of the circles. (c) Map of Iceland with the same length scale as in (b) showing locations of the fissure swarms (red color) where the plate spreading takes place and the current glaciers in white color. LGM = Last Glacial Maximum.

4.3.4 Ice Thickness

From equation (4.8) in Section 4.2, the aspect ratio of the ice sheet is determined by the basal shear stress (τ_{B}). Therefore, at any given time with a prescribed ice radius (Table 4.1), the model ice thickness is dependent of τ_{B}. Conversely, this means that τ_{B} can be determined from the IIS thickness. From equation (4.8),

$$h_{\mathrm{m}}(t) = \sqrt{\frac{2\tau_{\mathrm{B}}}{\rho_{\mathrm{i}} g} r_{\mathrm{m}}(t)}.$$

$$\text{Or,} \qquad \tau_{\mathrm{B}} = \frac{\rho_{\mathrm{i}} g h_{\mathrm{m}}^2}{2 r_{\mathrm{m}}}. \tag{4.14}$$

So, provided that the ice thickness h_{m} and the radius r_{m} at any given time are known, this equation can be used to obtain τ_{B}.

The thickness of the IIS on shore during the last deglaciation can be constrained by the table mountains, erosional trimlines and glacial striae. Table mountains are subglacial volcanoes that erupted subglacially until the summit emerged above the surface of the glacial lake (Thordarson and Höskuldsson, 2014). Hence, the altitude of a table mountain summit gives a minimum elevation of the IIS surface at the time when the table mountain was formed.

Exposure ages of the summits of 13 table mountains in the neovolcanic zones of Iceland have been dated using the cosmogenic ^{3}He in Licciardi et al. (2007). The summit elevations of these table mountains range from 280 to 1700 m a.s.l. This means that, at around the time that the table mountains were formed, the IIS thickness was at least 1.7 km, assuming that the Earth surface on Iceland was at about the present-day sea level. Most of these table mountains have ages between 14.4 and 10.2 kyrBP. The IIS radius during this period had radius of ≈ 180 km. We therefore use the radius of 180 km together with the thickness of 2 km to obtain the estimated $\tau_{\mathrm{B}} = 100$ kPa from equation (4.14). This is in the typical range of 40–150 kPa (Paterson, 1994).

In Figure 4.4, we plot the modelled ice surface profiles at 23, 15 and 12 kyrBP together with the summit elevations of 13 table mountains from Licciardi et al. (2007). We divide these table mountains into 4 age bins: > 20, 20-12.5, 12.5-10 and < 10 kyrBP, each of which is plotted with a different color that matches to the color we use for plotting the modelled ice. This figure shows that the modelled ice thickness history is in a reasonable agreement with the mountain summit elevations.

Table 4.3 summarizes the numerical parameters we use for the modelled ice load from the last interglacial (123 kyrBP) to just before the mid Holocene (6 kyrBP).

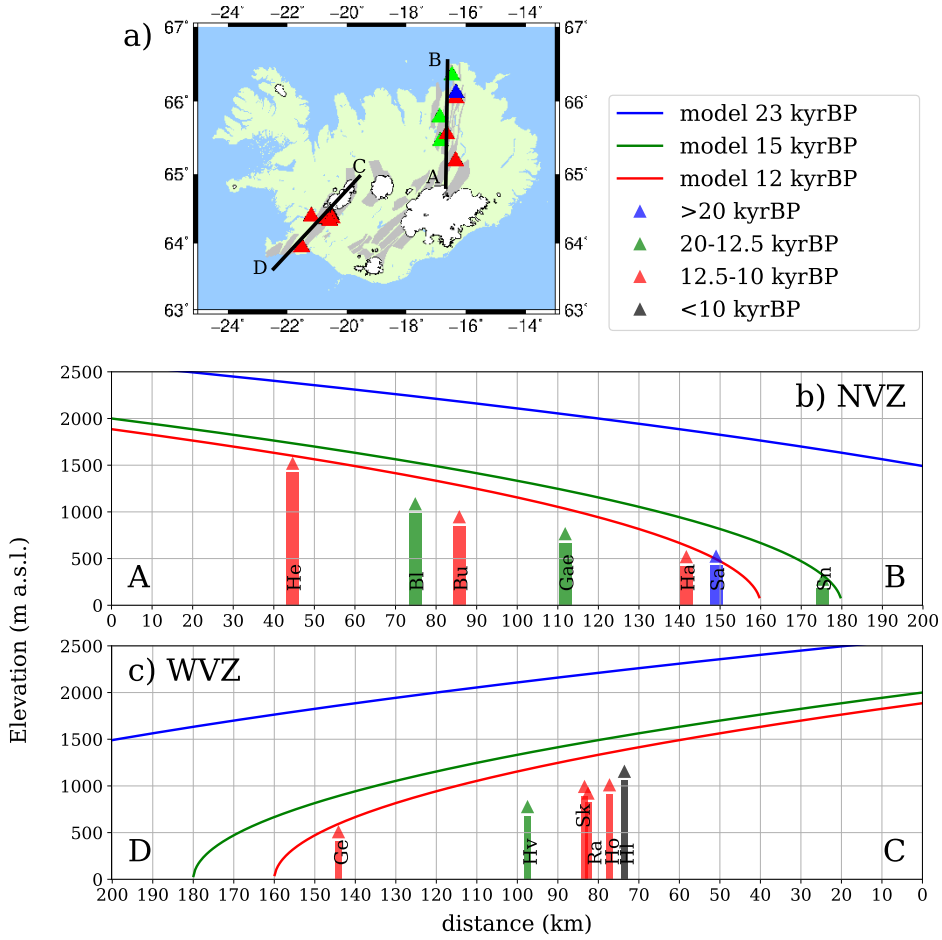

Fig. 4.4 (a) Map showing locations of cosmogenic-exposure dated table mountains in the Northern-Volcanic Zone (NVZ) and the Western-Volcanic Zone (WVZ) as triangles colored according to the age range as shown in the legend. The modelled ice center for NVZ and WVZ are at point A and C respectively. The fissure swarms where the plate spreading takes place are shaded in grey color and the present-day glaciers are shaded in white. (b) Transect through NVZ (line AB in panel (a)) showing the mountain summit elevations (triangles with the same color codes as in panel (a)) and the modelled ice surface profiles at three different ages as labelled in the legend. (c) Same as (b) but transect through WVZ (line CD in panel (a)). (Bl) Bláfjall, (Bú) Búrfell, (Gæ) Gæsafjöll, (Ge) Geitafell, (Ha) Hafrafell, (He) Herðubreið, (Hl) Hlöðufell, (Hö) Högnhöfði, (Hv) Hvalfell, (Ra) Rauðafell, (Sa) Sandfell, (Sk) Skriða and (Sn) Snartarstaðarnúpur. Age data are from Licciardi et al. (2007).

Table 4.3 Parameter values for the model ice between 123 and 6 kyrBP.

Parameter	**Meaning**	**Value**	**Dimensions**
g	gravitational acceleration	9.82	m/s^2
ρ_i	density of ice	900	kg/m^3
τ_B	yield stress of ice	100	kPa

Chapter 5

Last Deglaciation (23–10.5 kyrBP)

This Chapter is a modified version of Eksinchol et al. (2019). It explores how the finite rate of melt ascent affects the eruption rates and the La concentrations in lavas erupted during the last deglaciation. The model results are compared with the observational data in order to estimate the average melt ascent velocity.

5.1 Mantle Flow

We use the mantle flow model as discussed in Chapter 2 with the ice-load history in Chapter 4 as an input. Our models are similar to that of the Jull and McKenzie (1996) with the following key differences:

1. While Jull and McKenzie (1996) used an ice load with a constant radius, our ice sheet behaves like a gravity current with time-dependent radius and thickness (see Section 4.2).

2. Our ice-load input consists of multiple deglaciation stages (Chapter 4) beginning at 23.0 to 10.5 kyrBP designed to capture key features of ice-sheet reconstructions; whereas, the presumed ice load of Jull and McKenzie (1996) has only one deglaciation stage with the ice thickness decreasing linearly with time during 10–9 kyrBP.

3. We neglect the elastic response of the solid mantle. This is because the Maxwell relaxation time ($\tau_{\mathrm{M}} = \eta/\mu \approx 10^1$ yr) is much shorter than the viscous characteristic time ($\tau_{\mathrm{v}} = 2\eta k/\rho_{\mathrm{s}} g \approx 10^3$ yr) where μ is the elastic modulus, k is the wave number of the ice sheet profile in the radial direction (as defined in Section 4.2.2) and other variables are as defined in Table 5.1. This means that the elastic deformation

in the viscoelastic mantle model used in Jull and McKenzie (1996) is negligible and the deformation in the mantle is dominated by the viscous response. We therefore model the mantle as a viscous half-space incompressible fluid and the elastic thickness of the Icelandic lithosphere is assumed to be negligible. When using the same modelling inputs as in Jull and McKenzie (1996), our numerical model yields the same results, which verifies our assumption that the elastic deformation is insignificant.

4. We assume finite melt ascent velocity; whereas, Jull and McKenzie (1996) assumed instantaneous transport of melts from depths to the surface.

Numerical parameters used as inputs into the model are listed in Table 5.1.

Table 5.1 Parameter values for calculations.

Parameter	**Meaning**	**Value**	**Dimensions**
D^{La}	La partition coefficient	0.010	1
$-(\partial F/\partial P)_S$	isentropic melt productivity	10	wt%/GPa
g	gravitational acceleration	9.82	$\mathrm{m/s^2}$
P_{sol}	primitive solidus pressure	3.5	GPa
U_0	plate half-spreading rate	10	mm/yr
z_{c}	crustal thickness	20	km
α	ridge angle	45	deg
η	mantle viscosity	8.0×10^{18}	Pa s
ρ_{i}	density of ice	900	$\mathrm{kg/m^3}$
ρ_{l}	density of melt	2,900	$\mathrm{kg/m^3}$
ρ_{s}	density of solid mantle	3,300	$\mathrm{kg/m^3}$
τ_{B}	yield stress of ice	100	kPa

Numerical values of the plate half-spreading rate (U_0), crustal thickness (z_{c}), ridge angle (α) and mantle viscosity (η) are the same as in Jull and McKenzie (1996). $z_{\mathrm{c}} = 20$ km is at the lower bound of the Darbyshire et al. (2000) estimates (20–37 km) because our study areas are relatively far (> 100 km) from the mantle plume center. Numerical values of $U_0 = 10$ mm/yr and $\eta = 8.0\times10^{18}$ Pa s are similar to the Árnadóttir et al. (2009) estimates. The density of ice (ρ_{i}) is in the range of 830–917 $\mathrm{kg/m^3}$ in Paterson (1994). The densities of melt (ρ_{l}) and of solid mantle (ρ_{s}) follow Katz et al. (2003). Sources of the remaining numerical parameters will be mentioned later.

Similar to the assumption made by Jull and McKenzie (1996), in steady state, the spreading ridge induces passive up-welling of the mantle, which we assume to follow the corner flow (Batchelor, 2000; Spiegelman and McKenzie, 1987) (see Section 2.1).

The average up-welling velocity of the mantle at steady state is equal to the plate half-spreading rate of 10 mm/yr. Active upwelling induced by the mantle plume can also increase the melt production rate. However, the geological data in this chapter come from regions that are at least ~ 100 km away from the plume center. We therefore assume that the active upwelling is insignificant here.

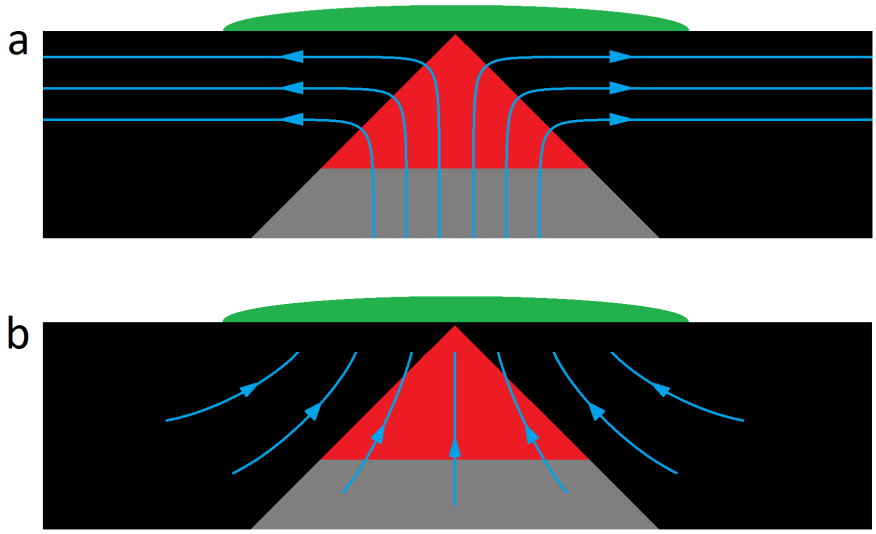

Fig. 5.1 Simplified diagrams illustrating the solid mantle streamlines of (a) corner flow and (b) Glacial Isostatic Adjustment (GIA) in a vertical plane passing through the center of ice perpendicular to the ridge axis. In steady state, the decompression melting comes from the upwelling of the mantle due to the spreading ridge (with half-spreading rate of 10 mm/yr) and the mantle plume (which we assume to be insignificant in the studied areas). During deglaciation, the GIA further increases the mantle upwelling rate and hence the decompression melting rate.

The glacial load on the surface affects the pressure in the mantle underneath. During deglaciation, the surface load drops, which leads to an increased mantle decompression melting rate from that induced by the steady state passive corner flow (Figure 5.1). Section 2.2 provides details about how we model the GIA in the mantle.

Figures 5.2 and 5.3 show our model results of the mantle velocity field at steady state (Figures 5.2a and 5.3a) and during the last deglaciation (Figures 5.2b-d and 5.3b-d) when the ice load history follows the timeline given in Chapter 4. These Figures illustrate that the deglaciation can significantly increase the up-welling velocity of the mantle in the melting region (enclosed by the dark green lines) more than 10 times. This will significantly increase the decompression melting rate in the mantle.

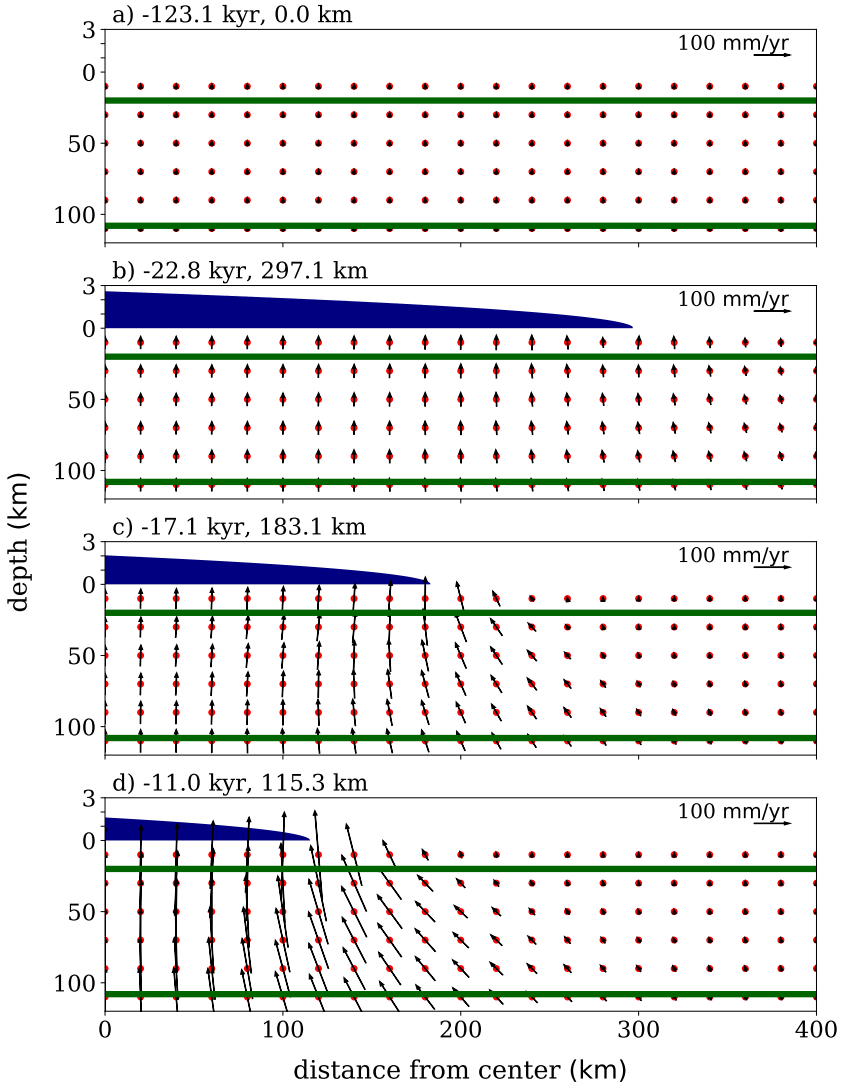

Fig. 5.2 Snapshots of the mantle velocity field in a vertical plane passing through the center of ice parallel to the ridge axis induced by the deglaciation and the corner flow. Each arrow is the velocity of the mantle at the red dot. The arrow length is proportional to the magnitude of the mantle velocity. An arrow of length corresponding to the velocity of 100 mm/yr is shown at the top-right corner of each panel. The time and ice radius of each panel are labelled just above the panel. The glaciation follows the timeline given in Chapter 4. The ice load profile (navy blue color) is drawn on top of the mantle with 15× vertical exaggeration. Boundaries of the mantle melting region are outlined by the dark green lines.

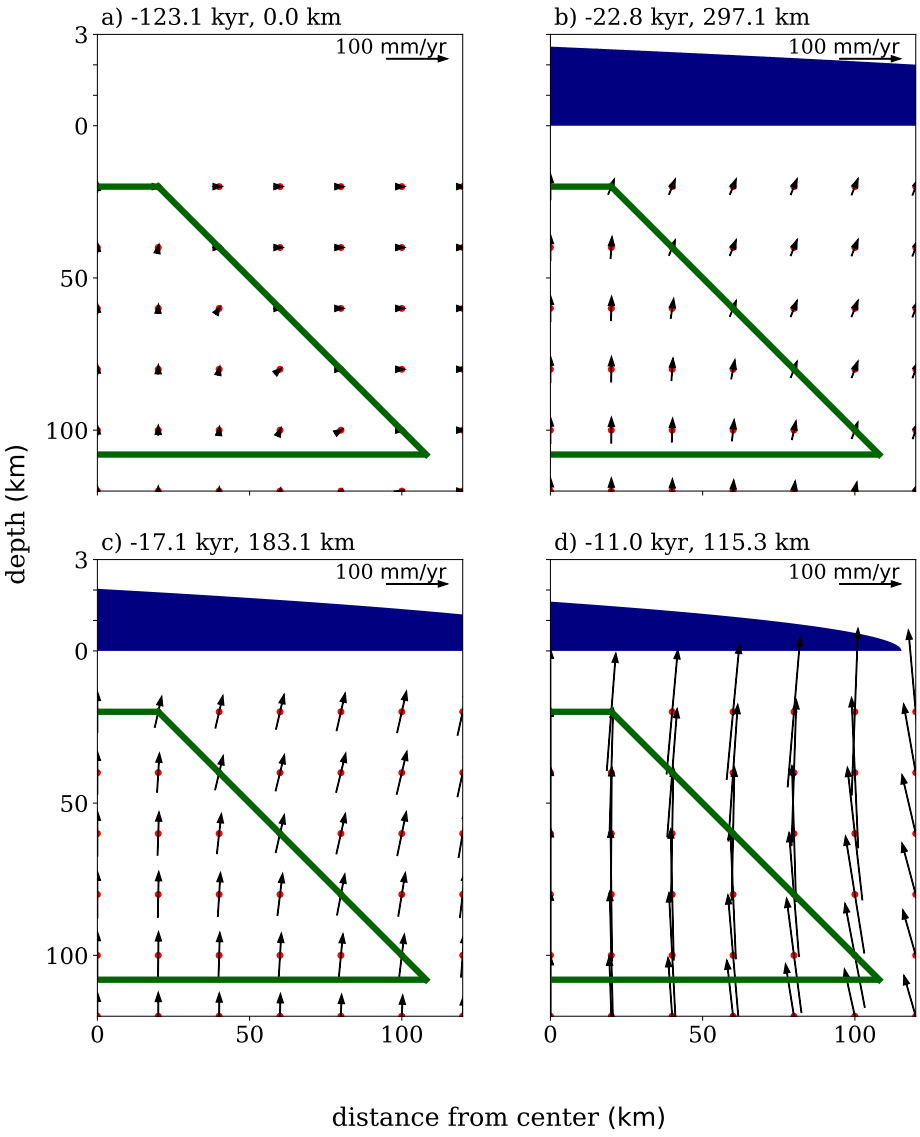

Fig. 5.3 Same as Figure 5.2 but in a vertical plane passing through the center of ice *perpendicular* to the ridge axis.

Figures 5.4 and 5.5 illustrate snapshots of the model results of the decompression rates in the mantle at steady state (Figures 5.4a and 5.5a) and during the deglaciation (Figures 5.4b-d and 5.5b-d) when the ice load history follows the timeline given in Chapter 4.

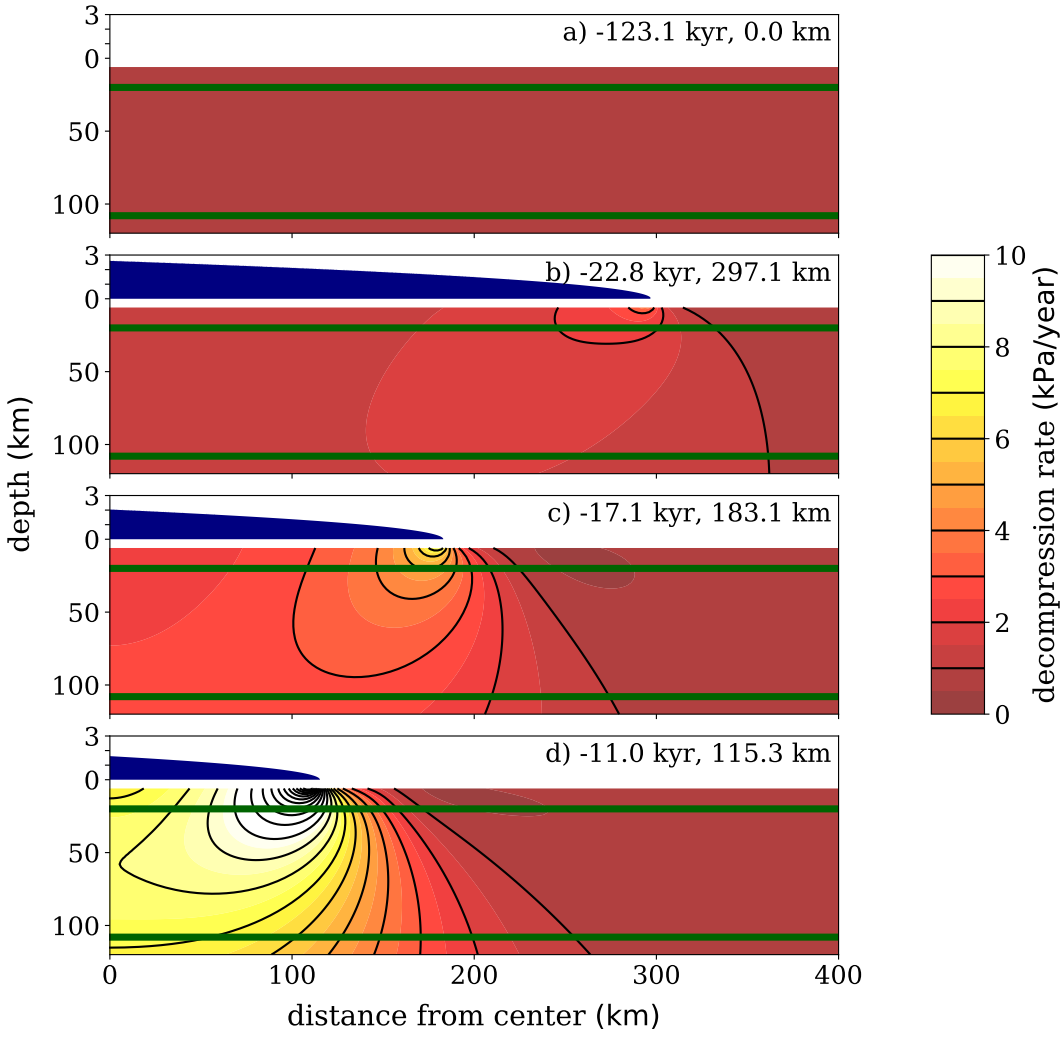

Fig. 5.4 Snapshots of the decompression rate in a vertical plane passing through the center of ice parallel to the ridge axis (ridge axis as red line in Figure 4.3b) induced by the postglacial rebound and the corner flow. Black contour lines are separated at equal intervals of 1 kPa/yr. The time and ice radius are shown in the upper right corner of each panel. The deglaciation is assumed to take place between time $t = 23.0$–10.5 kyrBP with two pauses in between at $t = 17.0$–15.0 kyrBP and 13.8–11.7 kyrBP during which the ice volume stays constant (see Chapter 4 for details). The ice load profile (navy blue color) is drawn on top of the mantle with 15× vertical exaggeration. Boundaries of the mantle melting region are outlined by the dark green lines.

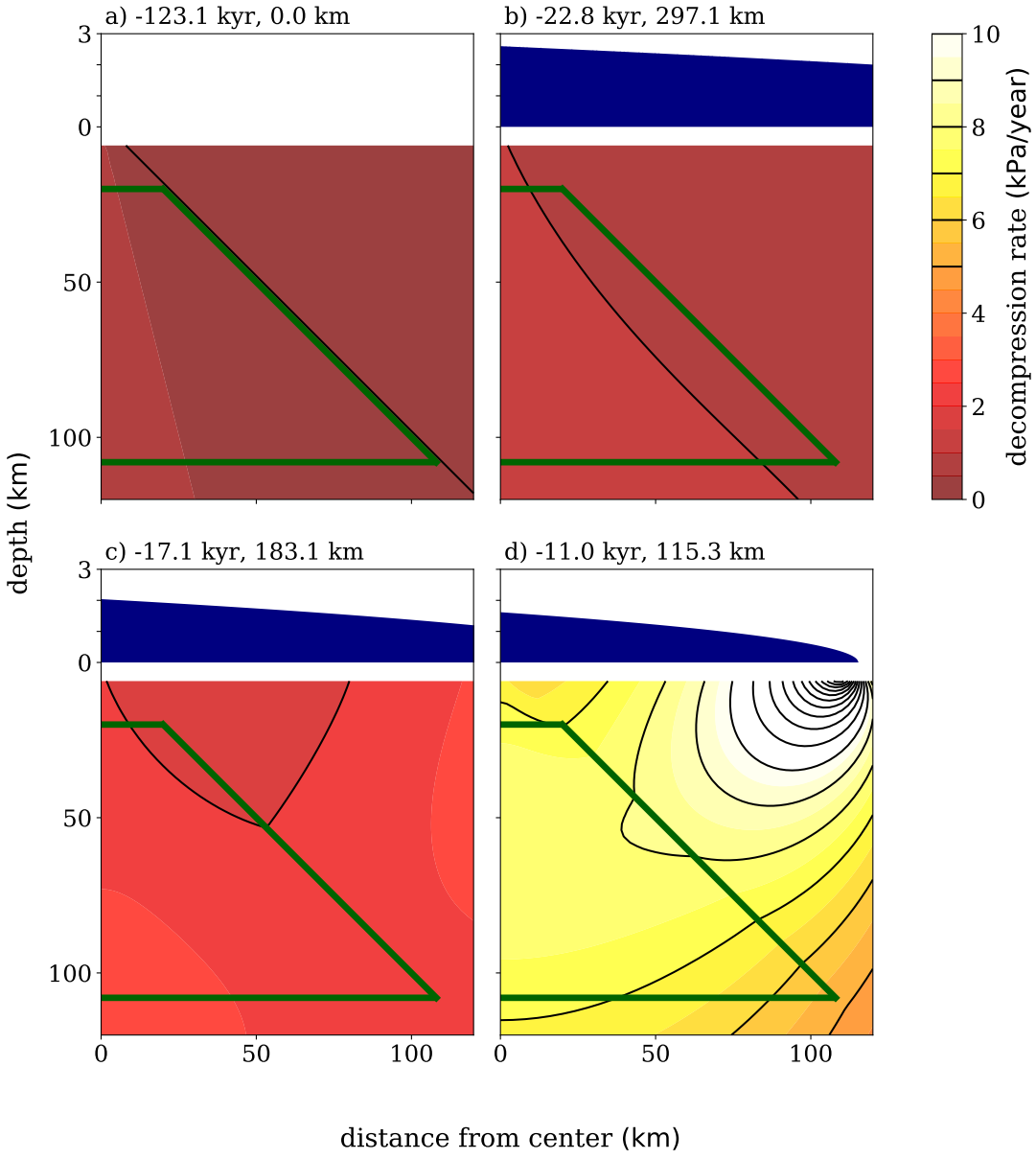

Fig. 5.5 Same as Figure 5.4 but in a vertical plane passing through the center of ice *perpendicular* to the ridge axis.

While the Jull and McKenzie (1996) model with constant radius of ice-load predicted that the region of maximum decompression rate is always below the center of the ice sheet (their Figure 3), our model with variable ice radius predicts that this region

is below the glacier terminus and is moving radially inward as the ice retreats. The glacially induced decompression causes the spatially dependent mantle melting rate underneath Iceland to increase from its steady state value by several fold during the deglaciation. These extra melts then transport to the surface, causing an increase in volcanic eruption rates.

5.1.1 Ridge Angle

The ridge angle α is dependent on the thickness profile of the lithospheric plate along the distance $r_\perp$ perpendicular to the ridge axis. The plate is formed from hot mantle at the ridge axis. Conductive heat loss to the Earth's surface cools the material, which causes the viscosity to increase, and the lithosphere gets thicker as it ages. At the same time, as the plate gets thicker, it is advected away from the ridge axis at a speed equal to the plate half-spreading rate U_0. The advection speed U_0 therefore controls the thickness profile and the ridge angle.

At a slower spreading rate (i.e. lower U_0), it takes longer for the plate to be advected from the ridge axis to a distance $r_\perp$. Hence, at a given distance $r_\perp$, ridge with a lower U_0 will have an older plate, which is thicker, meaning that the ridge angle α will also be larger (i.e. steeper inclination from the horizontal).

An example of how to estimate α can be found in Appendix B of Spiegelman and McKenzie (1987). At $U_0 = 10$ mm/yr, Spiegelman and McKenzie (1987) estimated that $\alpha = 40°$. By implementing the same method with a lower mantle shear viscosity (as in Table 5.1), we obtain a slightly steeper angle and therefore $\alpha = 45°$ is used. This is relatively steeper than in most of the Mid-Ocean Ridges due to a relatively slower plate spreading rate.

α also sets the model inclined boundary of the melting region. If α is smaller, the melting region will be larger. But also, based on the corner flow model (Equation (2.9)), a smaller α will have a slower average mantle upwelling rate, which will reduce the melting rate per unit volume. The net result will be that the total melt production rate due to the corner flow integrated over the melting region will remain unchanged with α.

For GIA, the upwelling rate and the decompression rate (Equation (2.45)) are independent of α. The decrease/increase of α, which enlarges/reduces the melting region, will increase/decrease the total GIA melt production rate while keeping the steady-state melt production rate unchanged. i.e. changing α will change the ratio of the GIA melt production rate to the steady-state melt production rate. Nevertheless, our melt ascent velocity estimate (see later in Figures 5.10, 5.11 and 5.12) is not

strongly dependent on the steady-state melt production rate. The reasons are as follows. The model results (Figures 5.10, 5.11 and 5.12) are dominated by the GIA melt volume (with less than $\sim 10\%$ contribution from the steady-state melt volume). Changing α will scale the GIA melt volume up/down approximately uniformly in the temporal space. All the model volumes, which are normalized to the total volume, will not be affected by the scaling. Hence, the uncertainty of α will not cause a significant uncertainty in our estimated value of melt ascent velocity.

While the bottom boundary of the modelled melting region is allowed to fluctuate with the change of pressure (following where the adiabat intersects the solidus), we assume that the inclined boundary is fixed by fixing the value of α. The change of the ice load will affect the pressure of the mantle underneath, which will cause the inclined boundary to move. However, since the ice load of 2-km thick is equivalent to ~ 600 meters of vertical column of rock, the movement of the inclined boundary in the vertical direction will be of the same order of ~ 600 meters. This is small compared to the length scale of the melting region of ~ 100 km, so, it will not affect the calculated melt production rate significantly. Also, since mantle at near the inclined boundary is already depleted in REEs, the small fluctuation of the inclined boundary will not cause a significant change in the amount of REE partitioning into melts. Hence, in practice, it is appropriate to neglect the inclined boundary fluctuation unless the calculated quantities vary sharply near the boundary over the length scale of ~ 600 meters.

5.2 Mantle Melting

Numerical results of the mantle flow model are input into the mantle melting model that we describe in Chapter 3. We advect the degree of melting F using the semi-Lagrangian scheme as discussed in Section 3.2.1. F as a function of location $\boldsymbol{x}$ and time t is then used for determining the solidus pressure p_{s} and the compositions of the residual solid mantle (see Section 3.2).

The isentropic melt productivity depends on several factors including the composition of the mantle, temperature and pressure (McKenzie, 1984). In numerical calculations, using different melt productivity functions will result in different profiles of depth-dependent mantle melting rate, and different eruptive REE concentrations (Slater et al., 1998). To investigate the effect of magma transport solely without the effect of melt productivity function on the eruptive REE concentrations, we use a constant isentropic melt productivity (Table 5.1) and the degree of melting as a

function of pressure follows a simple linear relation

$$F(P) = -\left(\frac{\partial F}{\partial P}\right)_S (P_{\rm sol} - P)\,. \tag{5.1}$$

Our presumed values of primitive solidus pressure and melt productivity (in Table 5.1) give a melt productivity function that closely resembles that obtained from the melt parametrization of Katz et al. (2003) at 1500 °C potential temperature.

Sims et al. (2013) have shown that the temporal variability of isotope ratios in lavas erupted during the last deglaciation in northern Iceland provide evidence for a lithologically heterogeneous mantle source beneath Iceland. We investigate the effect of mantle heterogeneities by comparing our simple homogeneous mantle model results to that of the pMELTS modelling (Ghiorso et al., 2002; Smith and Asimow, 2005) of a bi-lithological mantle as used in Rudge et al. (2013). We show these results in Appendix B that both mantle models yield the same conclusions for the rate of melt ascent. Our model is not very sensitive to the mantle heterogeneities because the model calculations do not involve isotopic composition.

At each time step, the pressure p calculated from equation (2.45) in Chapter 2 is compared with the solidus pressure $p_{\rm s}$ in order to determine if the solid mantle is on the solidus or at sub-solidus. On the solidus, the pressure p is *equal to* the solidus pressure $p_{\rm s}$; whereas, at sub-solidus, the pressure p is *greater than* the solidus pressure $p_{\rm s}$.

Mantle at sub-solidus has zero melting rate regardless of whether or not the net decompression rate is positive (= negative compression rate). Mantle melting can only occur at where the particle is on the solidus *and* the net decompression rate is positive. We define the excess pressure in equation (3.2), Chapter 3. On-solidus particles have zero excess pressure; whereas, sub-solidus particles have positive excess pressure.

Figures 5.6 and 5.7 show snapshots of the model results of the mantle melting rates at steady state (Figures 5.6a and 5.7a) and during the last deglaciation (Figures 5.6b-d and 5.7b-d) when the ice load history follows the timeline given in Chapter 4. In any region where the excess pressure is zero (non-blue region), the mantle is on the solidus and the decompresion melting rate is proportional to the decompression rate as shown in Figures 5.4 and 5.5.

Figures 5.6b and 5.7b show that, even though the deglaciation has already been proceeding for 200 years following the LGM at 23 kyrBP, the majority of the mantle melting region still has a positive excess pressure $\Delta p > 0$ (blue color). $\Delta p > 0$ indicates that the mantle is at sub-solidus, which is a result of the glacial loading prior to

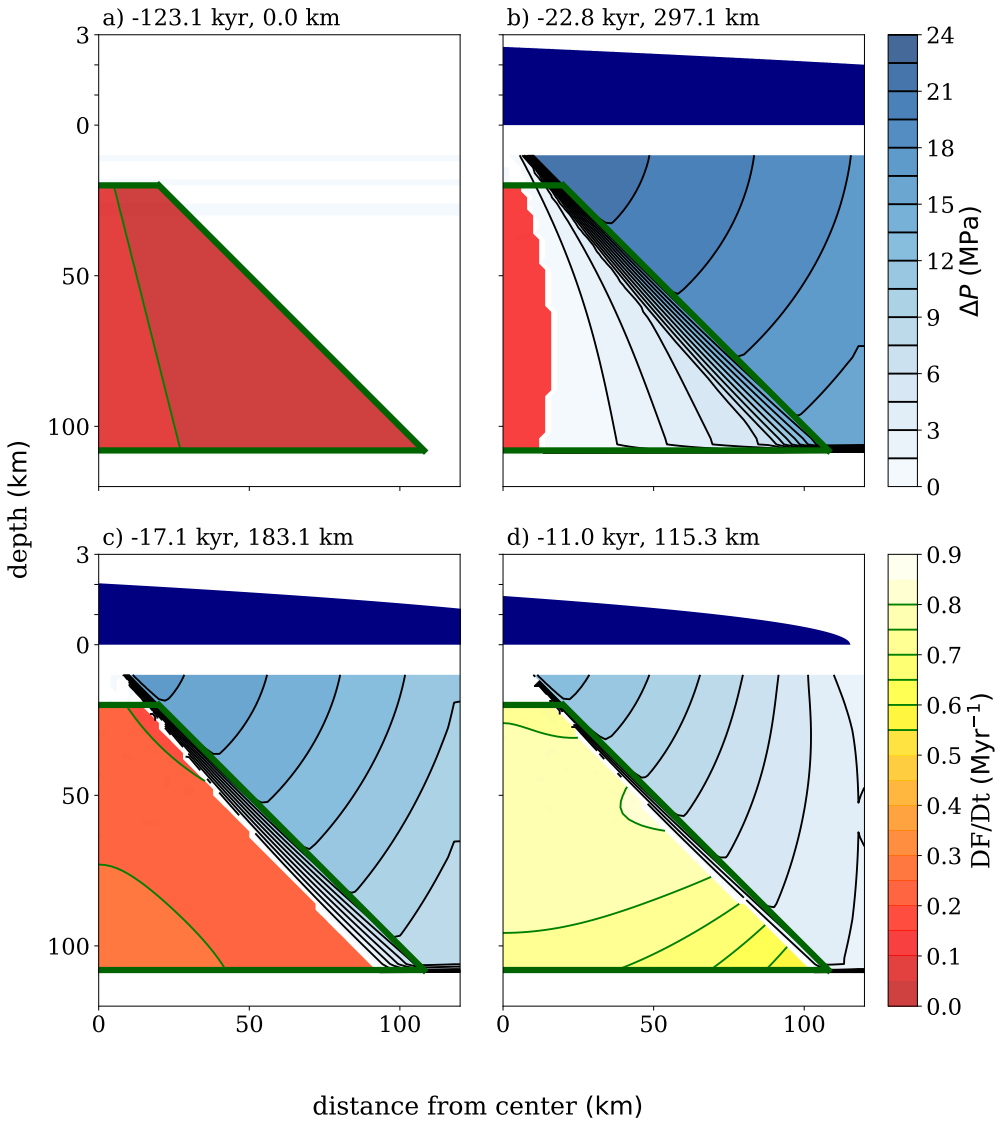

Fig. 5.6 Snapshots of the mantle melting rate DF/Dt and the excess pressure Δp in a vertical plane passing through the center of ice perpendicular to the ridge axis induced by the postglacial rebound and the corner flow. Contour lines are separated at equal intervals of 0.1 /Myr and 1.5 MPa for DF/Dt and Δp respectively. The time and ice radius are shown in the upper right corner of each panel. The deglaciation follows the timeline given in Chapter 4. The ice load profile (navy blue color) is drawn on top of the mantle with 15× vertical exaggeration. Boundaries of the mantle melting region are outlined by the dark green lines.

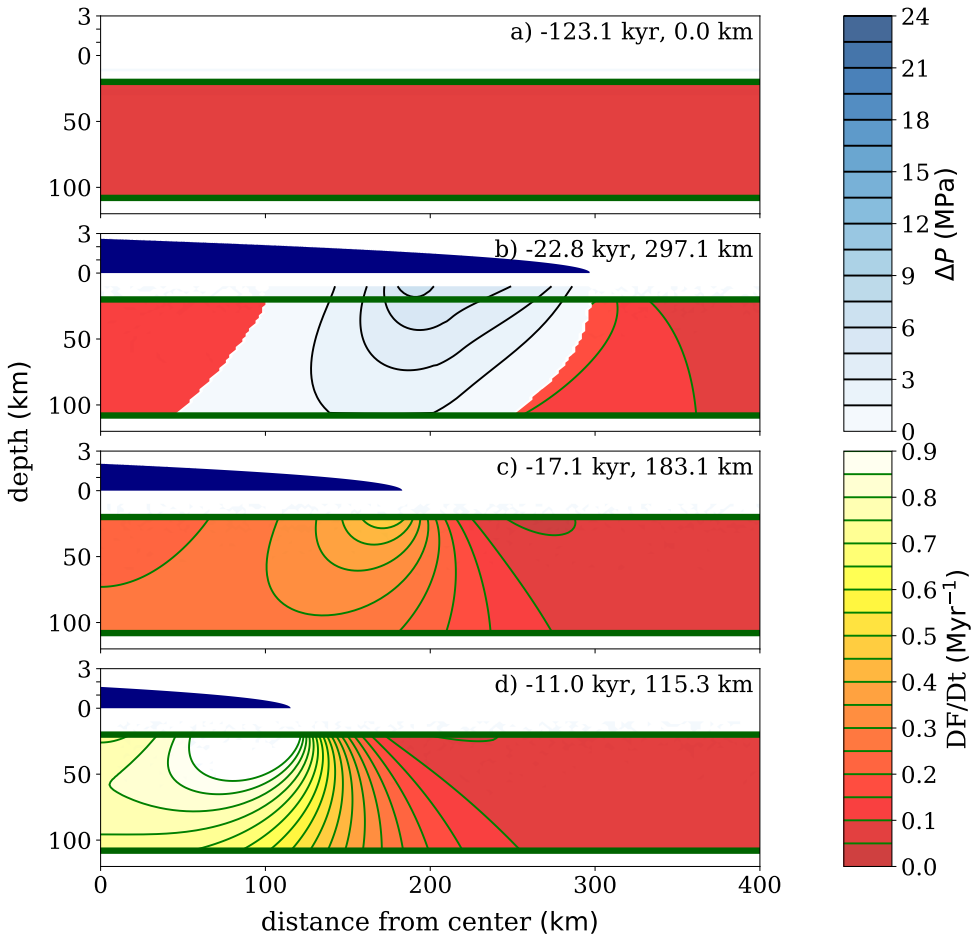

Fig. 5.7 Similar to Figure 5.6 but in a vertical plane passing through the center of ice *parallel* to the ridge axis.

23 kyrBP. Hence, these Figures illustrate that the melting rate does not only depend on the decompression rate but it also depends on whether or not the mantle is on the solidus, which is dependent of the history of the mantle flow. This is the reason why, when glacial loading is taken into account, a mantle melting model cannot simply assume what was assumed in the previous models (Eksinchol et al., 2019; Jull and McKenzie, 1996; Schmidt et al., 2013) that the mantle is melting wherever the decompression rate is positive (see Section 3.1). The mantle must also be on the solidus in order for it to melt when the decompression rate is positive.

5.2.1 Melting Rate

Once DF/Dt has been calculated over the desired spatial and temporal domains, we can calculate the rate of mass production of melt per unit volume as a function of space and time, which is assumed to follow

$$\begin{aligned}\Gamma(\boldsymbol{x},t) &= \rho_{\mathrm{s}}\frac{DF}{Dt}\\ &= \rho_{\mathrm{s}}\left(\frac{\partial F}{\partial P}\right)_S\frac{DP}{Dt}.\end{aligned} \tag{5.2}$$

Melts generated in the mantle have to be transported to the surface before they erupt. We assume that the effects of finite melt transport rate can be approximated by sampling the melt production rate field (equation (5.2)) with a time-lagged sampler. To the leading order, we assume that the vertical component of the melt velocity is constant $= v_t$. In this case, the time taken for melt produced at location (x, y, z) in the mantle to ascend to the surface is $\Delta t = |z|/v_t$, where $|z| = -z$ ($\because z < 0$ below the Earth's surface). That is, melt that reaches the surface at time t is assumed to have been produced at time $t' = t - |z|/v_t$ in the past. Therefore, the total mass flux of melt supply to the crust at time t is

$$\dot{M}(t) = \int_{\mathcal{V}}\Gamma\left(\boldsymbol{x}, t - \frac{|z|}{v_t}\right)\mathrm{d}V, \tag{5.3}$$

which is the integral of all the instantaneous melts produced in the melting region $\mathcal{V}$; however, the melts added from depth $|z|$ are assumed to have been produced at time $t' = t - |z|/v_t$ in the past.

The total volume flux $\dot{V}$ of melt supply to the crust at time t can be calculated from the mass flux:

$$\begin{aligned}\dot{V}(t) &= \frac{\dot{M}(t)}{\rho_{\mathrm{l}}}\\ &= \frac{1}{\rho_{\mathrm{l}}}\int_{\mathcal{V}}\Gamma\left(\boldsymbol{x}, t - \frac{|z|}{v_t}\right)\mathrm{d}V.\end{aligned} \tag{5.4}$$

5.2.2 REE Concentrations

We simplify the model by assuming that the concentration c_{l}^i of a highly incompatible element i with partition coefficient D^i in the instantaneous melt can be calculated

based on modal fractional melting (Shaw, 1970)

$$\frac{c_{\mathrm{l}}^i}{c_{s0}^i} = \frac{1}{D^i}\,(1-F)^{\frac{1}{D^i}-1} \tag{5.5}$$

where c_{s0}^i is the concentration of the element in the initial source.

Equation (5.5) gives the instantaneous concentration as a function of the degree of melting $c_{\mathrm{l}}^i = c_{\mathrm{l}}^i(F)$. The degree of melting as a function of pressure $F = F(P)$ is known from equation (5.1) and the pressure as a function of position and time $P = P(\boldsymbol{x}, t)$ is known from equation (2.45). We can therefore combine these equations to calculate at any location in the mantle at any time the instantaneous concentration $c_{\mathrm{l}}^i = c_{\mathrm{l}}^i(\boldsymbol{x}, t)$ in the melt generated. The bulk partition coefficient of La (Table 5.1) is assumed to follow that in Workman and Hart (2005).

This very simplified melting modelling of La gives results that are not significantly different from those (shown in Appendix B) obtained from a more elaborate model of mantle melting used in Rudge et al. (2013) because highly incompatible elements (such as La) partition into melts almost completely near the solidus intersection in the garnet field.

Given the concentration (by mass) c_{l}^i of a trace element i in the instantaneous melt as a function of space and time, the total mass flux of the trace element i in the melt supply to the crust is

$$\dot{M}_i(t) = \int_{\mathcal{V}} c_{\mathrm{l}}^i\,\Gamma\left(\boldsymbol{x}, t - \frac{|z|}{v_t}\right) \mathrm{d}V \tag{5.6}$$

where c_{l}^i is calculated at point $(\boldsymbol{x}, t - \frac{|z|}{v_t})$.

Similar to the volume flux of the whole melt defined in equation (5.4), we define the total "volume" flux of a trace element i in the melt supply to the crust as

$$\begin{aligned}\dot{V}_i(t) &= \frac{\dot{M}_i(t)}{\rho_{\mathrm{l}}} \\ &= \frac{1}{\rho_{\mathrm{l}}} \int_{\mathcal{V}} c_{\mathrm{l}}^i\,\Gamma\left(\boldsymbol{x}, t - \frac{|z|}{v_t}\right) \mathrm{d}V.\end{aligned} \tag{5.7}$$

Following these definitions, the mean concentration of the element i in the melt supply to the crust at time t is

$$\bar{c}_{\mathrm{l}}^i(t) = \frac{\dot{M}_i(t)}{\dot{M}(t)} = \frac{\dot{V}_i(t)}{\dot{V}(t)}. \tag{5.8}$$

5.3 Eruption Volumes

The time delay between the surge of mantle melting and the surge of volcanic eruptions depends on the melt transport speed and also on how long melts reside in crustal chambers before they erupt. Figure 5.8a shows the melt supply rates to crustal chambers predicted by our model from different input values of melt ascent velocity by integrating equation (5.4) in the melting region underneath Iceland along the ridge axis from 45 to 270 km from the ice center, taking into account the time delay due to finite melt ascent velocity. The prescribed ice volume is plotted in Figure 5.8e.

The graph demonstrates that if melt transport were instantaneous, the surge in the melt supply rate (black curve) would respond immediately after the deglaciation period (grey shaded area). Whereas, with slower melt transport, the surge in the melt supply rate will be delayed from the deglaciation period. At lower rates of melt transport, the shape of the melt supply rate curve will be more stretched in time because melts produced at the same time at different depths will arrive at crustal chambers at different times.

Note that the area under the curve over the whole time interval shown in the graph is independent of the melt ascent velocity. This is because, by the conservation of mass, the total melt supply is equal to the total melt produced regardless of how fast the melt is transported.

Before melts erupt on the surface, their compositions can be modified in the crustal chambers. We assume that the amount of melts accommodated in a chamber is constant. By conservation of mass, this implies that the total mass flux into is equal to the total mass flux out of the chamber. Therefore, the eruption rate is equal to the rate of melts entering the chamber (Figure 5.8a). However, the mass flux of each individual component do not need to follow this rule. Mixing and crystallization processes can modify the concentrations of REEs. We will discuss these two processes together with the remaining plots in Figure 5.8 later in Section 5.4.

Figure 5.8a also illustrates the effect of glacial loading on the magmatic response. The melt production rate (black curve) in response to the second and third deglaciation periods (the shaded intervals at 15.0–13.8 and 11.7–10.5 kryBP) increases instantaneously as a step jump from the beginning of each of the periods. Whereas, in the first deglaciation period (the shaded interval at 23.0–17.0 kryBP) the melt production rate (black curve) only increases gradually with time (no step jump). The reason is because, at the beginning of the first deglaciation period (23.0–17.0 kryBP), most of the mantle in the melting region is still sub-solidus due to the glacial loading prior to the LGM at 23.0 kryBP. Mantle at sub-solidus does not melt instantly in response to the

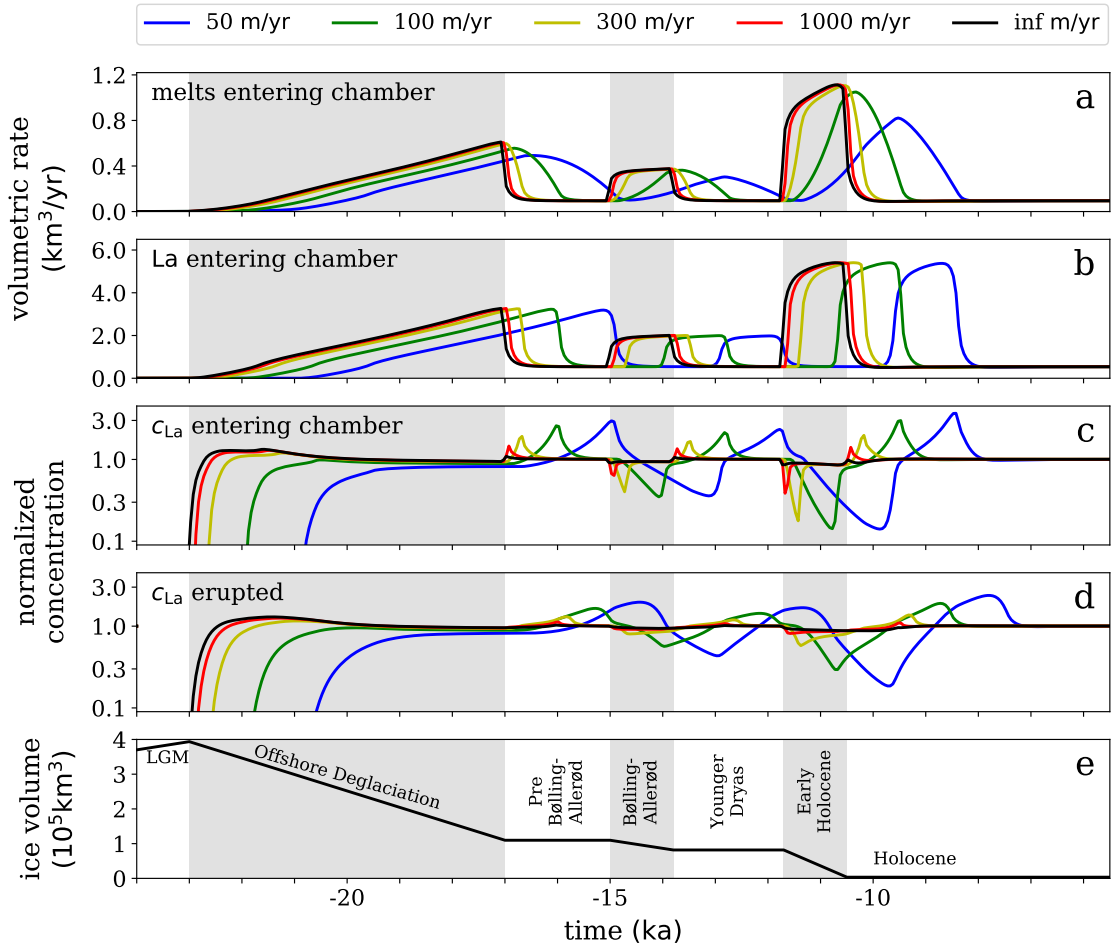

Fig. 5.8 (a) Volumetric rate of melt supply to the crustal chamber (equation (5.4)). (b) Volumetric rate of La supply to the crustal chamber (equation (5.7)) normalized to the La concentration in the source. (c) Concentration of La in melt supply to the crustal chamber (equation (5.8)) normalized to the steady-state La concentration. (d) Concentration of La in erupted lavas normalized to the steady-state La concentration. (e) Modelling-input ice load volume. (c) is the ratio of the La volume (b) to the melt volume (a); whereas, (d) is the ratio of the 1,000-year standard moving average (SMA) of the La volume (SMA of (b)) to the 1,000-year SMA of the melt volume (SMA of (a)). See Section 5.4 for physical meaning of SMA used in (d). Grey shaded regions indicate the time interval during which the ice is retreating. Different line colors correspond to different values of melt ascent velocity as labelled on top of the figure in m/yr. The melt and La volumetric supply rates to the crustal chamber are the sum along the ridge axis (red line in Figure 4.3b) between 45 and 270 km from the center of the ice. LGM = Last Glacial Maximum.

decompression. The mantle has to be recovered back to the solidus before it can begin to melt again. As more and more mantle is gradually recovered back to the solidus, more and more melting can proceed, which results in a gradual increase in the melt production rate in the first deglaciation period (23.0–17.0 kryBP). Whereas, at the beginning of the second and third deglaciation periods (15.0–13.8 and 11.7–10.5 kryBP), most of the sub-solidus mantle as a result of the glacial loading prior to the LGM at 23.0 kryBP has already recovered back to the solidus. Mantle on the solidus can instantly melt in response to the decompression. This results in step jumps in response to the initiation of the deglaciation in the second and third periods.

5.3.1 Eruptive Locations

The ages and volumes of eruptions from the last glacial and present postglacial are compiled using published maps and age estimates. The principal sources of information for the Northern Volcanic Zone (NVZ) are Sæmundsson (1991) and Sæmundsson et al. (2012). For the Western Volcanic Zone (WVZ) and Reykjanes Peninsula (REYK), the maps of Sinton et al. (2005), Eason et al. (2015) and Sæmundsson et al. (2016) are used. Appendix A lists all the sources of rock sample dataset we use.

Geological mapping, geomorphology and interpretation of the volcanic lithologies have been used to determine the eruptive facies: whether it is subglacial, finiglacial or postglacial. Finiglacial means that there is evidence of thin or recently disappeared ice when the eruption unit was being formed. Finiglacial units are likely to have formed when the glacier terminus was sweeping through the eruptive area during the glacial retreat.

Tephrochronology provides bounds on eruption ages for the postglacial events, meaning that the age constraints are expressed with a maximum and minimum age bound in our dataset. For early postglacial and finiglacial eruptions the maximum age has to be tied to the inferred age of deglaciation of the area, based on available reconstructions of the ice sheet history (Geirsdóttir et al., 2009; Patton et al., 2017). The ages of subglacial eruptions are, in general, not as well constrained as those of the postglacial. Minimum age constraints for these eruptions are obtained from ice-sheet reconstructions and maximum ages are set to 30 ka. Helium-3 exposure ages and the geomorphological characteristics of the uppermost surface of tuyas can also be used to infer a chronology for a subset of subglacial eruptions, using the approach of Eason et al. (2015) as informed by the data of Licciardi et al. (2007).

A table of eruptions for which age, volume and chemical data is available is provided in Appendix A. The information in this table is used to generate the plots provided for comparison with model results in this paper. The requirement of an unambiguous association between sample chemistry and eruption name, volume and age introduces some bias into our dataset: The lack of a clear link between the eruption name and chemistry means that our coverage of subglacial eruptions from the Reykjanes Peninsula is poor. Inevitably, erosion, superposition and lack of subsurface informaton introduce substantial uncertainties into any reconstruction of eruptive volumes.

We divide eruption units in WVZ further into WVZ-North (WVZN) and WVZ-South (WVZS) by latitude of $64°20'0''$. Locations and types of eruption units of all the data we use here are plotted on the map in Figure 5.9.

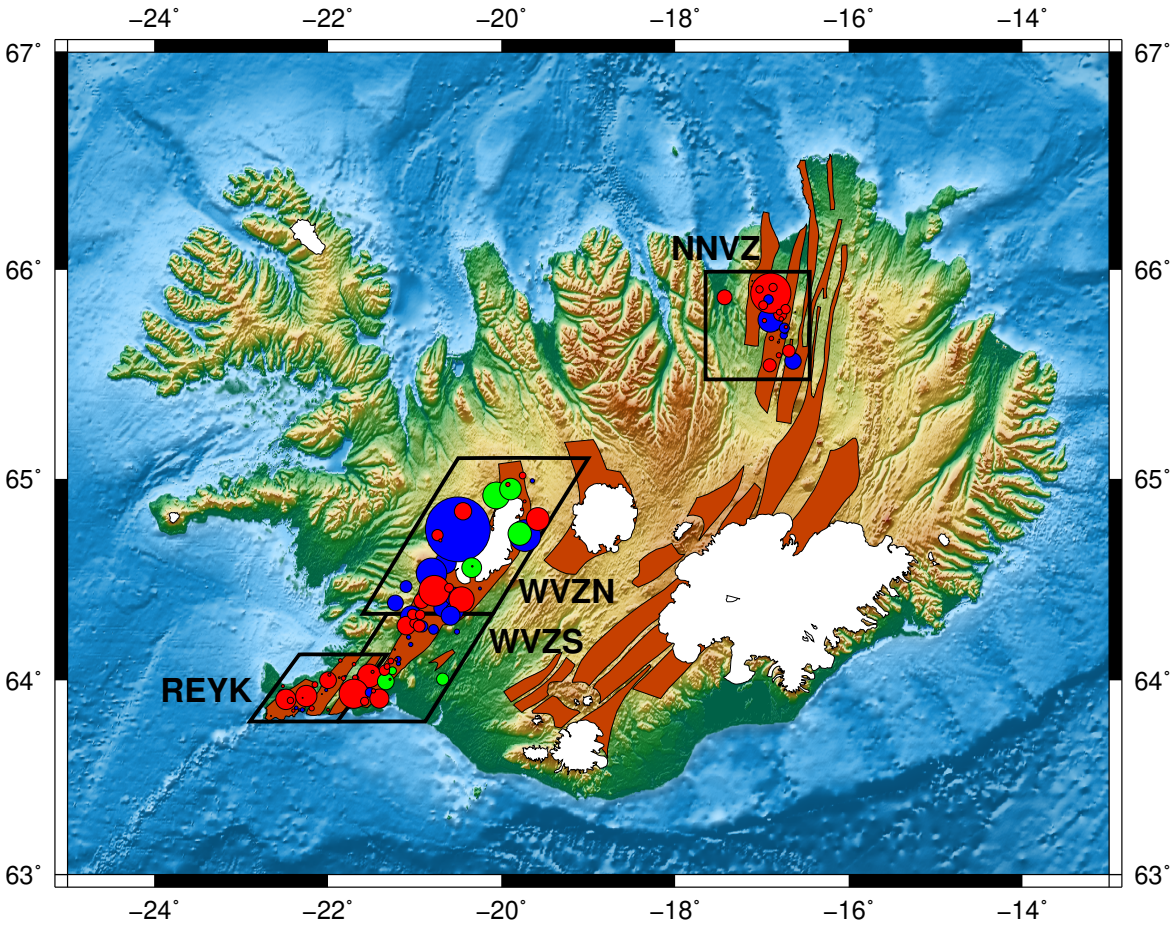

Fig. 5.9 Mercator projection map of Iceland showing locations of eruptive units in Northern Volcanic Zone-North (NNVZ), Western Volcanic Zone-North (WVZN), Western Volcanic Zone-South (WVZS) and Reykjanes Peninsula (REYK) as circles with areas proportional to the eruptive volumes. Colors on the circles indicate the eruption types (subglacial in blue, finiglacial in green and postglacial in red). See Section 5.3.2 for the definition of finiglacial type. White areas show the recent Icelandic glaciers. Active fissure swarms located at where plate divergence is taking place are shown in dark red color. Data are provided in Appendix.

The modelling-input distances of the four zones relative to the ice center shown in Table 5.2 are estimates with uncertainty of $\approx \pm 50$ km because the actual location of the ice center is unknown and also because of the uncertainty of the geometry of melt generation.

5.3.2 Eruption Types

In this section, we show how the melt ascent velocity can affect the relative volume proportion of different eruption types.

Table 5.2 Model distances of the zones from ice center.

Zone	Ranges (km)
Western Volcanic Zone-North (WVZN)	0–70
Western Volcanic Zone-South (WVZS)	70–180
Northern Volcanic Zone-North (NNVZ)	120–180
Reykjanes Peninsula (REYK)	180–250

The modelling-input ice coverage radius as a function of time is known. We can therefore identify if an infinitesimal volume of melt that arrives at the surface at a particular location and time is erupted within the ice coverage radius or not. In other words, the model can divide eruptive volumes into subglacial group and subaerial group. The subglacial group corresponds approximately to the observational subglacial and finiglacial types combined. The subaerial group corresponds to the observational postglacial type. Our model does not divide the subglacial group further into subglacial and finiglacial types.

Figure 5.10 illustrates the model prediction that at faster melt transport (Figure 5.10b) there is a greater proportion of the subglacial volume (colored blue) compared to that at slower melt transport (Figure 5.10a). This is because faster melt transport will allow melts from depth to arrive at the surface sooner before the ice has gone. The sharp changes of subglacial to subaerial volume at 45, 160 and 180 km are due to the three pauses of the glacial terminus at these three radial distances (Table 4.1).

The model also predicts that for the same time interval (such as 14.5–0 kyrBP) the relative proportion of the subglacial volume to the total volume is dependent of the distance from the ice center. This is because while most of the melts in any location are produced over the same time period during deglaciation (23.0–10.5 kyrBP), regions closer to the ice center remain covered by ice for a longer period of time. This allows a greater proportion of melts to arrive at the surface and erupt subglacially. The spatial dependence of the subglacial to subaerial volume ratio is also seen in observations. Figure 5.9 illustrates that in the regions closer to the center of Iceland there is a greater proportion of subglacial and finiglacial volumes (blue and green circles) than further out.

To compare our model results with the observations, we first note that the observational eruption volumes of units older than 14.5 kyrBP are highly uncertain not only due to glacial erosion but also due to some older units are buried underneath younger eruptions. We therefore filter out eruptions older than 14.5 kyrBP for both the model and the observational data. The model cumulative volumes at melt ascent

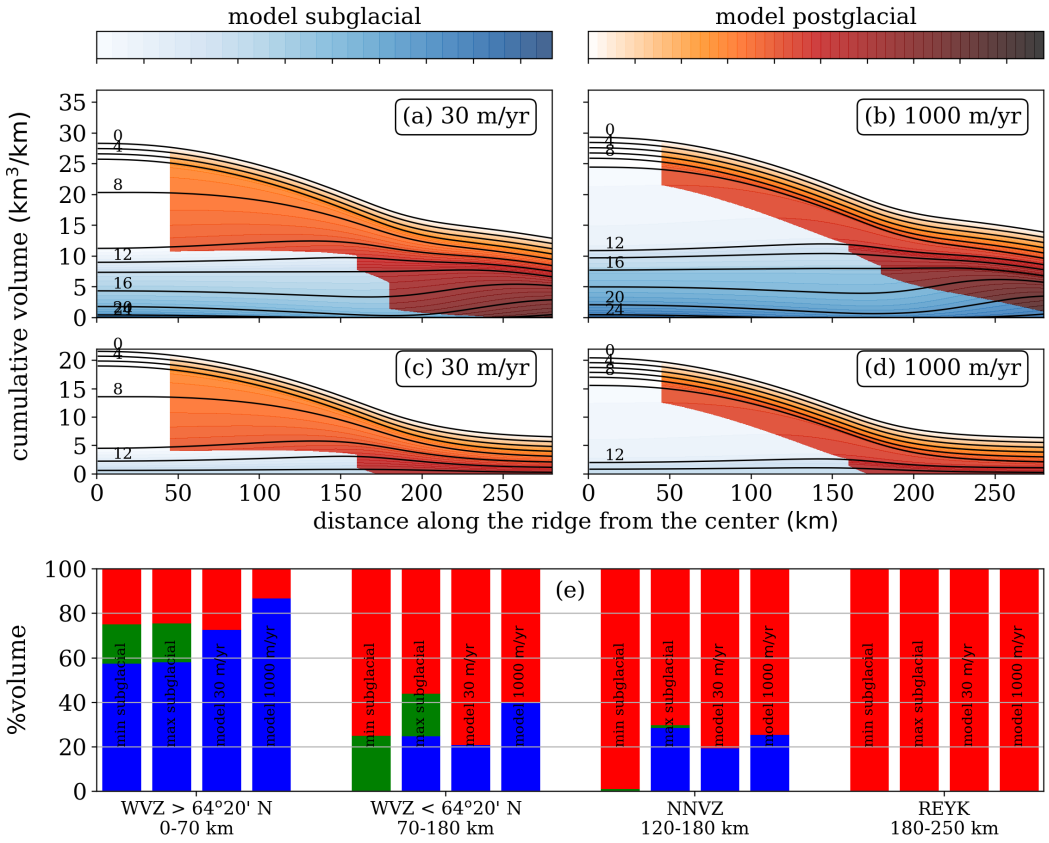

Fig. 5.10 (a)–(d): Isochrons of cumulative lava volume per unit length along the ridge axis as predicted by the model at melt ascent velocity of 30 m/yr for (a) and (c) and 1,000 m/yr for (b) and (d). Subglacial and postglacial lavas are indicated by blue and red colors (as indicated by the two color bars on top of the figure) with color intensity proportional to the lava age. Contour lines are separated at an equal interval of 2 kyr and the ages labelled on the lines are in kyrBP. (a) and (b) show volume accumulated from 24.0 kyrBP; whereas, (c) and (d) show volume accumulated from 14.5 kyrBP using the same modelling-inputs as in (a) and (b). (e): Volume proportions of different eruption types that erupted between 14.5 and 0 kyrBP in different volcanic zones. Observational data with lower and upper bounds of subglacial volumes are shown by the two left bars. The blue, green and red bars are the subglacial, finiglacial and postglacial volumes respectively. See Section 5.3.2 for how the lower and upper bounds are obtained. The model results with melt ascent velocity of 30 and 1,000 m/yr are shown on the two right bars with blue bars showing the subglacial and finiglacial types combined. WVZ = Western Volcanic Zone; NNVZ = Northern Volcanic Zone-North; and REYK = Reykjanes Peninsula.

velocity of 30 and 1,000 m/yr after the 14.5 kyrBP filter are shown on Figures 5.10c and 5.10d. We use results from these two panels to calculate the model proportions of the subglacial volume (= observational subglacial+finiglacial) and subaerial volume (= observational postglacial) as shown on the two right bars of Figure 5.10e. For example, the bar plot of the model 30 m/yr in NNVZ on Figure 5.10e has subglacial (blue) and subaerial (red) proportions equal to the subglacial (blue) and subaerial (red) plotting area proportions of Figure 5.10c in the x-axis range of 120–180 km.

We arrange the bar plot on Figure 5.10e from left to right by zone location from the closest to (WVZN) to the furthest from (REYK) the ice center. In each zone, the observational data has lower and upper estimates of subglacial volume due to age uncertainty of the subglacial units. The lower estimate (min. subglacial) shown on the left bar comes from the volume sum of the subglacial units with maximum age bound not exceeding 14.5 kyrBP. Whereas, the upper estimate (max. subglacial) comes from summing all the subglacial units with minimum age bound less than 14.5 kyrBP (while the maximum age bound can exceed 14.5 kyrBP).

The model predictions for spatial dependence in the diachronous response agree well with the observational data. In REYK, the whole area is already ice-free by 14.5 kyrBP and hence all the eruptions are subaerial. On the other hand, WVZN remains covered by ice over most of the time during the last deglaciation and so the majority of the eruption volumes are subglacial.

Results on Figure 5.10e also suggests that the melt ascent velocity is likely to be of the order of 100 m/yr. At below 30 m/yr, the subglacial volumes predicted by the model would be smaller than that of the observational lower bound estimates (min. subglacial). Nevertheless, we note that the model results depend on the distance along the ridge axis over which the melts are integrated (as estimated in Section 5.3.1). Similar to the model, the observational lava volumes in the four zones are also integrated over ridge lengths of $\sim$ 60–90 km.

5.3.3 Timing of the Peaks in Volcanic Productivity

Another way to estimate the melt ascent velocity is to use the timing of the peaks in volcanic productivity. On Figure 5.11, we plot the cumulative eruptive volume as a function of time for the model outputs and the observational data. This figure shows that the bursts in the cumulative lava volume predicted by the model at melt ascent velocities between 30 and 1,000 m/yr have timings approximately equal to that of the observations across all the volcanic zones to within the uncertainties of the lava ages and the modelling-input ice load history.

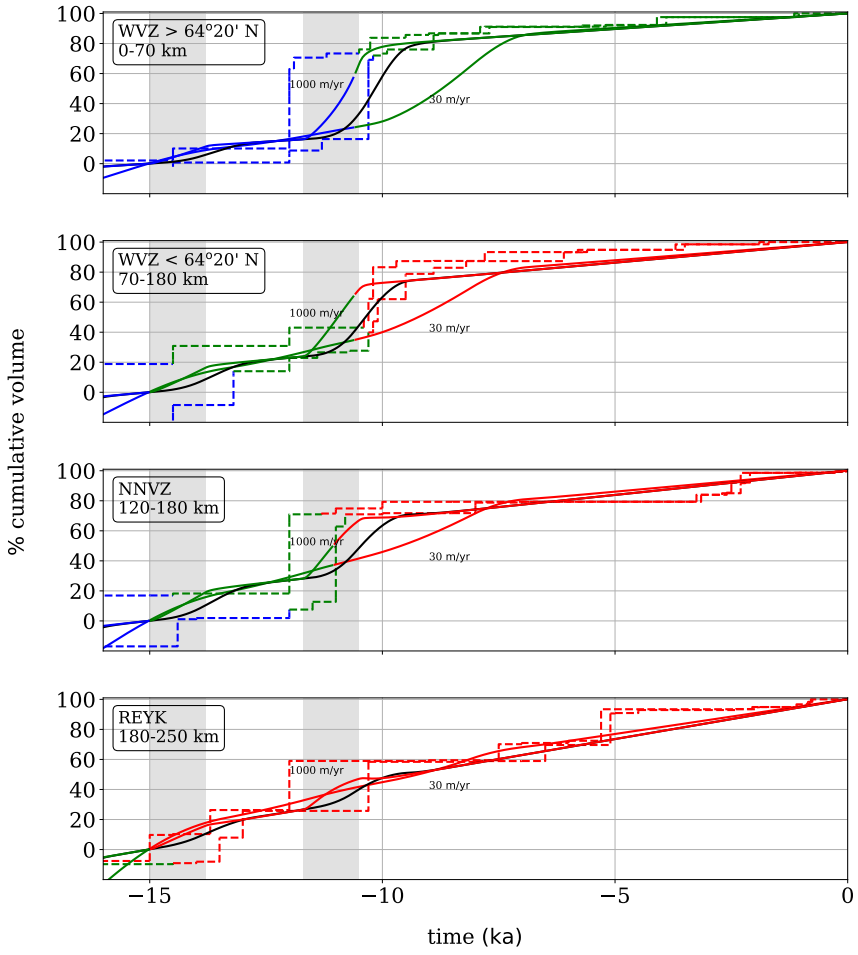

Fig. 5.11 Cumulative eruptive volume normalized to the total volume erupted between time $t = -15$ and 0 kyr. The cumulative volumes of the observational data plotted as steps (dashed lines) come from cumulating the eruptive volumes sorted by either the minimum age bounds or the maximum age bounds of the eruption units. The eruptive volume begins at 0% at −15 kyr and ends at 100% at 0 kyr. We use the mean cumulative volumes at these two ends to normalize the observational data. The model results for melt ascent velocity of 30 and 1,000 m/yr are plotted as non-black colored solid lines. Colors on these dashed and solid lines illustrate the eruption periods: subglacial in blue, transitional in green and postglacial in red (see Section 5.3.3 for definition of the transitional period). Black solid line in each panel shows the model result for melt ascent velocity of 100 m/yr. The timings of the eruption periods for the black curve are the same as those for the remaining model-result curves. Different panels correspond to different volcanic zones as indicated on the upper-left corner of each panel together with the corresponding modelling-input zone range (Section 5.3.1). Grey shaded regions indicate the time interval during which the modelling-input ice is retreating. WVZ = Western Volcanic Zone; NNVZ = Northern Volcanic Zone-North; and REYK = Reykjanes Peninsula.

In the period during which the glacier terminus was sweeping through each zone (called transitional period), some areas in the zone are already ice-free while some areas are still covered by ice. This means that, in the transitional period, eruptions can be either subglacial or subaerial.

In the observational data sorted by age, the transitional period can be identified approximately by the period during which there are some alternations of the timeline orders between subglacial, finiglacial and postglacial types. The remaining two end periods are called subglacial and postglacial periods. The subglacial period consists of only subglacial type and the postglacial period consists of only postglacial type. In the model, the transitional period is identified by the period during which the ice radius is in the zone range (as listed in Table 5.2).

The timing of the periods in the model is controlled by the input ice history and the input zone range. Therefore, a well-matched timing of the periods between the model and the observational data helps us identify if the modelling-input of ice load and zone range reasonably reflect the actual values. The discrepancy between the observations and the model results at our preferred estimate of 100 m/yr melt ascent velocity is likely to be because of the uncertainty of the observational eruption ages and the model axisymmetric ice assumption.

Nevertheless, the results in Figure 5.11 show that, at a melt ascent velocity of 30 m/yr or below, the difference of the timing in the burst in volcanism between the model results and the observational data becomes significant. More quantitatively, with the average mantle melting depth of ≈ 50 km, reducing the melt ascent velocity from 100 to 30 m/yr will delay the burst timing by ≈ 1.2 kyr, which is significant compared to the uncertainty of the eruption ages. Our model implies a similar lower bound value to that of 50 m/yr estimated in Maclennan et al. (2002) from the relative timing between the observed eruption ages and the deglaciation. An advantage of this work is that much broader geographical spread is accounted for. Our model examines eruptions in different volcanic zones; whereas, Maclennan et al. (2002) only examined eruptions in the NNVZ region.

5.4 Geochemical Response

5.4.1 Model Predictions

Figure 5.8b shows the volumetric supply rate of La to the crustal chambers normalized to the steady-state La concentration. Similarly to the whole melts in Figure 5.8a, the surge in the supply rate of La is delayed from the deglaciation period due to the finite speed of melt transport. However, while the volumetric melt supply rate curves (Figure 5.8a) are stretched in time, the La supply rate curves (Figure 5.8b) retain their shapes almost like the same time-series but time-shifted. This is because La is partitioned into melt at almost the same depth (near the solidus). Most of the La takes almost an equal time to arrive at the crust regardless of how fast the ascent rate is. Therefore, changing the ascent rate will not significantly spread the La flux out along the time axis. In contrast, melts are produced at different depths. They take different times to transport to the crust. The slower the ascent rate, the more the time delay between melts from different depths to arrive at the surface; hence, the more the spread of the melt supply rate curve along the time axis.

Figure 5.8c is the La concentration (c_{La}) in the melt supply to the crustal chambers, which is equal to Figure 5.8b divided by Figure 5.8a. This would correspond to the concentration in the lava erupted at the surface if the magma mixing process in the crustal chamber were not present. The longer the magma is allowed to mix in the crustal chamber, the smaller the variation signal of the REE concentrations.

In the model, the effect of magma mixing on c_{La} in the lavas is equivalent mathematically to the time average concentration. The time period over which the average is performed is equal to the time duration that the magmas mix in the crustal chamber before they erupt. In a study of the chemical disequilibria between olivine, its melt-inclusions and the whole melts that surround the olivine in rock samples collected from Iceland, Maclennan (2008) estimated that the magma residence time is of the order of a few hundreds to $\lesssim 1,000$ years. We therefore take the time average c_{La} over a period of $1,000$ years and the result is shown in Figure 5.8d. In other words, this panel is equal to the ratio between the $1,000$-year standard moving average (SMA) of La volume supply to the crustal chamber ($1,000$-year SMA of Figure 5.8b) and the $1,000$-year SMA of the whole melt volume supply to the crustal chamber ($1,000$-year SMA of Figure 5.8a).

Note that melt mixing also occurs "en-route" while melts are migrating from depths to the crustal chamber and meet together along the way. This geological process corresponds mathematically to the volume integration over the mantle melting domain

$\mathcal{V}$ as shown in equation (5.7), taking into account the time delay due to the finite rate of melt transport Δt. In other words, the model results shown in Figures 5.8b, 5.8c and 5.8d as calculated by equations (5.7) and (5.8) have already taken into account the effect of en-route melt mixing.

Our results in Figures 5.8c and 5.8d show that the variation of c_{La} is strongly dependent on the melt ascent velocity. The lower the melt ascent velocity the higher the variation of c_{La}. This effect can be explained as follows. During the deglaciation, the decompression rate in the mantle is maximum at the surface and decays exponentially with depth (as illustrated in Figures 5.4 and 5.7). This means that the extra melts generated during deglaciation are mostly produced at shallow depths in the mantle, which is depleted in La. If the melt transport had been instantaneous, the extra melts produced at any depth at the same time would have travelled to the crust and mixed instantly and would have erupted at the surface with La depletion of up to $\approx 20\%$ as predicted by Jull and McKenzie (1996). In contrast, when the melt ascent velocity is finite, the extra melts produced at shallower depths during deglaciation will arrive at the surface before the extra melts produced at deeper depths. The slower the rate of melt transport the more likely the extra melts from shallow depths (La depleted) are to erupt before they mix with the extra melts from deep depths (La enriched). As a result, when the melt ascent velocity is sufficiently low, the first arrival of the extra melts produced during deglaciation will be much more depleted in La than that predicted by the instantaneous melt transport model of Jull and McKenzie (1996).

The eruptive c_{La} will recover back to near the steady-state concentration after the extra melts from the bottom of the melting region (La enriched) catch up and mix with the extra melts from shallow depths (La depleted) before they erupt. Moreover, the recovery of the eruptive c_{La} back to the steady-state will overshoot after the deglaciation ends. This phenomenon can be explained as follows. Once the deglaciation terminates, the glacially-induced decompression melting in the mantle will also terminate at all depths at the same time and the extra melt supply to the surface from shallow depths (La depleted) will run out before the extra melt supply from deep depths (La enriched). This is because the melts from greater depths take a longer time to arrive at the surface. Therefore, once the La depleted melt supply from the shallow depths runs out, the remaining majority of the erupted lavas will be the La enriched melts from deep depths and the eruption will become enriched in La.

Figure 5.8d also shows that the timing of the periods during which the lavas are enriched or depleted in La is dependent on the melt ascent velocity. At slower melt ascent velocity, the peaks and the troughs of c_{La} are delayed further from the

deglaciation periods. Hence, we can use this timing combined with the magnitude of the c_{La} variations to estimate the melt ascent velocity. We note that the La depleted lava volume dominates the La enriched lava volume. This can be seen in Figure 5.8. The troughs of c_{La} (Figure 5.8d) fall in the periods of the bursts in eruption rates (Figure 5.8a); whereas, the peaks of c_{La} (Figure 5.8d) fall outside those periods. Therefore, the La-depletion signal is stronger than the La-enrichment signal, which is also seen in observational data. The majority of the eruptions during the last deglaciation are depleted in La.

5.4.2 Geological Observations

The eruptive La concentrations of observational data are from rock samples collected from Iceland by the previous studies (see Section 5.3.1 and Appendix A for further details). These rock samples are of melts that have gone through fractionation/accumulation during cooling and crystallization processes in the crustal chambers. These processes modify the melt compositions from their original pre-crustal compositions.

Crystallization/Accumulation

We make fractionation/accumulation correction of c_{La} in each rock sample based on the MgO content of the sample. We assume that the pre-crustal melts have 14.0 wt% MgO as estimated in Maclennan et al. (2001). Rock samples that have MgO between 9.5 and 14.0 wt% are assumed to have undergone crystallization of olivine-rich material with 40.0 wt% MgO. If the melts underwent crystallizing further below 9.5 wt% MgO, they generate a gabbroic solid with 11.0 wt% MgO. Some rock samples have higher MgO content than 14.0 wt% of the pre-crustal melts. We assume that these samples are from melts that have been influenced by the accumulation of olivine crystals with 40.0 wt% MgO. Below, we provide the derivation of equations related to the crystallization correction that are applied on the observational data of rock samples.

Suppose that the original mass of the liquid melt supply to the crustal chamber is M_o. The mass of the remaining liquid after crystallization is $F_r M_o$, where F_r is the degree of crystallization. The mass of the solid that comes from the crystallization of the original liquid melt is $(1 - F_r)M_o$.

The solid generated from the crystallization is enriched in MgO and very depleted in La. This is because La is a highly incompatible element, which is more favourable to stay in the liquid phase. Whereas, MgO is a major element with partition coefficient

greater than 1 (compatible element), which is more favourable to solidify. So, after the crystallization, the remaining liquid becomes depleted in MgO and enriched in La relative to the original melt. How much the enrichment in La and depletion in MgO depends on the degree of crystallization F_r.

By assuming that all the La stays in the liquid phase during the crystallization, the mass of La in the remaining liquid is equal to the mass of La in the original liquid. That is,

$$[\mathrm{La}]_o M_o = [\mathrm{La}]_r M_r \tag{5.9}$$

where $[\mathrm{La}]_o$ and $[\mathrm{La}]_r$ are the concentrations of La in the original melt and the remaining liquid after crystallization respectively and M_r is the mass of the remaining liquid after crystallization. From $M_r = F_r M_o$, equation (5.9) is simplified to

$$[\mathrm{La}]_o = [\mathrm{La}]_r F_r \tag{5.10}$$

Given that the La concentration in each rock sample ($= [\mathrm{La}]_r$) is known, equation (5.10) can be used to obtain the La concentration in the original melt ($= [\mathrm{La}]_o$) if the degree of crystallization F_r is known.

We estimate F_r based on the MgO content in the rock samples. Suppose that the concentrations of MgO in the remaining liquid and in the ultramafic cumulates generated by crystallization are c_r and c_u respectively. From the mass balance,

$$c_o = F_r c_r + (1 - F_r) c_u$$

where c_o is the concentration of MgO in the original liquid. By rearranging this equation, we obtain

$$F_r = \frac{c_o - c_u}{c_r - c_u}. \tag{5.11}$$

This means that the degree of crystallization F_r of each rock sample can be obtained from the MgO concentrations in the original liquid (c_o), the remaining liquid (c_r) and the ultramafic cumulates (c_u).

In Maclennan et al. (2001), the estimated MgO content of the original melts (c_o) is 14 wt%. This is going to vary on Iceland, from perhaps as low as 10 wt% to up to 16 wt%. We simplify the problem by assuming a single value of 14 wt%.

For the MgO concentration in the ultramafic cumulates (c_u), when c_r is between ≈ 9.5–14 wt%, the remaining liquid is crystallizing olivine-rich material with a solid composition containing ≈ 40 wt% MgO (Maclennan et al., 2001). Hence, by assuming that c_o and c_u are constant at 14 wt% and 40 wt% respectively, we can substitute F_r from equation (5.11) into equation (5.10) to obtain

$$[\mathrm{La}]_o = \left(\frac{c_o - c_u}{c_r - c_u}\right)[\mathrm{La}]_r. \tag{5.12}$$

This equation is applied to rock samples with MgO between 9.5–14 wt% for the crystallization correction.

When the MgO concentrations in the rock samples are below ≈ 9.5 wt%, the overall trend indicates that there is a shift in the composition of the crystallizing material. We assume that at below 9.5 wt% MgO, the liquid generates a gabbroic solid with 11 wt% MgO. In this case, the calculation can be divided into two steps.

First, the original melt at 14 wt% MgO underwent crystallization to an olivine-rich material until the MgO has reached 9.5 wt%. At this stage, the La concentration in the remaining liquid $[\mathrm{La}]_r^*$ is related to the concentration in the original melt by equation (5.12):

$$[\mathrm{La}]_o = \left(\frac{c_o - c_u}{c_r^* - c_u}\right)[\mathrm{La}]_r^* \tag{5.13}$$

where $c_r^* = 9.5$ wt% is the MgO concentration of the liquid after our first step of the calculation.

Second, the remaining liquid at 9.5 wt% MgO underwent crystallization to a gabbroic material until the MgO has reached c_r. In this step, equation (5.12) can be used by replacing $[\mathrm{La}]_o$ with $[\mathrm{La}]_r^*$, c_o with c_r^* and c_u with c_g, where $c_g = 11$ wt% MgO is the MgO content in the gabbroic material. That is,

$$[\mathrm{La}]_r^* = \left(\frac{c_r^* - c_g}{c_r - c_g}\right)[\mathrm{La}]_r. \tag{5.14}$$

We combine equation (5.13) with equation (5.14) to obtain

$$[\mathrm{La}]_o = \left(\frac{c_o - c_u}{c_r^* - c_u}\right)\left(\frac{c_r^* - c_g}{c_r - c_g}\right)[\mathrm{La}]_r. \tag{5.15}$$

This equation is applied to rock samples with MgO below 9.5 wt% for the crystallization correction.

Many of the samples are whole-rock samples, and contain a mixture of quenched carrier liquid and crystals that were carried from the walls of the magma chamber. Some of the rocks carry a large quantity of accumulated olivine and this can give them an MgO content that is substantially higher than the original melt supply to the chamber. In these cases, the erupted mass needs to be corrected for accumulation of the high MgO, low La olivine crystals. We assume that the La content in the accumulated olivine is negligible. Therefore, equation (5.10) still holds true. From the conservation of mass, mass of MgO in the erupted liquid is equal to the sum of the mass of MgO in the original melt and the mass of MgO in the accumulated olivine. That is,

$$c_r M_r = c_o M_o + c_a (M_r - M_o)$$

where c_a is the MgO concentration in the accumulated olivine. From $M_r = F_r M_o$, we have

$$\begin{aligned} c_r F_r &= c_o + c_a (F_r - 1) \\ \therefore F_r &= \frac{c_a - c_o}{c_a - c_r}. \end{aligned} \tag{5.16}$$

This equation is applied to rock samples with MgO above 14 wt% for the accumulation correction. We assume that the accumulated olivine has $c_a = 40$ wt% MgO.

In summary, we obtain the La concentration in the original melt ($= [\mathrm{La}]_o$) by applying the fractionation/accumulation correction on each rock sample with MgO concentration $= c_r$ and La concentration $= [\mathrm{La}]_r$ based on $M_r = M_o F_r$, $V_r = V_o F_r$ and $[\mathrm{La}]_o = [\mathrm{La}]_r F_r$ with

$$F_r = \begin{cases} \left(\frac{c_o - c_u}{c_r^* - c_u}\right)\left(\frac{c_r^* - c_g}{c_r - c_g}\right), & c_r < c_r^* \\ \left(\frac{c_o - c_u}{c_r - c_u}\right), & c_r^* \le c_r \le c_o \\ \left(\frac{c_a - c_o}{c_a - c_r}\right), & c_r > c_o \end{cases}$$

where $c_o = 14\%$, $c_u = c_a = 40\%$, $c_r^* = 9.5\%$ and $c_g = 11\%$.

Observations vs. Model Results

Due to the age uncertainty of eruption units, c_{La} cannot be plotted directly as that of the model in Figure 5.8. Most of the eruptions have their age estimated as a time band bounded by some geological events with identifiable age (e.g. tephra layers). In WVZ and NNVZ, most of the eruption units fall into one of the following age bands:

1. Glacial (pre 14.5/14.4 kyrBP)
2. Eruptive Pulse 1 (14.5/14.4 to 12.0 kyrBP)
3. Eruptive Pulse 2 (12.0 to 10.3 kyrBP)
4. Early Postglacial (10.3 to 8.9/8.0 kyrBP)
5. Steady-State Postglacial (post 8.9/8.0 kyrBP)

REYK zone is different in that it is the furthest from the ice center and became ice-free by 14.5 kyrBP, which is earlier than the other zones. Eruption units in REYK are divided into the following age bands:

1. Glacial (pre 14.5 kyrBP)
2. Early Postglacial 1 (14.5 to 13.0 kyrBP)
3. Early Postglacial 2 (13.0 to 10.2 kyrBP)
4. Steady-State Postglacial (post 10.2 kyrBP)

In each of these age bands, we take the volume-weighted average La concentration normalized to the Steady-State Postglacial La concentration and plot in Figure 5.12 for both the observational data and the model.

The right column of Figure 5.12 illustrates that different model melt ascent velocities result in different La concentration characteristics. In each age band, some values of melt ascent velocity may predict La depletion, whereas the others predict La enrichment. This is due to the effect of melt ascent velocity on the timing of the peaks and troughs of c_{La} (Figure 5.8d) that we discussed earlier.

The left column of Figure 5.12 shows that the model melt ascent velocity of 100 m/yr yields similar c_{La} characteristics to that of the observations. At two extreme melt ascent velocities of 30 and $1,000$ m/yr, the c_{La} characteristics are significantly different from that of the observations both in the timing and the magnitude of the c_{La} variations.

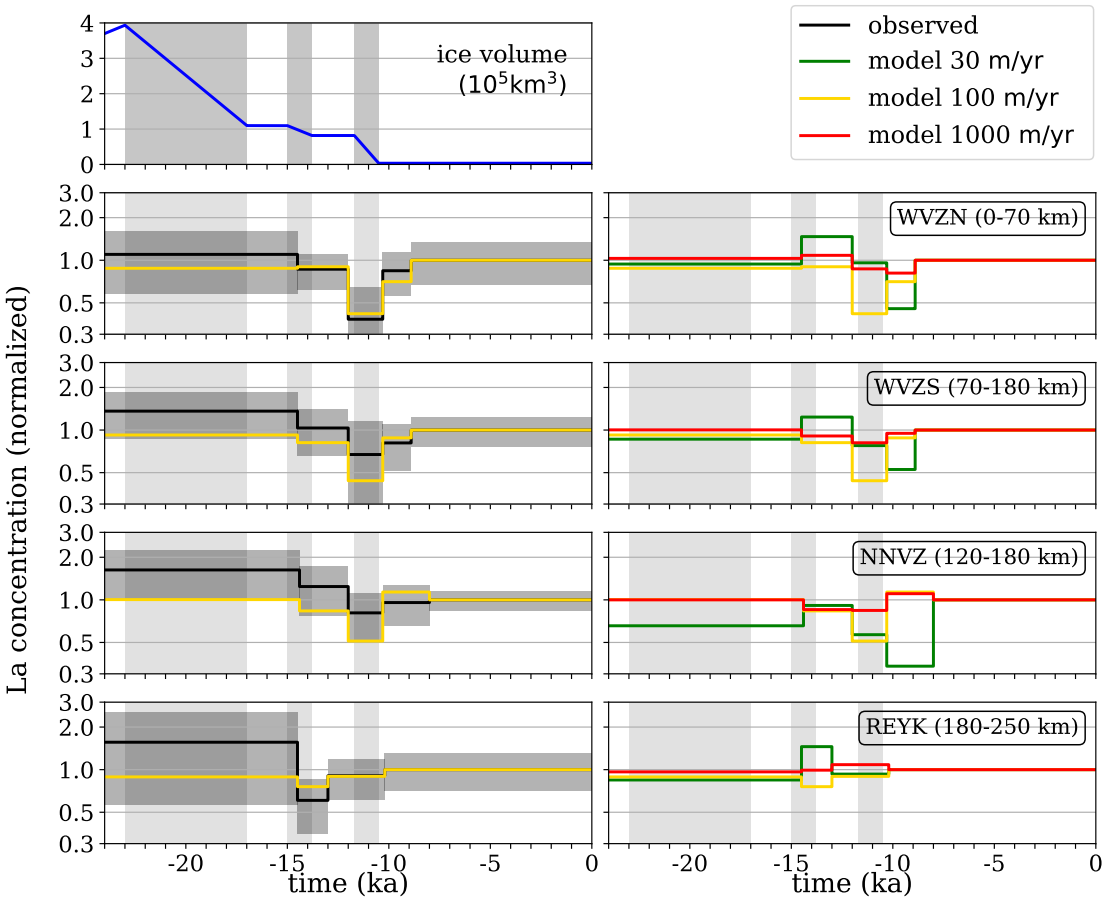

Fig. 5.12 Top panel is the modelling-input ice volume. Each row of the remaining panels shows La concentrations normalized to the steady-state concentration in each volcanic zone. The upper-right corner of the right panel labels the corresponding zone and the modelling-input zone range. On the left panel, the black curve shows the observational La concentrations together with grey bands indicating ±1 S.D. of rock samples. The yellow curve is the model result from a melt ascent velocity of 100 m/yr. The right panel illustrates the model La concentrations calculated from different values of melt ascent velocity labelled with different line colors. Details of how the La concentrations are calculated can be found in the text. WVZN = Western Volcanic Zone-North; WVZS = Western Volcanic Zone-South; NNVZ = Northern Volcanic Zone-North; and REYK = Reykjanes Peninsula.

5.5 Interpretation of the Melt Velocity Result

A melt ascent velocity of 100 m/yr is ~ 2 orders of magnitude faster than would be predicted from simple models of diffuse porous flow. Suppose that the melt transport is responsible by the diffuse porous flow. From Darcy's law,

$$\phi w = \frac{d^2 \phi^n}{C\mu} \Delta \rho g$$

where ϕ is the porosity, w is the vertical component of the melt velocity, d is the grain size, C is the geometric constant, μ is the melt viscosity, n is the permeability exponent, $\Delta\rho$ is the density difference between solid mantle and melt ($= \rho_s - \rho_l = 400$ kg/m^3) and g is the acceleration due to gravity (Table 5.1). We have neglected the compaction term because the compaction length is much smaller than the length scale of the melting region. We also have neglected the velocity of the solid mantle because it is much smaller than w.

By substituting numerical values of $\phi = 3\%$, $C = 58$, $\mu = 10$ Pa s, $n = 3$ (Miller et al., 2014; Rees Jones and Katz, 2018; Rudge, 2018) and $w = 3.2 \times 10^{-6}$ m/s ($= 100$ m/yr) into the equation above, we obtain the grain size $d = 13$ cm. This is significantly larger than that of olivine and pyroxene (~ 10 μm–10 mm) (Kelemen et al., 1997; Miller et al., 2014), suggesting that some focusing or channelization of melt must occur during transport as has been noted in several previous studies (e.g. Kelemen et al. (2000, 1992, 1995); Quick (1982)).

Also, our 100 m/yr estimate of the melt ascent velocity likely represents that of the melt produced during the glacially-induced isostatic adjustment (GIA). At steady state, the decompression melting rate is significantly less. This leads to a significantly lower mass flux of melt and likely results in a slower rate of melt transport. This could be one reason why our ascent rate estimate is significantly higher than that in models of melt transport at Mid-Ocean Ridges (Burley and Katz, 2015; Crowley et al., 2015).

5.6 Model Limitations

The accuracy of our results depends on several factors. The deviations of modelling input parameters from the actual geological values that are not well-constrained can be significant.

For example, the model La concentration is dependent on the time period over which the magma mixes in the crustal chamber. As mentioned in Section 5.4, the longer

the magma residence time, the lower the variations of La concentrations. Also, the residence time may not be the same throughout Iceland as assumed in our model. A better constraint on the effective magma residence time in the chamber may therefore be required.

In more elaborate fluid dynamic models (e.g. McKenzie (1984)), the melt velocity varies with depth. Melt flow starts slow at the base of the melting region and ascends at a faster rate as it migrates to a shallower depth where the porosity is higher. Therefore, in any region below the GIA average melting depth, the melt ascent velocity is likely to be below our estimate. This depth-dependent melt ascent velocity would cause a more time delay of the burst of the La supply rate to the crustal chamber than that predicted by our model in Figure 5.8b. A larger time delay between the melt supply and the La supply would increase the time intervals during which the La concentration (Figures 5.8c and 5.8d) is depleted or enriched.

2-D fluid dynamic models of melt and trace element transport (e.g. Spiegelman (1996)) also predict an across-axis variation in the erupted melt composition. In our model, we assume complete melt mixing and extraction on the ridge axis. This produces only a single average concentration of La at each snapshot in time. Spiegelman (1996) also showed that the convergence of melt to the ridge axis in passive ridge flow leads to an enrichment of incompatible elements in the erupted melt by almost a factor of 2 (for $D^i \leq 0.01$) from that in the 1-D column model. If the full solution of melt transport had been incorporated into our model, the La concentration at steady state would have also been increased by a factor of ~ 2. If the same enrichment factor (~ 2) also uniformly applies to that during the GIA, our model results of the La concentration (normalized to the steady state value) would remain unchanged. However, the flow fields of the solid mantle and of the melts during the GIA are certainly different from those at steady state. Therefore, the enrichment factor during the GIA is unlikely to be uniformly the same as that at the steady state. How much the enrichment factor varies still remains to be explored. In our future work, we would like to incorporate full melt transport solutions into the model to understand how good the constant ascent rate approximation is.

Last but not least, the real ice sheet shape may be significantly deviated from the axisymmetric shape that we use. While our axisymmetric assumption helps simplify the computations, a modelling-input ice sheet with more detailed 3-D shape may have an important role in controlling the accuracy of the model results.

5.7 Conclusions

The consequences of a finite melt ascent velocity on lavas erupted during the last deglaciation are the following:

1. Volume proportions of different eruption types: Faster melt transport will allow more melts to arrive at the surface and erupt sooner when the ice is still present. This means that there will be a greater proportion of subglacial and finiglacial volumes relative to postglacial volume.

2. Relative timing between the bursts in the eruption rates and the deglaciation: Higher melt ascent velocity will transport the extra melts produced during deglaciation to the surface faster. This will result in a smaller time-lag between the bursts in the eruption rates and the deglaciation.

3. Variations of REE concentrations: Slower melt ascent velocity will result in a greater time-lag between melts from shallow depth (REE depleted) and melts from deep depth (REE enriched) arriving at the surface. This will cause higher variations of REE concentrations in the lavas.

Our numerical model estimates that the Icelandic melt transport from the upper mantle melting region to the surface during the last-deglaciation has an average melt ascent velocity of the order of ~ 100 m/yr.

Chapter 6

Weichselian Glaciation (123–23 kyrBP)

6.1 Mantle Flow

In contrast to the deglaciation, glaciation increases the surface load. This induces compression in the mantle, which acts against the decompression induced by the up-welling corner flow. The increase of the surface load also induces down-welling flow in the mantle. Figure 6.1 illustrates that the down-welling flow of the Glacially-induced Isostatic Adjustment (GIA) is opposed to the up-welling corner flow. This leads to a net decrease in the up-welling rate of the mantle from its steady state. The net reduction in the decompression rate leads to a reduction in the decompression melting rate.

Figures 6.2 and 6.3 show our model results of the mantle velocity field at steady state (Figures 6.2a and 6.3a) and during the Weichselian glaciation (Figures 6.2b-d and 6.3b-d) when the ice load history follows the timeline given in Chapter 4. These Figures illustrate that the down-welling flow of the GIA is opposed to the up-welling steady-state corner flow. This decreases the net up-welling velocity (= GIA+corner flow) of the mantle in the melting region (enclosed by the dark green lines) and also decreases the decompression melting rate in the mantle. If the glaciation rate is sufficiently high (such as in Figures 6.2b and 6.3b), the glacially-induced down-welling flow will dominate the up-welling steady-state flow and will reverse the net velocity to the down-welling direction.

Figures 6.4 and 6.5 illustrate snapshots of the model results of the decompression rates in the mantle at steady state (Figures 6.4a and 6.5a) and during the Weichselian

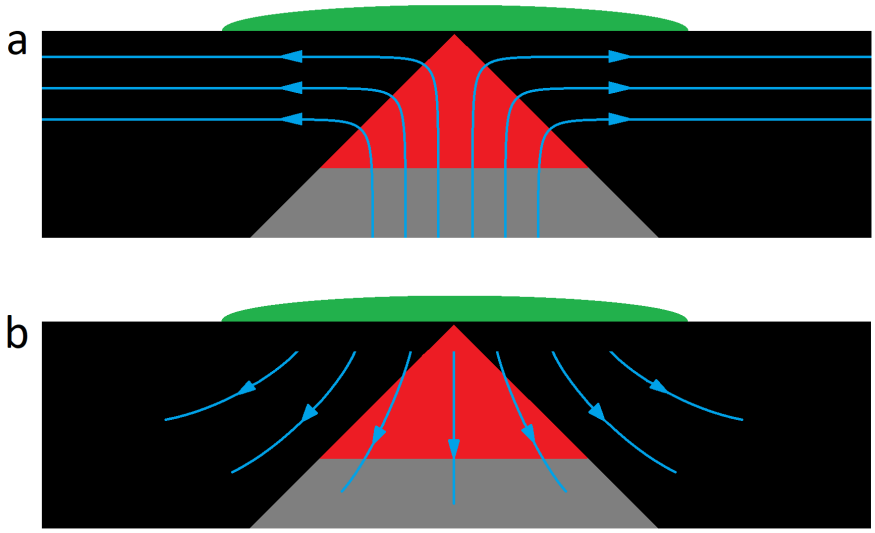

Fig. 6.1 Simplified diagrams illustrating the streamlines of (a) corner flow and (b) Glacial Isostatic Adjustment (GIA). In steady state, the decompression melting comes from the up-welling of the mantle due to the spreading ridge (with half-spreading rate of 10 mm/yr). During glaciation, the increase of the surface load leads to a down-welling flow of the GIA in the mantle. This down-welling flow is opposed to the up-welling corner flow and reduces the decompression melting rate.

glaciation (Figures 6.4b-d and 6.5b-d) when the ice load history follows the timeline given in Chapter 4.

The Weichselian glaciation induces a positive compression rate (= negative decompression rate) in the mantle. This positive GIA compression rate acts against the decompression rate (= negative compression rate) induced by the corner flow. Therefore, the net decompression rate (= GIA+corner flow) during the Weichselian glaciation is reduced. The reduction in the net decompression rate leads to the reduction in the decompression melting rate in the mantle underneath Iceland from its steady state value. This reduces the melt supply to the Earth's surface and, as a result, reduces the volcanic eruption rates in Iceland.

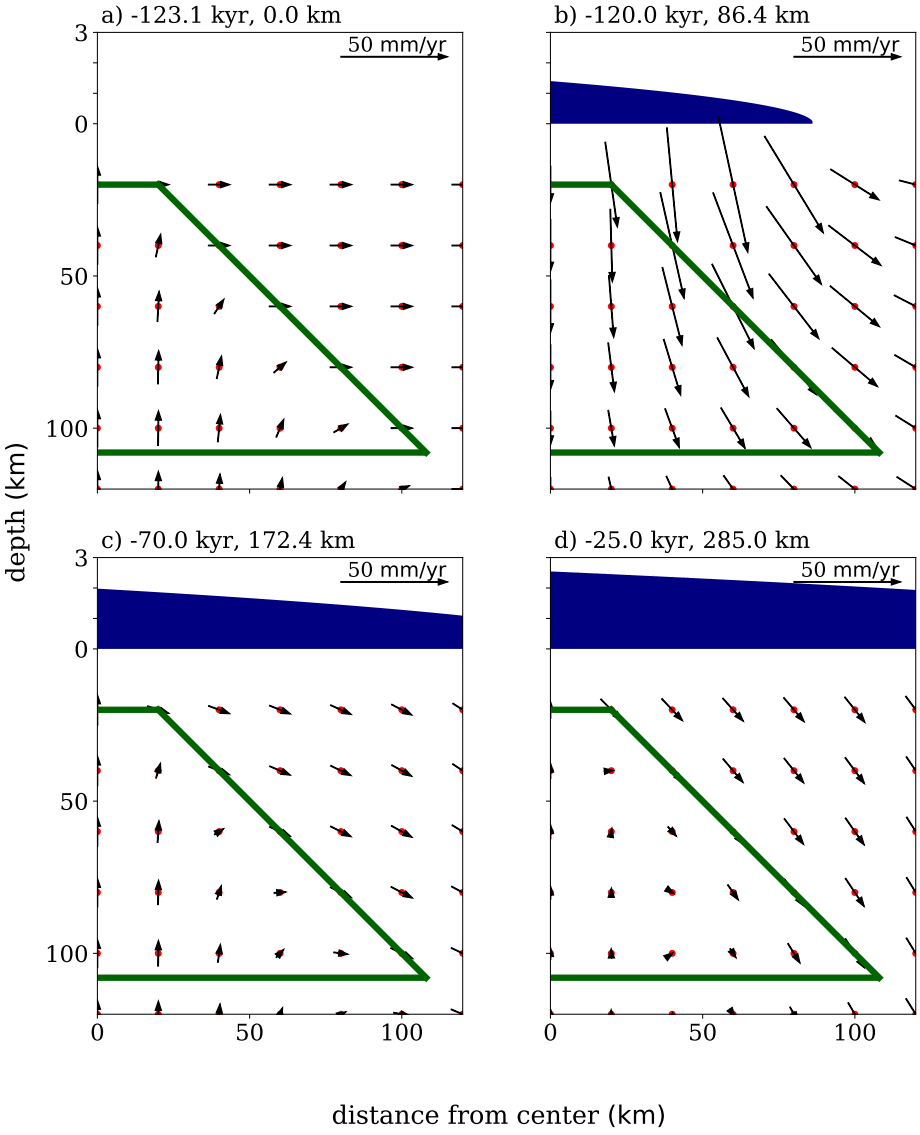

Fig. 6.2 Snapshots of the mantle velocity field in a vertical plane passing through the center of ice perpendicular to the ridge axis induced by the glacial loading and the corner flow. Each arrow is the velocity of the mantle at the red dot. The arrow length is proportional to the magnitude of the mantle velocity. An arrow of length corresponding to the velocity of 50 mm/yr is shown at the top-right corner of each panel. The time and ice radius of each panel are labelled just above the panel. The glaciation follows the timeline given in Chapter 4. The ice load profile (navy blue color) is drawn on top of the mantle with 15× vertical exaggeration. Boundaries of the mantle melting region are outlined by the dark green lines.

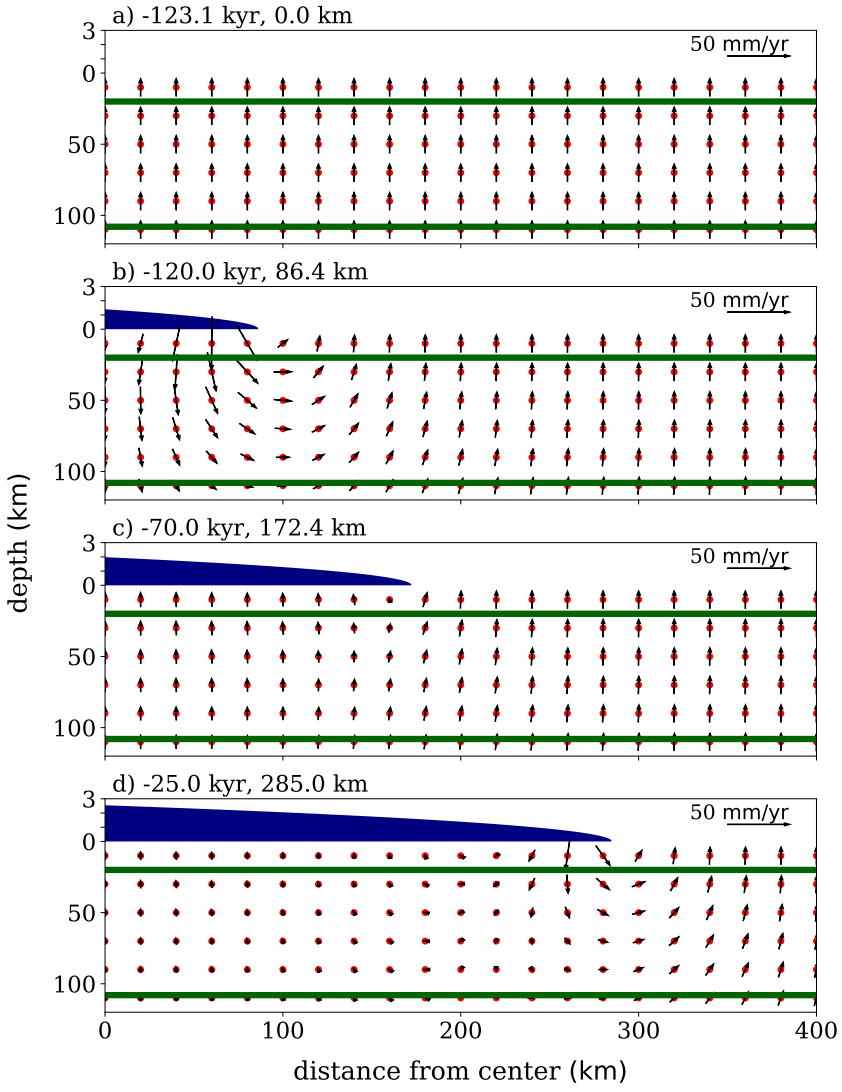

Fig. 6.3 Same as Figure 6.2 but in a vertical plane passing through the center of ice *parallel* to the ridge axis.

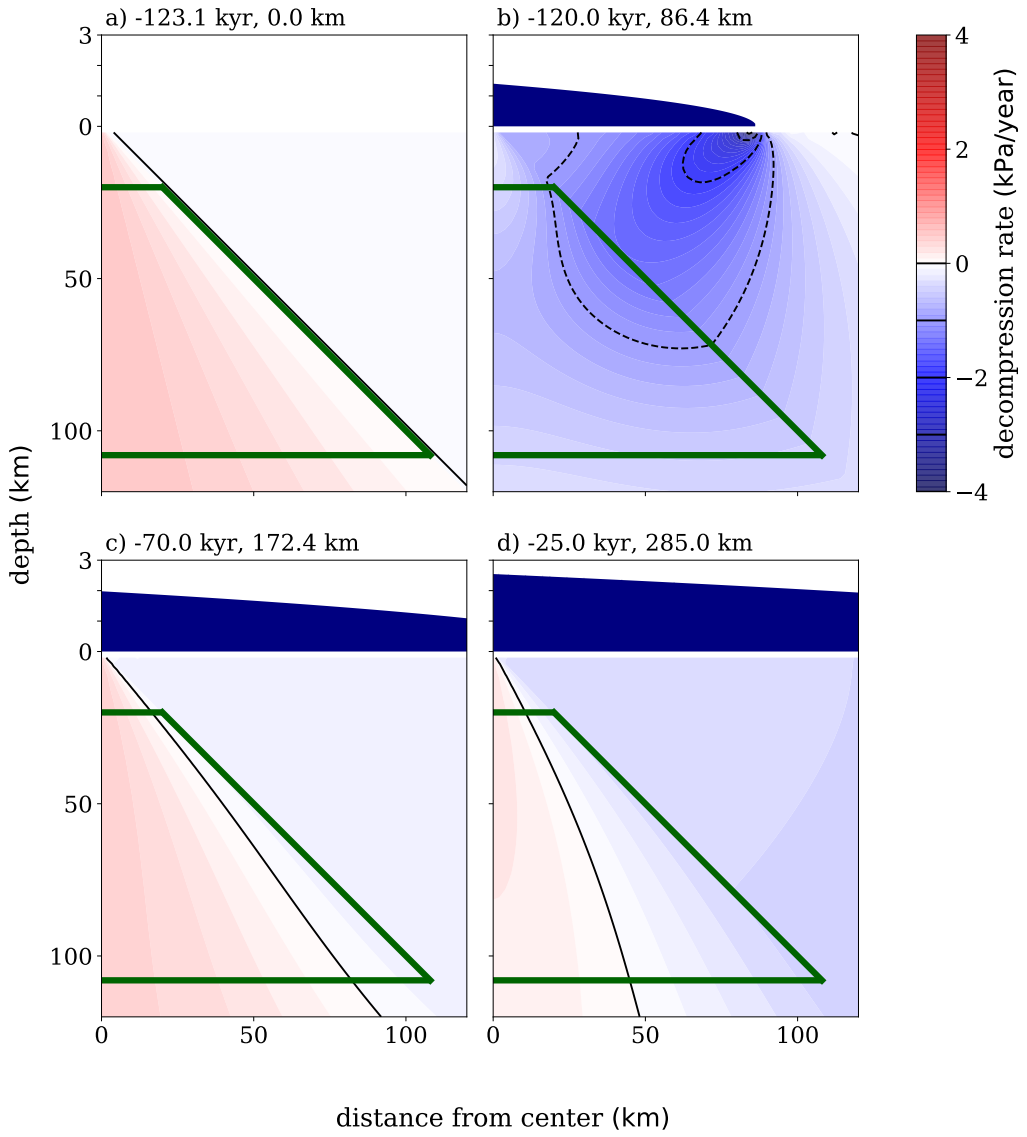

Fig. 6.4 Snapshots of the decompression rate in a vertical plane passing through the center of ice perpendicular to the ridge axis induced by the glacial loading and the corner flow. Black contour lines are separated at equal intervals of 1 kPa/yr. The time and ice radius of each panel are labelled just above the panel. The glaciation follows the timeline given in Chapter 4. The ice load profile (navy blue color) is drawn on top of the mantle with 15× vertical exaggeration. Boundaries of the mantle melting region are outlined by the dark green lines.

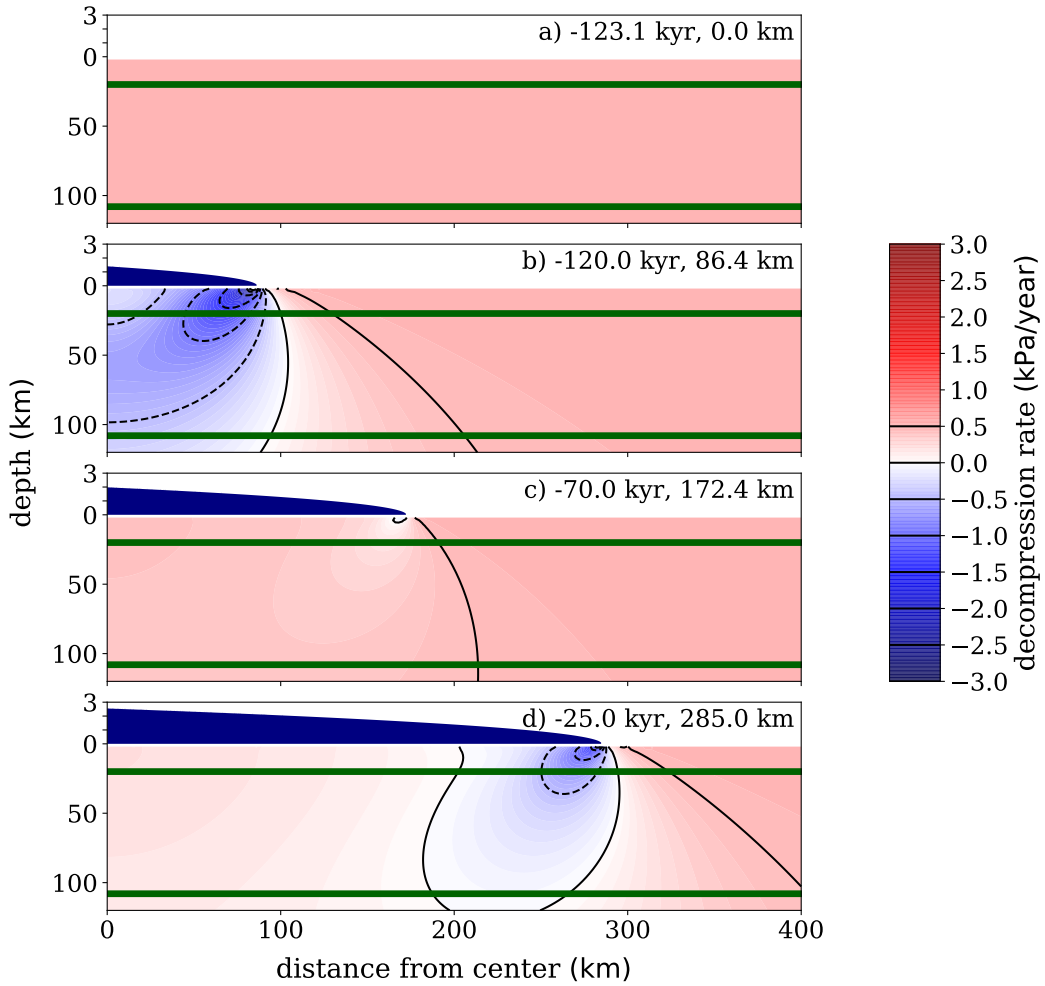

Fig. 6.5 Same as Figure 6.4 but in a vertical plane passing through the center of ice *parallel* to the ridge axis. Black contour lines are separated at equal intervals of 0.5 kPa/yr.

6.2 Mantle Melting

When the glacial loading is sufficiently rapid, the positive compression rate (= negative decompression rate) induced by the GIA in some region of the mantle can exceed the magnitude of the decompression rate (= negative compression rate) induced by the corner flow. This causes a net positive compression (= negative decompression) rate such as the region in blue color at time $t = -120$ kyr and -25 kyr in Figures 6.5b and 6.5d respectively. A net positive compression rate will compress the mantle to below the solidus. Once the mantle is sub-solidus, the decompression melting will cease regardless of whether or not the net decompression rate is positive. The mantle at sub-solidus has to be brought back to the solidus before the melting can recommence.

Figures 6.6 and 6.7 show snapshots of the model results of the mantle melting rates at steady state (Figures 6.6a and 6.7a) and during the Weichselian glaciation (Figures 6.6b-d and 6.7b-d) taken at the same times as snapshots in Figures 6.2, 6.3, 6.4 and 6.5 when the ice load history follows the timeline given in Chapter 4. Mantle at sub-solidus (any region in blue color) has a positive excess pressure $\Delta p > 0$, and hence, *zero* melting rate $DF/Dt = 0$ (see equation 3.2 in Chapter 3 for the definition of the excess pressure). Anywhere inside the melting region where the excess pressure Δp is zero (non-blue region), the mantle is on the solidus and the decompresion melting rate is proportional to the decompression rate of Figures 6.4 and 6.5.

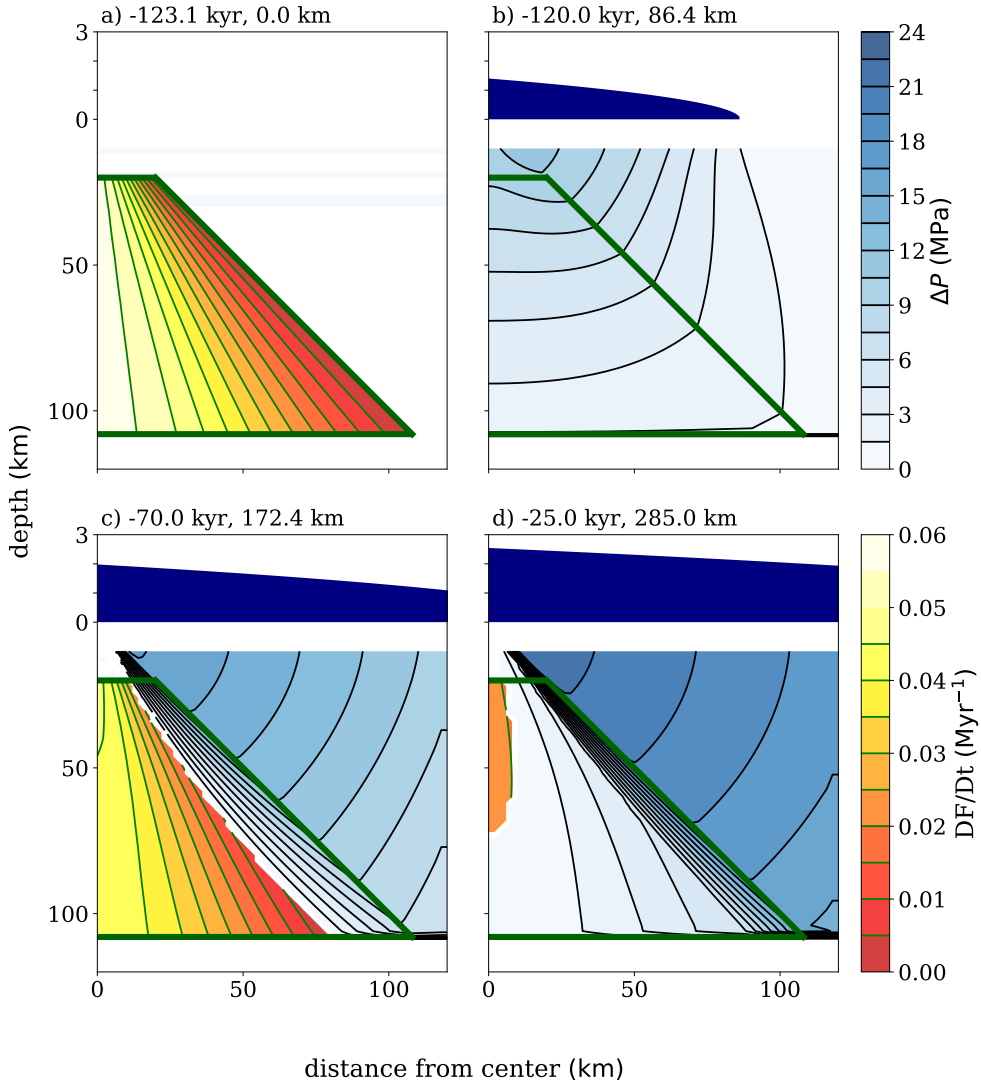

Fig. 6.6 Snapshots of the mantle melting rate DF/Dt and the excess pressure Δp in a vertical plane passing through the center of ice perpendicular to the ridge axis induced by the glacial loading and the corner flow. Contour lines are separated at equal intervals of 0.005 Myr^{-1} and 1.5 MPa for DF/Dt and Δp respectively. The time and ice radius are shown in the upper right corner of each panel. The glaciation follows the timeline given in Chapter 4. The ice load profile (navy blue color) is drawn on top of the mantle with 15× vertical exaggeration. Boundaries of the mantle melting region are outlined by the dark green lines.

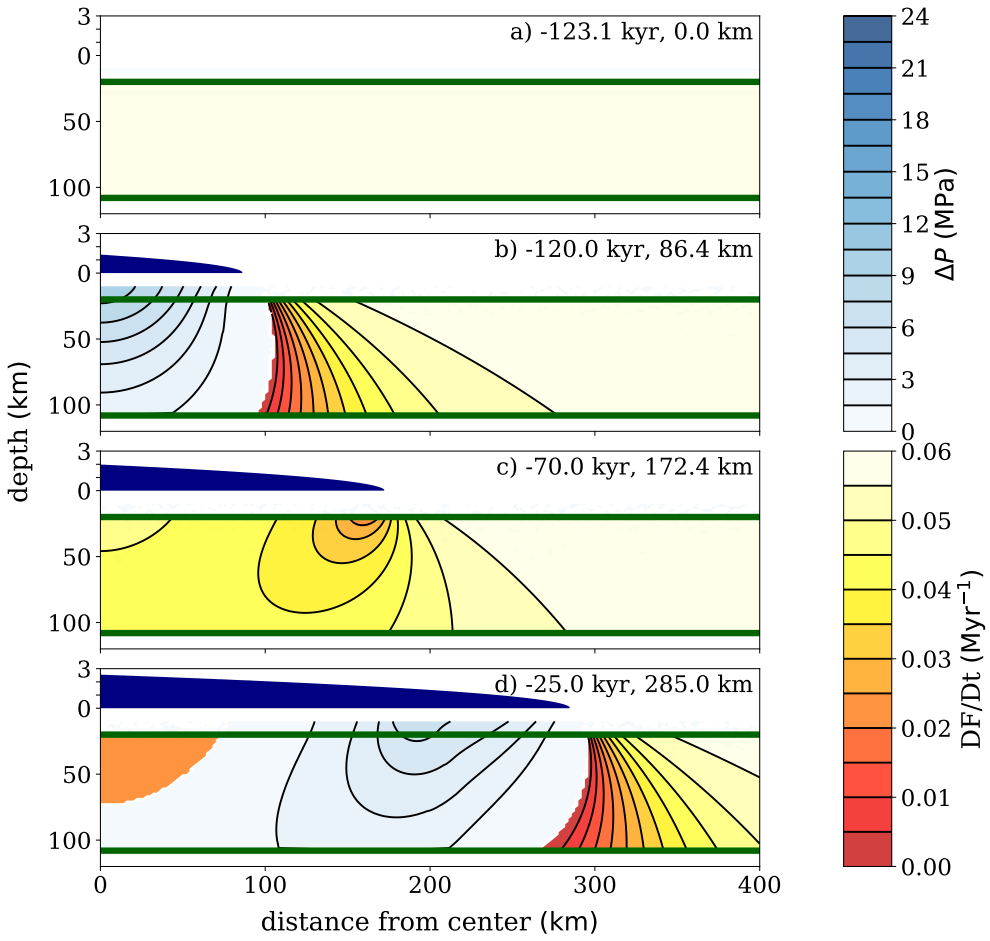

Fig. 6.7 Same as Figure 6.6 but in a vertical plane passing through the center of ice *parallel* to the ridge axis.

6.3 Volumetric Melting Rate

Once the melting response (DF/Dt) to the Weichselian glaciation has been calculated, we can obtain the melt and La volumetric supply rates to the crustal chamber using the method as described in Sections 5.2.1 and 5.2.2.

Figure 6.8 shows the model results when the volume integrations in equations (5.4) and (5.7) are performed over the melting region beneath the ridge axis in the range of 0–180 km from the ice center. At infinite melt ascent velocity, the volumetric rate of melt supply to the crust (red curve in Figure 6.8a) is equal to the volumetric melting rate in the mantle.

Glacial advance increases the surface load and reduces the decompression melting rate. This is the reason why the mantle melting rate (red curve in Figure 6.8a) is dropped from its steady-state value during the three glacial advance periods (blue-shaded regions). At the end of a glacial advance, some regions in the mantle may still be sub-solidus. Therefore, following the end of each glacial advance period, the recovery of the melting rate (red curve in Figure 6.8a) back to the steady-state value will be gradual over time as more and more sub-solidus mantle is recovered back to the solidus by the corner flow.

At finite rate of melt ascent (yellow, green and blue curves in Figure 6.8a), the melt supply rate is delayed from the melting rate (red curve in Figure 6.8a) due to the finite time spent by the melt to travel from depth to the crust. The slower the rate of melt ascent, the longer the time delay. The drop of the melt supply rate (yellow, green and blue curves in Figure 6.8a) following the beginning of each of the three glacial advance periods (blue-shaded regions) is therefore delayed from the drop of the melting rate (red curve in Figure 6.8a). We also discuss this effect for the increase in the melt supply rate following the initiation of a glacial retreat in Section 5.3.

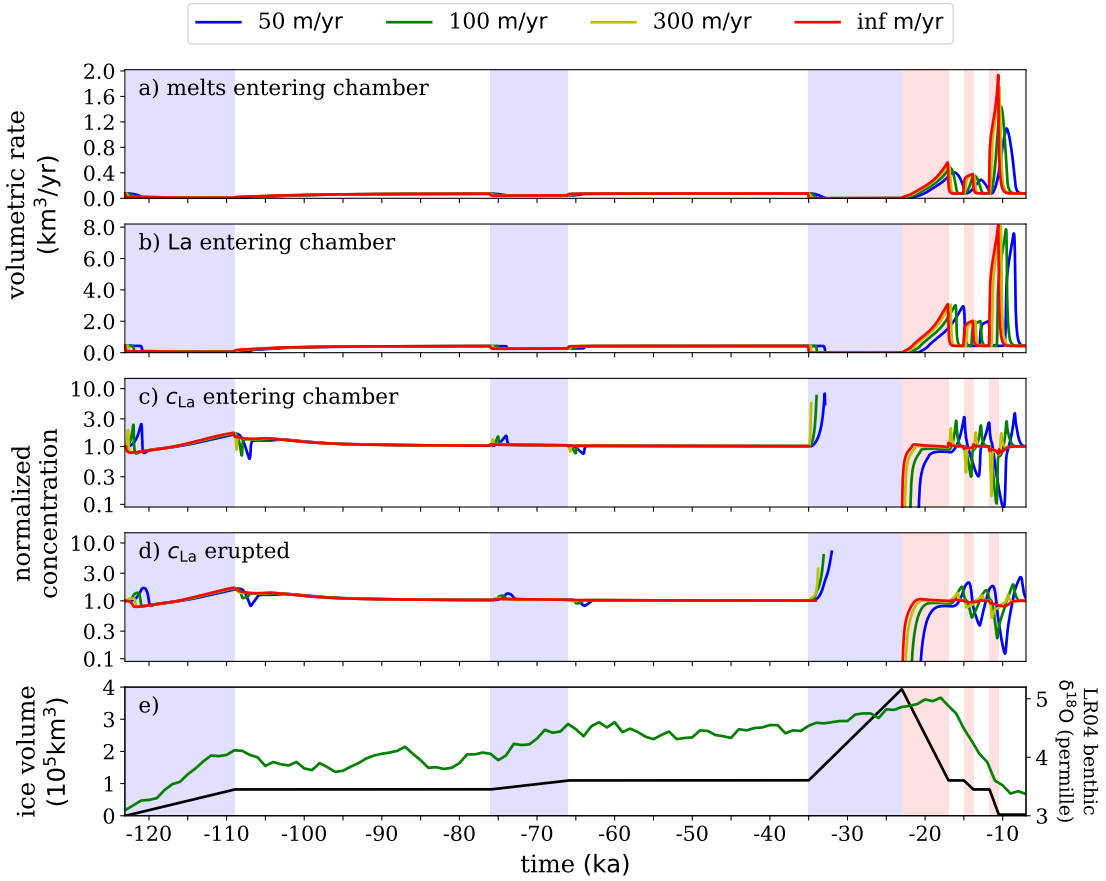

Fig. 6.8 a) volumetric rate of melt supply to the crustal chamber. b) normalized volumetric rate of La supply to the crustal chamber. c) concentration of La in melt supply to the crustal chamber normalized to the steady-state La concentration. d) concentration of La in eruptive lavas normalized to the steady-state La concentration. e) modelling-input ice load volume (black curve, y-axis on the left) and the δ^{18}O of Lisiecki and Raymo (2005) as a proxy for the globally-averaged temperature (green curve, y-axis on the right). (c) is the ratio of the La volume (b) to the melt volume (a); whereas, (d) is the ratio of the 1,000-year standard moving average (SMA) of the La volume (SMA of (b)) to the 1,000-year SMA of the melt volume (SMA of (a)). See Section 5.4 for physical meaning of SMA used in (d). Blue and red shaded regions indicate the time interval during which the ice is advancing and retreating respectively. Different line colors correspond to different values of melt ascent velocity as labelled on top of the figure in m/yr. The melt and La volumetric supply rates to the crustal chamber are the sum along the ridge axis between 0 and 180 km from the center of ice.

6.4 Lanthanum

6.4.1 Introduction

The volumetric rate of La (Figure 6.8b) also has similar behaviour to that of the melt. During the three glacial advance periods (blue-shaded regions), the rate of La partitioned to the melt (red curve in Figure 6.8b) is dropped from its steady-state value. It gradually recovers back after the end of each of the glacial advance periods.

At finite rate of melt ascent, the rate of La supply to the crust (yellow, green and blue curves in Figure 6.8b) is delayed from the melt partitioning rate. The dispersion effect of the finite rate of melt ascent on the volumetric melt (Figure 6.8a) is stronger than that on La (Figure 6.8b). This is because melts produced from different depths take different times to arrive at the crust. Slower rate of melt ascent causes more time lag between melt from shallow depth and melt from a deeper depth to arrive at the crust; and hence, disperse the supply volume out. Whereas, most of La is partitioned to the melt at depth near the primitive solidus (see Section 3.2 for the definition of the primitive solidus). This means that most of the La will take approximately an equal time to ascend from the primitive solidus to the crust regardless of how fast the rate of ascent is.

Concentration of La (c_{La}) supply to the crust is equal to the volumetric supply rate ratio between La (Figure 6.8b) and the melt (Figure 6.8a). Whether the effect of glaciation will enrich or deplete c_{La} from its steady-state value will depend on the relative change between the volumetric supply rates of La and of the melt.

At infinite rate of melt ascent, c_{La} supply to the crust (red curve in Figure 6.8c) is equal to the instantaneous c_{La} in the melt produced at a given time averaged over the melting region. Since the compression/decompression rate induced by the GIA is depth-dependent, the glaciation can change the average melting depth. As discussed in Section 5.4, the instantaneous c_{La} in the melt is maximum at the primitive solidus and decays rapidly as the depth decreases. This means that melts produced at shallower depths will be more depleted in La than melts produced at deeper depths. Therefore, whether the spatially-averaged melt over the melting region will be enriched or depleted in La will depend on whether the glaciation causes the average melting depth to increase or decrease.

6.4.2 123–76 kyrBP

Figure 6.9 illustrates snapshots of the melting rate (DF/Dt) and the excess pressure (Δp) calculated by the model at three different times during the first glacial advance (left most blue-shaded region in Figure 6.8) following the last interglacial at 123 kyrBP. During this glacial advance period, the ice radius is expanding from 0 km to 160 km (see Chapter 4 for details of the ice-load history). The ice-load expansion rate is sufficiently high that the GIA compression rate can dominate the corner flow decompression rate in most regions of the mantle beneath the ice sheet.

At 122 kyrBP (Figure 6.9a), the glacial loading suppresses more melting at deep depths than at shallow depths (melting is completely suppressed where $\Delta p > 0$ as illustrated by the blue-shaded region). By comparing this melting rate profile to that at steady state (Figure 6.7a), we can see that the average melting depth is shifted towards a shallower depth. This means that the initiation of the glacial advance causes the volume-averaged instantaneous c_{La} in the melt (Figure 6.8c, red curve at 123 kyrBP) to drop.

However, as the glacial advance proceeds, the Δp–DF/Dt boundary (Figures 6.9b and 6.9c where the blue and the red regions meet) changes inclination. At 120 kyrBP (Figure 6.9b), the Δp–DF/Dt boundary on average is approximately vertical. The average melting depth is now approximately equal to that at steady state. Therefore, at 120 kyrBP, c_{La} has recovered back to the steady-state value ($= 1$ in Figure 6.8c, red curve at ≈ 120 kyrBP).

After 120 kyrBP, the Δp–DF/Dt boundary evolves in such a way that the average melting depth increases gradually. Figures 6.9c shows that the majority proportion of the on-solidus mantle (non-blue region) at 110 kyrBP is at a deeper depth (La-enriched) than that at steady state. This explains why during ≈ 120–109 kyrBP, the instantaneous c_{La} (red curve in Figure 6.8c) gradually increases with time to above 1.

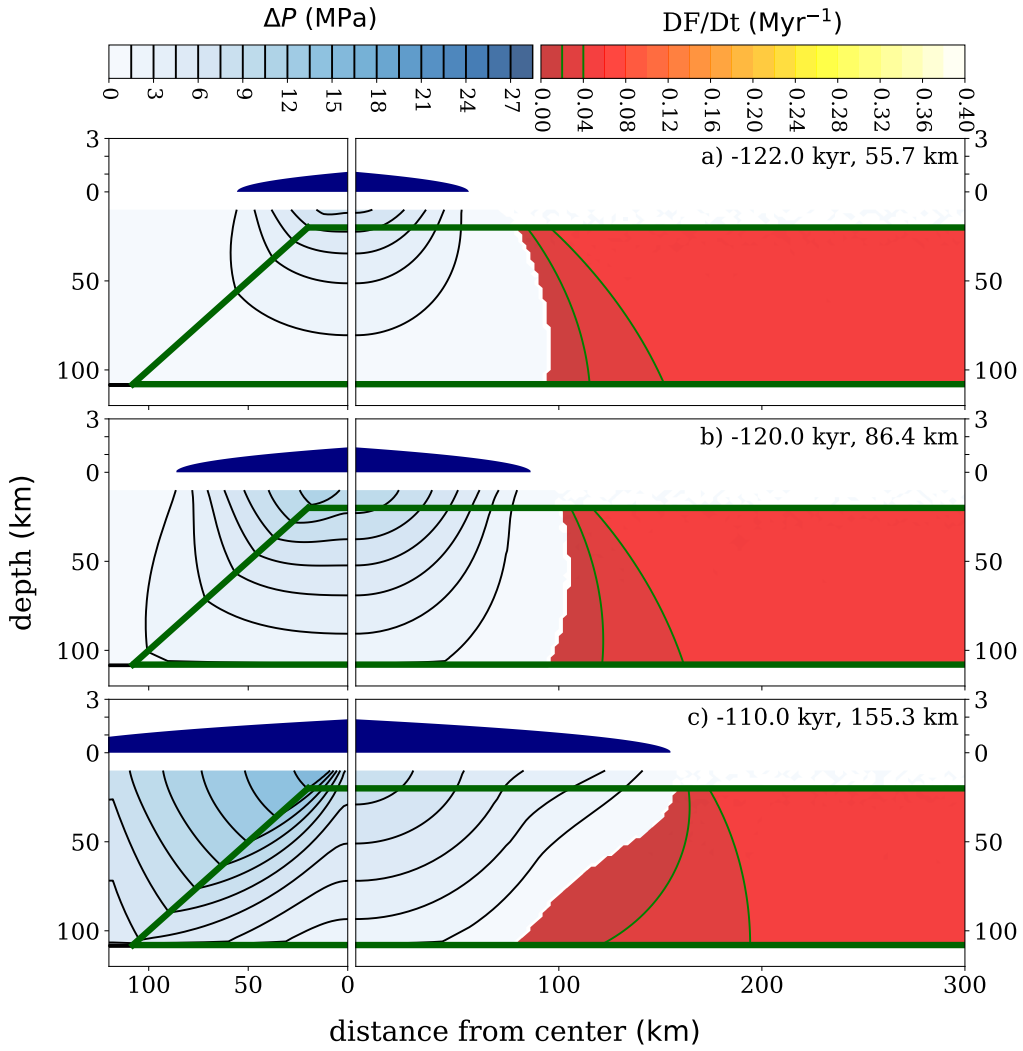

Fig. 6.9 Snapshots of the mantle melting rate DF/Dt and the excess pressure Δp in a vertical plane passing through the center of ice perpendicular (left column) and parallel (right column) to the ridge axis induced by the GIA and the corner flow. Black contour lines are separated at equal intervals of 0.02 Myr^{-1} and 1.5 MPa for DF/Dt and Δp respectively. The left and right panels in each row correspond to the same time. The time and ice radius are shown in the upper right corner of the right panel. The glaciation follows the timeline given in Chapter 4. The ice load profile (navy blue color) is drawn on top of the mantle with 15× vertical exaggeration. Boundaries of the mantle melting region are outlined by the dark green lines.

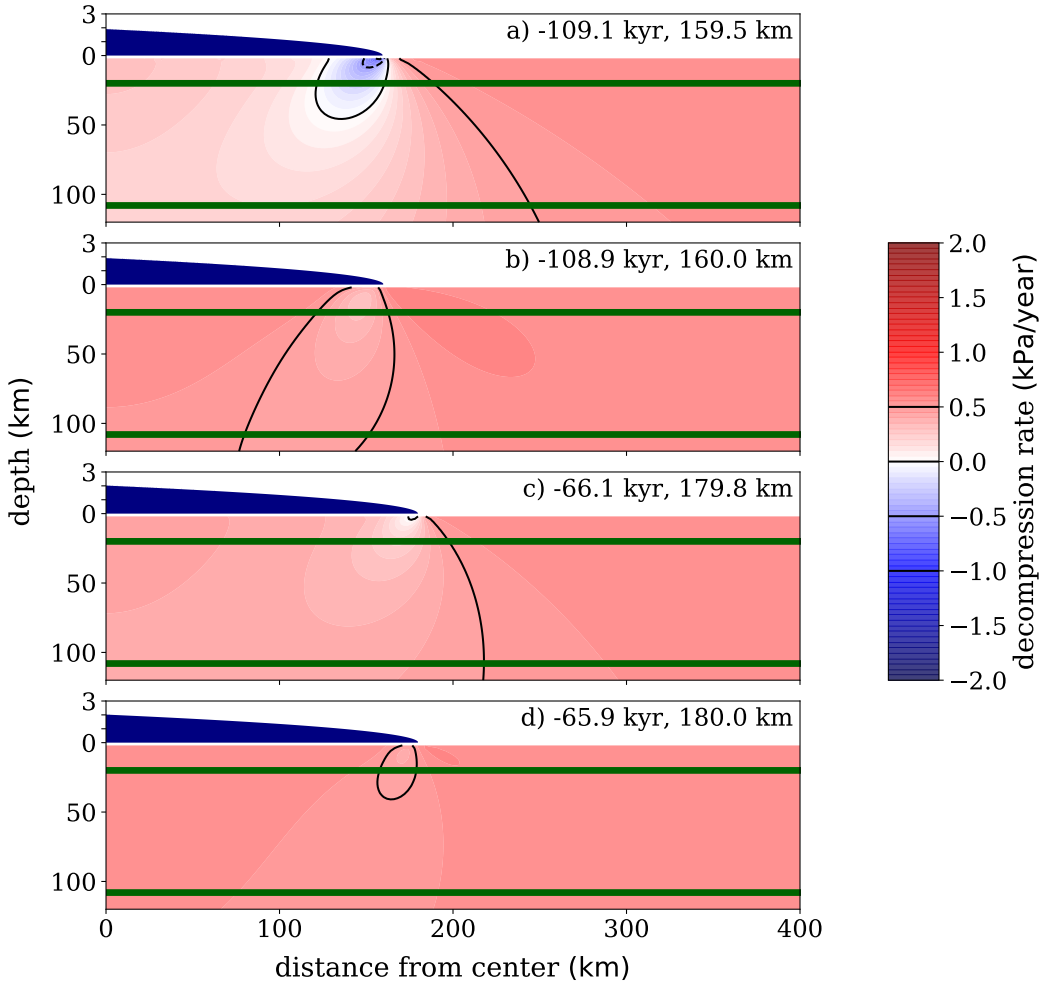

Fig. 6.10 Same as Figure 6.5 but at different times as indicated on the upper-right corners of the panels.

At 109 kyrBP, the first glacial advance (123–109 kyrBP) ends at the ice radius of 160 km. Figures 6.10a and 6.10b illustrate snapshots of the decompression rates just before (109.1 kyrBP) and just after (108.9 kyrBP) the glacial advance termination. Both Figures show that the compression rate induced by the glaciation is depth-dependent.

Let's define $r_{\parallel}$ as the distance measured along the ridge axis from the ice center (i.e. x-axis of the right panels of Figure 6.9) and $r_{\perp}$ as the distance measured perpendicular to the ridge axis from the ice center (i.e. x-axis of the left panels of Figure 6.9). Just before the termination (Figure 6.10a), the compression rate averaged over the range of $r_{\parallel} = 0$–180 km is stronger at shallow depth. This suppresses melting at shallow depth more than that at deep depth. Once a glacial advance period ends (Figure 6.10b), the majority of this GIA-induced depth-dependent compression rate also terminates. This means that, following the end of the glacial advance, the suppression of the melting rate at shallow depth will instantly drop. The melting rate at shallow depth will instantly recover. As a result, the average melting depth will instantly jump to a shallower, more La-depleted depth. This is the reason why c_{La} (red curve in Figure 6.8c at 109 kyrBP) instantly drops following the end of the first glacial advance.

After the end of the first glacial advance, the presumed ice load stays constant with time. The GIA compression rate eventually dies out. Figure 6.11 illustrates that, as time progresses (from Figure 6.11a to 6.11b to 6.11c), the corner flow gradually decompresses the sub-solidus (blue-shaded) mantle back to the solidus (non-blue shaded). More and more melting gradually recovers. But also, the average melting depth gradually decreases back to that at steady state. This means that the instantaneous c_{La} during this period (red curve in Figure 6.8c during 109–76 kyrBP) also gradually decays back to 1. More quantitatively, since the excess Δp in the mantle due to the first glacial advance is of the order of ~ 10 MPa, which is equivalent to moving the mantle downward by ~ 300 meters, it will take ~ 30 kyr for the 10 mm/yr steady-state upwelling rate to recover the 300-m sub-solidus mantle back to the solidus.

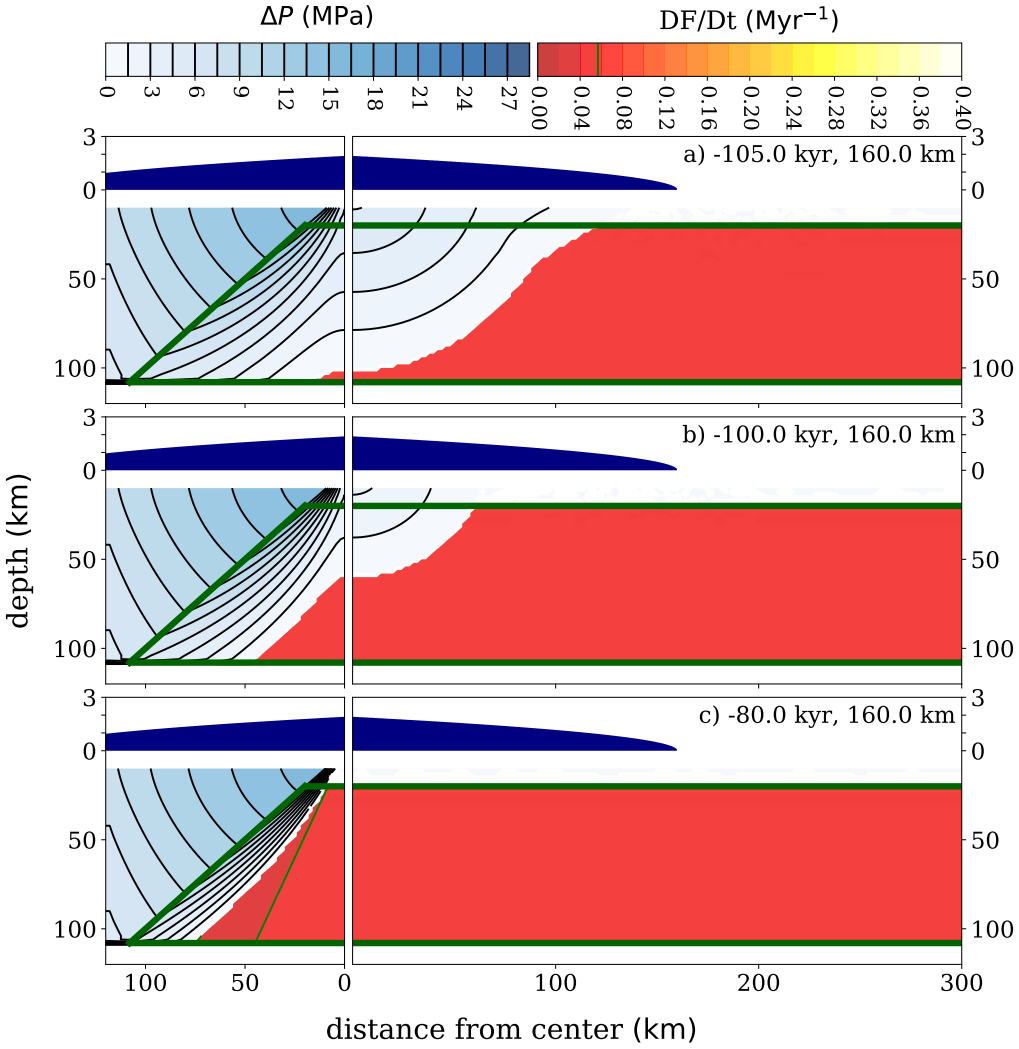

Fig. 6.11 Same as Figure 6.9 but at different times as indicated on the upper-right corners of the right panels.

6.4.3 76–35 kyrBP

At 76 kyrBP, the second stage of glacial advance begins. The ice radius is expanding slightly from 160 km to 180 km (see Chapter 4). The rate of the glacial loading in this period (76–66 kyrBP) is so small that the GIA compression rate is not sufficient to completely eliminate the corner flow decompression rate. The net decompression rate remains positive (= negative compression rate). And, the mantle stays on the solidus through out the whole of the period. This effect is illustrated in Figure 6.12a. By comparing Figure 6.12a to Figure 6.11c, we can see that the glacial advance does not change the shape of the $\Delta p > 0$ region very significantly.

However, the GIA compression rate is depth-dependent. It decays exponentially with depth. Therefore, the net decompression rate (= GIA+corner flow) during the glacial advance at shallower depth is suppressed more than that at deeper depth. As a result, at the beginning of the glacial advance, the average melting depth is instantly shifted towards a slightly deeper, more La-enriched depth. This is the reason why the instantaneous c_{La} (red curve in Figure 6.8c) is instantly slightly enriched at 76 kyrBP.

The termination of the second glacial advance at 66 kyrBP has similar effect on c_{La} to the termination of the first glacial advance at 109 kyrBP as disccussed in Section 6.4.2. At the end of the second glacial advance (at 66 kyrBP), most of the depth-dependent GIA compression rate instantly terminates. The effect of instantaneous c_{La} being enriched instantly by the glacial advance is now reversed. Figures 6.10c and 6.10d illustrate that the average depth of the decompression rate at 65.9 kyrBP just after the termination is slightly at a shallower depth (more La-deplted) than that at just before (66.1 kyrBP) the glacial advance termination. Hence, the instantaneous c_{La} is instantly slightly depleted at the end of the glacial advance.

The rapid change of the decompression rate induced by the GIA is dampened by the viscous mantle flow response. Therefore, following the rapid change at the beginning (76 kyrBP) and the end (66 kyrBP) of the glacial advance, the step jump of c_{La} gradually decays.

After 66 kyrBP, the glacial load is constant. The ice sheet neither advances nor retreats. The instantaneous c_{La} stays approximately constant at ≈ 1.

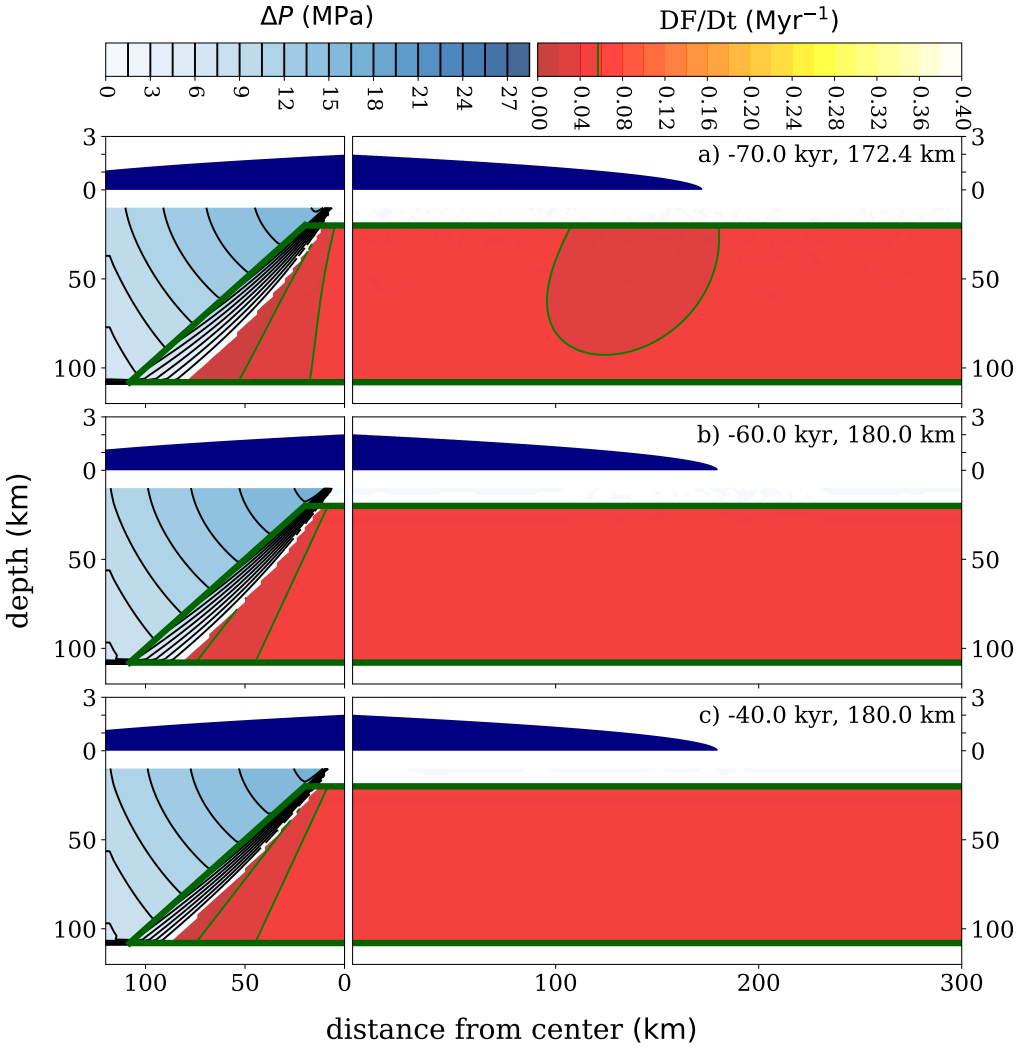

Fig. 6.12 Same as Figure 6.9 but at different times as indicated on the upper-right corners of the right panels.

6.4.4 35–17 kyrBP

After a pause between 66–35 kyrBP, the glacial advance recommences at 35 kyrBP. This is the final stage of glacial advance before the Last Glacial Maximum (LGM) at 23 kyrBP. During this stage (35–23 kyrBP), the model ice sheet expands from the radius of 180 km to 300 km at the LGM. The glacier terminus has advanced from the present-day coastline to the continental shelf break.

The right panel of Figure 6.13 shows that the rate of glacial loading is sufficiently high that the GIA compression completely suppresses the corner-flow decompression rate anywhere in the melting region in the range of $r_{\parallel} = 0$–180 km. The volumetric rates of melt production (red curve in Figure 6.8a) and La partitioned to the melt (red curve in Figure 6.8b) instantly drop to zero at the onset of glacial advance (35 kyrBP). Therefore, the instantaneous c_{La} (red curve in Figure 6.8c) during this time is not calculable until the melting recommences.

We have seen in Figure 6.5d that the compression rate (blue-shaded region of negative decompression rate) is the highest at around $r_{\parallel}$ below the glacier terminus and decreases as $r_{\parallel}$ decreases towards the ice center. Hence, the mantle below the glacier terminus is compressed away from the solidus at a more rapid rate than the mantle below the ice center. This effect is illustrated on the right panels of Figures 6.13b and 6.13c. Mantle below where the glacier terminus has recently swept through (from $r_{\parallel} = 180$ km at 35 kyrBP to the current location of each of the snapshots) has more Δp than mantle further away from this region. As a result, it will take longer for the corner flow to decompress the mantle in this region back to the solidus.

At ≈ 28 kyrBP (Figure 6.13b) while the glacial loading is still proceeding, the GIA compression rate below the ice center has dropped to below the magnitude of the corner-flow decompression rate. The net (=GIA+corner flow) decompression rate is positive, which decompresses the mantle beneath the ice center back to the solidus. Therefore, the mantle melting first recommences just below the ice center, which is very depleted in La. This is why the instantaneous c_{La} (red curve in Figure 6.8) at the first recovery of the melting is ≈ 0. It gradually increases as more and more mantle at deep depth (La-enriched) is recovered back to the solidus (Figure 6.13c vs. 6.13b, right panel beneath the ice center).

After the LGM at 23 kyrBP, glacial retreat begins. It induces GIA decompression, which decompresses the sub-solidus mantle (blue-shaded region in Figure 6.14a, right panel) back to the solidus (right panels of Figures 6.14a vs. 6.14b vs. 6.14c). The volumetric melt production rate (red curve in Figure 6.8) gradually increases. And, the instantaneous c_{La} eventually recovers back to ≈ 1.

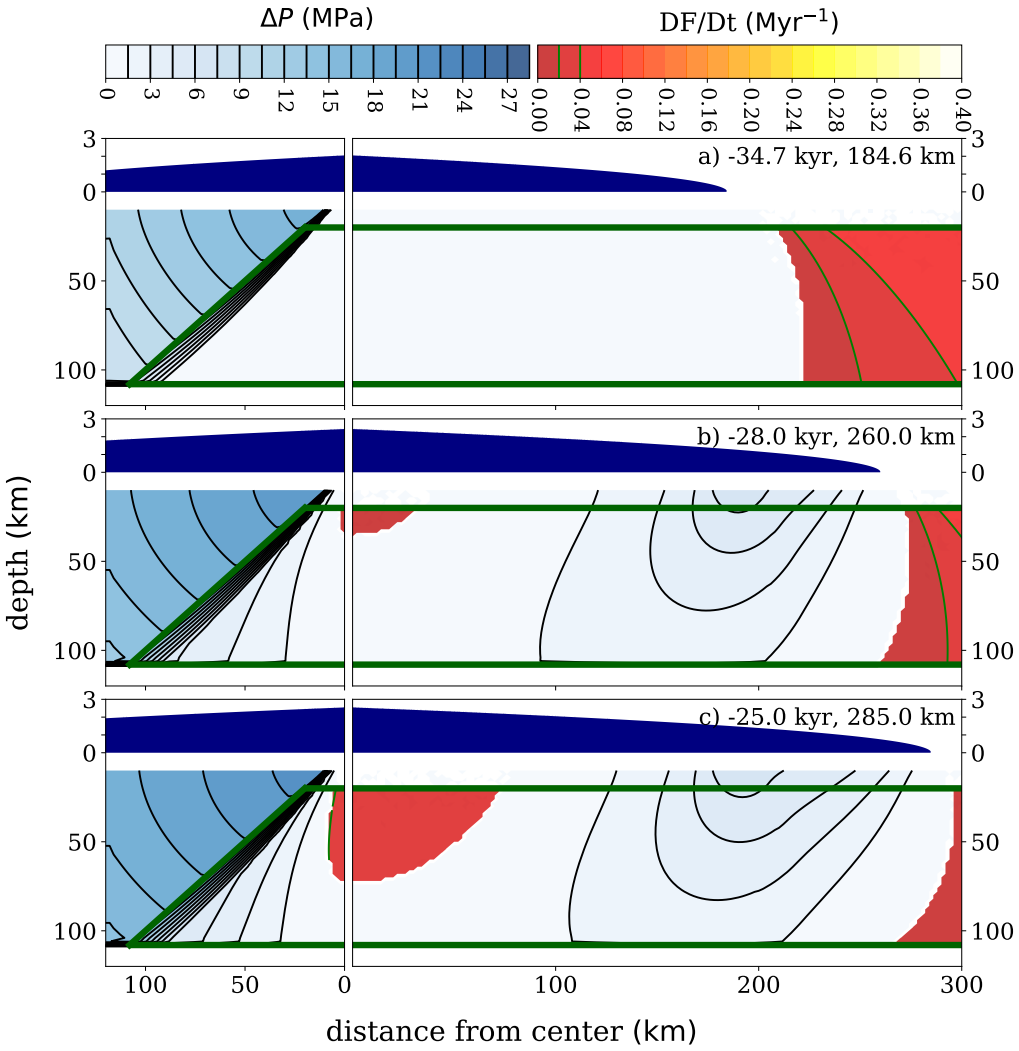

Fig. 6.13 Same as Figure 6.9 but at different times as indicated on the upper-right corners of the right panels.

6.4.5 Finite Rate of Melt Ascent

We discussed in Section 5.4 that, at a finite rate of melt ascent, there is a time lag of the crustal supply between shallow-depth-produced melt and deep-depth-produced melt that are produced at the same time. Any change in the melt production rate that is simultaneous at any depth will affect the crustal supply at different times due to a finite rate of melt ascent.

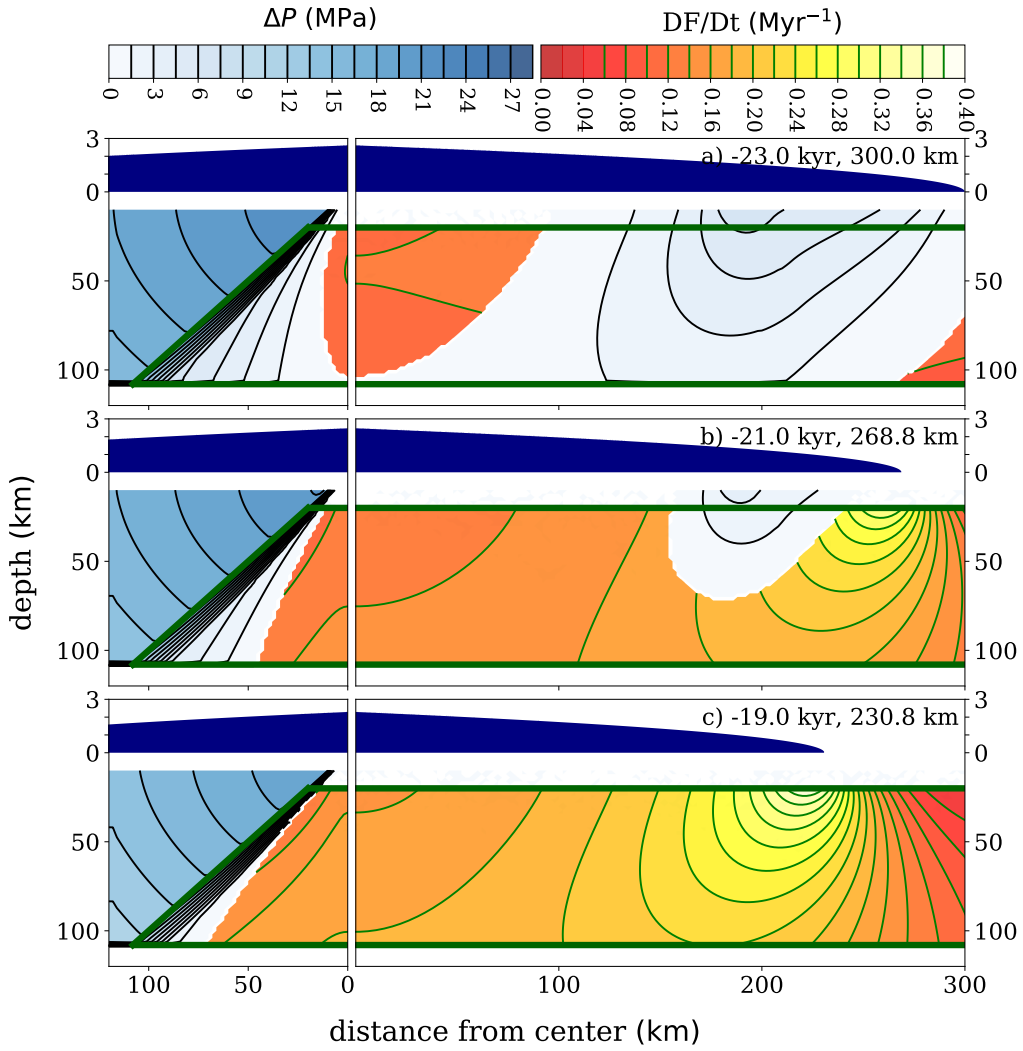

Fig. 6.14 Same as Figure 6.9 but at different times as indicated on the upper-right corners of the right panels.

At the initiation of a glacial advance period, the decompression melting at any depth is simultaneously dropped. The drop of the crustal supply from the melt produced at shallow depth (La-depleted) will happen before the drop of that produced at the same time but at a deeper depth (La-enriched). This is because the last pocket of melt produced at a deeper depth just before the glacial loading will arrive at the crust at a later time than that produced at a shallower depth. Once the crustal supply of

shallow depth (La-depleted) melt has dropped but that of deep depth (La-enriched) is still remaining high, the net average La concentration of melt supply to the crust will increase. Following the rise of the c_{La} supply, the relatively higher amount of the deep-depth-produced (La-enriched) melt supply (relative to the amount of the shallow-depth-produced melt supply) will eventually be exhausted. The spike of the average c_{La} supply will eventually disappear. This effect can be seen in Figure 6.8c. The crustal supply of c_{La} at a finite rate of melt ascent (yellow, green and blue curves) temporarily spikes above the production value (red curve) just after the initiation of the three glacial advance periods at 123, 76 and 35 kyrBP.

Once a glacial advance period terminates, most of the GIA compression rate instantly drops. Most of the decompression melting at any depth instantly recommences. This extra melt produced at a shallow depth (La-depleted) will arrive at the crust before the extra melt produced at a deeper depth (La-enriched). Hence, following the termination of a glacial advance, the average c_{La} supply to the crust will temporarily drop. Once the extra melt produced at a deep depth (La-enriched) has arrived at the crust, the average c_{La} supply to the crust will return back to the normal mean production value. This effect can be seen in Figure 6.8c. The crustal supply of c_{La} at a finite rate of melt ascent (yellow, green and blue curves) temporarily drops below the production value (red curve) just after the termination of the three glacial advance periods at 109, 66 and 23 kyrBP.

6.4.6 Spatial Variation

What we have discussed so far is the c_{La} averaged over the ridge axis in the range of $r_{\parallel} = 0$–180 km. In this Section, we examine as an example how c_{La} changes its behaviour when we change the ridge axis range to $r_{\parallel} = 45$–270 km.

Figure 6.15 shows the model results of the volumetric supply rates of melt (Figure 6.15a) and of La (Figure 6.15b), c_{La} supply (Figure 6.15c) and erupted c_{La} (Figure 6.15d). The results in this Figure are obtained from the same model parameters to those in Figure 6.8 except that the volume integrations in Equations (5.4) and (5.7) are now performed over the melting region in the range $r_{\parallel} = 45$–270 km.

Figure 6.15c shows that, during the first glacial advance (123–109 kyrBP), c_{La} partitioned into the melt (red curve) has a slightly smaller variation than that in Figure 6.8c. This is because the c_{La} here is the average over a larger spatial domain ($r_{\parallel}$ range of $270 - 45 = 225$ km) than that in Figure 6.8c ($r_{\parallel}$ range of $180 - 0 = 0$ km). This integrates over a larger volume of mantle, which includes a greater proportion of the mantle outside the ice coverage that is still melting at near the steady state with lower c_{La} temporal variation.

Following the termination of the first glacial advance at 109 kyrBP, c_{La} partitioned into the melt in Figure 6.15c (red curve) jumps up slightly; whereas, that in Figure 6.8c steps down. We discussed previously in Section 6.4.2 that there is a higher reduction at a shallower depth of the GIA compression rate at the end of the glacial advance when it is averaged over the range of $r_{\parallel} = 0$–180 km (Figures 6.10a vs. 6.10b). This reduction leads to instantly greater decompression melting at shallow depth (La-depleted), causing the c_{La} to instantly drop. However, Figures 6.10a vs. 6.10b also show that in the region of $r_{\parallel} > \approx 180$ km the decompression rate increases more at a deep depth (La-enriched). As a result, when averaged over the range of $r_{\parallel} = 45$–270 km, the c_{La} partitioned into melt (red curve in Figure 6.15c) is slightly increased at the end of the glacial advance at 109 kyrBP.

Another difference between Figures 6.8 and 6.15 is during the final glacial advance (35–23 kyrBP). Figure 6.13a shows that, at just after 35 kyrBP, the GIA compression has compressed all the mantle in the range of $r_{\parallel} = 0$–180 km to sub-solidus. This means that the volumetric melting rate integrated over the range $r_{\parallel} = 0$–180 km is dropped to zero, meaning that the c_{La} is not calculable. Whereas, over the range $r_{\parallel} = 45$–270 km, the non-zero volumetric melting rate at just after 35 kyrBP allows us to calculate the c_{La}.

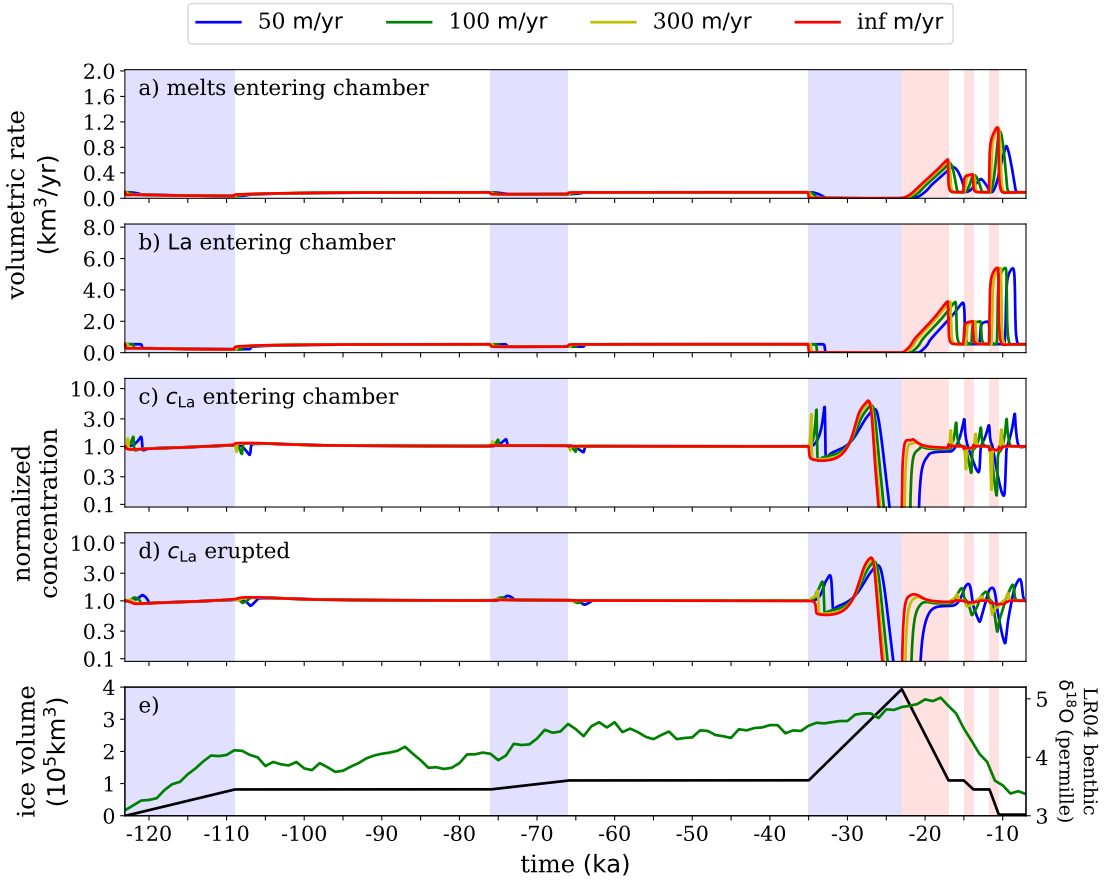

Fig. 6.15 Same as Figure 6.8 but the melt and La volumetric supply rates to the crustal chamber are the sum along the ridge axis between 45 and 270 km from the center of ice.

The right panel of Figure 6.13a shows that the Δp-DF/Dt boundary (where the blue- meets the red-shaded mantle) inclines in such a way to cause the average melting depth to be at a shallower (La-depleted) depth than that at steady state. This causes the initial drop of c_{La} (red curve in Figure 6.15c) at 35 kyrBP.

As the glacial advance proceeds, the Δp-DF/Dt boundary progressively changes its inclination (right panels of Figures 6.13b and 6.13c) that the average melting depth progressively gets deeper (more La-enriched). Hence, c_{La} (red curve in Figure 6.15c) after the initial drop at 35 kyrBP progressively increases and peaks at ≈ 27 kyrBP.

After the peak of c_{La} at ≈ 27 kyrBP, the Δp-DF/Dt boundary has passed the outer range $r_{\|} = 270$ km, meaning that all the mantle in this region is now sub-solidus and is not melting (right panel of Figure 6.13c at 270 km from the ice center). At the same time, however, mantle just below the ice center has recovered back to the solidus and begins to melt again (Figures 6.13b and 6.13c). The melt produced at just below the ice center is very depleted in La. As a result, c_{La} (red curve in Figure 6.15c) at ≈ 27 kyrBP sharply drops to ≈ 0.

Other features seen in Figure 6.15 including the effect of finite rate of melt transport are similar to those in Figure 6.8. The model calculation of the crustal chamber process is similar to that explained in Section 5.4.1. The model results of the erupted c_{La} shown in Figures 6.8d and 6.15d are the 1,000-year Standard Moving Average (SMA) of the volumetric supply rate of La (Figures 6.8b and 6.15b respectively) divided by the 1,000-year SMA of the volumetric supply rate of melt (Figures 6.8a and 6.15a respectively). This acts as a low-pass filter that smooths out the variation of c_{La} supply to the crustal chamber (Figures 6.8c and 6.15c).

Chapter 7

Termination II

7.1 Introduction

In previous chapters, we have seen that deglaciation increases decompression rates in the mantle. The increase has a depth-dependent profile that the maximum is at the Earth's surface and it decays exponentially with depth. As a result, it shifts the average melting depth from that at the steady state to a shallower more REE-depleted depth. Therefore, melts produced during a deglaciation period have average REE concentrations lower than the steady-state values. We investigated this REE depletion effect in lavas erupted on Iceland during the last deglaciation in Chapter 5.

An alternative name for the last deglaciation is **Termination I**. It means the termination of the last glacial climate. Likewise, **Termination II** refers to the termination of the second last glacial climate, which marks the beginning of the last interglacial (LIG).

Studies of the geochemical compositions of Icelandic lava shields that erupted soon after Termination I and II (during when the eruption rates were still significantly elevated from the steady state) found that incompatible element (IEM) compositions of the Termination II lava shields are significantly different from that of the Termination I lava shields that erupted around the same region. It can be seen in Figure 7.1 that the concentration ratios of an incompatible element (either Zirconium (Zr) or Niobium (Nb)) to a relatively more compatible element (Yttrium (Y)) in the Termination II lava shields (blue circles) differ from that in the adjacent Termination I lava shields (black triangles).

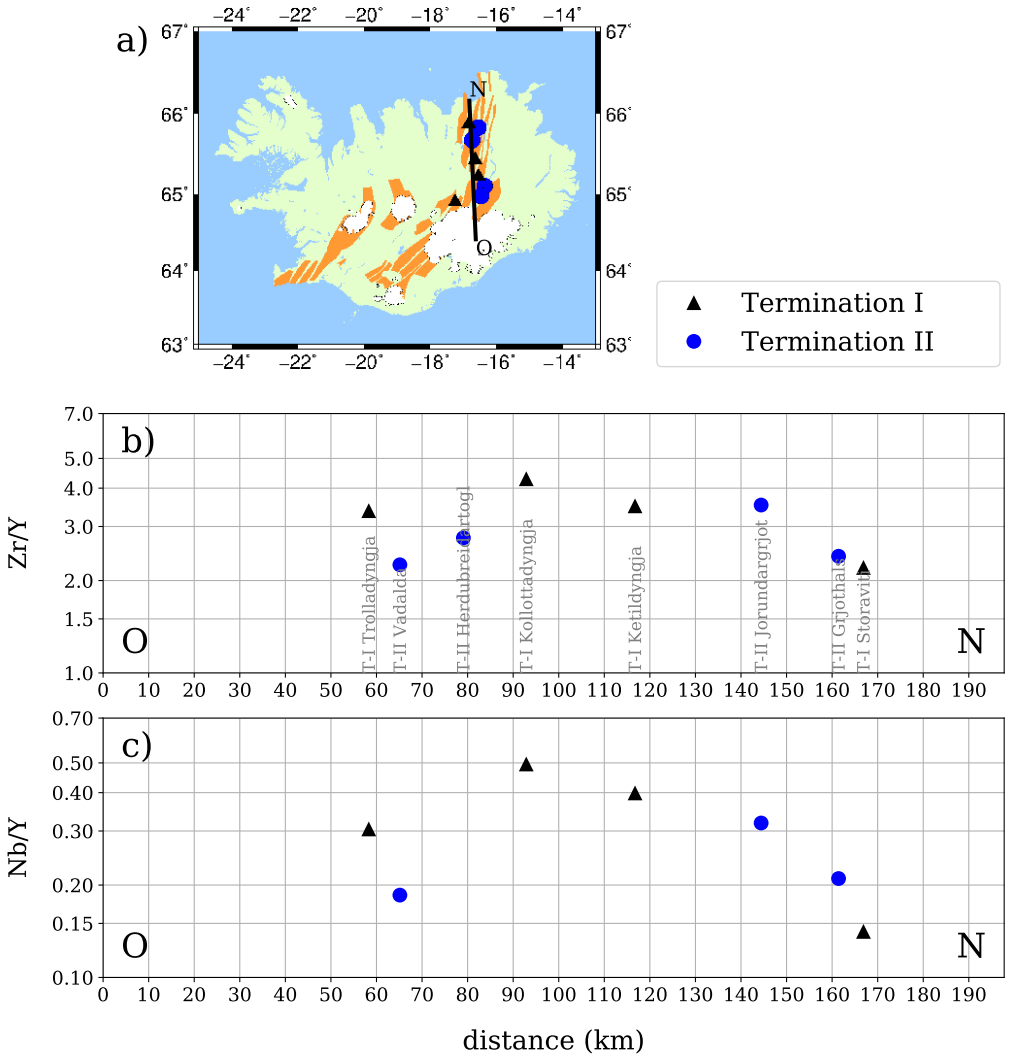

Fig. 7.1 (a) Map showing locations of the Termination I and II lava shields (as black triangles and blue circles respectively) in the Northern Volcanic Zone. (b) Transect through the Northern Volcanic Zone (along the black line in panel (a)) indicating locations and the Zirconium (Zr) to Yttrium (Y) concentration ratios of the Termination I (black triangles) and II (blue circles) lava shields. Name of each lava shield is also labelled just below the data point. (c) Similar to (b) but the y-axis is the concentration ratios of Niobium (Nb) to Yttrium (Y). In panel (c), there is no data point for Herðubreiðartögl at ~ 79 km because there is no available Nb data for this lava shield. Rock sample data collected from these lava shields are provided in Appendix A, Tables A.4 and A.5.

We hypothesize that the difference of the IEM contents is due to the difference of the deglaciation histories between the two Terminations. Lava shields are formed from subaerial eruptions. Different deglaciation histories have different melt production rates and different partitioning of eruption volumes into subglacial and subaerial lavas. This can change the partitioning of the IEM contents in the subglacial and subaerial lavas (and hence the IEM contents in the lava shields).

7.2 Glacial Load

Due to limited number of proxies that can constrain the Termination II deglaciation history, a modelling-input ice load that can appropriately represent the Termination II is not well-defined. Therefore, we do not attempt to run our numerical models with ice-load inputs that replicate the Termination II. Instead, we examine the effect of the deglaciation history by running our numerical models with a number of different deglaciation scenarios.

Two components of the deglaciation history effects on the IEM contents of subaerial lavas that we consider separately are

1. the deglaciation rates (Section 7.3.1) and

2. the deglaciation pauses (Section 7.3.2).

We examine the effect of the deglaciation rates by running the models with continuous deglaciation (i.e. no pause) at different deglaciation rates. Then, the effect of the deglaciation pauses is examined by running the models with different deglaciation scenarios of the same deglaciation rate, but, with a pause of different durations at the same ice radius.

In all the deglaciation scenarios, the center of the ice sheet is assumed to be on the ridge axis at the origin of the Cartesian coordinates (Figure 2.3 with ice center C coincides with the origin O). For simplicity, the time axis is shifted so that the onset of the Termination II deglaciation coincides with that of the Termination I at 23 kyrBP. Numerical parameters for the Termination II ice-load inputs are the same as those for the Termination I modelling in Chapter 5 (see Table 5.1). Prior to the deglaciation at 23 kyrBP, the glacial load is constant with the radius of 300 km equal to that in Chapter 5, the mantle is set to be in isostatic equilibrium and the mantle flow follows the steady-state corner flow. In this chapter, we use the bi-lithological mantle source of Rudge et al. (2013) for the geochemistry and mantle melting model; whereas, in the previous chapters, a simple (constant melt productivity) model is assumed.

7.3 Model Results

The modelled concentration ratio of an incompatible element to a relatively more compatible element (such as Zr/Y or Nb/Y) behaves in a similar way to the concentration of an incompatible element (such as La), but the behaviour of the latter is simpler to understand. In this section, we consider the model results of the melt flux and La flux supply to the crust subaerially when the eruption rates are still elevated from the steady-state values (referred to hereafter as **early-postglacial**). The crustal chamber process is not included just yet for simplicity. Once we understand the behaviours of the crustal supply of melt and La content, it will be straightforward to incorporate the crustal chamber process to determine the La concentrations in erupted lavas and also to extend the understanding to the Zr/Y and Nb/Y concentration ratios.

7.3.1 Deglaciation Rates

This section studies the effect of deglaciation rates on the La content of the erupted lavas. The model is run with four different prescribed deglaciation rates. These four deglaciation scenarios have the ice volume decreasing linearly with time from $t = -23$ kyr (= 23 kyrBP) with the same initial ice sheet profile (same volume, radial extent and thickness). The ice volume versus time is plotted in Figure 7.2. There is no pause during the deglaciation until the ice volume goes to zero. We name these four scenarios C1, C2, C3 and C4 in the ascending order of the deglaciation rates (C1/C4 has the lowest/highest deglaciation rate) as labelled on the Figure. "C" stands for "continuous", which means that the deglaciation proceeds continuously without any pause.

Figure 7.3 shows that the total melt production volumes between time $t = -24$ and 0 kyr (practically covering the whole elevated-eruption-rate period) in all the deglaciation scenarios have approximately the same spatial distribution along the ridge axis. This is because the net change of the degree of melting $\Delta F_{net}(r, z)$ at each location (r, z) in the mantle is directly proportional to the net pressure drop $-\Delta P_{net}(r, z)$, which is directly proportional to how much the ice-load is unloaded (see Section 7.5.2 for mathematical justification). Since all the deglaciation scenarios have the same unloading profile of ice (=*initial* minus *final* ice-load profile $= h_0(r) - 0$), they have the same net pressure drop (and hence the same net melting) regardless of how fast the ice is unloaded.

For the total subglacial lava volumes, the thick black line in Figure 7.3 shows that, while scenario C4 (Figure 7.3d) has a 7.5-fold shorter deglaciation duration than that of scenario C1 (Figure 7.3a) (2-kyr long vs. 15-kyr long, which means ≈ 7.5-fold narrower

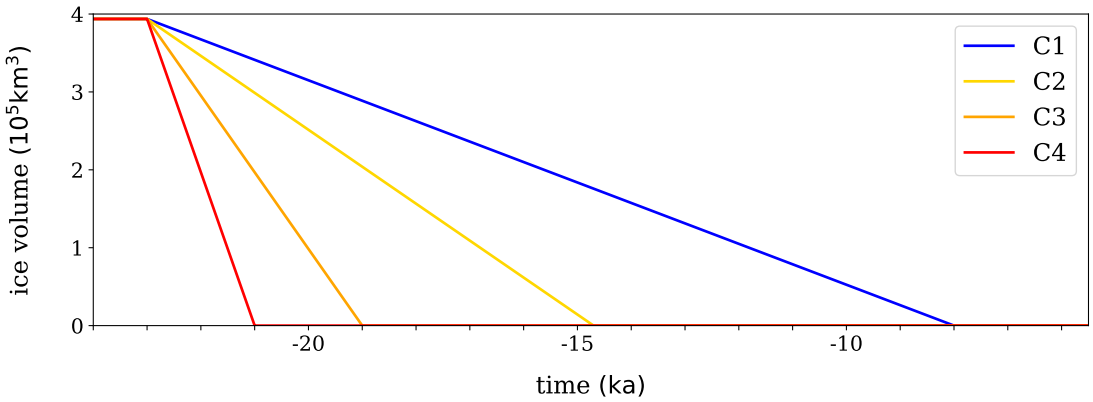

Fig. 7.2 The modelling-input ice volume histories of four different deglaciation-rate scenarios (shown as different line colors) with the same initial ice thickness profile (300 km radius, 1.39 km average thickness and 3.93×10^5 km^3 volume) and the same timing of the onset of deglaciation at $t = -23$ kyr ($= 23$ kyrBP). The name of each of the four scenarios (C1, C2, C3 and C4) is as labelled on the upper-right corner in the ascending order of the deglaciation rates, where C stands for "continuous" (i.e. no pause). The ice volumes go to zero at $t = -8.0$, -14.7, -19.0 and -21.0 kyr for the C1, C2, C3 and C4 scenarios respectively.

time window for melts to erupt subglacially), the C4-scenario subglacial volumes are not significantly dropped from that in the C1-scenario. This is because, although the subglacial time window is ≈ 7.5-fold narrower, the deglaciation rate and hence the melt production rates are 7.5-fold higher. The net result is that, when the deglaciation rate changes, the total amount of melt "produced subglacially" (= erupted subglacially if the melt transport were instantaneous) does not change significantly. This applies to the C2 and C3 scenarios too.

Since the total and the subglacial melt volumes in all the scenarios are about the same, the subaerial (=*total* minus *subglacial*) melt volumes (layer above the thick black line in Figure 7.3) also remain approximately the same for all the four deglaciation scenarios.

The vertical spacing between two adjacent isochrons is directly proportional to the eruption rate during that time interval. A very wide gap between the 22- and 20-kyrBP isochrons in Figure 7.3d is due to the fact that the eruption rate in scenario C4 during 22–20 kyrBP is significantly more elevated from the steady state than the other scenarios due to a higher deglaciation rate.

The thick black line in Figure 7.3 does not only indicate the subglacial lava volume. It also shows where the glacier terminus is at a given time (as indicated by the

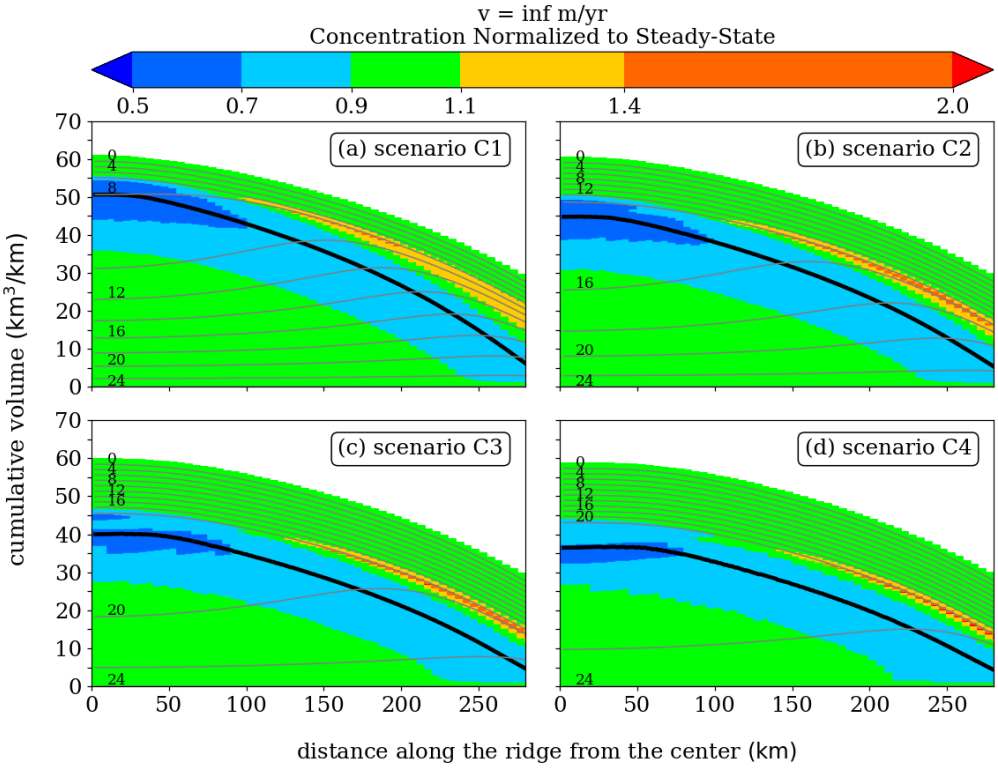

Fig. 7.3 Isochrons of cumulative lava volume per unit length along the ridge axis as predicted by the model assuming instantaneous melt transport from depths to the surface. In this case, the "erupted" lava volume and the La concentration are the same as that of the melt produced in the mantle. The volume accumulation begins at time $t = -24.0$ kyr ($= 24.0$ kyrBP) and ends at time $t = 0$ kyr ($= 0$ kyrBP). Different panels correspond to different deglaciation scenarios as labelled on the upper-right corner of each panel. Thick black line shows the total subglacial lava volume. That is, subglacial and subaerial lavas are separated by the thick black line, below/above which is the subglacial/subaerial volume. Contour lines (in grey) are separated at an equal interval of 2 kyr and the ages labelled on the lines are in kyrBP. Colors illustrate La concentration in the lava normalized to the steady-state value. The corresponding numerical values of these colors are indicated by the color bar on top of the figure.

intersection between the thick black line and the grey isochron). The blue band around the thick black line on Figure 7.3 shows that the La-depleted melts are produced around the glacier terminus. This is because the decompression rate in the mantle is high near the glacier terminus (as in Figure 5.4). This high decompression rate at shallow (La-depleted) depths in the mantle produces the La-depleted melt band in Figure 7.3 that distributes around the glacier terminus line (thick black line). Hence,

the horizontal width of the blue La-depleted band in Figure 7.3 is controlled by the spatial distribution of the decompression rate field in the mantle.

The La-depleted bands in all the ice scenarios have approximately the same width and La concentration distribution around the glacier terminus line. This can be explained by considering the decompression rate field $\frac{DP}{Dt}$ in the mantle. From equation (2.45), $\frac{DP}{Dt}$ is controlled by the rate of change of ice load. From equation (4.13), the rate of change of ice load in the spatial frequency (k) space is

$$\mathcal{H}_0[\dot{h}](k,t) = \frac{3\sqrt{2}}{32}\dot{V}(t)\left[\mathrm{J}_{-\frac{1}{4}}\left(\frac{k\,r_m(t)}{2}\right)\mathrm{J}_{\frac{1}{4}}\left(\frac{k\,r_m(t)}{2}\right)+\mathrm{J}_{-\frac{3}{4}}\left(\frac{k\,r_m(t)}{2}\right)\mathrm{J}_{\frac{3}{4}}\left(\frac{k\,r_m(t)}{2}\right)\right].$$

We can see in the square brackets on the right-hand side of this equation that, at a given radial extent of ice r_m, all the four deglaciation-rate scenarios have the same k-dependent profile of $\mathcal{H}_0[\dot{h}](k,t)$. The only difference between the scenarios is that the magnitudes of $\mathcal{H}_0[\dot{h}](k,t)$ are scaled differently by different values of $\dot{V}(t)$ in front of the square brackets. Hence, the same spectral distribution of $\mathcal{H}_0[\dot{h}](k,t)$ in the k-space of all the scenarios (even though the magnitude scaling factors are different) will give the same spatial profile of $\frac{DP}{Dt}$ with the same vertical and horizontal length scales (e.g the penetration depth and the horizontal extent of the decompression rate field). This means that, given the same radial extent of ice r_m (i.e. same horizontal coordinates (x-axis) on the glacier terminus line (thick black line) in Figure 7.3), the spatial distributions of $\frac{DP}{Dt}$ in all the four scenarios will be the same.

The spatial distribution of $\frac{DP}{Dt}$ controls the average melting depth (which controls the average La concentrations in the melts, and hence the La concentrations of the La-depleted band seen in Figure 7.3) and the horizontal extent of the high-melting-rate region (which controls the horizontal extent of the region of La-depleted melt production, and hence the width of the La-depleted band seen in Figure 7.3). Since, at a given glacier terminus location r_m, all the four deglaciation-rate scenarios have the same spatial distribution of $\frac{DP}{Dt}$, the La-depleted bands around the glacier terminus line of all the scenarios in Figure 7.3 are about the same.

In Figure 7.3, there is also a yellow-orange-red band of La-enriched lava in the subaerial portion. This La-enriched band is caused by the down-welling flow of the mantle outside the ice coverage region due to the isostatic adjustment. This down-welling flow is the strongest at shallow depths. Hence, it suppresses melting in the shallow (La-depleted) mantle. As a result, the average La concentration in the melt

produced is enriched. The faster the deglaciation, the faster the down-welling flow and the more the La enrichment in the melt.

The average La concentration $\bar{c}_{\rm ep}$ in the early-postglacial lava is the ratio of the early-postglacial mass of La to the early-postglacial mass of melts. The early-postglacial La and melts masses can be obtained by integrating the mass fluxes of La ($\dot{M}_{\rm La}$) and of melts ($\dot{M}$) over the early-postglacial time period. i.e. $\bar{c}_{\rm ep}$ as a function of the radial distance $r_{\parallel}$ from the ice center along the ridge axis is:

$$\begin{aligned}\bar{c}_{\rm ep}(r_{\parallel}) &= \frac{\int_{t_1}^{t_2} \dot{M}_{\rm La}(r_{\parallel},t)\,{\rm d}t}{\int_{t_1}^{t_2} \dot{M}(r_{\parallel},t)\,{\rm d}t} \\ &= \frac{\int_{t_1}^{t_2} \dot{V}_{\rm La}(r_{\parallel},t)\,{\rm d}t}{\int_{t_1}^{t_2} \dot{V}(r_{\parallel},t)\,{\rm d}t}\end{aligned}$$

where the lower limit of integration $t_1 = t_1(r_{\parallel})$ is the time when the location $r_{\parallel}$ transition from subglacial into subaerial. $t_1(r_{\parallel})$ is equal to the time when the glacier terminus is at $r_{\parallel}$. The upper limit of integration t_2 is the time when the mass fluxes have returned back to the steady-state values because we are interested in La concentrations of lavas erupted when the eruption rates are still elevated (i.e. early-postglacially). On the second line of this equation gives an expression in terms of volume fluxes, where the volume fluxes of La and of melts are defined by $\dot{V}_{\rm La}(r_{\parallel},t) = \frac{1}{\rho_f}\dot{M}_{\rm La}(r_{\parallel},t)$ and $\dot{V}(r_{\parallel},t) = \frac{1}{\rho_f}\dot{M}(r_{\parallel},t)$ respectively. We plot $\bar{c}_{\rm ep}$ (normalized to the steady-state value) against $r_{\parallel}$ for different presumed values of melt ascent velocity in Figure 7.4.

Figure 7.4a shows the results when the melt transport is assumed to be instantaneous. In this case, the eruption rate is equal to the mantle melting rate. We have discussed why, in Figure 7.3, the blue La-depleted bands around the glacier terminus path (thick black line) in all the four scenarios are about the same. The similarity of the blue La-depleted bands in Figure 7.3 explains why, in Figure 7.4a, $\bar{c}_{\rm ep}(r_{\parallel})$ profiles of all the scenarios at intermediate $r_{\parallel}$ are about the same.

We also have discussed about how the down-welling flow of the mantle outside the region below the ice coverage causes the La-enriched (yellow-orange-red) band in Figure 7.3. This down-welling flow effect results in a slight elevation of $\bar{c}_{\rm ep}$ at $r_{\parallel}$ near 300 km in Figure 7.4a. Different scenarios have different magnitudes of the down-welling flow and hence different magnitudes of mantle melting suppression at shallow (La-depleted) depths. This results in slightly different magnitudes of $\bar{c}_{\rm ep}$ elevation in different deglaciation-rate scenarios.

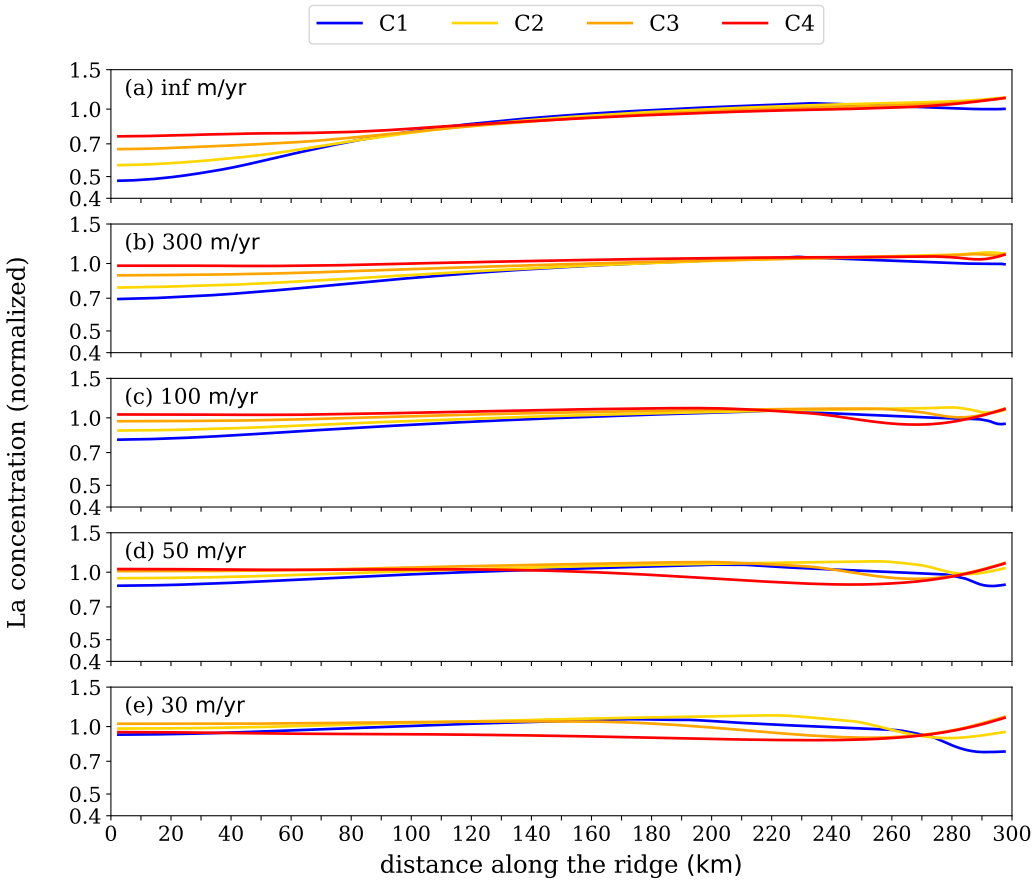

Fig. 7.4 Average La concentrations in early-postglacial lavas at different locations along the ridge axis. Each panel corresponds to a presumed value of melt ascent velocity as labelled on the upper-left corner of the panel. Different line colors correspond to different deglaciation scenarios as labelled on top of the figure. The ice volume history of each of the scenarios is shown in Figure 7.2 with the same color code.

The region near the ice center (at $r_{\|}$ around 0 km) is different from elsewhere in that it becomes subaerial not long before the deglaciation ends. Hence, the majority of the subaerial lavas in the $r_{\|} \approx 0$ region comes from mantle melting during the postglacial rebound. The postglacial rebound is due to the finite response time (τ) of the mantle flow to the change of the unloading of ice.

Figure 7.4a at $r_{\|}$ near 0 km shows that different deglaciation rates result in different La concentrations in the early-postglacial lavas. This feature can be explained as follows. The GIA decompression in the deep mantle is produced by long-wavelength (long-λ) components of the mantle flow due to their long attenuation depths (whereas,

shorter wavelength components are attenuated more rapidly with depth). These long-λ components are induced by the deglaciation during when the ice sheet is large at around the beginning of the deglaciation (with λ of the order of the horizontal extent of the ice sheet). At a lower deglaciation rate (i.e., slower deglaciation), the time interval Δt between when the ice sheet is large and the early-postglacial period is longer (i.e., larger Δt for a slower deglaciation scenario). A larger Δt means that the long-λ components decay more significantly over the time interval Δt. While the long-λ components have significantly decayed, the short-λ components still remain elevated due to their larger decay time constant $\tau = \frac{4\pi}{\rho_s g \lambda}$ (larger τ for a smaller λ). Hence, for a slower deglaciation scenario (larger Δt), the GIA decompression rate in the deep mantle during the early-postglacial period is dropped more significantly relative to the decompression rate in the shallow mantle. A smaller decompression rate in the deep La-enriched mantle means that the average La concentration in the instantaneous melt produced is less. Therefore, a slower deglaciation results in a less La-enriched (i.e., more La-depleted) early-postglacial lavas at near the center of the ice as seen in Figure 7.4a. We provide a more detailed explanation of this postglacial rebound effect in Section 7.5.1.

At a finite rate of melt ascent, there is a time lag between the surface arrivals of the shallow-depth-produced melts and the deep-depth-produced melts. This time lag causes different amounts of melts to erupt subglacially/subaerially from what would be if the melt transport were instantaneous. At near the ice center, for example, La-enriched melts produced at deep depths just before the deglaciation ends will erupt after the ice has gone if the melt transport is sufficiently slow. The slower the melt transport, the more the time lag and hence the more the La-enriched melts produced at deep depths just before the ice is gone (that would have erupted *subglacially* if the melt transport had been instantaneous) will erupt *subaerially* after the ice is gone. This will cause a more La enrichment (=less La depletion) in the early-postglacial lavas as can be seen in Figures 7.4b-e at near $r_{\|} = 0$ where the La concentrations are increased from that of the instantaneous melt transport case in Figure 7.4a.

Isochrons of cumulative lava volumes (similar to Figure 7.3) predicted by the model at melt ascent velocities of 100 and 30 m/yr are plotted in Figures 7.5 and 7.6 respectively. By comparing these two figures with Figure 7.3, we can see that a slower rate of melt ascent results in smaller subglacial volumes and higher La concentration variations as seen in Chapter 5.

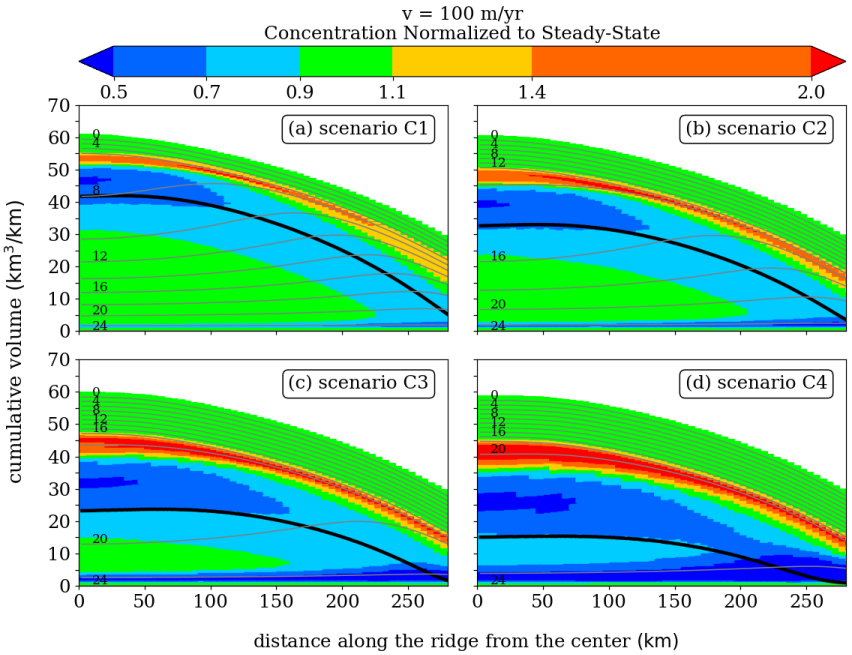

Fig. 7.5 Same as Figure 7.3 but with the melt ascent velocity of 100 m/yr.

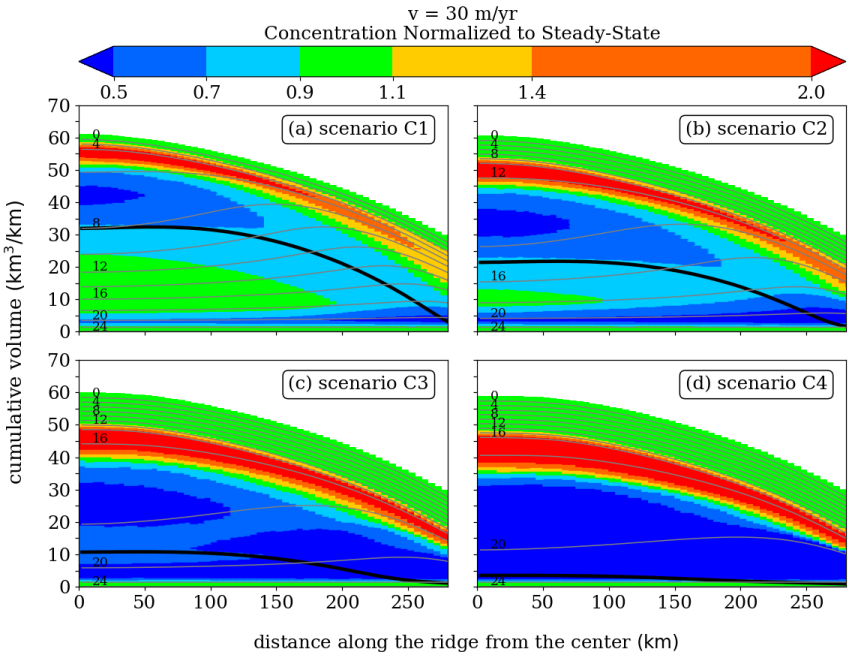

Fig. 7.6 Same as Figure 7.3 but with the melt ascent velocity of 30 m/yr.

7.3.2 Deglaciation Pause

In this section, we study the effect of a deglaciation pause on the La content of the early-postglacial lavas. The model is run with five different prescribed deglaciation-pause durations at the same ice radius of 180 km. The ice volume versus time of each of the scenarios is plotted in Figure 7.7.

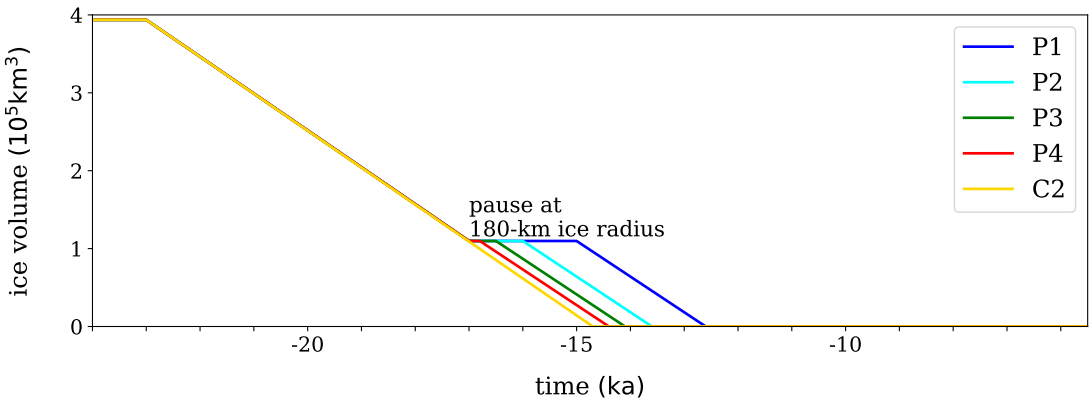

Fig. 7.7 The modelling-input ice volume histories of five different deglaciation-pause scenarios (shown as different line colors) with the same initial ice thickness profile (300 km radius, 1.39 km average thickness and 3.93×10^5 km^3 volume) and the same timing of the onset of deglaciation at $t = -23$ kyr ($= 23$ kyrBP). During the deglaciation, the ice volume loss rates in all the scenarios are the same. The name of each of the five scenarios (P1, P2, P3, P4 and C2) is as labelled on the upper-right corner in the descending order of the deglaciation-pause durations, where P stands for "pause" and C stands for "continuous" (i.e. no pause). The C2 scenario here is the same as that in Section 7.3.1 (Figure 7.2). The pause begins at time $t = -17.0$ kyr ($= 17.0$ kyrBP) at 180 km ice radius. The pause durations of the scenarios P1, P2, P3 and P4 are 2.0-, 1.0-, 0.5- and 0.2-kyr long respectively. The ice volumes go to zero at $t = -12.6$, -13.6, -14.1, -14.4 and -14.7 kyr for the P1, P2, P3, P4 and C2 scenarios respectively.

Outside the pause period, these five scenarios have the ice volume decreasing linearly with time at the same rate. Similar to Section 7.3.1, the deglaciation begins at time $t = -23$ kyr ($= 23$ kyrBP) with all the scenarios having the same initial ice sheet profile (same volume, radial extent and thickness). The names of the P1, P2, P3 and P4 scenarios are in the descending order of the pause durations (P1/P4 has the longest/shortest pause) as shown on the Figure. "P" stands for "pause", which refers to the deglaciation pause. Scenario C2 is the same as that in Section 7.3.1 (Figure 7.2). C2 has no pause, but it has the same ice volume loss rate as P1, P2, P3 and P4.

We plot the La concentration $\bar{c}_{\mathrm{ep}}$ of early-postglacial lavas (normalized to the steady-state value) as a function of $r_{\parallel}$ at different presumed values of melt ascent velocity in Figure 7.8 (see how $\bar{c}_{\mathrm{ep}}(r_{\parallel})$ is calculated in Section 7.3.1). Figure 7.8a shows the results when the melt transport is assumed to be instantaneous. In this case, the eruption rate is equal to the mantle melting rate. Away from where the glacier terminus pauses (at $r_{\parallel} = 180$ km), La concentrations in the early-postglacial lavas in all the scenarios are about the same due to the same deglaciation rates.

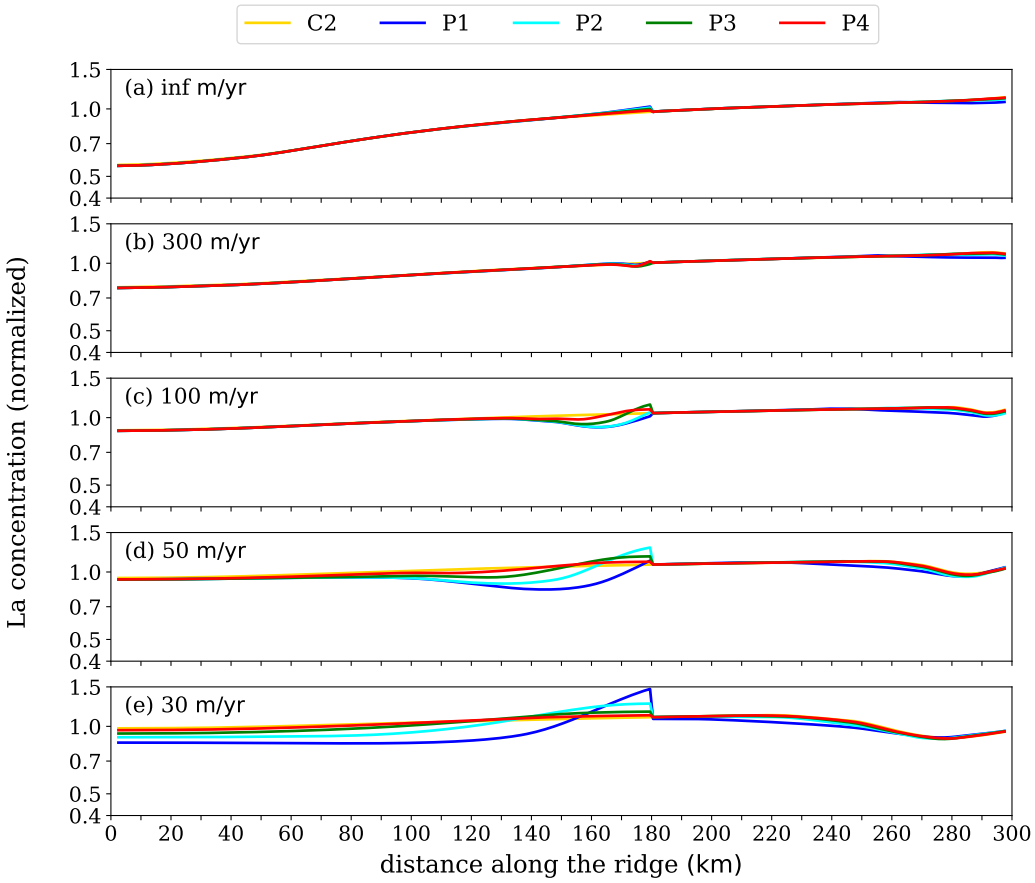

Fig. 7.8 See caption of Figure 7.4. The ice volume history of each of the scenarios is shown in Figure 7.7 with the same color code.

During the pause, the mantle up-welling still proceeds due to the finite response time τ of the mantle flow. This is similar to the postglacial rebound effect in Section 7.3.1 that the mantle up-welling produces La-depleted melts (as seen in Figure 7.4a at around $r_{\parallel} = 0$ and as mathematically justified in Section 7.5.1). Just inside where

the glacier terminus pauses (at just on the left of $r_{\|} = 180$ km), the La-depleted melts produced by the "postglacial rebound" erupt subglacially because this region is inside the ice coverage at 180 km during the pause. This means that the La-depleted melts (that would have erupted subaerially if there were no pause) have been "lost" to the subglacial eruptions. Since all the deglaciation scenarios have the same unloading profile of ice (=*initial* minus *final* ice-load profile $= h_0(r) - 0$), they have the same spatial distribution of the net pressure drop $-\Delta P_{\text{net}}$ and hence the same net masses of produced melts and La partitioned into melts (see Section 7.5.2 for mathematical justification). The "loss" of the La-depleted melts from the subaerial to the subglacial portion means that the subaerial portion gets La-enriched. This explains why we see a slight La enrichment in Figure 7.8a just inside $r_{\|} = 180$ km.

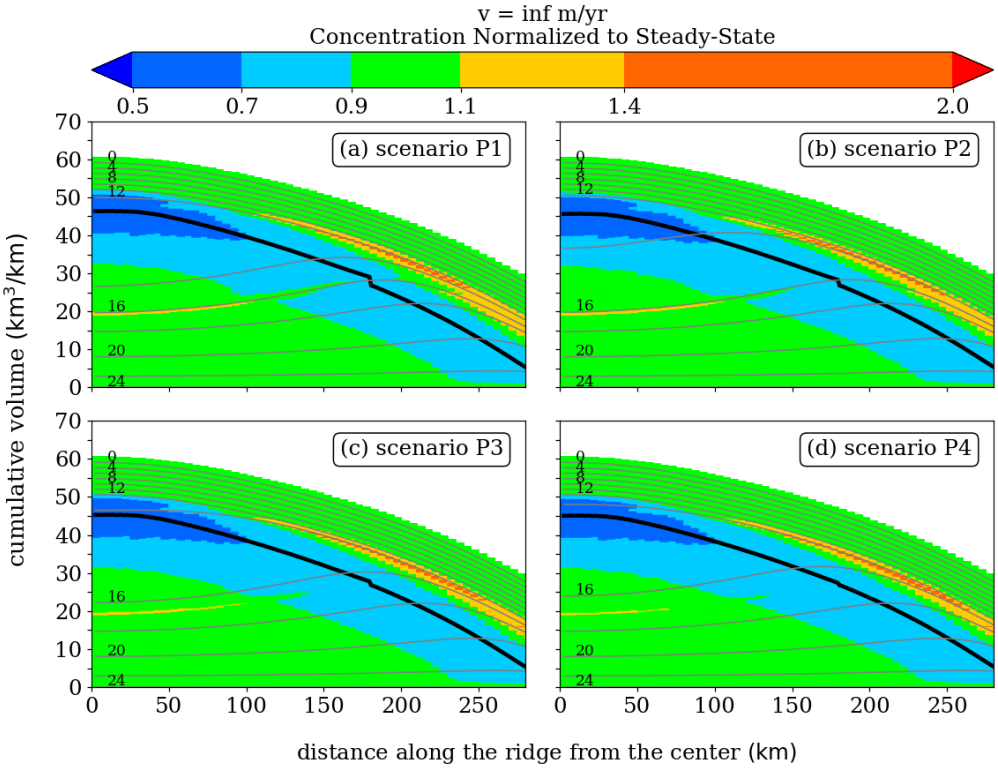

Fig. 7.9 Same as Figure 7.3 but with the P1, P2, P3 and P4 deglaciation scenarios.

At a finite rate of melt ascent, there is a time lag between the surface arrivals of the shallow-depth-produced melts and the deep-depth-produced melts. This time lag causes different amounts of melts of different La concentrations to erupt subglacially/subaerially from what would be if the melt transport were instantaneous.

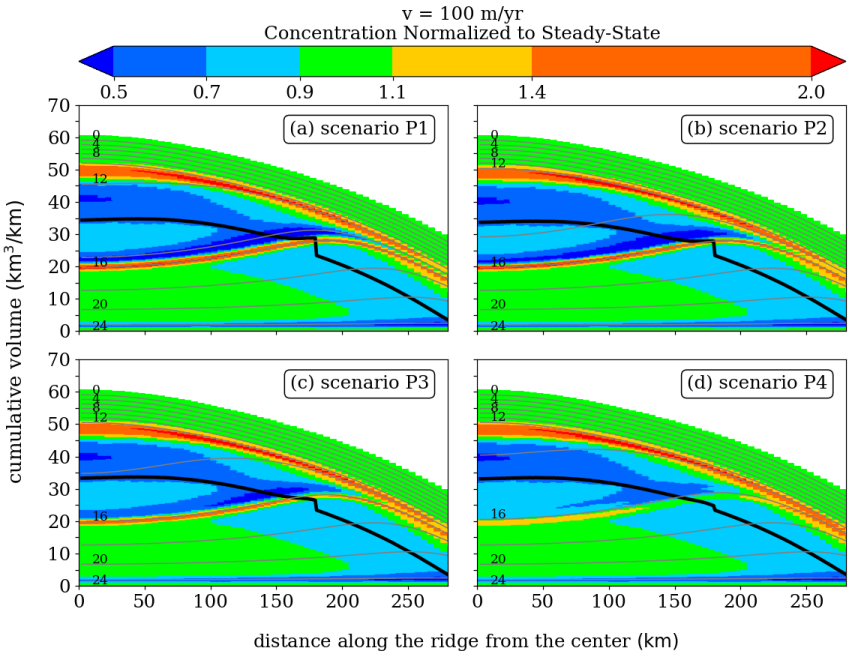

Fig. 7.10 Same as Figure 7.9 but with the melt ascent velocity of 100 m/yr.

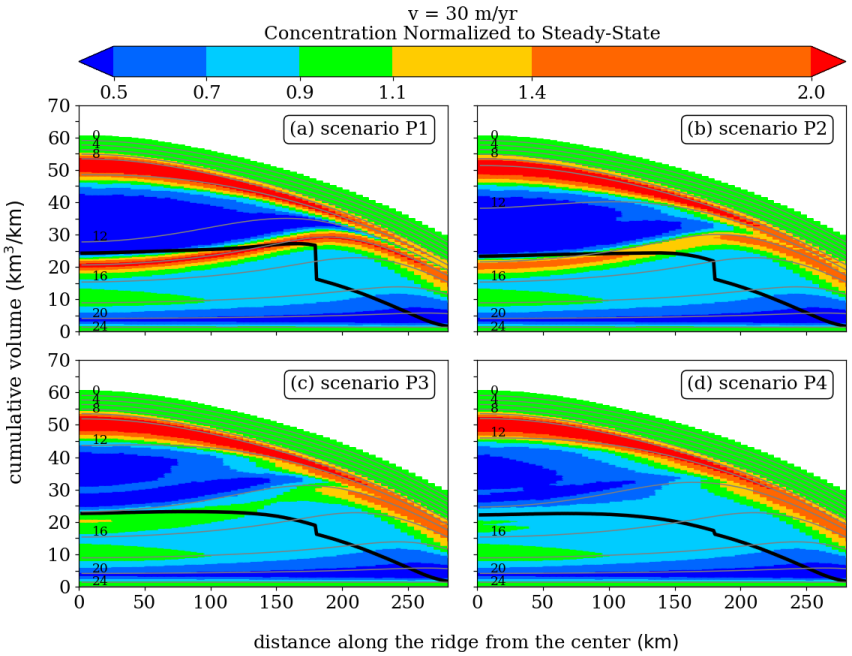

Fig. 7.11 Same as Figure 7.9 but with the melt ascent velocity of 30 m/yr.

Over the pause duration Δt_{pause}, melts will have ascended over a vertical distance of $d = v_f \, \Delta t_{\text{pause}}$ where v_f is the melt ascent velocity. At appropriate values of v_f and Δt_{pause} such that $v_f \, \Delta t_{\text{pause}} \sim 50$ km ($\sim$ one half of the primitive solidus depth), the shallow-depth-produced melts will erupt subglacially while the deep-depth-produced melts will erupt subaerially. This will further enrich the La concentrations in the early-postglacial lavas erupted just inside $r_{\parallel} = 180$ km where the glacier terminus pauses. As can be seen in Figures 7.8c-e, in each panel (of a given v_f), the scenario that has the highest peak La concentration is the one that has Δt_{pause} that satisfies the condition $v_f \, \Delta t_{\text{pause}} \sim 50$ km. i.e. in Figure 7.8c/d/e where $v_f = 100/50/30$ m/yr, the scenario P3/P2/P1 with a pause duration of 500/1000/2000 years (so that $v_f \, \Delta t_{\text{pause}} \sim 50$ km) has the highest peak La concentration.

Isochrons of cumulative lava volumes (similar to Figures 7.3, 7.5 and 7.6) predicted by the model for the P1, P2, P3 and P4 scenarios at melt ascent velocities of ∞, 100 and 30 m/yr are plotted in Figures 7.9, 7.10 and 7.11 respectively. The step jump of the thick black line at $r_{\parallel} = 180$ km is due to the deglaciation pause. By comparing these three Figures together, we can see that a slower rate of melt ascent results in smaller subglacial volumes and higher La concentration variations as in Chapter 5.

7.4 Model versus Observations

Previous studies (Denton et al., 2010; Marino et al., 2015) show that, while the last glacial termination (T-I) has at least a pause of ∼ 2-kyr long between the Heinrich stadial 1 (HS 1 at ∼ 18.0–14.7 kyrBP) and the Younger Dryas (YDS at ∼ 12.8–11.5 kyrBP), the penultimate glacial termination (T-II) is a continuous deglaciation that overlaps the Heinrich stadial 11 (HS 11 at ∼ 135–130 kyrBP) without a pause. However, the duration over which the Icelandic deglaciation during T-II took place is not well-constrained. Regarding this uncertainty, we therefore assume in our model that the ice volume during T-II can be approximated as a linearly decreasing function in time similar to the C1-4 scenarios in Section 7.3.1. Figure 7.12 plots the ice volume histories of the C1-4 scenarios together with the T1 scenario, which is the model ice volume for T-I (same as in Chapter 5).

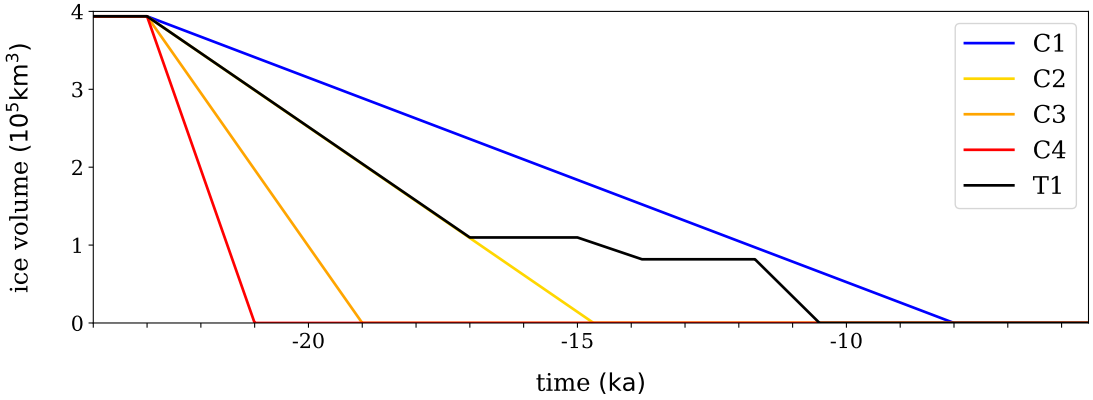

Fig. 7.12 Same as Figure 7.2 but with the T1 deglaciation scenario for the Termination I (T-I), which follows the deglaciation history in Chapter 4.

The model results of the Zr/Y and Nb/Y concentration ratios (which behave similarly to the La concentrations discussed in Section 7.3 but with the crystallization effect already been removed) are shown in Figures 7.13 and 7.14 respectively. With instantaneous melt transport, Figures 7.13a and 7.14a show that the deglaciation pauses in T1 scenario at the ice radius of 180 and 160 km lead to slight IEM enrichment in the early-postglacial lavas (black curve) at just inside where the glacier terminus pauses at 180 and 160 km similar to the slight La enrichment in Figure 7.8a at just inside 180 km.

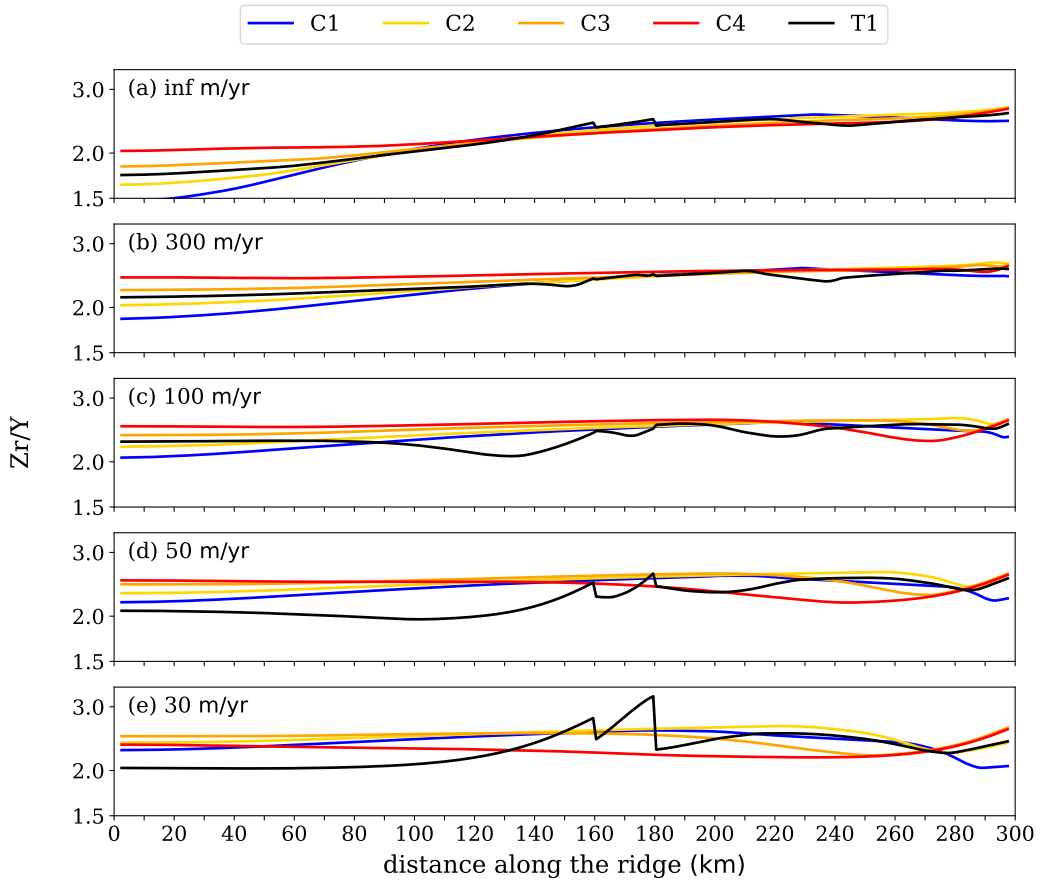

Fig. 7.13 Similar to Figure 7.4 but the y-axis is now the Zirconium to Yttrium (Zr/Y) concentration ratio and also with the model results of the T1 deglaciation scenario (black line) included. The ice volume history of each of the scenarios is shown in Figure 7.12 with the same color code.

At a finite rate of melt ascent, however, there is a time lag between the eruption of melts produced at shallow depths (IEM-depleted) and that produced at deep depths (IEM-enriched). When the deglaciation has no pause, the IEM-enriched melts from deep depths will erupt postglacially; whereas, if the deglaciation has a pause, some of the IEM-enriched melts may erupt subglacially if the pause duration is sufficiently long for IEM-enriched melts from deep depths to arrive at the surface when the ice is still present. For example, at 100 m/yr melt ascent velocity, it takes ~ 1.3 kyr for IEM-enriched melts from the deepest depth of the melting region (~ 131-km depth) to travel to the surface. The two pauses of the T1 scenario of 2.0- and 2.1-kyr long are longer than the 1.3-kyr threshold, meaning that both pauses are long enough to

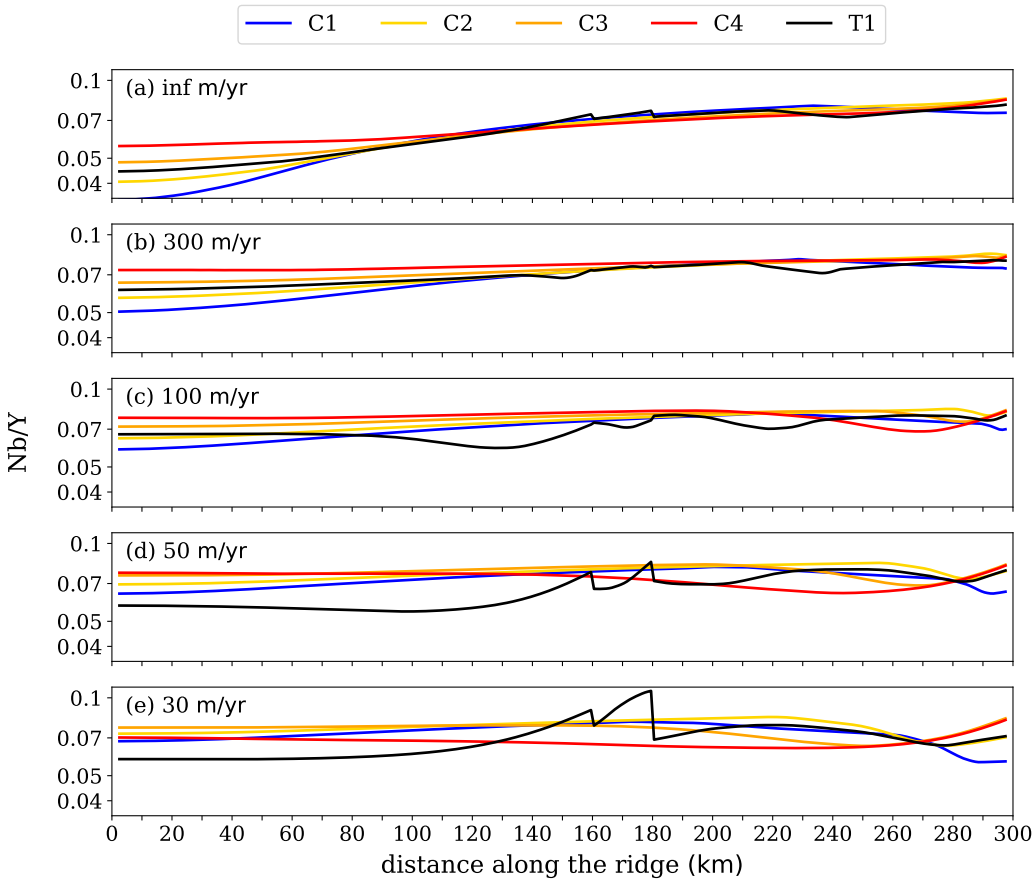

Fig. 7.14 Similar to Figure 7.13 but the y-axis is now the Niobium to Yttrium (Nb/Y) concentration ratio.

"trap" eruptions of the IEM-enriched melts in the subglacial condition. As a result, at 100 m/yr melt ascent velocity (Figures 7.13c and 7.14c), early-postglacial lavas in the T1 scenario are IEM-depleted relative to that in the C1-4 scenarios due to the loss of the IEM-enriched melts to the subglacial portion caused by the "pause trap".

In contrast, at 30 m/yr melt ascent velocity, it takes $\sim$ 4.4 kyr for IEM-enriched melts from the 131-km depth to travel to the surface. Therefore, the two pauses of the T1 scenario for 2.0 and 2.1 kyr are not long enough to trap the IEM-enriched melts in the subglacial condition. Both pauses only trap IEM-depleted melts that are produced at the top half of the melting region. As a result, at 30 m/yr melt ascent velocity (Figures 7.13e and 7.14e), the two pauses of the T1 scenario enrich IEMs in the early-postglacial lavas.

At our preferred melt ascent velocity of 100 m/yr (as estimated in Chapter 5), Figures 7.13c and 7.14c indicate that the C1 scenario relative to T1 (blue curve relative to black curve) has Zr/Y and Nb/Y profiles that are similar to the observational T-II concentration ratios relative to T-I (blue circles relative to black triangles in Figure 7.1). Within the radial distance ($r_{\parallel}$) of ~ 80 km from the ice center, Figures 7.13c and 7.14c show that the C1 scenario (blue curve) is IEM-depleted relative to T1 (black curve). This is similar to the observations in Figures 7.1b&c where the blue circles (Vaðalda and Herðubreiðartögl lava shields) are below the black triangles (trölladyngja and Kollóttadyngja lava shields). In addition, at $r_{\parallel}$ between 140–180 km, Figures 7.13c and 7.14c show that the C1 scenario (blue curve) is IEM-enriched relative to T1 (black curve), which is also seen in the observations in Figures 7.1b&c where the blue circles (Jörundargrjót and Grjóthváls lava shields) are above the black triangle (Stóravíti lava shield).

We note that, in Figures 7.13c and 7.14c at $r_{\parallel} > 90$ km, any of the four modelled continuous deglaciation scenarios (C1-4) relative to the T1 scenario can explain the IEM depletion of the T-I lava shields relative to the T-II lava shields because the IEM depletion is due to the deglaciation pauses in the T1 scenario and no pause in any of the C1-4 scenarios. Whereas, at $r_{\parallel} < 80$ km, the IEM depletion of the T-II lava shields relative to the T-I lava shields can only be explained by the model scenario C1. This is because the IEM contents of lava shields erupted at $r_{\parallel} < 80$ km are determined by the postglacial rebound effect discussed in Section 7.3.1. It is required for the T-I deglaciation rate post Younger Dryas (post ~ 12 kyrBP) to be higher than that of the T-II in order for the T-I lava shields to be IEM-enriched relative to T-II. i.e., for the model, the T1 ice volume curve in Figure 7.12 (black curve) after ~ -12 kyr needs to be steeper than that of the C1 (blue curve).

In summary, the model results in comparison with the observations present the possibilities that

1. the IEM depletion in the T-I lava shields at $r_{\parallel} = 140$–180 km relative to the adjacent T-II lava shields is due to the deglaciation pauses during T-I but no pause during T-II.

2. the IEM enrichment in the T-I lava shields at $r_{\parallel} < 80$ km relative to the adjacent T-II lava shields is due to a higher deglaciation rate post Younger Dryas relative to that during T-II.

Nevertheless, the IEM enrichment of the T-I lava shields at $r_{\parallel} < 80$ km relative to the adjacent T-II lava shields does not imply that the *overall average* deglaciation rate of T-II has to be lower than that of T-I. For example, if the actual deglaciation rate post Younger Dryas is higher than our presumed value in the modelled T1 scenario, the IEM contents of the T1 scenario at $r_{\parallel} < 80$ km (black curve in Figures 7.13c and 7.14c) can be increased to above the C2 scenario (yellow curve in Figures 7.13c and 7.14c). If this is the case, it will also be possible for the C2 scenario (which has a higher overall deglaciation rate than the T1 scenario) to explain the IEM depletion of the T-II lava shields at $r_{\parallel} < 80$ km relative to the adjacent T-I lava shields.

The modelled IEM contents of the T1 scenario at $r_{\parallel} < 80$ km may also be further increased by increasing the ice thinning rate at near the ice center during when the ice radius is still large. This will accelerate the production rate of IEM-depleted melts at around the ice center during when the ice sheet is still large, meaning that there will be more IEM-depleted melts to erupt subglacially at around the ice center. Hence, by the conservation of the total IEM masses in the melts produced (as discussed in Section 7.3 and also as justified mathematically in Section 7.5.2), a greater "loss" of IEM-depleted melts to the subglacial portion at near the ice center will result in IEM enrichment in the early-postglacial lavas near the ice center.

We also note that, although the model can qualitatively explain the geological observations, the quantitative results are still not quite fit. This is due to many reasons including the mismatch of the modelled and the actual IEM contents in the mantle source (here we use the bi-lithological source of Rudge et al. (2013)), and also, the Icelandic mantle plume (which we do not include in the model). Previous studies (Maclennan et al., 2001; Shorttle et al., 2010) have shown that the mantle plume can significantly affect the geochemistry of the lavas, especially at within the 100 km radial distance from the plume center. One of our future developments is to incorporate the mantle plume into the model.

7.5 Analysis

7.5.1 Postglacial Rebound Effect

Suppose that the deglaciation takes place between time t_0 and $t_0 + \Delta t$. The increase of the degree of melting at a location in the mantle after the deglaciation (postglacial) $= \Delta F_{\text{post}}$ will be the time integration of the melting rate $\frac{DF}{Dt}$ from the end of the deglaciation at time $t = t_0 + \Delta t$ to ∞. ΔF_{post} is a function of the spatial coordinates (r, z) and is independent of time.

The total melt volume produced postglacially is the spatial integration of ΔF_{post} over the whole melting region in the mantle, each depth of which has a different La concentration. Therefore, the average La concentration in the postglacial melts is controlled by the depth-dependent profile of ΔF_{post}. In this section, we analyse how different rates of deglaciation can affect the z-dependence of ΔF_{post} in order to understand why, at a higher deglaciation rate, the postglacial melt produced near the axis of the ice sheet (as seen in Figure 7.4a at $r_{\|} = 0$) is less depleted in La than in another scenario of a lower deglaciation rate.

We note that the analysis below only applies to the region near the axis of the ice sheet ($r_{\|} \approx 0$) because, at $r_{\|}$ further away from 0, the transition of the Earth's surface from subglacial to subaerial occurs before the deglaciation ends (i.e. subaerial begins before "postglacial", or, more precisely, "post-deglaciation"). Hence, the time integration from time $t = t_0 + \Delta t$ to ∞ will not include all the subaerial melts. It will only give the sum of the "post-deglaciation" melts because time $t = t_0 + \Delta t$ corresponds to when the deglaciation ends, not when the surface becomes subaerial. On the other hand, near $r_{\|} = 0$, the deglaciation ends as soon as the Earth's surface becomes subaerial. In this case, the "post-deglaciation" melt volume is about the same as the subaerial melt volume.

Since $\frac{DF}{Dt}$ is proportional to the decompression rate $-\frac{DP}{Dt}$, ΔF_{post} is proportional to the total postglacial pressure drop $-\Delta P_{\text{post}}$, which is equal to the time integration of $-\frac{DP}{Dt}$ from the end of the deglaciation at time $t = t_0 + \Delta t$ to ∞. i.e. $\Delta F_{\text{post}} \propto -\Delta P_{\text{post}} = -\int_{t_0+\Delta t}^{\infty} \frac{DP}{Dt}\, \mathrm{d}t$. From equation (2.45), $-\frac{DP}{Dt}$ consists of two terms:

1. $-\dot{P}_1(\boldsymbol{x}, t) = \rho_i g\, \mathcal{H}_0^{-1}\left[e^{kz}\left(\mathcal{H}_0[-\dot{h}](k,t)\right)\right]$
   is the instantaneous response to the deglaciation $-\dot{h}(r,t)$.

2. $-\dot{P}_2(\boldsymbol{x}, t) = \rho_i g\, \mathcal{H}_0^{-1}\left[e^{kz}\,(kz\,\widetilde{w}(k,t))\right]$
   is the rebound response to the deglaciation.

Definition of all the variables can be found at the end of equation (2.45).

In the $-\dot{P}_1$ term, $\mathcal{H}_0[-\dot{h}](k,t)$ is the zeroth-order Hankel transform of the ice thickness loss rate $-\dot{h}(r,t)$ along the radial coordinates r at a constant t. It decomposes the spatial profile of $-\dot{h}(r)$ (at a fixed t) into components of spatial frequencies k. The zeroth-order inverse Hankel transform operation $\mathcal{H}_0^{-1}$ then sums all the k components inside the square brackets back together. It transforms functions from the k space back to the r space.

Suppose, for simplicity, that the ice thickness decreases linearly with time. $-\dot{h}(r,t)$ and hence $\mathcal{H}_0[-\dot{h}](k,t)$ will simply be Top-Hat functions in the temporal space. These Top-Hat functions have width $= \Delta t$ in the temporal space since we previously defined the deglaciation to take place from time t_0 to $t_0 + \Delta t$. The instantaneous response term $-\dot{P}_1$ at a fixed location (r,z) in the mantle will also be a Top-Hat function with width $= \Delta t$ in the temporal space. Figure 7.15a illustrates the Top-Hat function $-\dot{P}_1(t)$.

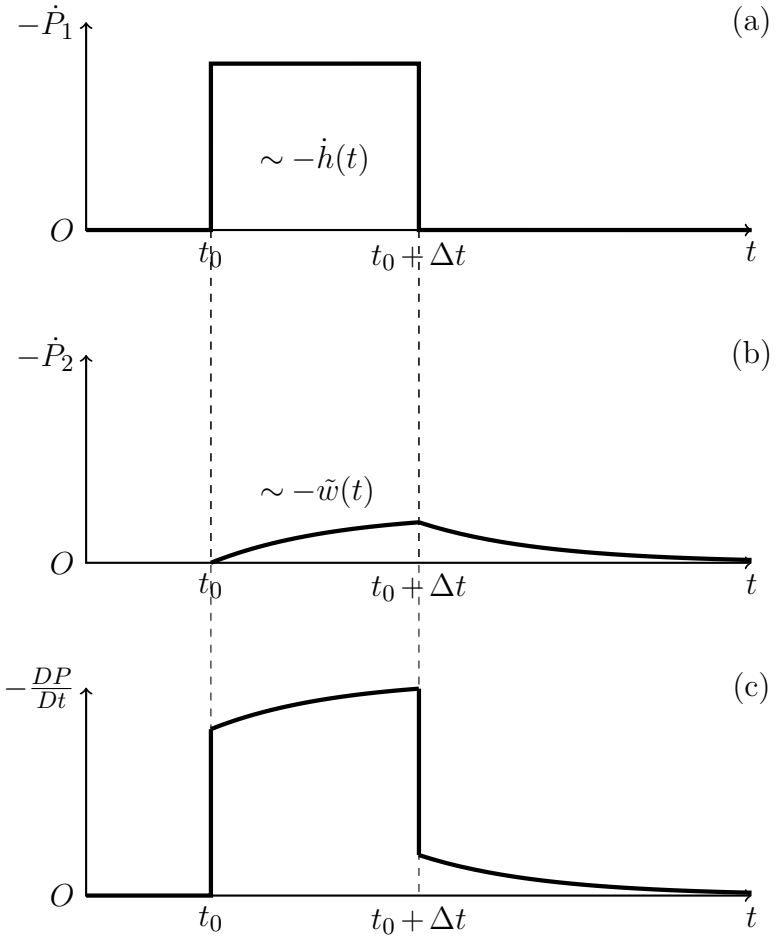

Fig. 7.15 Time dependence of the decompression rates at a fixed location in the mantle at a constant k.

Similar to the $-\dot{P}_1$ term, the $\mathcal{H}_0^{-1}$ operation in the $-\dot{P}_2$ term sums all the k components of the function inside the square bracket. $\widetilde{w}(k,t)$ is the temporal-convolution of $\mathcal{H}_0[\dot{h}](k,t)$ with an exponential decay function with time constant $\tau = \frac{2\eta k}{\rho_s g}$. This is equivalent to applying a low-pass filter with cut-off frequency $= 1/\tau$ on $\mathcal{H}_0[\dot{h}](k,t)$. Components of $\mathcal{H}_0[\dot{h}](k,t)$ with temporal frequencies higher than $1/\tau$ are attenuated by the low-pass filter.

Figure 7.15b illustrates the temporal profile of the function $-\widetilde{w}(k,t)$ in the case where $\mathcal{H}_0[-\dot{h}](k,t)$ is a Top-Hat function (as in Figure 7.15a). The rapid changes of $\mathcal{H}_0[-\dot{h}](k,t)$ at the two steps at the onset ($t = t_0$) and the end ($t = t_0 + \Delta t$) of the deglaciation consist of terms with frequencies higher than $1/\tau$. Hence, they are significantly attenuated. The low-pass filter transforms these steps into exponential decay functions with time constant $\tau = \frac{2\eta k}{\rho_s g}$.

The sum of $-\dot{P}_1$ and $-\dot{P}_2$ gives the net decompression rate $-\frac{DP}{Dt}$ in the mantle induced by the Top-Hat deglaciation rate. Figure 7.15c, which is the sum of Figures 7.15a and 7.15b, plots the temporal dependence of $-\frac{DP}{Dt}$ against time at a fixed location in the mantle at one k component.

Let the zeroth-order Hankel transform of the ice thickness profile before the deglaciation be $\mathcal{H}_0[h_0](k) = \tilde{h}_0(k)$, where inside the square brackets is the initial ice thickness profile $h_0 = h_0(r) = h(r, t < t_0)$. The height of the Top-Hat function $\mathcal{H}_0[-\dot{h}](k,t)$ will then be $= \tilde{h}_0/\Delta t$. That is,

$$\mathcal{H}_0[-\dot{h}](k,t) = \begin{cases} \frac{\tilde{h}_0(k)}{\Delta t}, & t_0 \le t \le t_0 + \Delta t, \\ 0, & \text{otherwise.} \end{cases} \tag{7.1}$$

From equation 2.45,

$$\widetilde{w}\,(k,t) = -\int_{t_{\text{iso}}}^{t} \left(\mathcal{H}_0[-\dot{h}](k,t')\right) \exp\left(-\frac{t-t'}{\tau}\right) \mathrm{d}t'/\tau.$$

Using the Top-Hat function $\mathcal{H}_0[-\dot{h}](k,t)$ from equation (7.1), we obtain

$$\tilde{w}(k,t) = \begin{cases} 0, & t < t_0, \\ -\frac{\tilde{h}_0(k)}{\Delta t}\left[1 - \exp\left(-\frac{t-t_0}{\tau}\right)\right], & t_0 \le t < t_0 + \Delta t, \\ -\frac{\tilde{h}_0(k)}{\Delta t}\left[\exp\frac{\Delta t}{\tau} - 1\right]\exp\left(-\frac{t-t_0}{\tau}\right), & t \ge t_0 + \Delta t. \end{cases} \tag{7.2}$$

Now, we can calculate the total postglacial pressure drop:

$$\begin{aligned}-\Delta P_{\text{post}} &= -\int_{t_0+\Delta t}^{\infty} \frac{DP}{Dt}\,\mathrm{d}t \\ &= \rho_i g\,\mathcal{H}_0^{-1}\left[e^{kz}\left(\int_{t_0+\Delta t}^{\infty}\mathcal{H}_0[-\dot{h}](k,t)\,\mathrm{d}t + kz\int_{t_0+\Delta t}^{\infty}\widetilde{w}(k,t)\,\mathrm{d}t\right)\right].\end{aligned}$$

The first term inside the round brackets $\int_{t_0+\Delta t}^{\infty}\mathcal{H}_0[-\dot{h}](k,t)\mathrm{d}t$ is zero because the ice thickness loss rate $\mathcal{H}_0[-\dot{h}](k,t)$ is zero for postglacial ($t > t_0+\Delta t$) (see equation (7.1)). The second term inside the round brackets $kz\int_{t_0+\Delta t}^{\infty}\widetilde{w}(k,t)\,\mathrm{d}t$ is non-zero due to the postglacial rebound in the mantle. This term can be evaluated using equation (7.2):

$$\begin{aligned}\int_{t_0+\Delta t}^{\infty}\widetilde{w}(k,t)\,\mathrm{d}t &= -\frac{\tilde{h}_0(k)}{\Delta t}\left[\exp\frac{\Delta t}{\tau}-1\right]\int_{t_0+\Delta t}^{\infty}\exp\left(-\frac{t-t_0}{\tau}\right)\mathrm{d}t \\ &= -\tilde{h}_0(k)\,\frac{\tau}{\Delta t}\left[1-\exp\left(-\frac{\Delta t}{\tau}\right)\right].\end{aligned}$$

Hence, the postglacial pressure drop is

$$-\Delta P_{\text{post}} = \rho_i g\,\mathcal{H}_0^{-1}\left[-kz\,e^{kz}\,\tilde{h}_0(k)\,\frac{\tau}{\Delta t}\left(1-\exp\left(-\frac{\Delta t}{\tau}\right)\right)\right].$$

We note that $z<0$ in the mantle. Hence, $-kz = k|z|$ and $e^{kz} = e^{-k|z|}$. Since $\tau = \frac{2\eta k}{\rho_s g}$ is directly proportional to k, we can re-write $-kz = k|z| = \frac{\rho_s g|z|\tau}{2\eta} = \frac{\tau}{\tau_z}$ where $\tau_z = \frac{2\eta}{\rho_s g|z|}$ is the effective response time of the mantle flow at depth $|z|$. So, we can re-write the postglacial pressure drop as

$$-\Delta P_{\text{post}} = \rho_i g\,\mathcal{H}_0^{-1}\left[\tilde{h}_0(k)\,F(\tau,\Delta t)\,R(\tau,\tau_z)\right] \tag{7.3}$$

where

$$F(\tau,\Delta t) = \frac{\tau}{\Delta t}\left(1-\exp\left(-\frac{\Delta t}{\tau}\right)\right)$$

and $$R(\tau,\tau_z) = \frac{\tau}{\tau_z}\,e^{-\frac{\tau}{\tau_z}}.$$

Δt is constant at a given deglaciation rate. τ_z is constant at a fixed depth $|z|$. The zeroth-order inverse Hankel transform sums all the k (and hence τ, which is directly proportional to k) components inside the square bracket. Figure 7.16 plots the functions $F(\tau,\Delta t)$ and $R(\tau,\tau_z)$ versus τ.

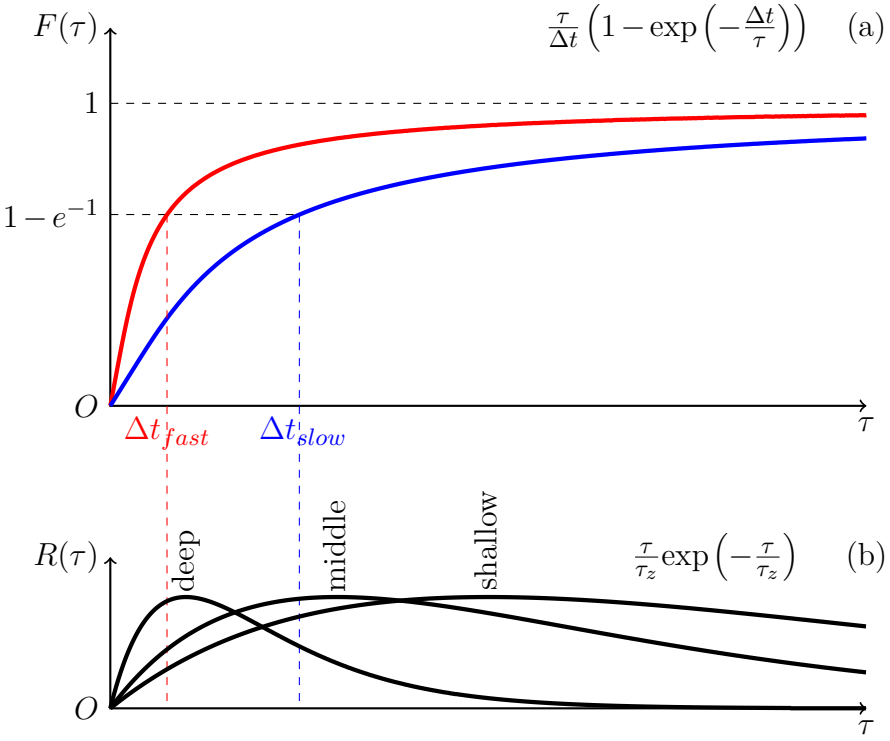

Fig. 7.16 (a) $F(\tau)=\frac{\tau}{\Delta t}\left(1-\exp\left(-\frac{\Delta t}{\tau}\right)\right)$ plotted against τ at two different values of Δt: $\Delta t=\Delta t_{\text{fast}}$ for the red curve and $\Delta t=\Delta t_{\text{slow}}$ for the blue curve. $\Delta t_{\text{fast}}<\Delta t_{\text{slow}}$. i.e. the deglaciation rate for the red curve is higher than that for the blue curve. Note that $F(\tau)$ drops sharply at $\tau<\Delta t$. (b) $R(\tau)=\frac{\tau}{\tau_z}\exp\left(-\frac{\tau}{\tau_z}\right)$ plotted against τ at three different depths $|z|$ in the mantle (one curve corresponds to one depth). Each of the three curves peaks at $\tau=\tau_z=\frac{2\eta}{\rho_s g|z|}$. i.e. the curve that peaks at the smallest τ (labelled "deep") has the smallest τ_z, which corresponds to the largest $|z|$ (deepest mantle) and the curve that peaks at the largest τ (labelled "shallow") has the largest τ_z, which corresponds to the smallest $|z|$ (shallowest mantle).

We can see on Figure 7.16a that $F(\tau)$ is a low-pass filter with cut-off frequency $=1/\Delta t$. Multiplying $F(\tau)$ on $R(\tau)$ will attenuate $R(\tau)$ at τ below Δt (or, equivalently, at k below $\frac{\rho_s g\Delta t}{2\eta}$ since $\tau=\frac{2\eta k}{\rho_s g}$). Figure 7.16b shows that $R(\tau)$ distribution is different at different depth. At a deeper location in the mantle, a greater proportion of the area under the curve of $R(\tau)$ falls in the high frequency region $\tau<\Delta t$ (area under the curve of $R(\tau)$ on the left-hand side of the vertical dashed line in Figure 7.16). i.e. $R(\tau)$ in the deeper mantle is attenuated by the low-pass filter $F(\tau)$ more strongly than $R(\tau)$ in the shallower mantle. This controls the depth-dependent profile of $-\Delta P_{\text{post}}$ since $-\Delta P_{\text{post}}$ is dependent of $F(\tau)$ times $R(\tau)$ (equation (7.3)).

Let's compare two deglaciation scenarios with the same initial ice thickness profile (and hence the same $\tilde{h}_0(k)$), but different deglaciation rates. Let the faster deglaciation

scenario (hereafter "fast-scenario") have time duration of deglaciation $\Delta t = \Delta t_{\text{fast}}$ and the slower deglaciation scenario (hereafter "slow-scenario") have $\Delta t = \Delta t_{\text{slow}}$ where $\Delta t_{\text{slow}} > \Delta t_{\text{fast}}$. At any depth, both scenarios have the same $R(\tau, \tau_z)$ since $R(\tau, \tau_z)$ is independent of Δt. The only difference between the two scenarios is that the low-pass filter $F(\tau, \Delta t)$ has different cut-off frequencies $(1/\Delta t)$.

Figure 7.16a plots $F(\tau)$ for these two deglaciation scenarios (the blue/red curve for the slower/faster deglaciation scenario). In the slow-scenario, $R(\tau)$ in the deep mantle (the curve labelled "deep" in Figure 7.16b) is attenuated by $F(\tau)$ more strongly than would be in the fast-scenario (blue curve vs. red curve in Figure 7.16a). This means that, at a slower deglaciation rate, the postglacial pressure drop (and hence the postglacial melt produced) in the deep mantle is less. Since, melt produced at deep depth is La-enriched, the attenuation of the postglacial melting in the deep mantle means that the average postglacial melt (which is the sum of the melts produced at all depths) for the slow-scenario is less La-enriched (i.e. more La-depleted) than the fast-scenario. This explains why, in Figure 7.4a near the center of the ice ($r_{\|} = 0$), a slower deglaciation rate scenario has more La-depleted in the early-postglacial melts.

7.5.2 Net GIA Pressure Drop

Similar to Section 7.5.1, we can calculate the net (=subglacial+subaerial) pressure drop due to the deglaciation by integrating the GIA decompression rate $-\frac{DP}{Dt}$ from the beginning of the deglaciation at time $t = t_0$ to ∞:

$$\begin{aligned} -\Delta P_{\text{net}}(r,z) &= -\int_{t_0}^{\infty} \frac{DP}{Dt}\,\mathrm{d}t \\ &= \rho_i g\, \mathcal{H}_0^{-1}\left[e^{kz}\left(\int_{t_0}^{\infty} \mathcal{H}_0[-\dot{h}](k,t)\,\mathrm{d}t + kz\int_{t_0}^{\infty} \widetilde{w}(k,t)\,\mathrm{d}t\right)\right]. \end{aligned}$$

The first term inside the round brackets $\int_{t_0}^{\infty} \mathcal{H}_0[-\dot{h}](k,t)\mathrm{d}t$ is equal to the area under the Top-Hat function $= \tilde{h}_0(k)$ (see equation (7.1)). The second term inside the round brackets $kz\int_{t_0}^{\infty} \widetilde{w}(k,t)\,\mathrm{d}t$ can be evaluated using equation (7.2):

$$\begin{aligned} \int_{t_0}^{t_0+\Delta t} \widetilde{w}(k,t)\,\mathrm{d}t &= -\frac{\tilde{h}_0(k)}{\Delta t}\int_{t_0}^{t_0+\Delta t}\left[1-\exp\left(-\frac{t-t_0}{\tau}\right)\right]\mathrm{d}t \\ &= -\tilde{h}_0(k)\left(1-\frac{\tau}{\Delta t}\left[1-\exp\left(-\frac{\Delta t}{\tau}\right)\right]\right) \end{aligned}$$

and

$$\int_{t_0+\Delta t}^{\infty} \widetilde{w}(k,t)\,\mathrm{d}t = -\frac{\tilde{h}_0(k)}{\Delta t}\left[\exp\frac{\Delta t}{\tau} - 1\right]\int_{t_0+\Delta t}^{\infty} \exp\left(-\frac{t-t_0}{\tau}\right)\mathrm{d}t$$
$$= -\tilde{h}_0(k)\,\frac{\tau}{\Delta t}\left[1-\exp\left(-\frac{\Delta t}{\tau}\right)\right].$$

Therefore,

$$\int_{t_0}^{\infty} \widetilde{w}(k,t)\,\mathrm{d}t = \int_{t_0}^{t_0+\Delta t} \widetilde{w}(k,t)\,\mathrm{d}t + \int_{t_0+\Delta t}^{\infty} \widetilde{w}(k,t)\,\mathrm{d}t$$
$$= -\tilde{h}_0(k).$$

Hence, the net (=subglacial+subaerial) pressure drop due to the deglaciation is

$$-\Delta P_{net}(r,z) = \rho_i g\,\mathcal{H}_0^{-1}\left[(1-kz)\,e^{kz}\,\tilde{h}_0(k)\right]$$
$$= \rho_i g\,\mathcal{H}_0^{-1}\left[(1+k|z|)\,e^{-k|z|}\,\tilde{h}_0(k)\right].$$

We note that the spatial profile of $-\Delta P_{net}(r,z)$ is independent of Δt. That is, the net pressure drop at any location in the mantle only depends on how much load $(=\rho_i g\tilde{h}_0(k))$ has been removed from the surface, but not on how fast we remove it.

This implies that the net mass of melts produced by the GIA is independent of Δt because the net increase of the degree of melting $\Delta F_{net} = \Delta F_{net}(r,z)$ (which is directly proportional to $-\Delta P_{net}(r,z)$) is independent of Δt. It also implies that the average melting depth and hence the net mass of La partitioned into the melts is independent of Δt. This result can be generalized to any time-dependent profile of deglaciation because any form of $\mathcal{H}_0[-\dot{h}](k,t)$ in the temporal space can be written as the sum of Top-Hat functions.

Chapter 8

Predicting the Future

8.1 Introduction

We have seen in Chapters 5 and 6 that deglaciation and glaciation can have pronounced effects on the magmatic production beneath Iceland. With currently increasing deglaciation rates of the Icelandic glaciers (Björnsson and Pálsson, 2008), the magmatic production rates are expected to rise. This will result in elevated volcanic eruption rates in the future.

Schmidt et al. (2013) has studied the effect of the present-day deglaciation on mantle melting beneath Iceland using 3-D models of Glacially-Isostatic Adjustment (GIA). Their presumed ice load includes a detailed deglaciation of the largest ice cap Vatnajökull (developed by Árnadóttir et al. (2009)) combined with several smaller glaciers (Langjökull, Hofsjökull, Mýrdalsjökull, Eyjafjallajökull etc.). They showed that the melt production rates at 2010 CE are elevated from the steady-state values by 100–135% due to the deglaciation. However, their models only calculated the melt production rates for 120 years in the past, from year 1890 CE to 2010 CE. The subglacial volcanic eruption rates after year 2010 CE have not been estimated.

In this chapter, we implement our numerical models of mantle flow, mantle melting and melt transport to predict the future of Icelandic volcanic activity in the next few thousand years. The timings and magnitudes of which will largely depend on the deglaciation rates and the rate of melt transport. We assume a simple constant melt productivity model (as implemented in Chapters 5 and 6) as it yields similar bulk volumetric melt production rates to that obtained from the bi-lithological mantle source of Rudge et al. (2013).

8.2 Glacial Load

The finite rate of melt transport, the viscous response of the mantle to the glacial load change and the dependence of mantle melting on the history of glacial loading (as investigated in Chapters 5 and 6) can cause a few thousand years time delay between the change in volcanic activity and the change in deglaciation rate. It is therefore essential in a numerical model to include the history of the glacial load back to a few thousand years before present. In our model, we prescribe the ice load history back to before the nucleation of the current Icelandic ice caps at ~ 5.5 kyrBP (Geirsdóttir et al., 2019).

A lake sediment study of Geirsdóttir et al. (2019) showed that the Icelandic climate during the Holocene Thermal Maximum (HTM) ($\sim$ 10–6 kyrBP) was relatively warm and that most areas on Iceland were likely to be ice-free. Climate proxies in sediments collected from Hvítárvatn (a glacial lake in the east of Langjökull) indicate that the nucleation of the Langjökull ice cap was at around 5.5 kyrBP (Geirsdóttir et al., 2019). This nucleation timing is similar to that in the Langjökull numerical modelling of Flowers et al. (2008).

The nucleation of the largest Icelandic ice cap, Vatnajökull, was likely to be at around the same time as that of Langjökull due to the similarity of the climates (e.g. precipitation rates and temperatures) and the glacier bed elevations (Björnsson and Pálsson, 2008). Although lake sediment studies of the glacial lake Lögurinn show that the return of glacial meltwater from Eyjabakkajökull (a North-Eastern outlet glacier of Vatnajökull) into the lake was at ~ 4.4 kyrBP (Geirsdóttir et al., 2019), it does not reflect the timing of the Vatnajökull nucleation in the Central-Southern area because the bed elevations and the precipitation rates at the Central-Southern Vatnajökull were higher than that in the North-Eastern area (Björnsson and Pálsson, 2008). As a result, the 4.4 kyrBP timing only gives a minimum age bound of the Vatnajökull nucleation.

In our model, we set the origin of time ($t = 0$) at year 0 CE. Since the standard "present" time is 1 January 1950, 0 kyrBP corresponds to the model time $t = 1950$ yr. We assume that the nucleations of the four largest Icelandic ice caps (Vatnajökull, Langjökull, Hofsjökull and Myrdalsjökull) were synchronous at 5.45 kyrBP ($t = -3500$ yr). We neglect the remaining smaller ice caps because the volume sum of these small glaciers at present day is less than 10% of the total Icelandic ice volume (Björnsson and Pálsson, 2008). These small glaciers are also distant from the volcanic zones. Hence, they do not have a significant effect on the stress field in the mantle melting region.

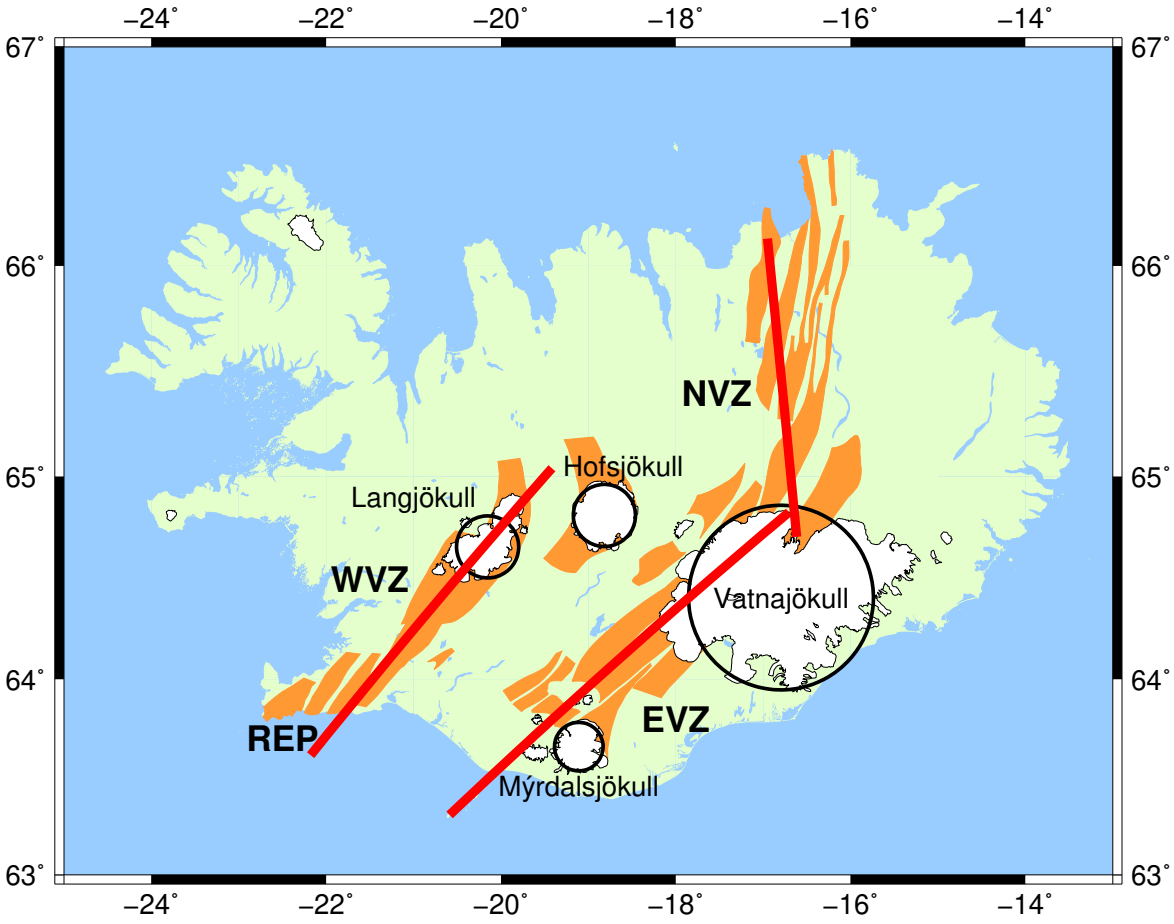

Fig. 8.1 Mercator projection map of Iceland showing the recent Icelandic glaciers in white color, active fissure swarms where plate divergence is taking place in orange, the model rift as red lines and the four model glaciers at year 2000 CE as black circles drawn on top of the actual glaciers. The glaciers are labelled with their names (Vatnajökull, Langjökull, Hofsjökull and Mýrdalsjökull). The model rift includes four volcanic zones (Eastern (EVZ), Northern (NVZ), Reykjanes (REP) and Western (WVZ) Volcanic Zones). The model assumes that the WVZ and REP rifts are on the same straight line.

From the onset of neoglaciation at ~ 5.5 kyrBP, Icelandic glaciers expanded progressively until they attained the Holocene glacial maximum during the Little Ice Age ($\sim$1750–1890 CE) (Björnsson and Pálsson, 2008; Flowers et al., 2008, 2007; Geirsdóttir et al., 2019; Pagli et al., 2007). The ice volumes then stayed approximately constant between 1750 and 1890 CE (Björnsson and Pálsson, 2008; Flowers et al., 2008, 2007; Geirsdóttir et al., 2019; Pagli et al., 2007).

In our model, we assume that, before $t = -3500$ yr (5.45 kyrBP), the ice load is zero and the mantle is in isostatic equilibrium. The model volumes of all the four major glaciers increase linearly with time from zero at $t = -3500$ yr (5.45 kyrBP) to

their maxima at $t = 1750$ yr (1750 CE). The presumed ice volumes then stay constant during the Little Ice Age until at 1890 CE when the ice volumes begin to decrease linearly with time. We take the volumes and the coverage areas of the four largest Icelandic ice caps at 2000 CE from Table 1 of Björnsson and Pálsson (2008). We then assume that the volumetric loss rates of the glaciers during 1890–2000 CE are constant and equal to that in Table 1 of Schmidt et al. (2013) in order to calculate the ice volumes at 1890 CE from the ice volumes at 2000 CE.

We approximate each of the four largest Icelandic ice caps as an axisymmetric gravity current as in Chapters 5 and 6. However, the centers of these ice caps are not necessarily on the ridge axis. Figure 8.1 outlines the locations of these four presumed glaciers at 2000 CE together with the model rifts drawn on top of the actual glaciers at present and the active fissure swarms. An advantage of the axisymmetric ice assumption is that the computational cost is cheaper. This allows us to calculate the melt production rates over a longer period of time than that in Schmidt et al. (2013).

The aspect ratio of an axisymmetric gravity current is controlled by the basal shear stress (τ_B) (see equation (4.9) in Chapter 4). Here, we obtain τ_B of each of the four ice caps from the ice volumes (V) and coverage areas (A) at 2000 CE as taken from Table 1 of Björnsson and Pálsson (2008) using

$$\begin{aligned} A &= \pi r_m^2 \\ &= \pi \left(\frac{15}{8\pi} V\right)^{\frac{4}{5}} \left(\frac{\rho_i g}{2\tau_B}\right)^{\frac{2}{5}} \\ \therefore \tau_B &= \frac{\rho_i g}{2} \left(\frac{\pi}{A}\right)^{\frac{5}{2}} \left(\frac{15V}{8\pi}\right)^2 \end{aligned} \tag{8.1}$$

where A is the ice coverage area, r_m is the ice radius, which is related to the ice volume V by equation (4.9) in Chapter 4, ρ_i is the density of ice and g is the acceleration due to gravity. The numerical values of ρ_i and g are as listed in Table 4.3 of Chapter 4. However, the numerical value of τ_B in Table 4.3 is now replaced by that calculated from equation (8.1) for each of the four glaciers, each of which is listed in Table 8.1.

Table 8.1 The model parameters for the four largest Icelandic ice caps at present: Vatnajökull, Langjökull, Hofsjökull and Mýrdalsjökull. The volumes and areas at 2000 CE are from Björnsson and Pálsson (2008). The basal shear stresses (τ_B) are calculated from the volumes and areas at 2000 CE using equation (8.1). The volume loss rates ($-\dot{V}$) during 1890–2000 CE are the same as in Table 1 of Schmidt et al. (2013). The volumes at 1890 CE are calculated from the volumes at 2000 CE and the volume loss rates during 1890–2000 CE. The areas at 1890 CE are calculated from τ_B and the volumes at 1890 CE using equation (8.1).

	Vatna jökull	Lang jökull	Hofs jökull	Mýrdals jökull
Volume (km^3) 2000 CE	3,100	190	200	140
Area (km^2) 2000 CE	8,100	900	890	590
τ_B (kPa)	44.8	40.9	46.6	63.8
$-\dot{V}$ (km^3/yr) 1890–2000 CE	3.817	0.666	0.634	0.448
Volume (km^3) 1890 CE	3,520	263	270	189
Area (km^2) 1890 CE	8,966	1,168	1,131	751

The deglaciation rate of Vatnajökull from year 2000 CE onwards has been estimated by the numerical modelling of Flowers et al. (2005). Flowers et al. (2005) calculated the time evolution of the Vatnajökull's volume based on 5 different climate warming rates: 0°, 1°, 2°, 3° and 4°C per century. For the warming rate of 0°C per century, the ice volume stays approximately constant, which would imply an approximately zero melt production rate by the GIA. For the warming rates of 1°, 2°, 3° and 4°C per century, the ice volume progressively drops to near zero at $\sim$ 2200, 2250, 2300 and 2450 CE respectively (see Figure 7 of Flowers et al. (2005)). Our presumed ice-load volumes of the four largest Icelandic ice caps from 2000 CE onwards are assumed to decrease linearly with time to zero at 2200, 2250, 2300 or 2450 CE, each of which corresponds approximately to each of the 4 scenarios of positive climate warming rates in Flowers et al. (2005). We plot the presumed volumes of the four glaciers as functions of time in Figure 8.2.

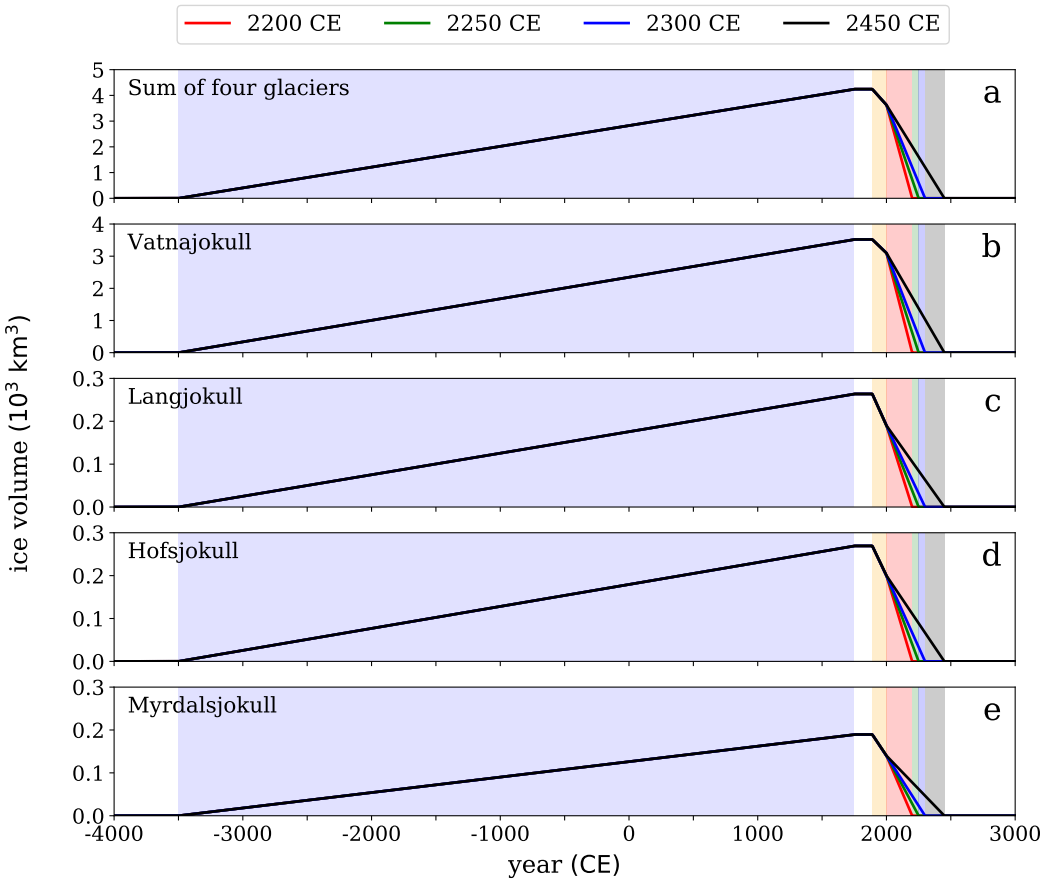

Fig. 8.2 (a) Sum of the volumes of the four largest Icelandic glaciers (Vatnajökull, Langjökull, Hofsjökull and Mýrdalsjökull), (b) Vatnajökull, (c) Langjökull, (d) Hofsjökull and (e) Mýrdalsjökull volumes during the mid- and late-Holocene. Different line colors correspond to different scenarios of ice volumes. The legend at the top of the figure shows the year when the ice volume goes to zero in each of the ice-load scenarios. Blue-shaded region from −3500 to 1750 CE is the period during which the ice volume increases linearly with time from zero to the maximum at the Little Ice Age. Yellow-shaded region from 1890 to 2000 CE is the period during which the ice volume loss rates follow that in Table 1 of Schmidt et al. (2013). After 2000 CE, the model is run with four different deglaciation scenarios, each of which has the ice volume decreasing linearly with time to zero at year as labelled in the legend. These four deglaciation scenarios correspond approximately to the ice model results in Flowers et al. (2005) for the climate warming rates of 1° (black line), 2° (blue line), 3° (green line) and 4°C (red line) per century.

8.3 Eruption Rates

8.3.1 Steady-State

At steady state, the decompression mantle melting beneath Iceland comes from upwelling mantle flow driven by the spreading ridge (passive upwelling) and the mantle plume (active upwelling) (White et al., 1992). The passive upwelling is assumed to follow the corner flow solution with the half-plate spreading rate and the average upwelling rate of 10 mm/yr similar to the previous chapters.

Studies of crustal thickness (Allen et al., 2002; Darbyshire et al., 2000; Kaban et al., 2002), the seismic velocity anomaly in the upper mantle (Wolfe et al., 1997), transition zone thickness (Shen et al., 2002) and the spatial distribution of geochemical profiles (Shorttle et al., 2010) indicate that the plume center is located somewhere near the Vatnajökull ice cap and the Eastern Volcanic Zone (EVZ). This explains why, in historical time, the EVZ had a significantly higher erupted magma volume than in other volcanic zones (Thordarson and Larsen, 2007). The mantle plume enhances mantle melting and the crustal-supply rates of melts in regions within ~ 100 km distance from the plume center (Ito et al., 1999). This elevates the eruption rates in the EVZ from that in other volcanic zones.

We assume that the effect of plume-enhancing mantle melting rates in the EVZ can be modelled by increasing the average upwelling rate of the corner flow in the solid mantle from 10 mm/yr to 45 mm/yr for mantle in the range of ± 50 km from the middle of the EVZ rift (i.e. with the modelled EVZ rift length of 240 km, the middle of the EVZ rift is at 120 km from the Northern end of the EVZ and the ± 50-km range is in between 70 and 170 km from the Northern end of the EVZ). The reason for choosing the enhanced-upwelling-rate location to be symmetric about the center of the EVZ rift is because Thordarson and Larsen (2007) found that during historical time the erupted volume in EVZ is divided approximately equally between the Northern EVZ (Grímsvötn+Veidivötn ~ 31 km^3) and the Southern EVZ (Hekla+Katla ~ 38 km^3) to within the uncertainty of the volume estimates ($\pm 25\%$). The reason for increasing the average upwelling rate to 45 mm/yr is because this value gives the proportion of the steady-state eruption rate in EVZ relative to the other volcanic zones close to the estimate of Thordarson and Höskuldsson (2008).

Table 8.2 shows the Thordarson and Höskuldsson (2008) estimated erupted magma volumes and % proportions together with the modelled steady-state eruption rates and % proportions in the four main volcanic zones. This table shows that the numerical choices of the 45 mm/yr plume-enhanced upwelling rate, the enhanced-upwelling-rate

Table 8.2 Estimated volumes of magma that erupted over the last 11 ka of Thordarson and Höskuldsson (2008) (their Table 2) in km^3 Dense Rock Equivalent (DRE) and the model melt supply rates at steady state in four volcanic zones. The % proportion is relative to the sum of the four volcanic zones.

	Th.& H.(2008)		Model	
	Erupted Volume		Steady-State Rate	
	km^3 DRE	%	km^3/yr	%
Eastern Volcanic Zone	337	60.8	0.261	60.7
Northern Volcanic Zone	94	17.0	0.072	16.75
Reykjanes Volcanic Belt	29	5.2	0.025	5.8
Western Volcanic Zone	94	17.0	0.072	16.75
Sum	554	100	0.430	100

range of ±50 km about the center of the EVZ rift and the model rift lengths of the four volcanic zones (as listed in Table 8.3) give the modelled % proportions of eruption rates in the four volcanic zones close to the observational % proportions of erupted volumes.

Table 8.3 The model rift lengths in different volcanic zones.

	Rift Length (km)
Eastern Volcanic Zone	240
Northern Volcanic Zone	170
Reykjanes Volcanic Belt	60
Western Volcanic Zone	170

Numerical models of dehydration melting of the mantle plume (e.g. Ito et al. (1999)) have shown that the upwelling velocity of solid mantle near the plume center is highly depth-dependent. Below the dry-solidus, the mantle viscosity increases sharply as the mantle rises and gets dehydrated, which significantly slows down the upwelling rate (Ito et al., 1999). Although this depth-dependent upwelling rate does not have a significant effect on the magma production rates, it affects the geochemical composition of the magmas and the erupted lavas (Maclennan et al., 2001; Shorttle et al., 2010). Any numerical models that involve the geochemical composition of magmas and/or lavas have to take the depth-dependent upwelling rate effect into account. Nevertheless, our goal in this chapter is simply to predict the future of the volcanic eruption rates in Iceland. We do not aim at predicting the geochemical composition in the lavas. We therefore assume a uniform plume-enhanced upwelling rate here to simplify the calculations.

8.3.2 Total Melt Flux

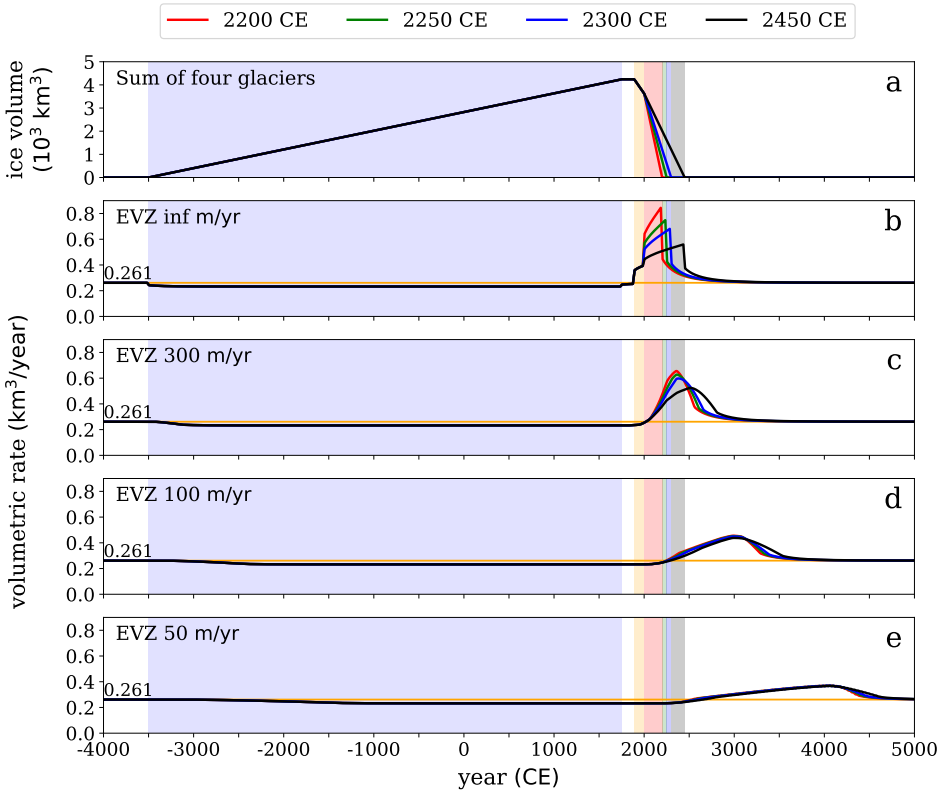

Fig. 8.3 (a) Sum of the volumes of the four largest Icelandic glaciers (Vatnajökull, Langjökull, Hofsjökull and Mýrdalsjökull) during the mid- and late-Holocene. (b)–(e) Volumetric rates of melt supply to the crust in EVZ. Each panel corresponds to a different value of presumed melt ascent velocity as shown on the upper left corner of the panel: (b) infinite velocity, (c) 300 m/yr, (d) 100 m/yr and (e) 50 m/yr. At infinite ascent velocity, the melt supply rate is equal to the melt production rate. Different line colors in (b)–(e) correspond to different scenarios of ice volumes in (a). The legend at the top of the figure shows the year when the ice volume goes to zero in each of the ice-load scenarios. Horizontal orange line in (b)–(e) is the steady-state volumetric rate, the numerical value of which is indicated just above the line near the y-axis. Blue-shaded region from -3500 to 1750 CE is the period during which the ice volume increases linearly with time from zero to the maximum at the Little Ice Age. Yellow-shaded region from 1890 to 2000 CE is the period during which the ice volume loss rates follow that in Table 1 of Schmidt et al. (2013). After 2000 CE, the model is run with four different deglaciation scenarios, each of which has the ice volume decreasing linearly with time to zero at year as labelled in the legend. These four deglaciation scenarios correspond approximately to the ice model results in Flowers et al. (2005) for the climate warming rates of 1° (black line), 2° (blue line), 3° (green line) and 4°C (red line) per century.

By inputting the ice-load parameters in Section 8.2 into the models as described in the previous Chapters, we obtain the crustal supply rates of melts in different volcanic zones. The results are shown in Figures 8.3, 8.4, 8.5 and 8.6 for EVZ, NVZ, WVZ and REP respectively. Each line color corresponds to each of the four deglaciation scenarios as discussed in Section 8.2.

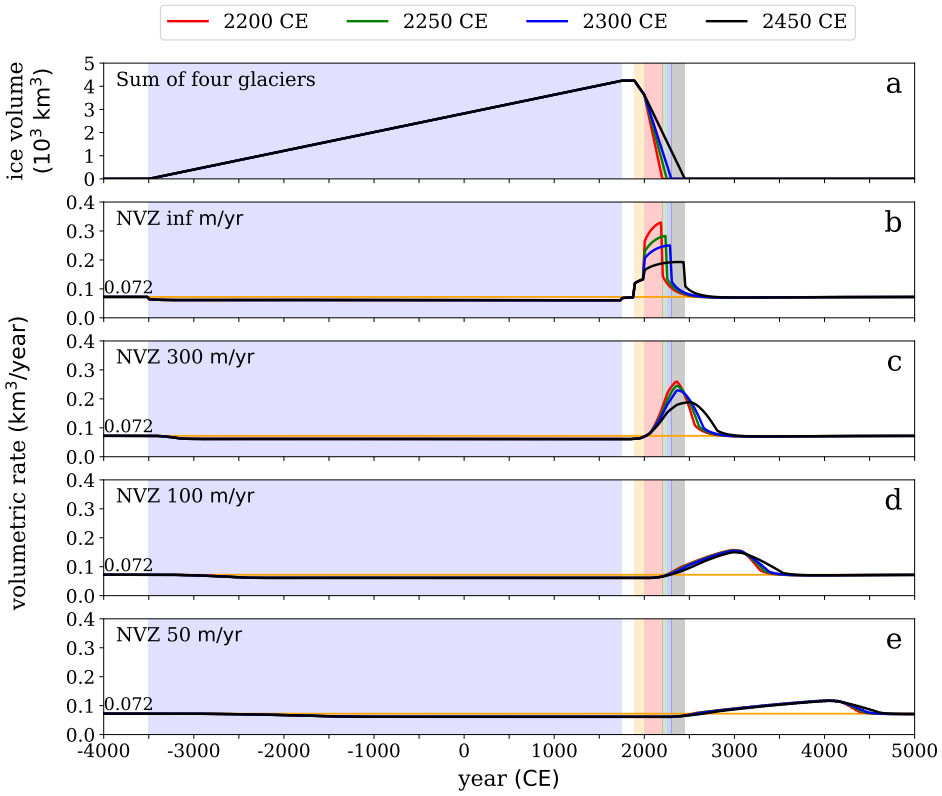

Fig. 8.4 Same as Figure 8.3 but for the volumetric rates of melt supply to the crust in NVZ.

Panel b in every one of the figures except the REP indicates that the current (year 2000 CE) melt production rates are already almost doubled from the steady-state rates. These results, despite being under a very simplified axisymmetric ice assumption, are consistent with the Schmidt et al. (2013) 3-D GIA calculations that the melt production rates at present-day are 100–135% increased from the steady-state rates. We note that the melt production rates during the glaciation period between $t = -3500$ and 1750 CE are slightly less than the steady-state values. This is because the increase in the glacial load reduces the decompression melting rates.

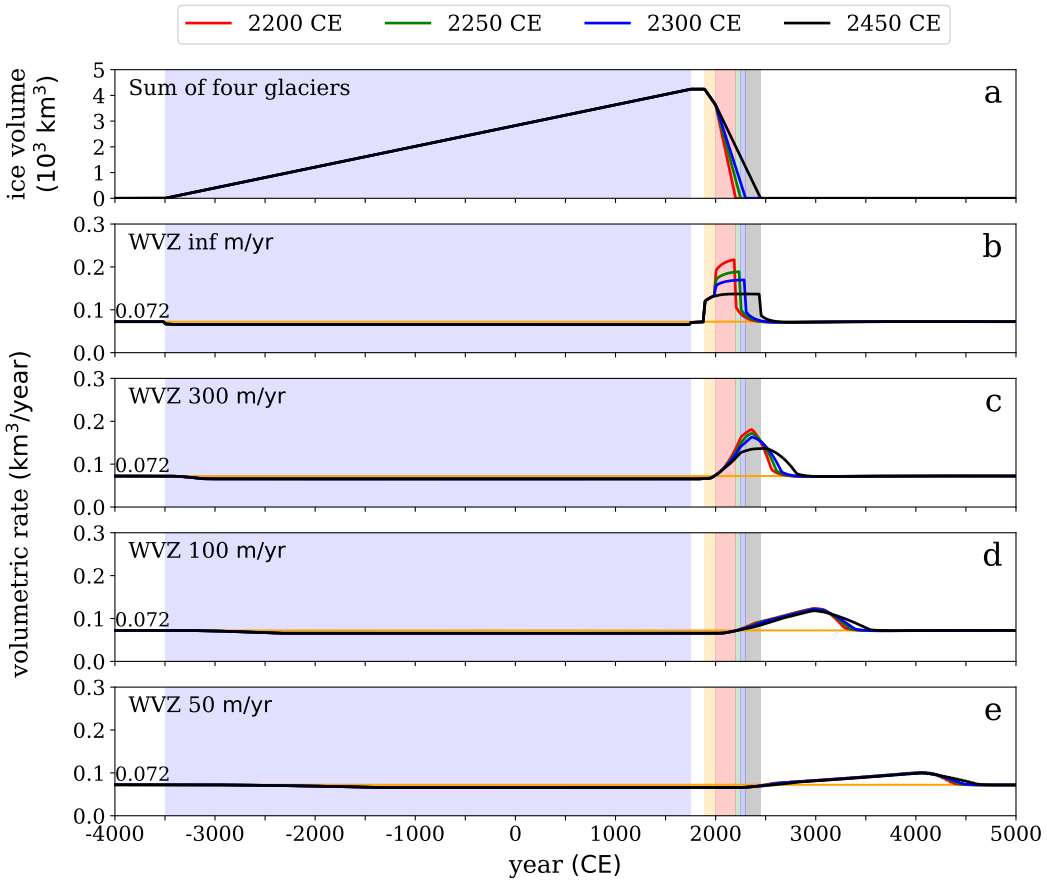

Fig. 8.5 Same as Figure 8.3 but for the volumetric rates of melt supply to the crust in WVZ.

Panels c, d and e show the volumetric supply rates of melts to the crust at different assumed values of melt ascent velocity. These panels indicate that, at a melt ascent rate of 300 m/yr or below, the increase of the volumetric supply rates at present-day are unnoticeable from the steady-state rates. However, the crustal supply rates of melts will eventually elevate within the next two thousand years if the melt ascent velocity is 50 m/yr or above. If the ratio of the melt volume erupted on the Earth's surface to the total melt volume supplied to the crust remains unchanged, the increase in the crustal supply rates will result in an increase in volcanic eruption rates in Iceland.

How high the supply rates will be at their peak will largely depend on how fast the melts ascend. Although previous studies (Maclennan et al. (2002) and Chapter 5) have shown that the melt ascent rate during the last deglaciation in Iceland was at least 50 m/yr, it does not set the lower bound limit for the melt ascent velocity

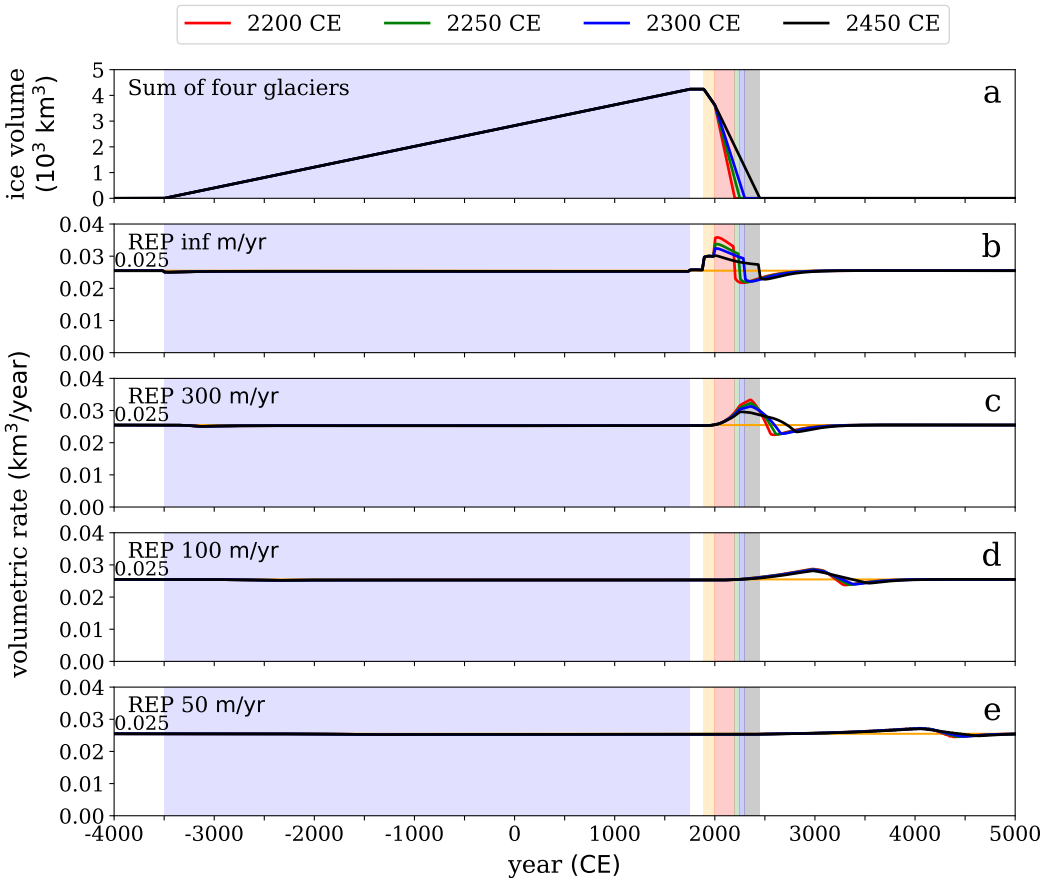

Fig. 8.6 Same as Figure 8.3 but for the volumetric rates of melt supply to the crust in REP.

at present-day and in the next few hundred years. This is because, the present-day melting rate is only about twice the steady-state rate; whereas, the melting rate during the last deglaciation was about 10-fold increase from that. A significantly lower melting rate at present-day than during the last deglaciation means that there is a lower melt flux and porosity, which likely implies a slower rate of melt transport velocity. If the present-day melt ascent velocity is below 50 m/yr, the peak of the melt supply rates to the crust in all the volcanic zones in the near future will stay below twice the steady-state values (Figures 8.3e, 8.4e, 8.5e and 8.6e). We hope this is the case!

8.3.3 Subglacial Melt Flux

The extra melts produced from the GIA-induced decompression melting in the mantle (hereafter as *GIA-produced melts*) are predominantly basaltic magmas that usually erupt effusively (non-explosively) due to their relatively low viscosity and gas content (Thordarson and Höskuldsson, 2014). However, if these magmas erupt subglacially or subaqueously, explosive hydromagmatic eruptions may occur due to their interaction with water (Thordarson and Höskuldsson, 2014). Subglacial eruptions can also melt a significant amount of ice in a short period of time, causing subglacial outburst floods known as *jökulhlaups* that can be very dangerous to humankind. In this section, we calculate how much the present-day deglaciation in Iceland will influence subglacial eruption rates in the future.

Of the four largest Icelandic ice caps at present, three of them are covering one of the four main rift zones (Vatnajökull on EVZ and NVZ, Langjökull on WVZ and Mýrdalsjökull on EVZ as shown in Figure 8.1). Figures 8.7, 8.8, 8.9 and 8.10 provide the model results of the melt supply rates to the crust in the rift segments that are covered by the modelled ice caps (hereafter as *subglacial melt supply*) for EVZ beneath Vatnajökull, NVZ beneath Vatnajökull, WVZ beneath Langjökull and EVZ beneath Mýrdalsjökull respectively.

These figures show that in any of the four deglaciation scenarios at any of the four modelled values of melt ascent velocity (infinite, 300, 100 or 50 m/yr), the subglacial melt supply rates in the future will not be significantly elevated from the present-day (year 2000 CE) values. The reason is because, as the ice caps deglaciate, subglacial melt supply rates decrease because a smaller proportion of the rift is covered by ice (i.e. less subglacial segment). Once all the ice caps have gone, subglacial eruption rates anywhere will be zero.

At an instantaneous rate of melt ascent (panel b of Figures 8.7, 8.8, 8.9 and 8.10), the crustal melt flux is equal to the melt production rate (panel b of Figures 8.3, 8.4, 8.5 and 8.6), which is instantaneous in response to the deglaciation. The subglacial melt flux is mainly controlled by how much ice remains on the rift for melts to erupt under. In this case, the subglacial melt supply rates would already be at their peaks at present day (year 2000 CE). As time goes by, ice caps melt and the subglacial melt supply rates drop because a smaller proportion of the rift is subglacial.

Panel b of each of the Figures 8.7, 8.8, 8.9 and 8.10 also shows that, if the melt ascent rate in the last few hundred years were very fast, subglacial melt supply rates at present (year 2000 CE) would be at least twice the rates before year 1500 CE. This implication may be useful for estimating an upper-bound limit of the late-Holocene

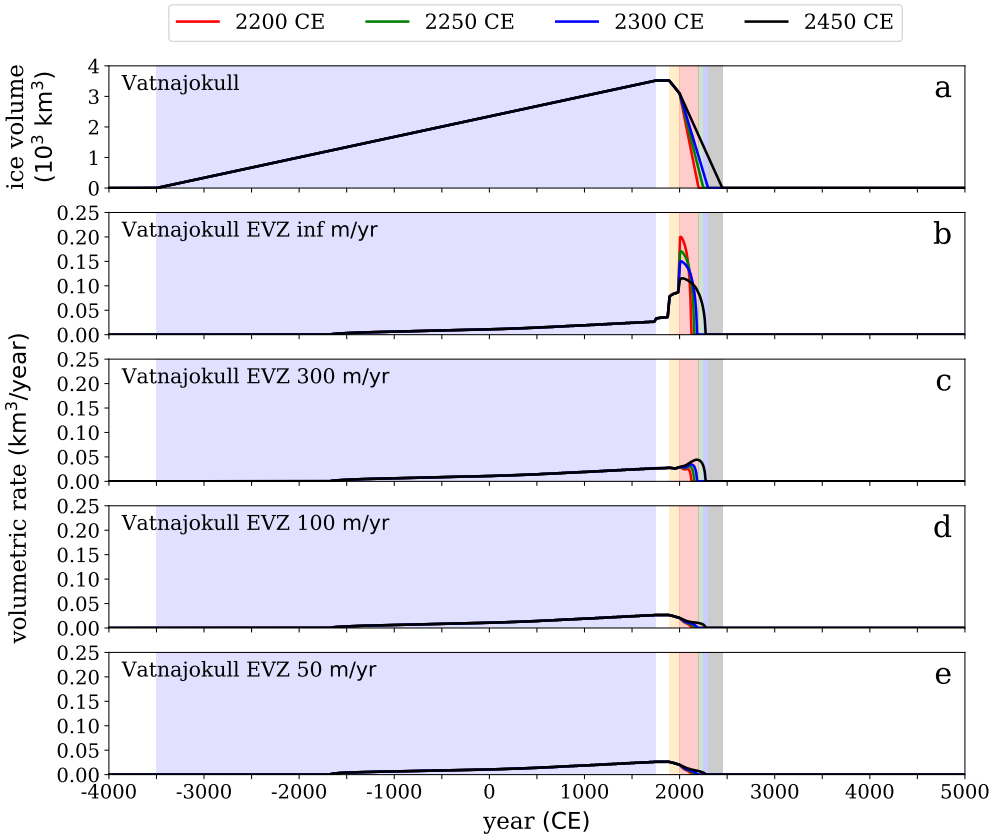

Fig. 8.7 (a) Modelling-input volume of the Vatnajökull glacier during the mid- and late-Holocene. (b)–(e) Subglacial volumetric rates of melt supply beneath Vatnajökull in EVZ. Other details are as in Figure 8.3.

melt ascent rate provided that the subglacial eruption rates before year 1500 CE are known.

At a finite rate of melt transport, the surge in crustal melt flux is delayed from the surge in melt production rate. Since the surge in melt production rate happens at the initiation of the deglaciation at 1890 CE (as shown in panel b of Figures 8.3, 8.4, 8.5 and 8.6), the peak of the total (=subglacial+subaerial) melt flux will happen after year 1890 CE (as shown in panels c, d and e of Figures 8.3, 8.4, 8.5 and 8.6). This means that the peak of the subglacial melt flux may happen after 1890 CE provided that a significant proportion of rift still remains covered by ice at around the time when the peak of the total (=subglacial+subaerial) melt flux occurs.

If the melt ascent velocity is at 100 m/yr or below, the surge of the total (=subglacial +subaerial) melt flux will happen so late that a significant proportion of ice will already

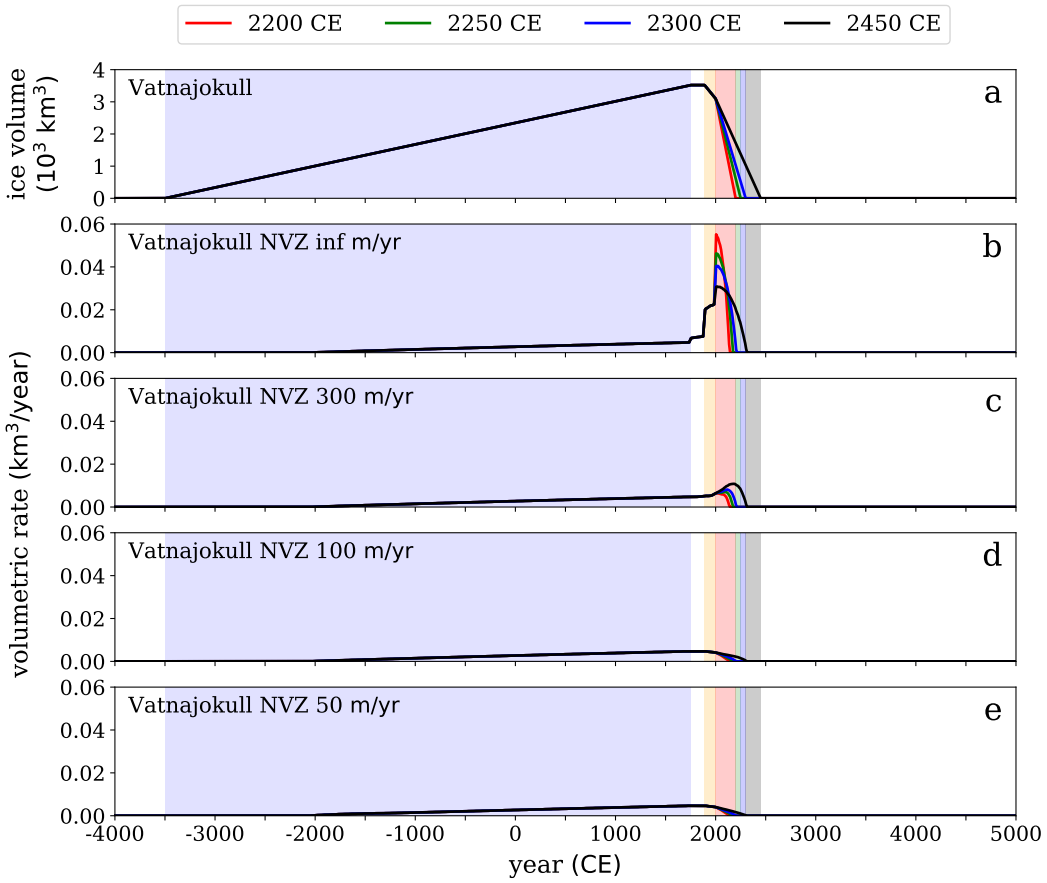

Fig. 8.8 (a) Modelling-input volume of the Vatnajökull glacier during the mid- and late-Holocene. b–e) Subglacial volumetric rates of melt supply beneath Vatnajökull in NVZ. Other details are as in Figure 8.3.

be gone (see panels d and e of Figures 8.3, 8.4, 8.5 and 8.6). In these cases, there will be no peak of the subglacial melt flux after year 1890 CE (as illustrated in Figures 8.7, 8.8, 8.9 and 8.10). The peak has already been reached at 1890 CE. On the other hand, at 300 m/yr melt ascent velocity, the surge of the total (=subglacial +subaerial) melt flux will be soon enough that a significant proportion of the rift is still covered by ice. In this case, the peaks of the subglacial melt supply rates in some areas will occur after year 1890 CE (e.g. beneath Vatnajökull and Langjökull as illustrated in panels c of Figures 8.7, 8.8 and 8.9).

The highest increase of the subglacial melt supply rate in the future from the present-day (year 2000 CE) value is seen at 300 m/yr melt ascent velocity (panel c of

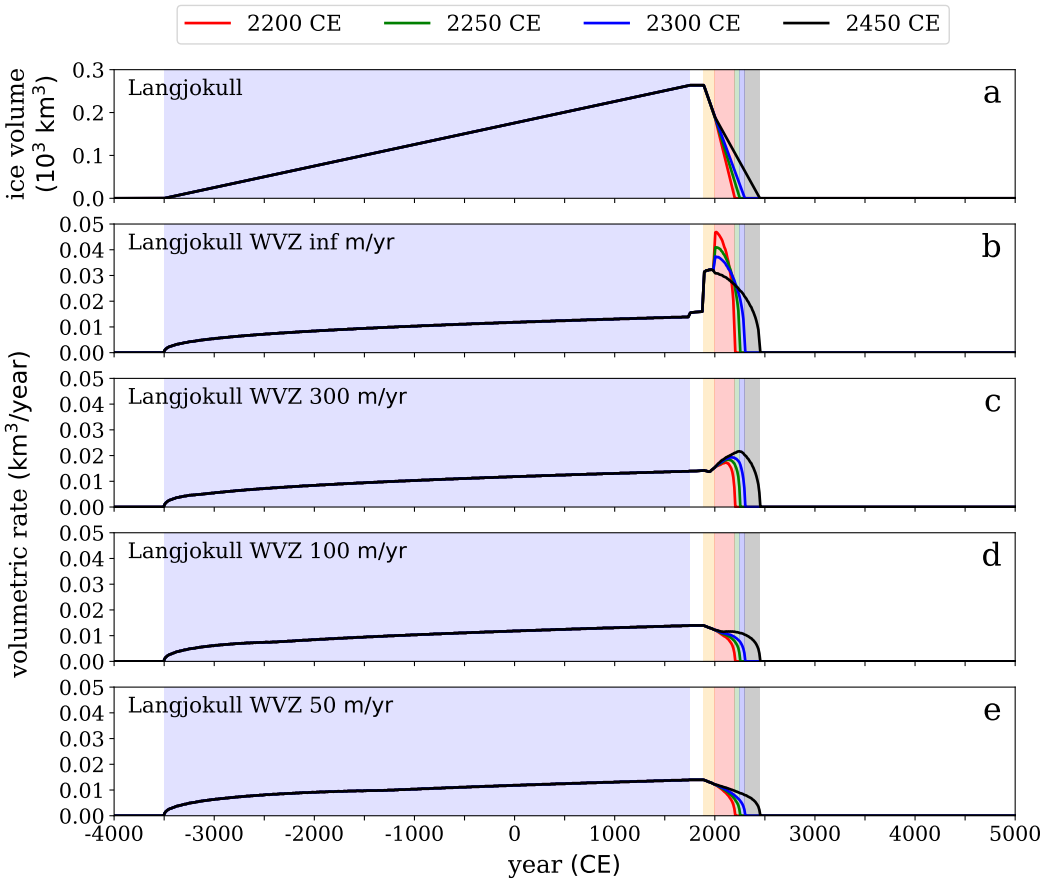

Fig. 8.9 (a) Modelling-input volume of the Langjökull glacier during the mid- and late-Holocene. b–e) Subglacial volumetric rates of melt supply beneath Langjökull in WVZ. Other details are as in Figure 8.3.

each of the four figures) in the scenario where the ice volume goes to zero the slowest at year 2450 CE. This is because this deglaciation scenario, in comparison to the other more rapid deglaciation scenarios, will have a greater proportion of the rift remain covered by ice at the time when the surge of melt supply rate comes. This will allow more melts to erupt subglacially.

We note that our model predictions of the subglacial melt supply rates are based on assumptions that the ice caps are axisymmetric (black circles in Figure 8.1) and that all the melt flux is focused to the rift axis (red lines in Figure 8.1). The axisymmetric ice causes a slight deviation of the proportion of subglacial rift from what would be obtained if the actual 3-D ice profile is used. A segment of a rift is counted as

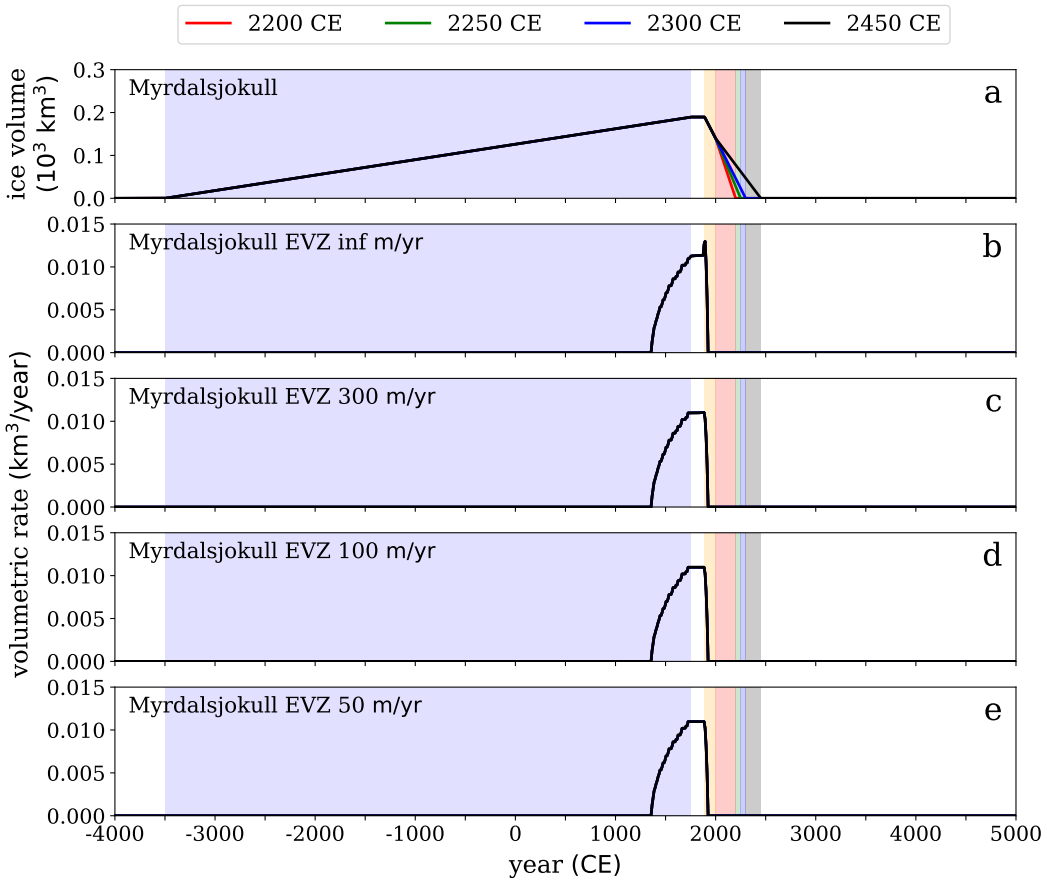

Fig. 8.10 (a) Modelling-input volume of the Mýrdalsjökull glacier during the mid- and late-Holocene. b–e) Subglacial volumetric rates of melt supply beneath Mýrdalsjökull in EVZ. Other details are as in Figure 8.3.

subglacial only if the rift axis in that segment is covered by ice. In real situations, however, eruptions can occur off-axis. More elaborate models of melt transport in 2-D passive mantle flow beneath mid-ocean ridges (e.g. Spiegelman (1996)) have shown that $\sim 80\%$ of the total melt flux is distributed over ~ 10-km width across the rift axis. While the rift axis has already been uncovered by ice, eruptions off-axis can still be subglacial if the ice still remains there. Hence, some degree of inaccuracy is present in our subglacial melt flux predictions due to the axisymmetric ice caps and on-axis melt flux assumptions.

Chapter 9

Conclusions

This dissertation studies the effects of glaciation, deglaciation and the finite rate of melt transport on Icelandic volcanism. Numerical models of mantle flow and mantle melting response to the glaciation and deglaciation are developed in Chapters 2, 3 and 4. In order for the calculations to be feasible over the whole last glacial cycle, the models need to be simplified so that the computational cost is not unreasonably expensive. The key simplifications made are the assumptions that

- the ice sheet has an axisymmetric shape,
- the solid mantle has a uniform viscosity and
- the melt transport effect can be represented by a time-lag sampler.

The time-lag sampler represents the time-lag between the melt production at depths and the eruption on the Earth's surface due to finite rate of melt transport.

Chapter 5 explores how, during the last deglaciation, the finite rate of melt transport can affect

- timing of the bursts in volcanic eruptions,
- volume proportions of the subglacial, finiglacial and postglacial eruptions and
- Lanthanum (La) concentrations in the erupted lavas.

The model results show that the La concentrations are strongly dependent on the melt ascent velocity. Comparison of the model results at different presumed values of melt ascent velocity with the geological observations suggests that the melt ascent velocity during the last deglaciation beneath Iceland is of the order of $\sim$100 m/year.

The effects of glacial loading during the last glacial period on mantle melting are investigated in Chapter 6. The model results show that glacial loading suppresses mantle melting and modulates the average La concentrations in the melts due to the depth-dependent profile of mantle melting suppression. However, due to extensive glacial erosion and the fact that the volumetric eruption rates during this period are small, there is no reliable geological data to be compared with.

Chapter 7 investigates how different deglaciation histories can result in different REE concentrations in the early-postglacial lavas. We found that the REE concentrations in the early-postglacial lavas erupted at

1. near the center of the ice sheet are affected by the deglaciation rate.

2. just inside where the glacier terminus pauses are affected by the pause duration.

This could be a reason why Icelandic lava shields formed during the Termination I and II (both have different deglaciation histories) have different REE compositions.

Lastly, Chapter 8 makes predictions for the future of the Icelandic volcanic eruption rates based on given estimated deglaciation rates of the current Icelandic glaciers. The model results of the eruption rates in the near future are highly dependent on the melt ascent velocity. At a melt ascent velocity of 100 m/yr or above, the models predict that the eruption rates in the Eastern Volcanic Zone (EVZ), the Northern Volcanic Zone (NVZ) and the Western Volcanic Zone (WVZ) will peak at no later than year 3000 CE with the peak values of around 2–3 times the present-day rates. The Reykjanes Penninsula (REP) will not have a significant elevation of eruption rates because this region is relatively far from the largest Icelandic ice caps at present-day, so, the decompression melting in the mantle is not significantly affected by the present-day deglaciation. At below 100 m/yr melt ascent velocity, the surface arrivals of melts produced from different depths will be so lagged that the eruption rates in any of the volcanic zones (EVZ, NVZ, REP and WVZ) will stay below twice the present-day rates. The model also predicts that, at any presumed value of melt ascent velocity, the subglacial eruption rates beneath the Vatnajöjull, Langjöjull and Mýrdalsjöjull ice caps will not be significantly elevated from the present-day values because these ice caps are currently retreating, which leaves less ice for melts to erupt under. Hence, volumetric rates of the subglacial outburst floods known as *jökulhlaups* are not expected to rise substantially.

Moving Forward

Our numerical models are neither the most efficient nor the most accurate for modelling the volcanic response to glaciation. Moving forward, we would like to improve the efficiency of the model algorithm so that more elaborate features (such as a fluid dynamic model of melt transport in 3-D and geochemical effects of melts from beneath on mantle melting at mid- and shallow-depths) can be incorporated.

A more detailed study on the melt transport in the crust is also required for a more accurate quantification of the volume ratio of extrusive melts (melts that erupt on the Earth's surface) to the total melts fed to the base of the crust (hereafter "extrusive-to-total volume ratio"). While we assume throughout this dissertation that the extrusive-to-total volume ratio is constant, this is not necessarily true as the ratio may vary with the volumetric melt supply rate to the crust.

We would also like to improve efficiency of the glacially-induced isostatic adjustment mantle flow model (hereafter "GIA model") so that the mantle flow over a glacial cycle can be calculated within a reasonable computational time for a 3-D laterally varying material layers of mantle. The 3-D GIA model of Schmidt et al. (2013) implemented in the commercial finite element software ABAQUS (ABAQUS, 2004) takes ~ 3 hours to calculate the mantle flow over 120-year time domain using 25.5 GB of RAM with 8 CPUs run in parallel (P. Schmidt, personal communication, May 30, 2019). Running this 3-D model with the same computational resource for the GIA mantle flow over a glacial cycle of ~ 120-kyr long would take $\sim 3{,}000$ hours (~ 4 months) of computation time, which is quite expensive. It will therefore be very helpful to work on improving the efficiency of the GIA model.

While deglaciation results in an increase of the mantle melting rate, lava eruption on the Earth's surface is also a source of heat flux that influences the dynamic of the deglaciation. It will be interesting to investigate how strong these effects are coupled. With more efficient numerical models (and hopefully also a more powerful computational resource available in the future), it will be possible to couple the GIA volcanic response with a numerical ice flow model (e.g. Patton et al. (2017)).

References

ABAQUS (2004). ABAQUS manuals version 6.5, ABAQUS Inc.

Allen, R. M., Nolet, G., Morgan, W. J., Vogfjörd, K., Nettles, M., Ekström, G., Bergsson, B. H., Erlendsson, P., Foulger, G. R., Jakobsdóttir, S., Julian, B. R., Pritchard, M., Ragnarsson, S., and Stefánsson, R. (2002). Plume-driven plumbing and crustal formation in Iceland. *Journal of Geophysical Research: Solid Earth*, 107(B8):ESE 4–1–ESE 4–19.

Andrews, J. T., Geirsdóttir, A., Hardardóttir, J., Principato, S., Grönvold, K., Kristjansdóttir, G. B., Helgadóttir, G., Drexler, J., and Sveinbjörnsdóttir, A. (2002a). Distribution, sediment magnetism and geochemistry of the Saksunarvatn (10 180 $\pm$ 60 cal. yr BP) tephra in marine, lake, and terrestrial sediments, northwest Iceland. *Journal of Quaternary Science*, 17(8):731–745.

Andrews, J. T., Hardardóttir, J., Geirsdóttir, Á., and Helgadóttir, G. (2002b). Late Quaternary ice extent and glacial history from the Djúpáll trough, off Vestfirdir peninsula, north-west Iceland: a stacked 36 cal. Ky environmental record. *Polar Research*, 21(2):211–226.

Andrews, J. T. and Helgadóttir, G. (2003). Late Quaternary Ice Cap Extent and Deglaciation, Húnaflóaáll, Northwest Iceland: Evidence from Marine Cores. *Arctic, Antarctic, and Alpine Research*, 35(2):218–232.

Árnadóttir, T., Lund, B., Jiang, W., Geirsson, H., Björnsson, H., Einarsson, P., and Sigurdsson, T. (2009). Glacial rebound and plate spreading: results from the first countrywide GPS observations in Iceland. *Geophysical Journal International*, 177(2):691–716.

Batchelor, G. K. (2000). *An Introduction to Fluid Dynamics*. Cambridge Mathematical Library. Cambridge University Press.

Björnsson, H. and Pálsson, F. (2008). Icelandic glaciers. *Jökull*, 58:365–386.

Boulton, G., Thors, K., and Jarvis, J. (1988). Dispersal of glacially derived sediment over part of the continental shelf of south Iceland and the geometry of the resultant sediment bodies. *Marine Geology*, 83(1):193–223.

Brandon, A. D., Graham, D. W., Waight, T., and Gautason, B. (2007). ^{186}Os and ^{187}Os enrichments and high-^{3}He/^{4}He sources in the Earth's mantle: Evidence from Icelandic picrites. *Geochimica et Cosmochimica Acta*, 71(18):4570–4591.

Brandon, A. D., Snow, J. E., Walker, R. J., Morgan, J. W., and Mock, T. D. (2000). ^{190}Pt-^{186}Os and ^{187}Re-^{187}Os systematics of abyssal peridotites. *Earth and Planetary Science Letters*, 177(3):319–335.

Breddam, K., Kurz, M. D., and Storey, M. (2000). Mapping out the conduit of the Iceland mantle plume with helium isotopes. *Earth and Planetary Science Letters*, 176(1):45–55.

Burley, J. M. and Katz, R. F. (2015). Variations in mid-ocean ridge CO_2 emissions driven by glacial cycles. *Earth and Planetary Science Letters*, 426:246–258.

Burnard, P. and Harrison, D. (2005). Argon isotope constraints on modification of oxygen isotopes in Iceland Basalts by surficial processes. *Chemical Geology*, 216(1):143–156.

Chauvel, C. and Hémond, C. (2000). Melting of a complete section of recycled oceanic crust: Trace element and Pb isotopic evidence from Iceland. *Geochemistry, Geophysics, Geosystems*, 1(2):1–22.

Crowley, J. W., Katz, R. F., Huybers, P., Langmuir, C. H., and Park, S.-H. (2015). Glacial cycles drive variations in the production of oceanic crust. *Science*, 347(6227):1237–1240.

Darbyshire, F. A., White, R. S., and Priestley, K. F. (2000). Structure of the crust and uppermost mantle of Iceland from a combined seismic and gravity study. *Earth and Planetary Science Letters*, 181(3):409–428.

Debaille, V., Trønnes, R. G., Brandon, A. D., Waight, T. E., Graham, D. W., and Lee, C. T. A. (2009). Primitive off-rift basalts from Iceland and Jan Mayen: Os-isotopic evidence for a mantle source containing enriched subcontinental lithosphere. *Geochimica et Cosmochimica Acta*, 73(11):3423–3449.

Denton, G. H., Anderson, R. F., Toggweiler, J., Edwards, R., Schaefer, J., and Putnam, A. (2010). The Last Glacial Termination. *science*, 328(5986):1652–1656.

Dixon, E. T. (2003). Interpretation of helium and neon isotopic heterogeneity in Icelandic basalts. *Earth and Planetary Science Letters*, 206(1-2):83–99.

Eason, D. E., Sinton, J. M., Grönvold, K., and Kurz, M. D. (2015). Effects of deglaciation on the petrology and eruptive history of the Western Volcanic Zone, Iceland. *Bulletin of Volcanology*, 77(6).

Egloff, J. and Johnson, G. L. (1979). Erosional and depositional structures of the southwest Iceland insular margin: thirteen geophysical profiles. In: Watkins, J.S., Montadert, L., Dickerson, P.W. (Eds.), Geological and Geophysical Investigations of ContinentalMargins, Geological and Geophysical Investigations of Continental Margins. *American Association of Petroleum Geologists, Tulsa, Oklahoma*, pages 43–63.

Eiríksson, J., Símonarson, L., Knudsen, K., and Kristensen, P. (1997). Fluctuations of the weichselian ice sheet in SW Iceland: A glaciomarine sequence from sudurnes, seltjarnarnes. *Quaternary Science Reviews*, 16(2):221–240.

Eksinchol, I., Rudge, J. F., and Maclennan, J. (2019). Rate of Melt Ascent beneath Iceland from the Magmatic Response to Deglaciation. *Geochemistry, Geophysics, Geosystems*, 20.

Elderfield, H., Ferretti, P., Greaves, M., Crowhurst, S., McCave, I. N., Hodell, D., and Piotrowski, A. M. (2012). Evolution of ocean temperature and ice volume through the mid-Pleistocene climate transition. *Science*, 337:704–709.

Elliott, T. R., Hawkesworth, C. J., and Grönvold, K. (1991). Dynamic melting of the Iceland plume. *Nature*, 351(6323):201–206.

Fitton, J. G., Saunders, A. D., Kempton, P. D., and Hardarson, B. S. (2003). Does depleted mantle form an intrinsic part of the Iceland plume? *Geochemistry, Geophysics, Geosystems*, 4(3):1–14.

Flowers, G. E., Björnsson, H., Geirsdóttir, Á., Miller, G. H., Black, J. L., and Clarke, G. K. (2008). Holocene climate conditions and glacier variation in central Iceland from physical modelling and empirical evidence. *Quaternary Science Reviews*, 27(7):797–813.

Flowers, G. E., Björnsson, H., Geirsdóttir, Á., Miller, G. H., and Clarke, G. K. (2007). Glacier fluctuation and inferred climatology of Langjökull ice cap through the Little Ice Age. *Quaternary Science Reviews*, 26(19):2337–2353.

Flowers, G. E., Marshall, S. J., Björnsson, H., and Clarke, G. K. C. (2005). Sensitivity of Vatnajökull ice cap hydrology and dynamics to climate warming over the next 2 centuries. *Journal of Geophysical Research: Earth Surface*, 110(F2).

Füri, E., Hilton, D., Halldórsson, S., Barry, P., Hahm, D., Fischer, T., and Grönvold, K. (2010). Apparent decoupling of the He and Ne isotope systematics of the Icelandic mantle: The role of He depletion, melt mixing, degassing fractionation and air interaction. *Geochimica et Cosmochimica Acta*, 74(11):3307–3332.

Gee, M. A. M., Taylor, R. N., Thirlwall, M. F., and Murton, B. J. (1998). Glacioisostacy controls chemical and isotopic characteristics of tholeiites from the Reykjanes Peninsula, SW Iceland. *Earth and Planetary Science Letters*, 164(1-2):1–5.

Geirsdóttir, Á. (2011). Chapter 16 - Pliocene and Pleistocene Glaciations of Iceland: A Brief Overview of the Glacial History. In Ehlers, J., Gibbard, P. L., and Hughes, P. D., editors, *Quaternary Glaciations - Extent and Chronology*, volume 15 of *Developments in Quaternary Sciences*, pages 199–210. Elsevier.

Geirsdóttir, Á., Andrews, J. T., Ólafsdóttir, S., Helgadóttir, G., and Hardardóttir, J. (2002). A 36 Ky record of iceberg rafting and sedimentation from north-west Iceland. *Polar Research*, 21(2):291–298.

Geirsdóttir, Á., Hardardóttir, J., and Eiríksson, J. (1997). The Depositional History of the Younger Dryas-Preboreal Búdi Moraines in South-Central Iceland. *Arctic and Alpine Research*, 29(1):13–23.

Geirsdóttir, Á., Miller, G. H., Andrews, J. T., Harning, D. J., Anderson, L. S., Florian, C., Larsen, D. J., and Thordarson, T. (2019). The onset of neoglaciation in Iceland and the 4.2 ka event. *Climate of the Past*, 15(1):25–40.

Geirsdóttir, Á., Miller, G. H., Axford, Y., and Ólafsdóttir, S. (2009). Holocene and latest Pleistocene climate and glacier fluctuations in Iceland. *Quaternary Science Reviews*, 28(21):2107–2118. Holocene and Latest Pleistocene Alpine Glacier Fluctuations: A Global Perspective.

Ghiorso, M. S., Hirschmann, M. M., Reiners, P. W., and Kress III, V. C. (2002). The pMELTS: A revision of MELTS for improved calculation of phase relations and major element partitioning related to partial melting of the mantle to 3 GPa. *Geochemistry, Geophysics, Geosystems*, 3(5):1–35.

Grönvold, K., Óskarsson, N., Johnsen, S. J., Clausen, H. B., Hammer, C. U., Bond, G., and Bard, E. (1995). Ash layers from Iceland in the Greenland GRIP ice core correlated with oceanic and land sediments. *Earth and Planetary Science Letters*, 135(1):149–155.

Hardarson, B., Fitton, J., Ellam, R., and Pringle, M. (1997). Rift relocation—A geochemical and geochronological investigation of a palaeo-rift in northwest Iceland. *Earth and Planetary Science Letters*, 153(3-4):181–196.

Hemond, C., Arndt, N. T., Lichtenstein, U., Hofmann, A. W., Oskarsson, N., and Steinthorsson, S. (1993). The heterogeneous Iceland plume: Nd-Sr-O isotopes and trace element constraints. *Journal of Geophysical Research*, 98(B9):15833.

Hubbard, A., Sugden, D., Dugmore, A., Norddahl, H., and Pétursson, H. G. (2006). A modelling insight into the Icelandic Last Glacial Maximum ice sheet. *Quaternary Science Reviews*, 25(17-18):2283–2296.

Huppert, H. E. (1982). The propagation of two-dimensional and axisymmetric viscous gravity currents over a rigid horizontal surface. *Journal of Fluid Mechanics*, 121:43–58.

Ito, G., Shen, Y., Hirth, G., and Wolfe, C. J. (1999). Mantle flow, melting, and dehydration of the Iceland mantle plume. *Earth and Planetary Science Letters*, 165(1):81–96.

Jakobsson, S. P., Jónsson, J., and Shido, F. (1978). Petrology of the Western Reykjanes Peninsula, Iceland. *Journal of Petrology*, 19(4):669–705.

Jónasson, K. (2005). Magmatic evolution of the Heiðarsporður ridge, NE-Iceland. *Journal of Volcanology and Geothermal Research*, 147(1-2):109–124.

Jull, M. and McKenzie, D. (1996). The effect of deglaciation on mantle melting beneath Iceland. *Journal of Geophysical Research: Solid Earth*, 101(B10):21815–21828.

Kaban, M. K., Flóvenz, Ó. G., and Pálmason, G. (2002). Nature of the crust-mantle transition zone and the thermal state of the upper mantle beneath Iceland from gravity modelling. *Geophysical Journal International*, 149(2):281–299.

Katz, R. F., Spiegelman, M., and Langmuir, C. H. (2003). A new parameterization of hydrous mantle melting. *Geochemistry, Geophysics, Geosystems*, 4(9).

Kelemen, P. B., Braun, M., and Hirth, G. (2000). Spatial distribution of melt conduits in the mantle beneath oceanic spreading ridges: Observations from the Ingalls and Oman ophiolites. *Geochemistry, Geophysics, Geosystems*, 1(7).

Kelemen, P. B., Dick, H. J. B., and Quick, J. E. (1992). Formation of harzburgite by pervasive melt/rock reaction in the upper mantle. *Nature*, 358(6388):635–641.

Kelemen, P. B., Hirth, G., Shimizu, N., Spiegelman, M., and Dick, H. J. B. (1997). A review of melt migration processes in the adiabatically upwelling mantle beneath oceanic spreading ridges. *Philosophical Transactions of the Royal Society of London. Series A: Mathematical, Physical and Engineering Sciences*, 355(1723):283–318.

Kelemen, P. B., Whitehead, J. A., Aharonov, E., and Jordahl, K. A. (1995). Experiments on flow focusing in soluble porous media, with applications to melt extraction from the mantle. *Journal of Geophysical Research: Solid Earth*, 100(B1):475–496.

Kempton, P., Fitton, J., Saunders, A., Nowell, G., Taylor, R., Hardarson, B., and Pearson, G. (2000). The Iceland plume in space and time: a Sr-Nd-Pb-Hf study of the North Atlantic rifted margin. *Earth and Planetary Science Letters*, 177(3):255–271.

Kokfelt, T. F., Hoernle, K., Hauff, F., Fiebig, J., Werner, R., and Garbe-Schönberg, D. (2006). Combined trace element and Pb-Nd-Sr-O isotope evidence for recycled oceanic crust (upper and lower) in the Iceland mantle plume. *Journal of Petrology*, 47(9):1705–1749.

Koornneef, J. M., Stracke, A., Bourdon, B., and Grönvold, K. (2012). The influence of source heterogeneity on the U-Th-Pa-Ra disequilibria in post-glacial tholeiites from Iceland. *Geochimica et Cosmochimica Acta*, 87:243–266.

Licciardi, J. M., Kurz, M. D., and Curtice, J. M. (2007). Glacial and volcanic history of Icelandic table mountains from cosmogenic ^{3}He exposure ages. *Quaternary Science Reviews*, 26(11-12):1529–1546.

Lisiecki, L. E. and Raymo, M. E. (2005). A Pliocene-Pleistocene stack of 57 globally distributed benthic δ18O records. *Paleoceanography*, 20(1).

Maclennan, J. (2008). Concurrent mixing and cooling of melts under Iceland. *Journal of Petrology*, 49(11):1931–1953.

Maclennan, J., Hulme, T., and Singh, S. C. (2004). Thermal models of oceanic crustal accretion: Linking geophysical, geological and petrological observations. *Geochemistry, Geophysics, Geosystems*, 5(2).

Maclennan, J., Jull, M., McKenzie, D., Slater, L., and Grönvold, K. (2002). The link between volcanism and deglaciation in Iceland. *Geochemistry, Geophysics, Geosystems*, 3(11):1–25.

Maclennan, J., Mckenzie, D., and Gronvöld, K. (2001). Plume-driven upwelling under central Iceland. *Earth and Planetary Science Letters*, 194(1-2):67–82.

Maclennan, J., McKenzie, D., Gronvöld, K., Shimizu, N., Eiler, J. M., and Kitchen, N. (2003). Melt mixing and crystallization under Theistareykir, northeast Iceland. *Geochemistry, Geophysics, Geosystems*, 4(11).

Macpherson, C. G., Hilton, D. R., Day, J. M., Lowry, D., and Grönvold, K. (2005). High-$^3He/^4He$, depleted mantle and low-$\delta^{18}O$, recycled oceanic lithosphere in the source of central Iceland magmatism. *Earth and Planetary Science Letters*, 233(3):411–427.

Marino, G., Rohling, E., Rodríguez-Sanz, L., Grant, K., Heslop, D., Roberts, A., Stanford, J., and Yu, J. (2015). Bipolar seesaw control on last interglacial sea level. *Nature*, 522(7555):197.

McDonald, A. (1984). Accuracy of Multiply-Upstream, Semi-Lagrangian Advective Schemes. *Monthly Weather Review*, 112(6):1267–1275.

McDonald, A. (1987). Accuracy of Multiply-Upstream Semi-Lagrangian Advective Schemes II. *Monthly Weather Review*, 115(7):1446–1450.

McKenzie, D. (1984). The Generation and Compaction of Partially Molten Rock. *Journal of Petrology*, 25(3):713–765.

McKenzie, D. and Bickle, M. J. (1988). The Volume and Composition of Melt Generated by Extension of the Lithosphere. *Journal of Petrology*, 29(3):625–679.

McKenzie, D. and O'Nions, R. K. (1991). Partial Melt Distributions from Inversion of Rare Earth Element Concentrations. *Journal of Petrology*, 32:1021–1091.

Michell, J. H. (1899). On the Direct Determination of Stress in an Elastic Solid, with application to the Theory of Plates. *Proceedings of the London Mathematical Society*, s1-31(1):100–124.

Miller, K. J., lu Zhu, W., Montési, L. G., and Gaetani, G. A. (2014). Experimental quantification of permeability of partially molten mantle rock. *Earth and Planetary Science Letters*, 388:273–282.

Nicholson, H. (1990). *The Magmatic Evolution of Krafla, NE Iceland*. PhD thesis, University of Edinburgh.

Nicholson, H., Condomines, M., Fitton, J. G., Fallick, A. E., Grönvold, K., and Rogers, G. (1991). Geochemical and Isotopic Evidence for Crustal Assimilation Beneath Krafla, Iceland. *Journal of Petrology*, 32(5):1005–1020.

Nielsen, S. G., Rehkämper, M., Brandon, A. D., Norman, M. D., Turner, S., and O'Reilly, S. Y. (2007). Thallium isotopes in Iceland and Azores lavas — Implications for the role of altered crust and mantle geochemistry. *Earth and Planetary Science Letters*, 264(1-2):332–345.

Norðdahl, H. and Pétursson, H. G. (2005). 3. Relative sea-level changes in Iceland: new aspects of the Weichselian deglaciation of Iceland. In Caseldine, C., Russell, A., Harðardóttir, J., and Knudsen, Ó., editors, *Iceland — Modern Processes and Past Environments*, volume 5 of *Developments in Quaternary Sciences*, pages 25–78. Elsevier.

Pagli, C., Sigmundsson, F., Lund, B., Sturkell, E., Geirsson, H., Einarsson, P., Árnadóttir, T., and Hreinsdóttir, S. (2007). Glacio-isostatic deformation around the Vatnajókull ice cap, Iceland, induced by recent climate warming: GPS observations and finite element modeling. *Journal of Geophysical Research: Solid Earth*, 112(B8).

Past Interglacials Working Group of PAGES (2016). Interglacials of the last 800,000 years. *Reviews of Geophysics*, 54(1):162–219.

Paterson, W. (1994). *The Physics of Glaciers*. Pergamon, Amsterdam, third edition.

Patton, H., Hubbard, A., Bradwell, T., and Schomacker, A. (2017). The configuration, sensitivity and rapid retreat of the Late Weichselian Icelandic ice sheet. *Earth-Science Reviews*, 166:223–245.

Peate, D. W., Baker, J. A., Jakobsson, S. P., Waight, T. E., Kent, A. J., Grassineau, N. V., and Skovgaard, A. C. (2009). Historic magmatism on the Reykjanes Peninsula, Iceland: A snap-shot of melt generation at a ridge segment. *Contributions to Mineralogy and Petrology*, 157(3):359–382.

Peate, D. W., Breddam, K., Baker, J. A., Kurz, M. D., Barker, A. K., Prestvik, T., Grassineau, N., and Skovgaard, A. C. (2010). Compositional characteristics and spatial distribution of enriched Icelandic mantle components. *Journal of Petrology*, 51(7):1447–1475.

Pétursson, H., Norðdahl, H., and Ingólfsson, Ó. (2015). Late Weichselian history of relative sea level changes in Iceland during a collapse and subsequent retreat of marine based ice sheet. *Cuadernos de Investigación Geográfica*, 41(2):261–277.

Press, W. H., Teukolsky, S. A., Vetterling, W. T., and Flannery, B. P. (2007). *Numerical Recipes 3rd Edition: The Art of Scientific Computing*. Cambridge University Press, New York, NY, USA, 3 edition.

Principato, S. M., Jennings, A. E., Kristjaánsdóttir, G. B., and Andrews, J. T. (2005). Glacial-Marine or Subglacial Origin of Diamicton Units from the Southwest and North Iceland Shelf: Implications for the Glacial History of Iceland. *Journal of Sedimentary Research*, 75:968–983.

Quick, J. E. (1982). The origin and significance of large, tabular dunite bodies in the Trinity peridotite, northern California. *Contributions to Mineralogy and Petrology*, 78(4):413–422.

Rees Jones, D. W. and Katz, R. F. (2018). Reaction-infiltration instability in a compacting porous medium. *Journal of Fluid Mechanics*, 852:5–36.

Rohling, E., Grant, K., Bolshaw, M., Roberts, A., Siddall, M., Hemleben, C., and Kucera, M. (2009). Antarctic temperature and global sea level closely coupled over the past five glacial cycles. *Nature Geoscience*, 2:500–504.

Rudge, J. F. (2018). Textural equilibrium melt geometries around tetrakaidecahedral grains. *Proceedings of the Royal Society A: Mathematical, Physical and Engineering Sciences*, 474(2212):20170639.

Rudge, J. F., Maclennan, J., and Stracke, A. (2013). The geochemical consequences of mixing melts from a heterogeneous mantle. *Geochimica et Cosmochimica Acta*, 114:112–143.

Sæmundsson, K. (1991). Jardfrædi Kröflukerfisins. In: Gardarsson A, Einarsson A (eds) Náttúra Mývatns. *Hid islenska náttúrufrædifélg, Reykjavík*, pages 24–95.

Sæmundsson, K., Hjartarson, Á., Kaldal, I., Sigurgeirsson, M. Á., Kristinsson, S. G., and Víkingsson, S. (2012). Geological Map of Northern Volcanic Zone, Iceland. Northern Part. 1:100 000. Reykjavík: Iceland GeoSurvey and Landsvirkjun.

Sæmundsson, K., Sigurgeirsson, M. Á., Hjartarson, Á., Kaldal, I., and Kristinsson, S. G. (2016). Geological Map of of Southwest Iceland, 1:100 000 (2nd ed.). Reykjavík: Iceland GeoSurvey.

Schmidt, P., Lund, B., Hieronymus, C., Maclennan, J., Árnadóttir, T., and Pagli, C. (2013). Effects of present-day deglaciation in Iceland on mantle melt production rates. *Journal of Geophysical Research: Solid Earth*, 118(7):3366–3379.

Shaw, D. M. (1970). Trace element fractionation during anatexis. *Geochimica et Cosmochimica Acta*, 34(2):237–243.

Shen, Y., Solomon, S. C., Bjarnason, I. T., Nolet, G., Morgan, W., Allen, R. M., Vogfjörd, K., Jakobsdóttir, S., Stefánsson, R., Julian, B., and Foulger, G. (2002). Seismic evidence for a tilted mantle plume and north–south mantle flow beneath Iceland. *Earth and Planetary Science Letters*, 197(3):261–272.

Shorttle, O., Maclennan, J., and Jones, S. M. (2010). Control of the symmetry of plume-ridge interaction by spreading ridge geometry. *Geochemistry, Geophysics, Geosystems*, 11(7).

Shorttle, O., Maclennan, J., and Piotrowski, A. M. (2013). Geochemical provincialism in the Iceland plume. *Geochimica et Cosmochimica Acta*, 122:363–397.

Sigmundsson, F. (1991). Post-glacial rebound and asthenosphere viscosity in Iceland. *Geophysical Research Letters*, 18(6):1131–1134.

Sigurdsson, H., Schilling, J.-G., and Meyer, P. S. (1978). Skagi and Langjökull Volcanic Zones in Iceland: 1. Petrology and structure. *Journal of Geophysical Research*, 83(B8):3971.

Sigvaldason, G. E., Annertz, K., and Nilsson, M. (1992). Effect of glacier loading/deloading on volcanism: postglacial volcanic production rate of the Dyngjufjöll area, central Iceland. *Bulletin of Volcanology*, 54(5):385–392.

Sims, K. W., Maclennan, J., Blichert-Toft, J., Mervine, E. M., Blusztajn, J., and Grönvold, K. (2013). Short length scale mantle heterogeneity beneath Iceland probed by glacial modulation of melting. *Earth and Planetary Science Letters*, 379:146–157.

Sinton, J., Grönvold, K., and Sæmundsson, K. (2005). Postglacial eruptive history of the Western Volcanic Zone, Iceland. *Geochemistry, Geophysics, Geosystems*, 6(12).

Skovgaard, A. C., Storey, M., Baker, J., Blusztajn, J., and Hart, S. R. (2001). Osmium-oxygen isotopic evidence for a recycled and strongly depleted component in the Iceland mantle plume. *Earth and Planetary Science Letters*, 194(1-2):259–275.

Slater, L., Jull, M., McKenzie, D., and Gronvöld, K. (1998). Deglaciation effects on mantle melting under Iceland: Results from the Northern Volcanic Zone. *Earth and Planetary Science Letters*, 164(1-2):151–164.

Slater, L., McKenzie, D., Grönvold, K., and Shimizu, N. (2001). Melt Generation and Movement beneath Theistareykir, NE Iceland. *Journal of Petrology*, 42(2):321–354.

Smith, P. M. and Asimow, P. D. (2005). Adiabat_1ph: A new public front-end to the MELTS, pMELTS, and pHMELTS models. *Geochemistry, Geophysics, Geosystems*, 6(2).

Sólnes, J., Ásgeirsson, Á., Bessason, B., and Sigmundsson, F. (2013). Reykjavík: Viðlagatrygging/ Háskólaútgáfan. *Náttúruvá Á Íslandi, Eldgos og Jarðskjálftar*.

Spagnolo, M. and Clark, C. (2009). A geomorphological overview of glacial landforms on the Icelandic continental shelf. *Journal of Maps*, pages 37–52.

Spiegelman, M. (1996). Geochemical consequences of melt transport in 2-D: The sensitivity of trace elements to mantle dynamics. *Earth and Planetary Science Letters*, 139(1):115–132.

Spiegelman, M. and McKenzie, D. (1987). Simple 2-D models for melt extraction at mid-ocean ridges and island arcs. *Earth and Planetary Science Letters*, 83(1-4):137–152.

Staniforth, A. and Côté, J. (1991). Semi-Lagrangian Integration Schemes for Atmospheric Models–A Review. *Monthly Weather Review*, 119(9):2206–2223.

Stolper, E. and Asimow, P. (2007). Insights into mantle melting from graphical analysis of one-component systems. *American Journal of Science*, 307(8):1051–1139.

Stracke, A., Zindler, A., Salters, V. J., McKenzie, D., Janne, B. T., Albarède, F., and Grönvold, K. (2003). Theistareykir revisited. *Geochemistry, Geophysics, Geosystems*, 4(2).

Swindles, G. T., Watson, E. J., Savov, I. P., Lawson, I. T., Schmidt, A., Hooper, A., Cooper, C. L., Connor, C. B., Gloor, M., and Carrivick, J. L. (2017). Climatic control on Icelandic volcanic activity during the mid-Holocene. *Geology*, 46(1):47–50.

Syvitski, J. P., Jennings, A. E., and Andrews, J. T. (1999). High-Resolution Seismic Evidence for Multiple Glaciation across the Southwest Iceland Shelf. *Arctic, Antarctic, and Alpine Research*, 31(1):50–57.

Thirlwall, M. F., Gee, M. A., Lowry, D., Mattey, D. P., Murton, B. J., and Taylor, R. N. (2006). Low δ^{18}O in the Icelandic mantle and its origins: Evidence from Reykjanes Ridge and Icelandic lavas. *Geochimica et Cosmochimica Acta*, 70(4):993–1019.

Thirlwall, M. F., Gee, M. A., Taylor, R. N., and Murton, B. J. (2004). Mantle components in Iceland and adjacent ridges investigated using double-spike Pb isotope ratios. *Geochimica et Cosmochimica Acta*, 68(2):361–386.

Thordarson, T. and Höskuldsson, Á. (2008). Postglacial volcanism in Iceland. *Jökull*, 58:197–228.

Thordarson, T. and Höskuldsson, Á. (2014). *Iceland (Classic Geology in Europe)*. Dunedin Academic Press, Edinburgh, EH1 3QB, UK, 2 edition.

Thordarson, T. and Larsen, G. (2007). Volcanism in Iceland in historical time: Volcano types, eruption styles and eruptive history. *Journal of Geodynamics*, 43(1):118–152. Hotspot Iceland.

Werner, R. (1994). Struktur und Entstehung subglazialer/sublakustrischer Vulkane am Beispiel des Vulkankomplexes Herdubreid/Herdubreidartögl in Island.

White, R. S., McKenzie, D., and O'Nions, R. K. (1992). Oceanic crustal thickness from seismic measurements and rare earth element inversions. *Journal of Geophysical Research: Solid Earth*, 97(B13):19683–19715.

Wolfe, C. J., Th. Bjarnason, I., VanDecar, J. C., and Solomon, S. C. (1997). Seismic structure of the Iceland mantle plume. *Nature*, 385(6613):245–247.

Workman, R. K. and Hart, S. R. (2005). Major and trace element composition of the depleted MORB mantle (DMM). *Earth and Planetary Science Letters*, 231(1-2):53–72.

Appendix A

Data of Rock Samples

Table A.1 Rock sample data from eruption units in the Northern Volcanic Zones used in Chapter 5. Name of each eruption unit is in bold font with the estimated eruption volume and age bounds following after when available. V_c and La_c are the eruption volume and the La concentration after the crystallization correction (see Section 5.4.2).

Eruption Sample	Reference	Lat. (deg.)	Lon. (deg.)	MgO (wt%)	La (ppm)	V_c (km^3)	La_c (ppm)
Arnahvammurhraun 0.01 km^3 8500–10300 yrBP							
408643	Breddam et al. (2000); Peate et al. (2010); Skovgaard et al. (2001)	65.95	-17.11	12.54	1.0	0.01	0.94
l9371	Slater et al. (2001); Stracke et al. (2003)	65.95	-17.11	9.84	1.6	0.01	1.38
l9372	Slater et al. (2001); Stracke et al. (2003)	65.95	-17.13	11.24	1.36	0.01	1.23
l9378	Slater et al. (2001); Stracke et al. (2003)	65.94	-17.1	9.68	1.73	0.01	1.48
Baejarfjall 1.0 km^3 11000–30000 yrBP							
l9319	Maclennan et al. (2001)	65.86	-16.92	8.01	8.3	2.34	3.55
l9320	Maclennan et al. (2001)	65.86	-16.93	8.79	6.95	1.73	4.02
Bondholshraun 0.2 km^3 7000–11300 yrBP							
58	Hardarson et al. (1997); Kempton et al. (2000)	65.73	-16.78	10.69	2.08	0.23	1.85
H129	Kokfelt et al. (2006)	65.77	-16.97	10.39	2.15	0.23	1.89

Table A.1 Continued:

Eruption Sample	Reference	Lat. (deg.)	Lon. (deg.)	MgO (wt%)	La (ppm)	V_c (km^3)	La_c (ppm)
l9332	Slater et al. (2001); Stracke et al. (2003)	65.77	-17.03	10.79	2.17	0.22	1.93
l9333	Slater et al. (2001); Stracke et al. (2003)	65.77	-17.03	11.1	2.1	0.22	1.89
l9334	Slater et al. (2001)	65.77	-17.01	11.14	2.26	0.22	2.04
l9369	Slater et al. (2001)	65.76	-16.98	11.24	2.16	0.22	1.95
l9497	Slater et al. (2001)	65.75	-16.93	10.69	2.1	0.23	1.86
l9499	Slater et al. (2001); Stracke et al. (2003)	65.76	-17.04	11.38	2.1	0.22	1.91
Borgarhraun 0.9 km^3 8000–10000 yrBP							
FH9801	Maclennan et al. (2003)	65.881	-16.985	11.39	1.66	0.99	1.51
FH9804	Maclennan et al. (2003)	65.884	-16.985	11.92	1.79	0.97	1.66
FH9805	Maclennan et al. (2003)	65.884	-16.975	11.46	1.63	0.99	1.49
FH9807	Maclennan et al. (2003)	65.882	-16.977	10.73	1.55	1.01	1.38
FH9808	Maclennan et al. (2003)	65.877	-16.969	11.41	1.63	0.99	1.48
FH9810	Maclennan et al. (2003)	65.814	-16.988	12.18	1.64	0.96	1.53
FH9812	Maclennan et al. (2003)	65.813	-16.981	11.21	1.74	1.0	1.57
FH9813	Maclennan et al. (2003)	65.814	-17.0	12.94	1.82	0.94	1.75
FH9814	Maclennan et al. (2003)	65.814	-17.008	12.48	1.62	0.95	1.53
FH9815	Maclennan et al. (2003)	65.814	-17.008	12.62	1.74	0.95	1.65
FH9817	Maclennan et al. (2003)	65.814	-17.014	12.39	1.67	0.96	1.57
FH9818	Maclennan et al. (2003)	65.816	-17.019	11.48	1.67	0.99	1.52
FH9819	Maclennan et al. (2003)	65.817	-17.021	12.13	1.67	0.96	1.56
FH9820	Maclennan et al. (2003)	65.815	-17.023	13.0	1.42	0.93	1.37
FH9821	Maclennan et al. (2003)	65.801	-17.022	11.29	1.8	0.99	1.63
FH9822	Maclennan et al. (2003)	65.803	-17.027	12.11	1.78	0.97	1.66
FH9823	Maclennan et al. (2003)	65.804	-17.025	11.23	1.75	1.0	1.58
FH9824	Maclennan et al. (2003)	65.807	-17.025	11.33	1.63	0.99	1.48
FH9825	Maclennan et al. (2003)	65.835	-17.059	13.25	1.5	0.93	1.46
FH9826	Maclennan et al. (2003)	65.835	-17.059	12.08	1.88	0.97	1.75
FH9827	Maclennan et al. (2003)	65.835	-17.059	11.33	1.79	0.99	1.62
FH9828	Maclennan et al. (2003)	65.834	-17.058	11.51	1.82	0.99	1.66
FH9829	Maclennan et al. (2003)	65.835	-17.058	11.37	1.85	0.99	1.68
FH9830	Maclennan et al. (2003)	65.834	-17.037	11.05	1.51	1.0	1.36

Table A.1 Continued:

Eruption Sample	Reference	Lat. (deg.)	Lon. (deg.)	MgO (wt%)	La (ppm)	V_c (km^3)	La_c (ppm)
FH9831	Maclennan et al. (2003)	65.833	-17.038	11.31	1.67	0.99	1.51
FH9833	Maclennan et al. (2003)	65.83	-17.032	11.84	1.66	0.97	1.53
FH9834	Maclennan et al. (2003)	65.83	-17.032	11.35	1.68	0.99	1.52
FH9835	Maclennan et al. (2003)	65.83	-17.019	12.73	1.65	0.94	1.57
FH9836	Maclennan et al. (2003)	65.831	-17.012	11.42	1.58	0.99	1.44
FH9837	Maclennan et al. (2003)	65.834	-17.007	11.44	1.6	0.99	1.46
FH9838	Maclennan et al. (2003)	65.838	-17.011	11.97	1.55	0.97	1.44
FH9839	Maclennan et al. (2003)	65.84	-17.018	11.86	1.43	0.97	1.32
FH9840	Maclennan et al. (2003)	65.844	-17.028	11.88	1.53	0.97	1.41
FH9841	Maclennan et al. (2003)	65.844	-17.048	11.02	1.55	1.0	1.39
FH9842	Maclennan et al. (2003)	65.843	-17.054	11.99	1.57	0.97	1.46
FH9843	Maclennan et al. (2003)	65.842	-17.056	11.55	1.65	0.98	1.51
FH9844	Maclennan et al. (2003)	65.835	-17.054	12.03	1.66	0.97	1.54
FH9845	Maclennan et al. (2003)	65.833	-17.055	13.3	1.52	0.92	1.48
FH9846	Maclennan et al. (2003)	65.845	-17.054	11.48	1.46	0.99	1.33
FH9847	Maclennan et al. (2003)	65.849	-17.057	10.76	1.76	1.01	1.57
FH9848	Maclennan et al. (2003)	65.854	-17.046	10.71	1.81	1.01	1.61
FH9849	Maclennan et al. (2003)	65.859	-17.04	11.78	1.55	0.98	1.43
FH9850	Maclennan et al. (2003)	65.865	-17.032	12.1	1.64	0.97	1.53
FH9851	Maclennan et al. (2003)	65.868	-17.028	11.37	1.62	0.99	1.47
FH9852	Maclennan et al. (2003)	65.871	-16.987	11.48	1.75	0.99	1.6
FH9853	Maclennan et al. (2003)	65.863	-16.998	11.74	1.56	0.98	1.44
FH9854	Maclennan et al. (2003)	65.821	-16.973	12.82	1.78	0.94	1.7
FH9855	Maclennan et al. (2003)	65.82	-16.962	12.45	1.69	0.95	1.59
FH9856	Maclennan et al. (2003)	65.821	-16.931	12.2	1.7	0.96	1.59
FH9857	Maclennan et al. (2003)	65.825	-16.876	12.86	1.77	0.94	1.7
FH9858	Maclennan et al. (2003)	65.825	-16.881	11.6	1.72	0.98	1.57
FH9859	Maclennan et al. (2003)	65.825	-16.881	12.01	1.81	0.97	1.68
FH9860	Maclennan et al. (2003)	65.833	-16.9	11.86	1.86	0.97	1.72
FH9861	Maclennan et al. (2003)	65.838	-16.891	11.35	1.92	0.99	1.74
FH9862	Maclennan et al. (2003)	65.839	-16.884	12.42	1.74	0.95	1.64
FH9863	Maclennan et al. (2003)	65.784	-17.045	12.3	1.74	0.96	1.63
FH9864	Maclennan et al. (2003)	65.788	-17.047	12.22	1.75	0.96	1.64
FH9865	Maclennan et al. (2003)	65.791	-17.045	12.18	1.82	0.96	1.7
FH9866	Maclennan et al. (2003)	65.794	-17.034	12.03	1.72	0.97	1.6

Table A.1 Continued:

Eruption Sample	Reference	Lat. (deg.)	Lon. (deg.)	MgO (wt%)	La (ppm)	V_c (km^3)	La_c (ppm)
FH9867	Maclennan et al. (2003)	65.808	-16.984	11.68	1.72	0.98	1.58
FH9868	Maclennan et al. (2003)	65.812	-16.948	11.91	1.74	0.97	1.61
FH9869	Maclennan et al. (2003)	65.813	-16.955	13.03	1.57	0.93	1.51
FH9870	Maclennan et al. (2003)	65.814	-16.963	11.83	1.61	0.98	1.49
FH9871	Maclennan et al. (2003)	65.815	-16.974	11.71	1.73	0.98	1.59
FH9872	Maclennan et al. (2003)	65.817	-16.981	11.96	1.78	0.97	1.65
FH9873	Maclennan et al. (2003)	65.826	-16.975	12.98	1.48	0.94	1.42
FH9874	Maclennan et al. (2003)	65.827	-16.973	11.52	1.78	0.99	1.62
FH9875	Maclennan et al. (2003)	65.851	-16.999	11.92	1.62	0.97	1.5
FH9876	Maclennan et al. (2003)	65.851	-16.999	11.43	1.62	0.99	1.47
FH9877	Maclennan et al. (2003)	65.853	-17.015	10.91	1.83	1.01	1.64
H127	Kokfelt et al. (2006)	65.85	-17.0	11.04	1.66	1.0	1.49
TH15	Hemond et al. (1993)	65.7	-16.87	19.17	1.61	0.72	2.01
TH40	Peate et al. (2010); Skovgaard et al. (2001)	65.83	-16.87	18.84	1.5	0.73	1.84
TH40elliott	Elliott et al. (1991); Slater et al. (2001)	65.84	-17.05	18.9	1.2	0.73	1.48
TH40xrf	Slater et al. (2001)	65.84	-17.05	13.8	1.73	0.91	1.72
l9304	Slater et al. (2001)	65.83	-16.87	10.3	2.11	1.03	1.85
l9305	Slater et al. (2001)	65.83	-16.87	10.22	2.09	1.03	1.82
l9306	Slater et al. (2001); Stracke et al. (2003)	65.83	-16.87	10.19	1.93	1.03	1.68
l9307	Slater et al. (2001)	65.83	-16.87	10.81	1.93	1.01	1.72
l9308	Slater et al. (2001)	65.83	-16.87	9.89	2.79	1.04	2.41
l9309	Slater et al. (2001); Stracke et al. (2003)	65.83	-16.9	12.33	1.81	0.96	1.7
l9310	Slater et al. (2001)	65.82	-16.9	12.7	1.87	0.95	1.78
l9311	Slater et al. (2001); Stracke et al. (2003)	65.83	-16.88	13.2	1.55	0.93	1.5
l9312	Slater et al. (2001)	65.83	-16.88	13.26	2.26	0.93	2.2
l9313	Slater et al. (2001); Stracke et al. (2003)	65.83	-16.88	15.76	1.47	0.84	1.58
l9314	Slater et al. (2001)	65.83	-16.88	13.23	1.7	0.93	1.65
l9335	Slater et al. (2001)	65.79	-17.05	13.72	2.0	0.91	1.98
l9374	Slater et al. (2001)	65.86	-16.99	11.83	1.69	0.98	1.56

Table A.1 Continued:

Eruption Sample	Reference	Lat. (deg.)	Lon. (deg.)	MgO (wt%)	La (ppm)	V_c (km^3)	La_c (ppm)
l9375	Slater et al. (2001); Stracke et al. (2003)	65.96	-16.82	11.14	1.63	1.0	1.47
l9409	Slater et al. (2001); Stracke et al. (2003)	65.84	-17.05	12.17	1.48	0.96	1.38
l9435	Slater et al. (2001); Stracke et al. (2003)	65.84	-17.05	13.46	1.39	0.92	1.36
Burfell 3.14 km^3 10800–30000 yrBP							
NAL-458	Füri et al. (2010)	65.568	-16.643				
Burfellshraun 1.8 km^3 3150–3250 yrBP							
IC161	Hardarson et al. (1997)	65.6	-16.66	7.74	6.5	4.59	2.55
IC45	Hardarson et al. (1997); Kempton et al. (2000)	65.6	-16.66	7.37	7.56	5.11	2.66
NV44	Koornneef et al. (2012)	65.649	-16.75	7.72	6.7	4.62	2.61
Dalseldar 0.05 km^3 1050–1150 yrBP							
KK107	Nicholson et al. (1991)	65.67	-16.78	5.39	10.41	0.22	2.37
KK92	Nicholson et al. (1991)	65.64	-16.86	6.95	7.68	0.16	2.42
NV48	Koornneef et al. (2012)	65.664	-16.79	5.71	9.3	0.21	2.25
Earlypostglacialeruptions 0.01 km^3 8000–11000 yrBP							
KK144	Nicholson et al. (1991)	65.74	-16.85	5.39	11.0	0.04	2.51
KK154	Nicholson et al. (1991)	65.72	-16.85	5.61	7.72	0.04	1.83
KK156	Nicholson et al. (1991)	65.72	-16.85	5.71	7.88	0.04	1.9
KK66	Nicholson et al. (1991)	65.76	-16.73	5.45	10.4	0.04	2.4
KK93	Nicholson et al. (1991)	65.64	-16.83	5.45	10.08	0.04	2.32
Eilifur 0.01 km^3 12000–70000 yrBP							
l9343	Maclennan et al. (2001)	65.8	-16.617	7.43	7.55	0.03	2.7
Einbui 0.1 km^3 12000–70000 yrBP							
l9301	Maclennan et al. (2001)	65.83	-16.87	9.34	4.06	0.13	3.13
l9302	Maclennan et al. (2001)	65.83	-16.87	9.6	3.4	0.12	2.91
l9303	Maclennan et al. (2001)	65.83	-16.87	8.96	3.48	0.16	2.18

Table A.1 Continued:

Eruption Sample	Reference	Lat. (deg.)	Lon. (deg.)	MgO (wt%)	La (ppm)	V_c (km^3)	La_c (ppm)
Gaesafjoll 7.0 km^3 14400–30000 yrBP							
408718	Breddam et al. (2000); Peate et al. (2010)	65.754	-16.926	8.36	8.22	14.47	3.98
408719	Breddam et al. (2000); Peate et al. (2010)	65.754	-16.926	8.19	8.15	15.4	3.7
408722	Breddam et al. (2000); Peate et al. (2010)	65.759	-16.924	8.17	8.14	15.49	3.68
408723	Breddam et al. (2000); Peate et al. (2010)	65.759	-16.924	8.38	8.05	14.33	3.93
GAE01	Maclennan et al. (2004)	65.75	-16.927	12.04	7.83	7.53	7.28
GAE02	Maclennan et al. (2004)	65.75	-16.927	8.8	7.36	12.06	4.27
GAE03	Maclennan et al. (2004)	65.75	-16.927	8.58	8.31	13.27	4.38
GAE04	Maclennan et al. (2004)	65.749	-16.916	8.76	7.52	12.28	4.29
GAE05	Maclennan et al. (2004)	65.749	-16.916	11.29	7.34	7.73	6.64
GAE06	Maclennan et al. (2004)	65.749	-16.916	8.65	6.34	12.86	3.45
GAE07	Maclennan et al. (2004)	65.749	-16.917	9.08	7.29	10.52	4.85
GAE08	Maclennan et al. (2004)	65.749	-16.918	8.97	7.44	11.1	4.69
GAE09	Maclennan et al. (2004)	65.75	-16.918	11.32	6.67	7.72	6.05
GAE10	Maclennan et al. (2004)	65.75	-16.918	9.41	6.73	8.71	5.41
GAE11	Maclennan et al. (2004)	65.75	-16.923	8.23	8.72	15.17	4.02
GAE12	Maclennan et al. (2004)	65.751	-16.925	10.23	6.9	8.02	6.02
GAE13	Maclennan et al. (2004)	65.75	-16.926	10.45	6.87	7.96	6.05
GAE14	Maclennan et al. (2004)	65.783	-16.883	8.7	7.94	12.61	4.41
GAE15	Maclennan et al. (2004)	65.785	-16.876	8.43	7.58	14.06	3.77
GAE16	Maclennan et al. (2004)	65.785	-16.867	7.19	11.13	20.88	3.73
GAE17	Maclennan et al. (2004)	65.778	-16.854	8.34	7.33	14.57	3.52
GAE18	Maclennan et al. (2004)	65.776	-16.849	7.67	8.44	18.21	3.24
GAE19	Maclennan et al. (2004)	65.772	-16.846	7.12	7.61	21.23	2.51
GAE20	Maclennan et al. (2004)	65.772	-16.846	8.97	7.33	11.14	4.6
GAE21	Maclennan et al. (2004)	65.768	-16.849	7.82	7.99	17.42	3.21
GAE22	Maclennan et al. (2004)	65.763	-16.86	7.48	7.76	19.29	2.82
GAE23	Maclennan et al. (2004)	65.758	-16.873	7.83	7.69	17.34	3.1
GAE24	Maclennan et al. (2004)	65.761	-16.885	7.43	8.34	19.57	2.98
GAE25	Maclennan et al. (2004)	65.764	-16.897	7.4	8.38	19.7	2.98

Table A.1 Continued:

Eruption Sample	Reference	Lat. (deg.)	Lon. (deg.)	MgO (wt%)	La (ppm)	V_c (km^3)	La_c (ppm)
GAE26	Maclennan et al. (2004)	65.767	-16.91	8.33	7.74	14.61	3.71
GAE27	Maclennan et al. (2004)	65.778	-16.917	7.72	7.83	17.94	3.06
IC44A	Hardarson et al. (1997)	65.79	-16.92	10.3	4.7	8.0	4.11
IC44B	Hardarson et al. (1997)	65.79	-16.92	11.17	2.8	7.76	2.53
IC44C	Hardarson et al. (1997)	65.79	-16.92	14.41	5.3	6.89	5.38
KK151	Maclennan et al. (2001)	65.76	-16.93	8.38	7.37	14.34	3.6
KK30	Maclennan et al. (2001)	65.76	-16.93	9.56	6.9	8.2	5.89
l9362	Maclennan et al. (2001)	65.79	-16.92	11.74	7.19	7.61	6.62
l9363	Maclennan et al. (2001)	65.77	-16.92	9.12	7.44	10.29	5.06
l9364	Maclennan et al. (2001)	65.77	-16.85	7.57	8.14	18.78	3.03
l9463	Maclennan et al. (2001)	65.76	-16.93	11.88	6.05	7.57	5.59
l9491	Maclennan et al. (2001)	65.76	-16.93	8.9	7.2	11.5	4.38
Gjastykkisbunga 2.0 km^3 11500–12000 yrBP							
KK31	Nicholson et al. (1991)	65.79	-16.79	9.43	2.51	2.46	2.04
KK31r	Nicholson et al. (1991)	65.79	-16.79	9.43	2.33	2.46	1.9
KK58	Nicholson et al. (1991)	65.79	-16.79	9.82	2.18	2.32	1.88
Heidarspordur 0.3 km^3 10000–11000 yrBP							
KK116	Nicholson et al. (1991)	65.65	-16.79	8.35	3.9	0.62	1.88
KK52	Nicholson et al. (1991)	65.53	-16.81	9.15	3.2	0.43	2.21
KK53	Nicholson et al. (1991)	65.53	-16.82	9.19	2.06	0.42	1.46
KR45	Jónasson (2005)	65.6	-16.8	1.39	30.66	2.25	4.08
KR46	Jónasson (2005)	65.6	-16.81	2.45	26.3	2.01	3.93
KR86	Jónasson (2005)	65.61	-16.8	3.53	21.34	1.75	3.65
KR88	Jónasson (2005)	65.55	-16.81	8.91	3.44	0.49	2.1
KR90	Jónasson (2005)	65.64	-16.79	6.06	12.96	1.16	3.35
KR91	Jónasson (2005)	65.64	-16.78	5.58	9.44	1.27	2.23
Hofudreidarmuli 0.01 km^3 12000–15000 yrBP							
9370	Stracke et al. (2003)	65.959	-17.089	13.64	1.16	0.01	1.14
9376	Stracke et al. (2003)	65.942	-17.074	10.96	2.42	0.01	2.17
9377	Stracke et al. (2003)	65.942	-17.091	12.32	1.42	0.01	1.33
9395	Stracke et al. (2003)	65.959	-17.07	11.7	1.29	0.01	1.19
9476	Stracke et al. (2003)	65.932	-17.072	12.16	1.36	0.01	1.27

Table A.1 Continued:

Eruption Sample	Reference	Lat. (deg.)	Lon. (deg.)	MgO (wt%)	La (ppm)	V_c (km^3)	La_c (ppm)
Holseldar 0.15 km^3 2200–2600 yrBP							
KK113	Nicholson et al. (1991)	65.75	-16.73	6.42	7.26	0.54	2.03
KK114	Nicholson et al. (1991)	65.73	-16.72	6.57	7.79	0.52	2.25
KK123	Nicholson et al. (1991)	65.71	-16.72	6.37	8.11	0.54	2.24
Hrafntinnuhryggur 0.05 km^3 24000–30000 yrBP							
KK25	Hemond et al. (1993)	65.72	-16.73	1.53	42.8	0.37	5.78
KK29	Hemond et al. (1993)	65.72	-16.73	0.06	32.6	0.43	3.81
Hverfjall 0.4 km^3 2600–2700 yrBP							
KK149	Nicholson et al. (1991)	65.8	-16.8	6.31	7.4	1.47	2.02
HyaloclastiteRidges1.15km3 1.15 km^3 12000–70000 yrBP							
KK32	Nicholson et al. (1991)	65.78	-16.73	8.57	4.22	2.19	2.22
KK33	Nicholson et al. (1991)	65.78	-16.73	7.03	6.71	3.57	2.16
KK59	Nicholson et al. (1991)	65.63	-16.82	6.02	7.58	4.48	1.95
KK63	Nicholson et al. (1991)	65.73	-16.72	6.95	8.61	3.64	2.72
KK69	Nicholson et al. (1991)	65.78	-16.68	5.25	10.37	5.17	2.31
KK87	Nicholson et al. (1991)	65.65	-16.77	7.18	8.87	3.44	2.97
Ketilfjall 0.06 km^3 12000–70000 yrBP							
H125	Kokfelt et al. (2006)	65.89	-16.93	8.49	3.39	0.12	1.73
l9350	Maclennan et al. (2001)	65.9	-16.91	5.95	6.36	0.24	1.61
l94110	Maclennan et al. (2001)	65.9	-16.91	5.96	7.37	0.24	1.87
Klappahraun 0.5 km^3 12000–14500 yrBP							
408653	Peate et al. (2010); Skovgaard et al. (2001)	65.92	-16.92	11.36	0.41	0.55	0.37
KraflaMountain 0.3 km^3 14000–30000 yrBP							
KK21	Nicholson et al. (1991)	65.71	-16.73	9.06	5.78	0.46	3.81
KK22	Nicholson et al. (1991)	65.71	-16.73	7.42	6.17	0.84	2.2
Kroflueldar 0.25 km^3 25–35 yrBP							

Table A.1 Continued:

Eruption Sample	Reference	Lat. (deg.)	Lon. (deg.)	MgO (wt%)	La (ppm)	V_c (km^3)	La_c (ppm)
H131	Kokfelt et al. (2006)	65.66	-16.4	5.94	9.68	0.99	2.45
IC10	Nicholson et al. (1991)	65.71	-16.8	7.73	7.04	0.64	2.75
K8405	Nicholson et al. (1991)	65.72	-16.8	7.64	5.93	0.66	2.26
KRA01	Maclennan et al. (2004)	65.726	-16.853	5.95	9.71	0.99	2.46
KRA02	Maclennan et al. (2004)	65.725	-16.85	5.91	9.47	0.99	2.38
KRA03	Maclennan et al. (2004)	65.751	-16.84	5.96	9.59	0.99	2.43
KRA04	Maclennan et al. (2004)	65.751	-16.84	6.0	9.65	0.98	2.47
KRA05	Maclennan et al. (2004)	65.776	-16.766	7.58	7.07	0.67	2.65
KRA06	Maclennan et al. (2004)	65.776	-16.767	7.28	7.66	0.73	2.64
KRA07	Maclennan et al. (2004)	65.776	-16.767	7.27	7.7	0.73	2.64
KRA08	Maclennan et al. (2004)	65.781	-16.746	7.7	6.67	0.65	2.58
KRA09	Maclennan et al. (2004)	65.781	-16.746	7.64	6.74	0.66	2.56
KRA10	Maclennan et al. (2004)	65.805	-16.739	7.73	6.56	0.64	2.57
KRA11	Maclennan et al. (2004)	65.805	-16.739	7.7	6.92	0.65	2.68
KRA12	Maclennan et al. (2004)	65.806	-16.738	7.56	6.77	0.67	2.52
KRA13	Maclennan et al. (2004)	65.806	-16.738	7.71	6.37	0.64	2.47
KRA13	Maclennan et al. (2004)	65.806	-16.738	7.68	6.64	0.65	2.56
KRA13	Maclennan et al. (2004)	65.806	-16.738	7.7	6.67	0.64	2.59
KRA14	Maclennan et al. (2004)	65.845	-16.722	7.74	6.44	0.64	2.52
KRA15	Maclennan et al. (2004)	65.847	-16.72	7.71	6.59	0.64	2.56
KRA16	Maclennan et al. (2004)	65.833	-16.722	7.7	6.26	0.64	2.43
KRA17	Maclennan et al. (2004)	65.795	-16.821	7.54	6.62	0.68	2.44
KRA18	Maclennan et al. (2004)	65.795	-16.826	7.63	6.6	0.66	2.51
KRA19	Maclennan et al. (2004)	65.795	-16.83	7.54	7.05	0.68	2.6
KRA20	Maclennan et al. (2004)	65.795	-16.842	7.56	7.07	0.67	2.63
NV45	Koornneef et al. (2012)	65.718	-16.78	6.0	9.5	0.98	2.43
NV47	Koornneef et al. (2012)	65.716	-16.79	5.87	9.8	1.0	2.44
NV49	Koornneef et al. (2012)	65.795	-16.84	7.39	7.5	0.71	2.66
NV50	Koornneef et al. (2012)	65.795	-16.84	7.39	7.7	0.71	2.73
SNA-24	Nicholson et al. (1991)	65.83	-16.79	8.72	5.99	0.45	3.36
SNA26	Nicholson et al. (1991)	65.81	-16.76	7.76	6.92	0.63	2.73
k81	Hemond et al. (1993)	65.71	-16.815	7.03	6.78	0.78	2.18
Krofluhalshraun 1.0 km^3 8000–11000 yrBP							
9366	Stracke et al. (2003)	65.903	-16.487	5.49	11.3	4.31	2.62

Table A.1 Continued:

Eruption Sample	Reference	Lat. (deg.)	Lon. (deg.)	MgO (wt%)	La (ppm)	V_c (km^3)	La_c (ppm)
9396	Stracke et al. (2003)	65.903	-16.487	5.48	11.12	4.32	2.57
KK158	Nicholson et al. (1991)	65.78	-16.75	8.11	4.22	2.26	1.87
KK65	Nicholson et al. (1991)	65.76	-16.72	7.3	4.54	2.89	1.57
KK68	Nicholson et al. (1991)	65.77	-16.8	8.67	4.36	1.82	2.39
KK78	Nicholson et al. (1991)	65.81	-16.69	9.73	2.36	1.16	2.03
l9365	Nicholson et al. (1991)	65.79	-16.85	5.55	11.55	4.26	2.71
l9366	Nicholson et al. (1991)	65.79	-16.9	5.49	12.08	4.31	2.8
l9396	Nicholson et al. (1991)	65.82	-16.87	5.48	10.2	4.32	2.36
Kviholafjoll 0.06 km^3 12000–30000 yrBP							
l9315	Maclennan et al. (2001)	65.84	-16.95	9.62	5.17	0.07	4.42
l9316	Maclennan et al. (2001)	65.84	-16.93	9.8	5.46	0.07	4.7
l9317	Maclennan et al. (2001)	65.84	-16.92	9.86	5.15	0.07	4.44
l9318	Maclennan et al. (2001)	65.83	-16.92	9.97	4.7	0.07	4.07
Langaviti 0.8 km^3 8000–10000 yrBP							
408647	Breddam et al. (2000); Peate et al. (2010); Skovgaard et al. (2001)	65.88	-16.87	14.63	1.08	0.78	1.1
IT4elliott	Elliott et al. (1991); Slater et al. (2001)	65.88	-16.87	7.92	3.0	1.93	1.25
l9353	Slater et al. (2001); Stracke et al. (2003)	65.96	-16.84	8.39	3.92	1.63	1.92
l9354	Slater et al. (2001); Stracke et al. (2003)	65.94	-16.89	13.0	1.42	0.83	1.37
l9356	Slater et al. (2001); Stracke et al. (2003)	65.96	-16.9	14.35	0.88	0.79	0.89
l9367	Slater et al. (2001)	65.89	-16.87	9.72	2.55	0.93	2.19
l9368	Slater et al. (2001)	65.91	-16.86	9.45	2.25	0.97	1.86
l9393	Slater et al. (2001); Stracke et al. (2003)	65.93	-16.89	8.0	3.72	1.88	1.59
l9394	Slater et al. (2001); Stracke et al. (2003)	65.93	-16.87	13.83	1.39	0.81	1.38
l94112	Slater et al. (2001); Stracke et al. (2003)	65.94	-16.87	12.26	1.63	0.85	1.53

Table A.1 Continued:

Eruption Sample	Reference	Lat. (deg.)	Lon. (deg.)	MgO (wt%)	La (ppm)	V_c (km^3)	La_c (ppm)
l9412	Slater et al. (2001); Stracke et al. (2003)	65.89	-16.86	9.73	1.99	0.93	1.71
l9416	Slater et al. (2001); Stracke et al. (2003)	65.89	-16.87	9.43	2.02	0.98	1.65
Laxarhraun yngra 2.5 km^3 2100–2300 yrBP							
H16	Kokfelt et al. (2006)	65.87	-17.43	7.52	5.91	6.8	2.17
Myvatnseldar 0.25 km^3 270–271 yrBP							
KRA118	Nicholson et al. (1991)	65.72	-16.8	6.17	7.98	0.94	2.11
Namafjall 0.01 km^3 12000–70000 yrBP							
KK141	Nicholson et al. (1991)	65.67	-16.8	8.96	2.92	0.02	1.83
KK142	Nicholson et al. (1991)	65.67	-16.8	8.63	4.43	0.02	2.39
Picrites 0.01 km^3 12000–15000 yrBP							
408634	Breddam et al. (2000); Peate et al. (2010); Skovgaard et al. (2001)	65.93	-17.07	24.44	0.47	0.01	0.78
408635	Breddam et al. (2000); Peate et al. (2010); Skovgaard et al. (2001)	65.93	-17.07	20.23	0.36	0.01	0.47
9381	Stracke et al. (2003)	65.93	-17.07	18.76	0.56	0.01	0.69
ICE-6	Brandon et al. (2007); Debaille et al. (2009); Nielsen et al. (2007)	65.96	-17.069	12.59	1.57	0.01	1.49
TH29	Peate et al. (2010); Skovgaard et al. (2001)	65.93	-17.07	15.87	0.54	0.01	0.58
TH29elliott	Slater et al. (2001); Thirlwall et al. (2004)	65.93	-17.07	15.87	0.5	0.01	0.54
TH29id	Slater et al. (2001)	65.93	-17.07	20.24	0.47	0.01	0.62
l9390	Slater et al. (2001); Stracke et al. (2003)	65.93	-17.08	21.65	0.52	0.01	0.74
l9391	Slater et al. (2001); Stracke et al. (2003)	65.93	-17.07	20.19	0.45	0.01	0.59

Table A.1 Continued:

Eruption Sample	Reference	Lat. (deg.)	Lon. (deg.)	MgO (wt%)	La (ppm)	V_c (km^3)	La_c (ppm)
l9397	Slater et al. (2001); Stracke et al. (2003)	65.93	-17.08	20.23	0.49	0.01	0.64
th29	Fitton et al. (2003); Hemond et al. (1993)	65.95	-17.081	15.87	0.43	0.01	0.46
Raudholl 0.01 km^3 12000–70000 yrBP							
l9351	Maclennan et al. (2001)	65.96	-16.97	6.25	8.19	0.04	2.2
l9351A	Maclennan et al. (2001)	65.96	-16.97	6.15	9.12	0.04	2.4
Sandnabotnafjall 0.6 km^3 24000–70000 yrBP							
KK19	Nicholson et al. (1991)	65.69	-16.75	7.44	5.96	1.67	2.14
KK20	Nicholson et al. (1991)	65.69	-16.75	7.6	7.61	1.6	2.86
Skessuhraun 0.01 km^3 7500–8500 yrBP							
TH13elliott	Elliott et al. (1991); Slater et al. (2001)	65.92	-17.12	9.76	1.42	0.01	1.22
TH13id	Slater et al. (2001)	65.92	-17.12	9.29	2.03	0.01	1.52
Storavitishraun 18.4 km^3 11000–12000 yrBP							
408640	Breddam et al. (2000); Peate et al. (2010); Skovgaard et al. (2001)	65.88	-16.84	11.14	1.37	20.42	1.23
IT1elliott	Elliott et al. (1991); Slater et al. (2001)	65.88	-16.84	9.18	1.86	26.19	1.31
IT3Aelliott	Elliott et al. (1991); Slater et al. (2001)	65.88	-16.84	9.08	2.52	27.63	1.68
SH43xrf	Slater et al. (2001)	65.88	-16.84	9.61	2.73	21.51	2.34
TH03xrf	Slater et al. (2001)	65.93	-17.07	9.97	3.6	21.25	3.12
TH16xrf	Slater et al. (2001)	65.88	-16.84	8.93	3.26	29.79	2.01
THO5xrf	Slater et al. (2001)	65.93	-17.07	7.26	3.0	53.82	1.03
l9330xrf	Slater et al. (2001); Stracke et al. (2003)	65.79	-17.01	10.22	2.75	21.08	2.4
l9331	Slater et al. (2001)	65.79	-17.01	8.86	2.59	30.79	1.55
l9338	Slater et al. (2001)	65.96	-17.12	8.82	2.36	31.37	1.38

Table A.1 Continued:

Eruption Sample	Reference	Lat. (deg.)	Lon. (deg.)	MgO (wt%)	La (ppm)	V_c (km^3)	La_c (ppm)
l9339xrf	Slater et al. (2001); Stracke et al. (2003)	65.96	-17.02	8.42	2.25	37.13	1.12
l9352	Slater et al. (2001)	65.96	-16.93	8.28	1.52	39.14	0.71
l9358	Slater et al. (2001)	65.97	-17.15	8.81	2.23	31.51	1.3
l9359	Slater et al. (2001); Stracke et al. (2003)	65.96	-16.99	8.44	1.77	36.84	0.88
l9360	Slater et al. (2001)	65.94	-16.96	8.63	2.55	34.1	1.38
l9361	Slater et al. (2001)	65.94	-16.95	8.92	2.21	29.93	1.36
l9385	Slater et al. (2001); Stracke et al. (2003)	65.91	-17.06	8.35	1.98	38.13	0.96
l9388	Slater et al. (2001)	65.9	-17.06	8.15	1.92	41.01	0.86
l9389	Slater et al. (2001); Stracke et al. (2003)	65.93	-17.07	7.85	1.8	45.33	0.73
l94101	Slater et al. (2001); Stracke et al. (2003)	65.88	-16.84	10.54	1.92	20.85	1.69
l94102	Slater et al. (2001); Stracke et al. (2003)	65.88	-16.84	10.62	1.76	20.79	1.56
l94103	Slater et al. (2001)	65.88	-16.84	10.31	1.85	21.01	1.62
sh1	Slater et al. (2001)	65.88	-16.84	8.6	1.62	34.54	0.86
sh19	Slater et al. (2001)	65.88	-16.84	7.7	4.1	47.49	1.59
sh23	Slater et al. (2001)	65.88	-16.84	8.13	3.28	41.3	1.46
sh27	Slater et al. (2001)	65.88	-16.84	7.41	4.84	51.66	1.72
sh40	Slater et al. (2001)	65.88	-16.84	10.35	2.63	20.98	2.31
sh42	Slater et al. (2001)	65.88	-16.84	11.22	2.74	20.37	2.48
Theistareykirhraun 0.6 km^3 2300–2500 yrBP							
IT2elliott	Elliott et al. (1991); Slater et al. (2001)	65.96	-17.05	8.05	3.04	1.38	1.32
l9341	Slater et al. (2001)	65.96	-17.05	7.73	3.49	1.53	1.36
l9383	Slater et al. (2001); Stracke et al. (2003)	65.92	-17.05	7.44	2.89	1.67	1.04
l94116	Slater et al. (2001); Stracke et al. (2003)	65.94	-17.04	8.1	3.21	1.36	1.42
Thorunnarfjoll 0.2 km^3 12000–70000 yrBP							

Table A.1 Continued:

Eruption Sample	Reference	Lat. (deg.)	Lon. (deg.)	MgO (wt%)	La (ppm)	V_c (km^3)	La_c (ppm)
l9424A	Maclennan et al. (2001)	65.88	-16.92	8.08	10.07	0.46	4.41
l9454	Maclennan et al. (2001)	65.84	-16.86	8.07	9.99	0.46	4.36
l9455	Maclennan et al. (2001)	65.84	-16.86	7.63	10.13	0.53	3.84
Threngslaborgir 2.0 km^3 2300–2500 yrBP							
KK54	Nicholson et al. (1991)	65.52	-16.87	7.69	5.57	5.18	2.15
NV41	Koornneef et al. (2012)	65.575	-16.95	7.82	6.2	4.97	2.5
Thrihyrningur 0.06 km^3 12000–70000 yrBP							
l94100	Maclennan et al. (2001)	65.84	-16.83	6.84	12.9	0.2	3.97
l9420A	Maclennan et al. (2001)	65.84	-16.83	7.34	10.47	0.17	3.66
l9421	Maclennan et al. (2001)	65.84	-16.83	7.53	9.61	0.16	3.54

Table A.2 Rock sample data from eruption units in the Reykjanes Peninsula used in Chapter 5. Name of each eruption unit is in bold font with the estimated eruption volume and age bounds following after when available. V_c and La_c are the eruption volume and the La concentration after the crystallization correction (see Section 5.4.2).

Eruption Sample	Reference	Lat. (deg.)	Lon. (deg.)	MgO (wt%)	La (ppm)	V_c (km^3)	La_c (ppm)
Afstaparhraun 0.4 km^3 1950–2050 yrBP							
456723	Peate et al. (2009)	63.94	-22.13	7.67	6.11	1.04	2.35
RP2	Koornneef et al. (2012)	64.016	-22.17	7.56	6.2	1.08	2.3
Arnarseturhraun 0.48 km^3 760–790 yrBP							
408673	Peate et al. (2009)	63.87	-22.52	6.6	9.19	1.65	2.67
456722	Peate et al. (2009)	63.92	-22.43	6.95	8.69	1.52	2.74
H36	Kokfelt et al. (2006)	63.89	-22.42	6.85	8.73	1.56	2.69
H84	Kokfelt et al. (2006)	63.87	-22.51	6.47	8.84	1.7	2.5
NI-8554	Peate et al. (2009)	63.88	-22.46	7.01	8.61	1.5	2.76
RP1	Koornneef et al. (2012)	64.054	-21.99	8.02	8.28	1.12	3.55
RP117A	Gee et al. (1998)	63.87	-22.42	7.02	6.4	1.49	2.06
RP3	Koornneef et al. (2012)	63.928	-22.43	6.9	9.01	1.54	2.81
RP6	Koornneef et al. (2012)	63.822	-22.6	8.52	7.76	0.93	4
RP66D-3F	Gee et al. (1998)	63.95	-22.42	6.93	9.2	1.53	2.89
RP7	Koornneef et al. (2012)	63.819	-22.56	7.6	8.59	1.28	3.23
RP8	Koornneef et al. (2012)	63.909	-22.42	6.87	8.76	1.55	2.71
RP9	Koornneef et al. (2012)	63.89	-22.43	6.91	9	1.54	2.81
Breiddalshraun 0.1 km^3 1000–1100 yrBP							
456732	Peate et al. (2009)	63.93	-21.83	8.0	7.62	0.23	3.25
456733	Peate et al. (2009)	63.93	-21.83	8.11	7.74	0.23	3.42
Eldborgarhraun 0.04 km^3 1900–2400 yrBP							
9810	Brandon et al. (2007); Debaille et al. (2009); Dixon (2003); Nielsen et al. (2007)	63.856	-22.002	10.83	6.02	0.04	5.37
IC215	Hardarson et al. (1997)	63.97	-21.43	7.79	7	0.1	2.79
NI-8629	Peate et al. (2009)	63.97	-22.1	7.77	6.29	0.1	2.49
Fagradalshraun 0.01 km^3 7000–14500 yrBP							

Table A.2 Continued:

Eruption Sample	Reference	Lat. (deg.)	Lon. (deg.)	MgO (wt%)	La (ppm)	V_c (km^3)	La_c (ppm)
9809	Brandon et al. (2007); Debaille et al. (2009); Nielsen et al. (2007)	63.912	-22.295	25.07	0.36	0.01	0.63
RE149	Hardarson et al. (1997)	63.91	-22.29	18.49	0.4	0.01	0.48
Festarfjall 0.05 km^3 14500–30000 yrBP							
RP93A	Gee et al. (1998)	63.85	-22.33	8.63	8.2	0.09	4.42
RP93B	Gee et al. (1998)	63.85	-22.33	8.44	10	0.1	4.99
Fiskidalsfjall 0.15 km^3 14500–30000 yrBP							
RP5	Gee et al. (1998)	63.85957	-22.36466	8.15	5	0.33	2.24
Haleyjabunga 0.013000000000000001 km^3 14000–16300 yrBP							
9805	Brandon et al. (2007); Breddam et al. (2000); Debaille et al. (2009); Nielsen et al. (2007); Peate et al. (2009)	63.82	-22.65	28.63	0.23	0.01	0.51
H80	Kokfelt et al. (2006)	63.82	-22.66	12.38	0.54	0.01	0.51
OS207901	Skovgaard et al. (2001)	63.82	-22.65	24.93	0.57	0.01	0.98
RE291	Hardarson et al. (1997); Kempton et al. (2000)	63.82	-22.65	17.6	1.1	0.01	1.28
RE46	Hardarson et al. (1997)	63.82	-22.65	10.45	0.6	0.01	0.53
RE47	Hardarson et al. (1997)	63.82	-22.65	29.0	1.7	0.01	4.02
RP80A	Gee et al. (1998)	63.82	-22.65	16.63	-	0.01	-
RP80D	Gee et al. (1998); Thirlwall et al. (2004)	63.82	-22.65	16.44	-	0.01	-
rsg54	Hemond et al. (1993)	63.82	-22.682	10.08	0.52	0.01	0.45
Heidin ha 9.8 km^3 10300–12000 yrBP							
IC221	Hardarson et al. (1997)	63.89	-21.97	9.2	4.9	13.8	3.48
IT-313	Sinton et al. (2005)	63.89	-21.65	7.71	7.37	25.21	2.86
IT-404A	Sinton et al. (2005)	63.91	-21.7	7.93	4.15	23.53	1.73
IT-405	Sinton et al. (2005)	64.0	-21.64	7.52	5.36	26.67	1.97

Table A.2 Continued:

Eruption Sample	Reference	Lat. (deg.)	Lon. (deg.)	MgO (wt%)	La (ppm)	V_c (km^3)	La_c (ppm)
Holmshraun 0.16 km^3 2400–14500 yrBP							
RP17	Koornneef et al. (2012)	64.081	-21.7	7.78	7.07	0.4	2.8
Hrolfsvik 0.001 km^3 7000–16300 yrBP							
RE100	Hardarson et al. (1997)	63.97	-21.69	10.94	2.8	0.0	2.51
Hrutafell 0.01 km^3 16300–30000 yrBP							
RP57B-1L	Gee et al. (1998)	63.93	-22.07	8.57	4.1	0.02	2.16
RP57F-1L	Gee et al. (1998)	63.93	-22.07	8.16	2.8	0.02	1.26
Hrutagjardyngja 3.2 km^3 6500–7500 yrBP							
RE119	Jakobsson et al. (1978)	64.0	-22.0	8.33		6.68	
Husafell 0.04 km^3 16300–30000 yrBP							
RP132C	Gee et al. (1998)	64.02	-21.8	9.28	5.4	0.05	4.01
Husfellsbruni 0.3 km^3 900–1100 yrBP							
456740	Peate et al. (2009)	64.01	-21.66	8.24	8.28	0.65	3.84
456741	Peate et al. (2009)	64.01	-21.66	8.25	8.21	0.65	3.82
456742	Peate et al. (2009)	64.02	-21.74	8.34	7.13	0.62	3.43
Kapelluhraun 0.1 km^3 800–850 yrBP							
456745	Peate et al. (2009)	64.02	-21.96	7.73	6.28	0.26	2.46
456746	Peate et al. (2009)	64.02	-21.96	7.76	6.27	0.25	2.47
RP55	Koornneef et al. (2012)	64.043	-22.03	7.55	6.77	0.27	2.51
Keilir 0.1 km^3 16300–30000 yrBP							
RP69C	Gee et al. (1998)	63.95	-22.02	8.92	14.7	0.16	9.04
RP69E	Gee et al. (1998)	63.95	-22.02	8.82	3	0.17	1.76
Lagafell 0.28 km^3 14000–16300 yrBP							

Table A.2 Continued:

Eruption Sample	Reference	Lat. (deg.)	Lon. (deg.)	MgO (wt%)	La (ppm)	V_c (km^3)	La_c (ppm)
408672	Breddam et al. (2000); Peate et al. (2009); Skovgaard et al. (2001)	63.88	-22.53	25.95	0.32	0.15	0.59
H82	Kokfelt et al. (2006)	63.88	-22.53	22.02	0.49	0.19	0.71
H83	Kokfelt et al. (2006)	63.88	-22.53	24.58	0.41	0.17	0.69
Ice2	Brandon et al. (2007); Debaille et al. (2009); Nielsen et al. (2007); Peate et al. (2009)	63.88	-22.53	20.94	0.44	0.21	0.6
RP95C	Gee et al. (1998); Thirlwall et al. (2006, 2004)	63.88	-22.53	11.78	0.5	0.3	0.46
RP95D	Gee et al. (1998)	63.88	-22.53	10.43	-	0.32	-
Langholl 0.8 km^3 16300–30000 yrBP							
RE32	Jakobsson et al. (1978)			9.14		1.16	
RE60	Jakobsson et al. (1978)			9.84		0.93	
RE61	Jakobsson et al. (1978)			9.82		0.93	
Leitahraun 6.3 km^3 5100–5300 yrBP							
IT-16	Sinton et al. (2005)	64.1	-21.5	8.22		13.7	
IT-173	Sinton et al. (2005)	63.96	-21.37	8.44		12.61	
IT-192	Sinton et al. (2005)	63.94	-21.33	8.4		12.81	
IT-302	Sinton et al. (2005)	64.12	-21.67	9.09		9.41	
IT-303	Sinton et al. (2005)	64.11	-21.63	9.26		8.57	
IT-314	Sinton et al. (2005)	64.06	-21.54	8.25		13.55	
IT-315	Sinton et al. (2005)	64.05	-21.54	8.1		14.29	
IT-332	Sinton et al. (2005)	63.92	-21.81	8.97		10.0	
Mavahlidarhraun 0.1 km^3 800–850 yrBP							
NI-11140	Peate et al. (2009)	63.97	-22.52	7.65	6.89	0.26	2.63
Ogmundarhraun 0.3 km^3 830–860 yrBP							
408666	Peate et al. (2009)	63.86	-22.17	7.77	6.33	0.76	2.51
RP10	Koornneef et al. (2012)	63.854	-22.23	7.56	6.52	0.81	2.42
RP56	Koornneef et al. (2012)	63.859	-22.16	7.66	6.36	0.78	2.43

Table A.2 Continued:

Eruption Sample	Reference	Lat. (deg.)	Lon. (deg.)	MgO (wt%)	La (ppm)	V_c (km^3)	La_c (ppm)
Sandfell 0.1 km^3 16300–30000 yrBP							
RP101A	Gee et al. (1998)	63.87	-22.57	11.05	4.6	0.11	4.13
RP115J	Gee et al. (1998); Thirlwall et al. (2004)	63.9	-22.22	9.84	8.1	0.12	6.98
RP134A	Gee et al. (1998)	63.97	-21.97	6.86	4	0.32	1.24
RP134C	Gee et al. (1998)	63.97	-21.97	8.72	3.7	0.18	2.08
Sandfellshaed 4.8 km^3 13500–13700 yrBP							
RP59H	Gee et al. (1998)	63.97	-22.4	9.53	2.7	5.63	2.3
RP59J-1F	Gee et al. (1998)	63.97	-22.4	9.09	3.1	7.17	2.08
RP59N-2F	Gee et al. (1998)	63.97	-22.4	8.55	2.8	9.2	1.46
RP96F	Gee et al. (1998)	63.85	-22.43	7.73	2.2	12.28	0.86
Skala-Maelifell 0.02 km^3 16300–30000 yrBP							
RP42N-1P	Gee et al. (1998)	63.85	-22.27	10.53	7.9	0.02	6.97
RP42P-2P	Gee et al. (1998); Thirlwall et al. (2006, 2004)	63.85	-22.27	9.7	9.5	0.02	8.15
Skalafell 0.15 km^3 8000–9000 yrBP							
RP80C	Gee et al. (1998); Thirlwall et al. (2006)	63.82	-22.65	8.15	2	0.33	0.9
Slaga 0.2 km^3 16300–30000 yrBP							
RP43A	Gee et al. (1998)	63.85	-22.27	10.22	7.6	0.23	6.64
RP51A	Gee et al. (1998)	63.85	-22.3	8.8	8.8	0.34	5.11
RP51B	Gee et al. (1998)	63.85	-22.3	8.86	8.7	0.33	5.2
RP51C-P	Gee et al. (1998)	63.85	-22.3	8.84	9	0.34	5.33
RP51D	Gee et al. (1998)	63.85	-22.3	8.83	8.3	0.34	4.89
RP51E	Gee et al. (1998)	63.85	-22.3	8.63	8.6	0.37	4.64
RP51G	Gee et al. (1998)	63.85	-22.3	8.17	8	0.44	3.61

Table A.2 Continued:

Eruption Sample	Reference	Lat. (deg.)	Lon. (deg.)	MgO (wt%)	La (ppm)	V_c (km^3)	La_c (ppm)
Stamparhraun yngra 0.01 km^3 750–800 yrBP							
456714	Peate et al. (2009)	63.83	-22.71	7.43	6.16	0.03	2.21
456716	Peate et al. (2009)	63.83	-22.71	7.63	5.34	0.03	2.03
RP5	Koornneef et al. (2012)	63.83	-22.71	7.35	6.01	0.03	2.1
Stapafell 0.5 km^3 16300–30000 yrBP							
456712	Peate et al. (2009)	63.91	-22.53	8.39	10.27	1.02	5.03
456749	Peate et al. (2009)	63.91	-22.53	12.28	9.01	0.53	8.45
456749g	Peate et al. (2009)	63.91	-22.53	8.4	9.26	1.02	4.55
Ice3	Brandon et al. (2007); Breddam et al. (2000); Debaille et al. (2009); Nielsen et al. (2007); Peate et al. (2009)	63.911	-22.522	18.19	7.11	0.42	8.47
RP1A	Gee et al. (1998); Thirlwall et al. (2006)	63.95	-22.53	9.56	7.3	0.59	6.24
RP1B	Gee et al. (1998)	63.95	-22.53	18.7	5.3	0.41	6.47
RP1C	Gee et al. (1998)	63.95	-22.53	8.84	9.3	0.84	5.51
RP67A-1	Gee et al. (1998)	63.95	-22.53	9.07	5.2	0.75	3.45
RP67B2-2	Gee et al. (1998)	63.95	-22.53	9.19	12	0.71	8.48
RP67E-3	Gee et al. (1998); Thirlwall et al. (2006, 2004)	63.95	-22.53	14.04	5	0.5	5.01
RP67F-4	Gee et al. (1998)	63.95	-22.53	9.42	8.2	0.62	6.64
RP67G-4	Gee et al. (1998)	63.95	-22.53	10.41	10.6	0.57	9.31
RP67HB-5	Gee et al. (1998)	63.95	-22.53	12.8	5.6	0.52	5.35
RP67J-6	Gee et al. (1998)	63.95	-22.53	9.33	5	0.65	3.83
Stora-Eldborg 0.08 km^3 5000–6000 yrBP							
RP64D	Gee et al. (1998)	63.85	-22.0	11.35	4.3	0.09	3.9
Strompahraun 0.36 km^3 4500–6000 yrBP							
RP109B	Gee et al. (1998)	63.98	-21.63	8.9	4.6	0.59	2.8

Table A.2 Continued:

Eruption Sample	Reference	Lat. (deg.)	Lon. (deg.)	MgO (wt%)	La (ppm)	V_c (km^3)	La_c (ppm)
Sulur 0.2 km^3 16300–30000 yrBP							
RP56B-1H	Gee et al. (1998)	63.92	-22.55	10.92	8.2	0.22	7.33
RP56DD-2H	Gee et al. (1998)	63.92	-22.55	9.14	8	0.29	5.5
RP56DH-2DH	Gee et al. (1998)	63.92	-22.55	10.04	7.7	0.23	6.68
RP56E	Gee et al. (1998)	63.92	-22.55	14.05	6.5	0.2	6.51
Svinahraunsbruni 0.1 km^3 900–1100 yrBP							
456736	Peate et al. (2009)	64.04	-21.45	9.3	8.14	0.13	6.12
456737	Peate et al. (2009)	64.02	-21.48	8.95	8.76	0.16	5.46
IT-15	Sinton et al. (2005)	64.06	-21.45	9.21	7.86	0.14	5.61
WV16	Koornneef et al. (2012)	64.028	-21.45	9.38	8.21	0.13	6.46
Thrainsskjoldur 5.2 km^3 13000–15000 yrBP							
RE56	Jakobsson et al. (1978)	63.92	-22.25	10.06		5.99	
RE57	Jakobsson et al. (1978)	63.92	-22.25	9.77		6.05	
RE70	Jakobsson et al. (1978)	63.92	-22.25	9.47		6.22	
RE71	Jakobsson et al. (1978)	63.92	-22.25	10.0		6.0	
Thrihnukahraun eldra 0.24 km^3 4500–7000 yrBP							
	Sólnes et al. (2013)	64.01	-21.82				
Tvibollahraun 0.04 km^3 1000–1100 yrBP							
456743	Peate et al. (2009)	63.99	-21.79	8.14	7.81	0.09	3.49
456744	Peate et al. (2009)	64.02	-21.87	7.75	6.2	0.1	2.44
456747	Peate et al. (2009)	64.03	-21.95	8.18	7.58	0.09	3.44
Vatnsheidi 0.14 km^3 13000–16300 yrBP							
208222	Peate et al. (2009); Skovgaard et al. (2001)	63.84	-22.43	16.38	1.11	0.13	1.22

Table A.2 Continued:

Eruption Sample	Reference	Lat. (deg.)	Lon. (deg.)	MgO (wt%)	La (ppm)	V_c (km^3)	La_c (ppm)
9806	Brandon et al. (2007, 2000); Debaille et al. (2009); Nielsen et al. (2007)	63.844	-22.391	15.27	1.22	0.13	1.28
D8B-1	Fitton et al. (2003); Hemond et al. (1993)	63.84	-22.43	17.82	1.02	0.12	1.2
RE78	Hardarson et al. (1997)	63.84	-22.43	19.0	1.3	0.11	1.61
RP82A	Gee et al. (1998)	63.85	-22.37	11.28	1.2	0.15	1.09
RP82B	Gee et al. (1998)	63.85	-22.37	12.54	0.1	0.15	0.09
RP82C	Gee et al. (1998); Thirlwall et al. (2006, 2004)	63.85	-22.37	10.12	1.5	0.16	1.31
RP82D	Gee et al. (1998); Thirlwall et al. (2004)	63.85	-22.37	11.31	0.9	0.15	0.82

Table A.3 Rock sample data from eruption units in the Western Volcanic Zones used in Chapter 5. Name of each eruption unit is in bold font with the estimated eruption volume and age bounds following after when available. V_c and La_c are the eruption volume and the La concentration after the crystallization correction (see Section 5.4.2).

Eruption Sample	Reference	Lat. (deg.)	Lon. (deg.)	MgO (wt%)	La (ppm)	V_c (km^3)	La_c (ppm)
Armannsfell 5.31 km^3 13200–30000 yrBP							
IC91	Hardarson et al. (1997)	64.32	-21.05	9.07	6.7	8.01	4.44
IC92	Hardarson et al. (1997)	64.32	-21.05	9.89	6.6	6.15	5.7
IC94	Hardarson et al. (1997)	64.32	-21.05	8.5	5.9	10.38	3.02
IC95	Hardarson et al. (1997)	64.32	-21.05	8.72	6.7	9.47	3.76
IC96	Hardarson et al. (1997)	64.32	-21.05	8.65	7.0	9.76	3.81
Arnarfell 0.2 km^3 13200–30000 yrBP							
DICE9	Burnard and Harrison (2005)	64.216	-21.073	7.53		0.54	
Asar 0.2 km^3 9500–10200 yrBP							
208224	Peate et al. (2009); Skovgaard et al. (2001)	63.97	-21.42	13.3	0.63	0.21	0.61
9812	Brandon et al. (2007); Debaille et al. (2009); Nielsen et al. (2007)	63.909	-21.398	16.06	0.55	0.18	0.6
D27	Skovgaard et al. (2001)	63.97	-21.42	13.8	0.59	0.2	0.59
Bitra 0.7 km^3 12000–14500 yrBP							
IS-6	Eason et al. (2015)	64.063	-21.2789	7.4	5.07	1.97	1.8
IS-7	Eason et al. (2015)	64.0568	-21.2751	7.72	5.62	1.8	2.19
Brunnar Skogarkot 1.2 km^3 8200–10200 yrBP							
IT-131	Eason et al. (2015); Sinton et al. (2005)	64.3	-21.07	10.52	3.62	1.36	3.19
IT-167	Sinton et al. (2005)	64.32	-21.05	9.29	4.32	1.6	3.23
Burfell 0.1 km^3 9500–10200 yrBP							
D26	Peate et al. (2009); Skovgaard et al. (2001)	63.95	-21.47	11.45	1.09	0.11	0.99
Dimmadalshaed 0.06 km^3 9500–14500 yrBP							

Table A.3 Continued:

Eruption Sample	Reference	Lat. (deg.)	Lon. (deg.)	MgO (wt%)	La (ppm)	V_c (km^3)	La_c (ppm)
OS208225	Peate et al. (2009); Skovgaard et al. (2001)	64.08	-21.11	11.36	0.79	0.07	0.71
Eiriksjokull 48.2 km^3 10300–12000 yrBP							
IS-91	Eason et al. (2015)	64.7566	-20.5362	7.85	2.32	118.74	0.94
IS-92	Eason et al. (2015)	64.7606	-20.5213	6.71	2.58	161.71	0.77
Eldborgir 1.6 km^3 6100–7800 yrBP							
IT-98	Sinton et al. (2005)	64.26	-20.97	9.17	6.2	2.29	4.33
Fanntofell 0.7 km^3 14500–30000 yrBP							
IS-99	Eason et al. (2015)	64.5356	-20.9428	11.09	12.46	0.78	11.21
Geitafell 1.0 km^3 11400–30000 yrBP							
IS-30	Eason et al. (2015)	63.9454	-21.5062	8.06	12.21	2.3	5.31
IS-31	Eason et al. (2015)	63.9412	-21.518	7.33	13.07	2.87	4.55
Geitlandshraun I 0.1 km^3 1100–12000 yrBP							
502	Kokfelt et al. (2006)	64.71	-20.81	9.79	2.92	0.12	2.51
502b	Kokfelt et al. (2006)	64.7	-20.79	10.01	2.78	0.12	2.41
Geitlandshraun II 1.5 km^3 8800–9000 yrBP							
IT-250	Sinton et al. (2005)	64.74	-20.88	9.7		1.75	
IT-254	Sinton et al. (2005)	64.7	-20.61	8.89		2.48	
IT-267	Sinton et al. (2005)	64.76	-20.8	9.6		1.75	
IT-268	Sinton et al. (2005)	64.72	-20.72	10.17		1.72	
IT-269	Sinton et al. (2005)	64.7	-20.68	9.4		1.88	
Geitlandsjokull 5.2 km^3 12000–14500 yrBP							
IS-108	Eason et al. (2015)	64.5913	-20.6558	8.37	6.69	10.7	3.25
IS-110	Eason et al. (2015)	64.5811	-20.6348	7.33	5.92	14.92	2.06
Gjabakkahraun 1.1 km^3 8900–9700 yrBP							
IT-82R	Sinton et al. (2005)	64.27	-21.03	7.43	6.01	3.07	2.15
IT-87	Sinton et al. (2005)	64.27	-21.05	8.63	5.47	2.04	2.95

Table A.3 Continued:

Eruption Sample	Reference	Lat. (deg.)	Lon. (deg.)	MgO (wt%)	La (ppm)	V_c (km^3)	La_c (ppm)
Hafnarhraun 4.2 km^3 9500–10200 yrBP							
IT-308	Sinton et al. (2005)	63.89	-21.38	8.25		9.03	
IT-316	Sinton et al. (2005)	64.05	-21.54	9.82		4.88	
ThN23-1	Sinton et al. (2005)	63.88	-21.39	8.64		7.75	
ThN23-2	Sinton et al. (2005)	63.88	-21.39	8.91		6.86	
ThN23-3	Sinton et al. (2005)	63.88	-21.39	7.86		10.31	
ThN23-4	Sinton et al. (2005)	63.88	-21.39	9.08		6.31	
ThN23-5	Sinton et al. (2005)	63.88	-21.39	8.68		7.62	
ThN38-1	Sinton et al. (2005)	63.91	-21.4	8.86		7.03	
ThN38-2	Sinton et al. (2005)	63.91	-21.4	8.41		8.51	
ThN38-3	Sinton et al. (2005)	63.91	-21.4	9.1		6.24	
ThN38-4	Sinton et al. (2005)	63.91	-21.4	9.04		6.44	
Hagafell shield 4.5 km^3 10300–12000 yrBP							
IT451A	Sinton et al. (2005)	64.58	-20.33	8.94		7.25	
IT453A	Sinton et al. (2005)	64.57	-20.34	8.28		9.57	
IT455	Sinton et al. (2005)	64.54	-20.36	8.76		7.88	
Hagafellshraun 0.03 km^3 5200–5700 yrBP							
IT451B	Sinton et al. (2005)	64.58	-20.33	7.82		0.07	
IT453B	Sinton et al. (2005)	64.57	-20.34	7.57		0.08	
IT454	Sinton et al. (2005)	64.56	-20.34	7.54		0.08	
MIL-89	Sinton et al. (2005)	64.56	-20.34	7.54		0.08	
Hagavikurhraun 0.4 km^3 5600–5800 yrBP							
IT-19	Sinton et al. (2005)	64.06	-21.28	7.93	6.06	0.96	2.52
Hallmundarhraun 3.4 km^3 1050–1150 yrBP							
503	Kokfelt et al. (2006)	64.74	-20.83	9.16	2.14	4.89	1.49
IC106	Hardarson et al. (1997)	64.81	-20.55	9.21	3.2	4.76	2.29
IC108	Hardarson et al. (1997)	64.81	-20.55	10.41	5.5	3.87	4.83
MIL10	Chauvel and Hémond (2000)	64.78	-20.72	24.58	3.92	2.02	6.61
WV30	Koornneef et al. (2012)	64.728	-20.92	9.11	4.2	5.03	2.84

Table A.3 Continued:

Eruption Sample	Reference	Lat. (deg.)	Lon. (deg.)	MgO (wt%)	La (ppm)	V_c (km^3)	La_c (ppm)
WV31	Koornneef et al. (2012)	64.745	-20.84	9.41	7.9	4.23	6.36
Hellisheidi 1.2 km^3 10200–10400 yrBP							
IT-18	Sinton et al. (2005)	64.05	-21.35	8.12		2.7	
Hestfjall 1.7 km^3 12000–14500 yrBP							
IS-10A	Eason et al. (2015)	64.0197	-20.6744	8.42	7.1	3.43	3.52
IS-17B	Eason et al. (2015)	64.0118	-20.6904	7.41	10.19	4.77	3.63
IS-27	Eason et al. (2015)	63.9872	-20.6702	8.67	7.01	3.1	3.85
Hlodufell 3.9 km^3 10200–11200 yrBP							
IC80	Hardarson et al. (1997)	64.42	-20.55	11.88	2.3	4.22	2.13
IS-127	Eason et al. (2015)	64.4203	-20.5342	6.15	7.62	14.79	2.01
IS-66	Eason et al. (2015)	64.4026	-20.5473	8.21	5.49	8.51	2.52
Hognhofdi 3.8 km^3 9900–10500 yrBP							
IS-69A	Eason et al. (2015)	64.3486	-20.539	8.32	9.22	7.96	4.4
Hrafnabjorg 1.5 km^3 14500–30000 yrBP							
IS-1	Eason et al. (2015)	64.2636	-20.9172	7.63	9.83	3.95	3.73
IS-3	Eason et al. (2015)	64.2726	-20.9216	7.95	9.54	3.58	4.0
Hromundartindar 0.2 km^3 14500–30000 yrBP							
DICE43	Burnard and Harrison (2005)	64.084	-21.189	6.89		0.64	
Hrutfell 11.5 km^3 14500–70000 yrBP							
IS-104	Eason et al. (2015)	64.7207	-19.7152	7.83	5.67	28.51	2.29
IS-107	Eason et al. (2015)	64.7233	-19.7777	8.41	8.02	23.29	3.96
Hvalfell 2.9 km^3 14500–70000 yrBP							
IS-37A	Eason et al. (2015)	64.3895	-21.235	8.63	9.3	5.38	5.02
Jarlhettur 0.1 km^3 10200–30000 yrBP							
HS-603	Sigurdsson et al. (1978)	64.46	-20.25	11.91	5.9	0.11	5.46

Table A.3 Continued:

Eruption Sample	Reference	Lat. (deg.)	Lon. (deg.)	MgO (wt%)	La (ppm)	V_c (km^3)	La_c (ppm)
Jokulkrokur 0.1 km^3 5700–7800 yrBP							
IT-407	Sinton et al. (2005)	64.85	-19.76	9.1		0.15	
IT-408	Sinton et al. (2005)	64.85	-19.77	8.82		0.17	
IT-409	Sinton et al. (2005)	64.85	-19.77	8.72		0.18	
Jokullstallar 8.1 km^3 10300–12000 yrBP							
IT-349B	Sinton et al. (2005)	64.93	-20.09	10.08		9.32	
IT-351A	Sinton et al. (2005)	64.91	-20.07	9.4	3.19	10.14	2.55
IT-412	Sinton et al. (2005)	64.96	-20.01	8.4	4.11	16.47	2.02
Kalfstindar 1.1 km^3 14500–30000 yrBP							
DICE15	Burnard and Harrison (2005)	64.231	-20.931	7.61		2.92	
IS-122A	Eason et al. (2015)	64.3742	-20.4747	9.63		1.28	
Kjalfell 0.8 km^3 10300–12000 yrBP							
IS-43	Eason et al. (2015)	64.7748	-19.5191	9.28	4.64	1.08	3.45
IS-46B	Eason et al. (2015)	64.7805	-19.538	9.04	4.23	1.23	2.76
Kjalhraun 6.0 km^3 7700–7900 yrBP							
HS-619	Sigurdsson et al. (1978)	64.84	-19.65	8.87	3.4	9.99	2.04
IC120	Hardarson et al. (1997)	64.79	-19.56	10.32	3.6	6.85	3.15
mil25	Hemond et al. (1993)	64.86	-19.56	10.19	3.41	6.88	2.97
Krakshraun 0.5 km^3 4000–5200 yrBP							
HS-609	Sigurdsson et al. (1978)	65.03	-19.75	11.94	3.6	0.54	3.34
MIL27	Hardarson et al. (1997)	64.99	-19.84	9.33	3.4	0.65	2.6
MIL27	Hardarson et al. (1997)	64.99	-19.84	8.84	3.73	0.84	2.21
Krakur 0.8 km^3 10300–12000 yrBP							
IS-116	Eason et al. (2015)	64.9664	-19.8683	8.62	4.41	1.49	2.37
Lambahraun 7.3 km^3 3900–4100 yrBP							
H13	Kokfelt et al. (2006)	64.41	-20.25	7.73	8.2	18.67	3.21

Table A.3 Continued:

Eruption Sample	Reference	Lat. (deg.)	Lon. (deg.)	MgO (wt%)	La (ppm)	V_c (km^3)	La_c (ppm)
HS-629	Sigurdsson et al. (1978)	64.28	-20.44	8.81	7.3	12.5	4.26
IC77	Hardarson et al. (1997)	64.46	-20.41	7.75	7.7	18.55	3.03
IT-181	Sinton et al. (2005)	64.39	-20.57	9.17	6.26	10.45	4.37
IT-182	Sinton et al. (2005)	64.42	-20.55	7.75	8.54	18.55	3.36
IT-184	Sinton et al. (2005)	64.49	-20.45	6.67	8.07	24.72	2.38
Leggjabrjotur 6.3 km^3 10300–12000 yrBP							
IT-439	Sinton et al. (2005)	64.75	-19.74	9.04	2.74	9.66	1.79
IT-441	Sinton et al. (2005)	64.74	-19.85	8.15	3.18	14.04	1.43
Litla-Bjornsfell 0.4 km^3 14500–30000 yrBP							
IS-80B	Eason et al. (2015)	64.4936	-20.7753	9.18	6.92	0.57	4.86
Maelifell 0.4 km^3 13200–30000 yrBP							
ICE-4a	Brandon et al. (2007); Debaille et al. (2009); Nielsen et al. (2007)	64.111	-21.196	25.55	0.61	0.22	1.1
ICE-4b	Brandon et al. (2007); Debaille et al. (2009); Nielsen et al. (2007)	64.111	-21.196	24.11	0.65	0.24	1.06
Midfell 0.19 km^3 13200–30000 yrBP							
DMF-9101	Brandon et al. (2007); Debaille et al. (2009); Nielsen et al. (2007)	64.177	-21.047	22.59	0.57	0.13	0.85
IC70	Hardarson et al. (1997)	64.19	-21.03	9.92	6.5	0.22	5.62
ICE-5	Brandon et al. (2007); Debaille et al. (2009); Nielsen et al. (2007)	64.175	-21.049	18.91	0.66	0.15	0.81
NE Langjokull 0.1 km^3 5500–7800 yrBP							
IT-236	Sinton et al. (2005)	64.89	-19.75	8.86		0.17	
IT-237	Sinton et al. (2005)	64.89	-19.74	8.82		0.17	
IT-238	Sinton et al. (2005)	64.89	-19.73	8.91		0.16	
IT-239	Sinton et al. (2005)	64.89	-19.72	8.95		0.16	

Table A.3 Continued:

Eruption Sample	Reference	Lat. (deg.)	Lon. (deg.)	MgO (wt%)	La (ppm)	V_c (km^3)	La_c (ppm)
N Langjokull 5.3 km^3 10300–12000 yrBP							
IT-369	Sinton et al. (2005)	64.95	-19.89	9.72	2.37	6.17	2.04
IT-370	Sinton et al. (2005)	64.95	-19.9	9.13	2.26	7.75	1.55
Nesjahraun 0.4 km^3 1700–1900 yrBP							
H11	Kokfelt et al. (2006)	64.12	-21.25	7.64	6.83	1.05	2.6
IT-21	Sinton et al. (2005)	64.16	-21.24	7.71	7.07	1.03	2.75
RP112C	Gee et al. (1998)	64.13	-21.22	7.8	5.4	1.0	2.16
RP15	Koornneef et al. (2012)	63.956	-21.45	7.79	7.06	1.01	2.81
RSG35	Chauvel and Hémond (2000)	64.12	-21.27	6.92	6.82	1.28	2.14
WV27	Koornneef et al. (2012)	64.124	-21.25	7.81	6.9	1.0	2.76
Raudafell 4.1 km^3 14500–70000 yrBP							
IS-123	Eason et al. (2015)	64.3293	-20.5667	9.5	9.78	4.81	8.34
IS-73	Eason et al. (2015)	64.3308	-20.5931	9.33	8.82	5.35	6.75
Sandkulufell 0.21 km^3 10000–30000 yrBP							
BL4	Hemond et al. (1993)	64.98	-19.65	11.23	6.53	0.23	5.9
HS-611	Sigurdsson et al. (1978)	65.0	-19.64	7.94	4.9	0.5	2.05
Selvogsheidi 0.8 km^3 10200–14500 yrBP							
IC217	Hardarson et al. (1997)	63.92	-21.58	8.56	9.1	1.53	4.77
IC218	Hardarson et al. (1997)	63.92	-21.58	7.8	3.1	2.0	1.24
Skjaldbreidur I 2.7 km^3 8900–9500 yrBP							
H34	Kokfelt et al. (2006)	64.44	-20.94	8.34	5.89	5.62	2.83
IC81	Hardarson et al. (1997)	64.42	-20.8	7.99	3.3	6.36	1.4
IT-143	Sinton et al. (2005)	64.47	-20.95	8.2	5.23	5.91	2.39
IT-39	Sinton et al. (2005)	64.34	-20.97	9.78	5.08	3.14	4.37
IT-5	Sinton et al. (2005)	64.4	-20.92	9.81	4.04	3.14	3.48
WV18	Koornneef et al. (2012)	64.437	-20.92	9.07	5.41	4.08	3.58
Skjaldbreidur II 10.8 km^3 8900–10200 yrBP							

Table A.3 Continued:

Eruption Sample	Reference	Lat. (deg.)	Lon. (deg.)	MgO (wt%)	La (ppm)	V_c (km^3)	La_c (ppm)
IT-148A	Sinton et al. (2005)	64.45	-20.75	5.63	6.09	45.36	1.45
IT-179	Sinton et al. (2005)	64.42	-20.89	8.13	5.79	24.24	2.58
IT-22B	Sinton et al. (2005)	64.48	-20.76	7.6	5.32	28.72	2.0
MIL15	Chauvel and Hémond (2000)	64.4	-20.76	9.44	3.77	13.18	3.09
WV19	Koornneef et al. (2012)	64.439	-20.87	8.34	5.57	22.48	2.68
WV20	Koornneef et al. (2012)	64.444	-20.78	7.48	6.72	29.71	2.44
WV22	Koornneef et al. (2012)	64.446	-20.69	7.85	6.8	26.61	2.76
Skoflungur 0.9 km^3 5200–5700 yrBP							
IT-30	Sinton et al. (2005)	64.49	-20.52	8.47	6.63	1.78	3.35
IT-48	Sinton et al. (2005)	64.47	-20.64	7.54	7.67	2.44	2.83
IT-49	Sinton et al. (2005)	64.48	-20.63	8.17	6.83	1.99	3.09
WV21	Koornneef et al. (2012)	64.447	-20.65	8.57	6.79	1.71	3.57
WV21B	Koornneef et al. (2012)	64.447	-20.65	7.71	7.9	2.32	3.07
Skrida 3.4 km^3 12000–14500 yrBP							
IS-83	Eason et al. (2015)	64.3672	-20.6677	9.57	3.78	3.98	3.23
IS-84A	Eason et al. (2015)	64.3663	-20.673	8.49	4.25	6.67	2.17
IS-87	Eason et al. (2015)	64.3529	-20.6628	8.57	6.27	6.46	3.3
Stangarhals 0.03 km^3 5700–8900 yrBP							
IT-101	Sinton et al. (2005)	64.16	-21.22	8.13		0.07	
IT-102	Sinton et al. (2005)	64.15	-21.24	8.28		0.06	
Stora-Bjornsfell 2.6 km^3 12000–14500 yrBP							
IS-76A	Eason et al. (2015)	64.4917	-20.7182	8.82	5.31	4.43	3.11
IS-78	Eason et al. (2015)	64.4816	-20.7295	8.73	5.66	4.62	3.19
Stryturhraun 0.2 km^3 5200–5700 yrBP							
IT-359A	Sinton et al. (2005)	64.98	-19.91	8.78		0.35	
IT-359B	Sinton et al. (2005)	64.98	-19.91	8.59		0.38	
IT-374	Sinton et al. (2005)	64.97	-19.93	8.59		0.38	
IT-410	Sinton et al. (2005)	64.96	-19.96	8.65		0.37	

Table A.3 Continued:

Eruption Sample	Reference	Lat. (deg.)	Lon. (deg.)	MgO (wt%)	La (ppm)	V_c (km^3)	La_c (ppm)
Thingvallahraun 4.0 km^3 10100–10300 yrBP							
IC71	Hardarson et al. (1997)	64.27	-21.13	8.03	5.7	9.29	2.45
IT-109	Sinton et al. (2005)	64.23	-21.08	7.84	7.24	9.89	2.93
IT-194	Sinton et al. (2005)	64.31	-21.12	7.18	9.2	11.95	3.08
WV26	Koornneef et al. (2012)	64.145	-21.03	8.81	6.7	6.86	3.9
Thjofahraun 1.0 km^3 3500–3700 yrBP							
IT-133	Sinton et al. (2005)	64.35	-20.98	8.91	8.04	1.63	4.92
IT-144A	Sinton et al. (2005)	64.32	-21.0	7.52	9.45	2.72	3.47
IT-35	Sinton et al. (2005)	64.32	-20.94	8.03	8.61	2.32	3.71
WV25	Koornneef et al. (2012)	64.263	-21.05	8.5	9.4	1.95	4.81
Thorisjokull 10.7 km^3 11300–11900 yrBP							
IS-61	Eason et al. (2015)	64.5338	-20.8194	8.85	1.48	17.99	0.88
IS-64A	Eason et al. (2015)	64.5414	-20.7984	9.75	1.3	12.45	1.12
IS-65A	Eason et al. (2015)	64.5304	-20.8031	8.6	1.46	20.08	0.78
Thorolfsfell 0.3 km^3 10700–30000 yrBP							
IC79	Hardarson et al. (1997)	64.04	-20.51	10.71	3.2	0.34	2.84
Thverfell 1.6 km^3 10000–30000 yrBP							
IC83	Hardarson et al. (1997)	64.47	-21.1	11.98	3.3	1.72	3.06
Tjarnahnukur 0.1 km^3 10300–12000 yrBP							
IT-113	Sinton et al. (2005)	64.11	-21.21	5.51		0.43	
IT-114	Sinton et al. (2005)	64.1	-21.22	5.97		0.39	
Trolladalur 3.2 km^3 10300–12000 yrBP							
IS-55B	Eason et al. (2015)	64.0083	-21.3303	7.6	3.28	8.51	1.23
IS-57A	Eason et al. (2015)	63.9897	-21.3429	8.39	3.41	6.53	1.67

Table A.4 Rock sample data from the Termination I lava shields in the Northern Volcanic Zones used in Chapter 7. Name of each eruption unit is in bold font with the estimated eruption volume and age bounds following after when available.

Eruption Sample	Reference	Lat. (deg.)	Lon. (deg.)	Nb (ppm)	Zr (ppm)	Y (ppm)
Ketildyngja 20.0 km^3 2900–4500 yrBP						
NAL-239	Macpherson et al. (2005)	65.045	-16.7166667	12.4	105.5	24.9
NAL-36	Hemond et al. (1993)	65.421111	-16.67388889	7.6	70	25.2
Kollottadyngja 14.5 km^3 1150–7000 yrBP						
KO01	Maclennan et al. (2001)	65.2	-16.53	8.9	79.6	15.5
KO02	Maclennan et al. (2001)	65.2	-16.53	13.9	117.4	23.9
KO03	Maclennan et al. (2001)	65.2	-16.53	11.2	97.2	24.1
KO04	Maclennan et al. (2001)	65.2	-16.53	11.9	101.9	24.4
KO05	Maclennan et al. (2001)	65.2	-16.53	10.6	91.3	18.7
KO06	Maclennan et al. (2001)	65.19	-16.54	12.2	103.4	24.4
KO07	Maclennan et al. (2001)	65.19	-16.54	9.8	86.1	19.8
KO08	Maclennan et al. (2001)	65.19	-16.54	9.3	85.1	21.3
KO09	Maclennan et al. (2001)	65.2	-16.58	11.1	94.1	20.8
KO10	Maclennan et al. (2001)	65.2	-16.63	13.6	110.4	24.2
KO11	Maclennan et al. (2001)	65.22	-16.65	12.9	108.2	24.5
KO12	Maclennan et al. (2001)	65.22	-16.63	12.9	110.6	26.1

Table A.4 Continued:

Eruption Sample	Reference	Lat. (deg.)	Lon. (deg.)	Nb (ppm)	Zr (ppm)	Y (ppm)
KO13	Maclennan et al. (2001)	65.22	-16.63	13.1	111.8	25
KO14	Maclennan et al. (2001)	65.21	-16.6	11.7	101	24
KO15	Maclennan et al. (2001)	65.22	-16.47	12.2	100.7	23.4
KO16	Maclennan et al. (2001)	65.21	-16.49	9.9	84.3	18.6
KO17	Maclennan et al. (2001)	65.21	-16.49	11	94.8	21.9
KO18	Maclennan et al. (2001)	65.22	-16.51	15.4	127.5	27
KO19	Maclennan et al. (2001)	65.21	-16.51	11.7	101.2	24.7
KO20	Maclennan et al. (2001)	65.22	-16.55	8.3	76.9	19.1
KO21	Maclennan et al. (2001)	65.22	-16.55	12.8	107.3	24.4
KO22	Maclennan et al. (2001)	65.22	-16.55	10.5	93.3	23.3
KO23	Maclennan et al. (2001)	65.22	-16.55	10.2	90.7	23
KO24	Maclennan et al. (2001)	65.22	-16.55	12.5	108.7	27.4
KO24-b	Maclennan et al. (2001)	65.22	-16.55	12.5	108.7	27.4
KO25	Maclennan et al. (2001)	65.19	-16.55	11.5	102.4	25
KO26	Maclennan et al. (2001)	65.19	-16.55	10.9	94.9	22.6
KO27	Maclennan et al. (2001)	65.19	-16.55	9.4	83.5	18.6

Table A.4 Continued:

Eruption Sample	Reference	Lat. (deg.)	Lon. (deg.)	Nb (ppm)	Zr (ppm)	Y (ppm)
KO28	Maclennan et al. (2001)	65.19	-16.55	8.8	78.5	18.3
KOT09-1	Shorttle et al. (2013)	65.18925	-16.55205	8.4	73.1	17.7
KOT09-2	Shorttle et al. (2013)	65.18897	-16.55183	11.4	103.5	25.9
KOT09-3	Shorttle et al. (2013)	65.21676	-16.55318	12.4	112.7	26.6
Storavitishraun 18.4 km^3 11000–12000 yrBP						
IT1elliott	Elliott et al. (1991); Slater et al. (2001)	65.88	-16.84	1.6	47.4	17
IT3Aelliott	Elliott et al. (1991); Slater et al. (2001)	65.88	-16.84	4.5	46.5	16.3
NAL20	Chauvel and Hémond (2000)	65.88	-16.84	2.1	34	16.8
SH43xrf	Slater et al. (2001)	65.88	-16.84	NA	45	20
TH03xrf	Slater et al. (2001)	65.93	-17.07	3.9	42.6	19.7
TH16xrf	Slater et al. (2001)	65.88	-16.84	3.5	41.6	17.8
THO5xrf	Slater et al. (2001)	65.93	-17.07	3.6	49.6	20.4
l9330xrf	Slater et al. (2001); Stracke et al. (2003)	65.79	-17.01	3.34	40.4	19.5
l9331	Slater et al. (2001)	65.79	-17.01	3.9	42.2	20.5
l9338	Slater et al. (2001)	65.96	-17.12	2.3	36	17.8
l9339xrf	Slater et al. (2001); Stracke et al. (2003)	65.96	-17.02	2.3	36.6	17.5
l9352	Slater et al. (2001)	65.96	-16.93	1.8	30.8	16.5
l9358	Slater et al. (2001)	65.97	-17.15	2.7	43.1	20.6
l9359	Slater et al. (2001); Stracke et al. (2003)	65.96	-16.99	1.97	36	16.9
l9360	Slater et al. (2001)	65.94	-16.96	2.7	44.3	21.2
l9361	Slater et al. (2001)	65.94	-16.95	2.6	43.1	21

Table A.4 Continued:

Eruption Sample	Reference	Lat. (deg.)	Lon. (deg.)	Nb (ppm)	Zr (ppm)	Y (ppm)
l9385	Slater et al. (2001); Stracke et al. (2003)	65.91	-17.06	2.21	40.7	19
l9388	Slater et al. (2001)	65.9	-17.06	2.2	34.1	17.2
l9389	Slater et al. (2001); Stracke et al. (2003)	65.93	-17.07	2.01	37	17.1
l94101	Slater et al. (2001); Stracke et al. (2003)	65.88	-16.84	2.24	29.3	16.1
l94102	Slater et al. (2001); Stracke et al. (2003)	65.88	-16.84	2.08	27.7	16.2
l94103	Slater et al. (2001)	65.88	-16.84	2.1	28	16.1
sh1	Slater et al. (2001)	65.88	-16.84	NA	45	21
sh19	Slater et al. (2001)	65.88	-16.84	NA	54	20
sh23	Slater et al. (2001)	65.88	-16.84	NA	55	20
sh27	Slater et al. (2001)	65.88	-16.84	NA	63	26
sh40	Slater et al. (2001)	65.88	-16.84	NA	45	20
sh42	Slater et al. (2001)	65.88	-16.84	NA	41	17
Trolladyngja 17.0 km^3 1150–4500 yrBP						
IC38	Hardarson et al. (1997)	64.81	-17.3	7.2	73.9	24.9
Q10	Kokfelt et al. (2006)	64.81	-17.3	12	139	35.7
Q9	Kokfelt et al. (2006)	64.86	-17.6	6.7	74.3	24.4
TRO-53	Macpherson et al. (2005)	64.9	-17.1	NA	NA	NA

Table A.5 Rock sample data from the Termination II lava shields in the Northern Volcanic Zones used in Chapter 7. Name of each eruption unit is in bold font with the estimated eruption volume and age bounds following after when available.

Eruption Sample	Reference	Lat. (deg.)	Lon. (deg.)	Nb (ppm)	Zr (ppm)	Y (ppm)
Grjothals 24.0 km^3						
9346	Slater et al. (1998)	65.834799	-16.551395	2	26.0	15.0
9347	Slater et al. (1998)	65.834799	-16.551395	2	26.0	15.0
9348	Slater et al. (1998)	65.834799	-16.551395	2	25.0	14.0
94118	Slater et al. (1998)	65.834799	-16.551395	5	53.0	17.0
94119	Slater et al. (1998)	65.834799	-16.551395	3	40.0	18.0
94120	Slater et al. (1998)	65.834799	-16.551395	7	70.0	21.0
Herdubreidartogl 7.6 km^3 12000.0–70000.0 yrBP						
44::89	Werner (1994)	65.16	-16.36	NA	47.0	19.0
45::89	Werner (1994)	65.16	-16.36	NA	39.0	13.0
48::89	Werner (1994)	65.16	-16.36	NA	49.0	17.0
Jorundargrjot						
KK16	Nicholson (1990)	65.678367	-16.738398	7.9	87.4	24.8
Vadalda 0.25 km^3 70000.0–210000.0 yrBP						
NAL1	Hardarson et al. (1997)	64.97	-16.5	2.5	25.7	12.1
VA1	Hemond et al. (1993)	64.982	-16.56	2.6	36.2	15.4

Appendix B

Bi-lithological Mantle Source

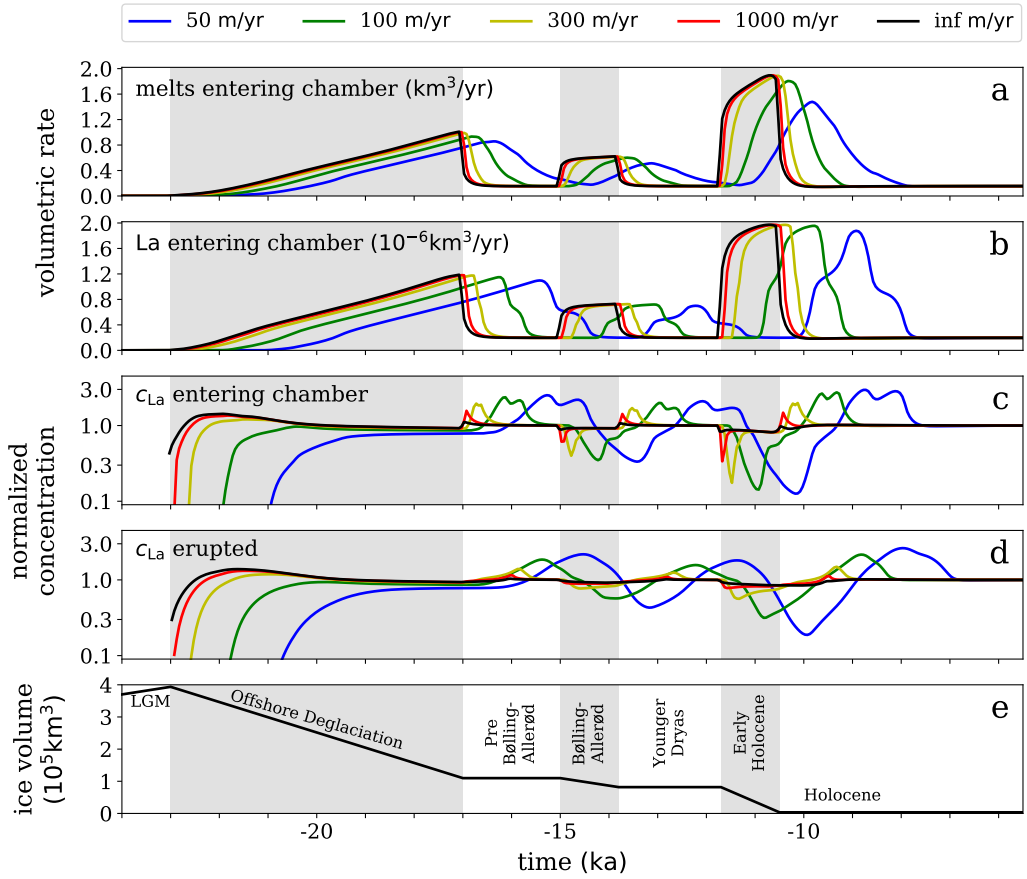

Fig. B.1 Same as Figure 5.8 but with the bi-lithological mantle source of Rudge et al. (2013).

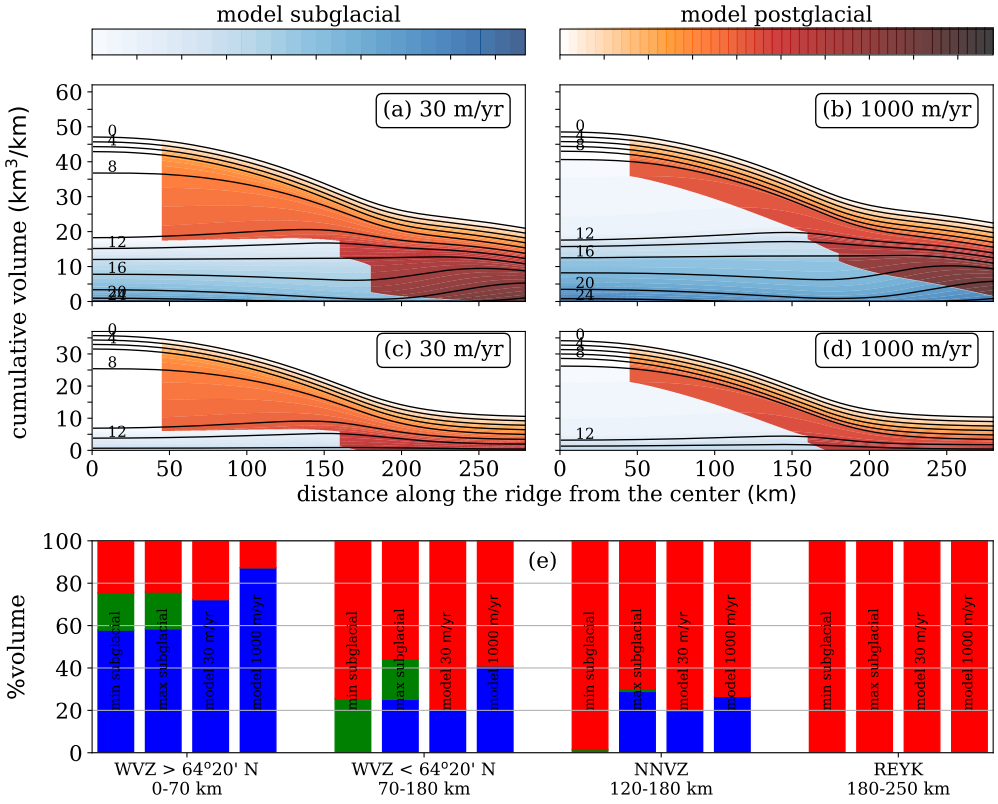

Fig. B.2 Same as Figure 5.10 but with the bi-lithological mantle source of Rudge et al. (2013).

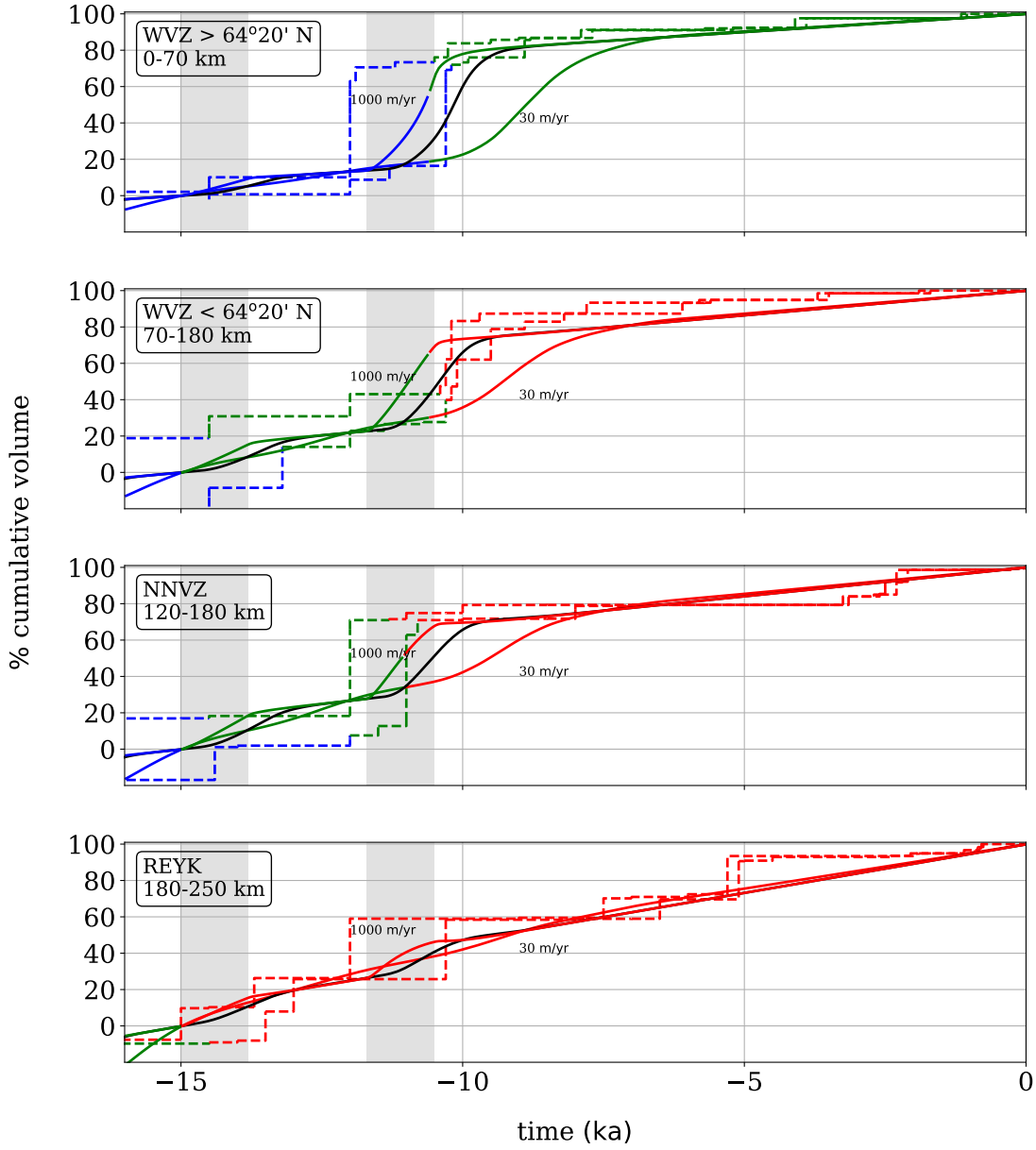

Fig. B.3 Same as Figure 5.11 but with the bi-lithological mantle source of Rudge et al. (2013).

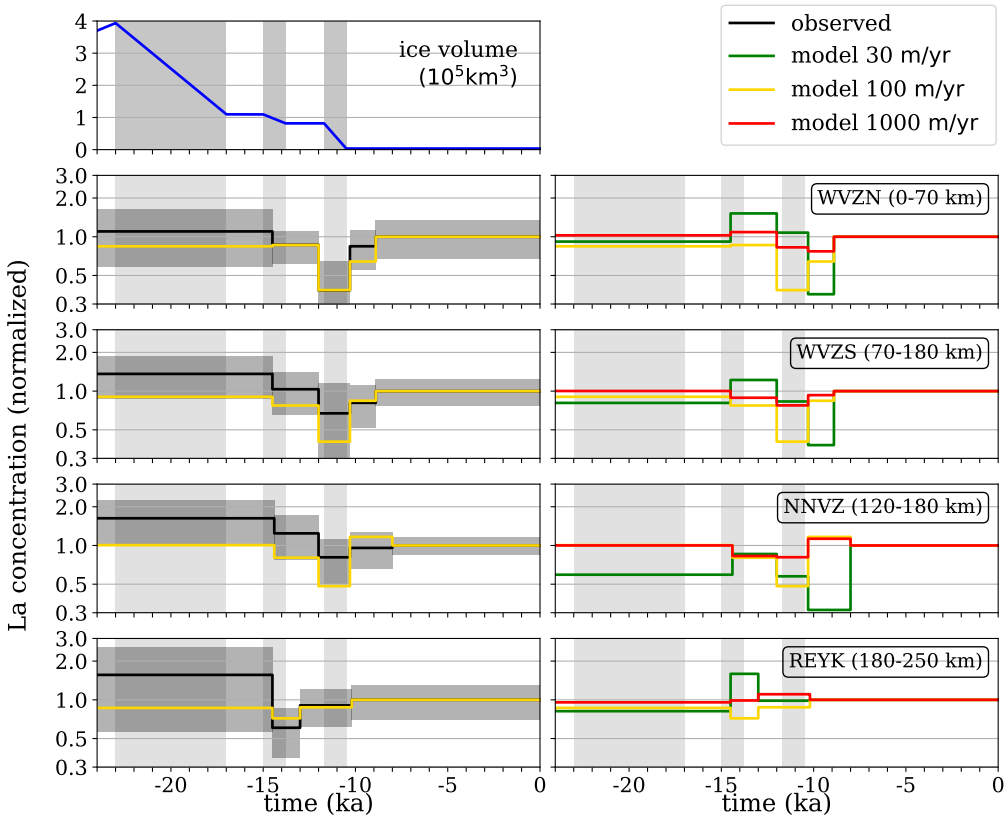

Fig. B.4 Same as Figure 5.12 but with the bi-lithological mantle source of Rudge et al. (2013).